

**Many-body physics in long-range interacting quantum
systems**

by

Bihui Zhu

B.S., Physics, Peking University

M.S., Physics, Chinese Academy of Sciences

A thesis submitted to the
Faculty of the Graduate School of the
University of Colorado in partial fulfillment
of the requirements for the degree of
Doctor of Philosophy
Department of Physics

2017

This thesis entitled:
Many-body physics in long-range interacting quantum systems
written by Bihui Zhu
has been approved for the Department of Physics

Prof. Ana Maria Rey

Prof. Murray J. Holland

Date _____

The final copy of this thesis has been examined by the signatories, and we find that both the content and the form meet acceptable presentation standards of scholarly work in the above mentioned discipline.

Zhu, Bihui (Ph.D., Physics)

Many-body physics in long-range interacting quantum systems

Thesis directed by Prof. Ana Maria Rey

Ultracold atomic and molecular systems provide a useful platform for understanding quantum many-body physics. Recent progresses in AMO experiments enable access to systems exhibiting long-range interactions, opening a window for exploring the interplay between long-range interactions and dissipation. In this thesis, I develop theoretical approaches to study non-equilibrium dynamics in systems where such interplay is crucial.

I first focus on a system of KRb molecules, where dipolar interactions and fast chemical reactions coexist. Using a classical kinetic theory and Monte Carlo methods, I study the evaporative cooling in a quasi-two-dimensional trap, and develop a protocol to reach quantum degeneracy. I also study the case where molecules are loaded into an optical lattice, and show that the strong dissipation induces a quantum Zeno effect, which suppresses the molecule loss. The analysis requires including multiple bands to explain recent experimental measurements, and can be used to determine the molecular filling fraction.

I also investigate a system of radiating atoms, which experience long-range elastic and dissipative interactions. I explore the collective behavior of atoms and the role of atomic motion. The model is validated by comparison with a recent light scattering experiment using Sr atoms. I also show that incoherently pumped dipoles can undergo a dynamical phase transition to synchronization, and study its signature in the quantum regime.

Note: This work was jointly supervised by Prof. Murray Holland.

Dedication

To my Mom.

Acknowledgements

First and foremost, I would like to thank my advisors Prof. Ana Maria Rey and Prof. Murray Holland, for giving me the invaluable opportunity to work with them. Without them the completion of this thesis would have been impossible. I am very grateful for their generous financial support and helpful guidance. Through their encouragement, ingenious ideas and enthusiasm for physics, Ana Maria and Murray have been not only constant sources of inspiration, but also incredible mentors and collaborators to me in the past six years of my life. I feel very fortunate to have had them as my advisors.

I would also like to acknowledge other members of my thesis committee. The courses I took with Prof. Victor Gurarie were my favorites in graduate school. They stimulated my interest in quantum many-body physics. I also benefited from discussions with Prof. James Thompson and Prof. Juan Restrepo, who led me to think from a different angle on the same topic and helped me to expand my knowledge.

I owe special gratitude to Prof. Jun Ye. Jun is one of the most brilliant scientists I have met, with inspiring perspective and ingenious ideas. He also possesses such a great personality, and everyone around him respects and likes him from the bottom of their hearts. It has been my tremendous pleasure to collaborate with him and join his group meetings.

I benefited from interactions with many people, at or outside of JILA. Prof. Deborah Jin was an inspiring and kind collaborator and teacher to me. Prof. Mikhail Lukin, Prof. Susanne Yelin, Prof. Robin Kaiser and Prof. John Cooper helped me to gain a better understanding of light-matter interactions. I would like to thank Goulven Quémener, Sergey Syzranov, Michael Wall,

and Johannes Schachenmayer for the helpful discussions we had.

My years at JILA and University of Colorado have left me with a lot of memories. I would like to thank those who have influenced me in one way or another during these years, although due to the limited space I cannot list all of them. To name just some of them: Bo Yan, Xibo Zhang, Kaden Hazzard, Michael Foss-Feig, Steven Moses, Jake Covey, Sarah Bromley, Bryce Gadway, Norman Yao, Prof. John Bohn, Prof. Matthew Davis, Prof. Darrick Chang, Prof. Alexey Gorshkov, Prof. Leo Radzihovsky, Prof. Juha Javaneinen, Arghavan Safavi-Nani, Leonid Isaev, Tony Lee, Marco Manzoni, Salvatore Manmana, Dong-Ling Deng, Zhe-Xuan Gong, Xiao-Peng Li, Minghui Xu, David Tieri, Dominic Meiser, Yiheng Lin, Shuming Li, Hao Wu, Hao Song and Andrew Koller.

Finally, I am deeply indebted to my parents, for their love and support.

Contents

Chapter

1	Introduction	1
1.1	Quantum many-body physics	1
1.2	Long-range interactions	2
1.3	Dissipation	4
1.4	Outline of this thesis	4
2	Radiating dipoles	8
2.1	Dipolar interactions: origin and characteristics	8
2.2	Near-field and far-field interactions	11
2.3	Superradiance and subradiance	14
3	Evaporative cooling of reactive polar molecules confined in a two-dimensional geometry	16
3.1	Introduction	16
3.2	Evaporative cooling with anisotropic collisions	18
3.2.1	Anisotropic elastic collisions between polar molecules	18
3.2.2	Thermalization rate	19
3.2.3	Evaporation with anisotropic collisions	22
3.3	Evaporative cooling in 2D traps	24
3.4	Evaporative cooling of KRb molecules	25
3.5	Anti-evaporation in quasi-2D	27

3.6	Conclusion	32
4	Suppressing the loss of ultracold molecules via the continuous quantum Zeno effect	34
4.1	Experiment with KRb molecules	36
4.2	Theoretical description	38
4.2.1	Single-band rate equation	38
4.2.2	Multiband rate equation	39
4.2.3	Mean-field and DMRG	40
4.3	Comparison with experiment measurement	41
4.3.1	Mean-field vs. experiment	41
4.4	Conclusion	42
5	Synchronization of Interacting Quantum Dipoles	44
5.1	Introduction	44
5.2	Dipole-dipole interaction and master equation	47
5.3	Mean-field treatment and connection to the Kuramoto model	48
5.4	Quantum synchronization for the collective system	52
5.4.1	Phase Diagram	52
5.4.2	Quantum correlations and entanglement	53
5.5	Synchronization with finite-range interactions	55
5.6	Synchronization of dipoles with elastic interactions	57
5.7	Experimental implementation	59
5.8	Conclusion	61
6	Light scattering from dense cold atomic media	63
6.1	Introduction	63
6.2	Coherent dipole model	66
6.2.1	Equations of motion for coherent dipoles	66

6.2.2	Collective effects in fluorescence	67
6.2.3	Anisotropic features of scattered light	73
6.3	Random walk model	74
6.4	Role of atomic motion	78
6.4.1	Modified frozen dipole model	78
6.4.2	Semi-classical approach	80
6.5	Comparison with experiment	83
6.6	Conclusion	88
7	Emergent Weyl excitations in systems of polar particles	90
7.1	Introduction	90
7.2	Phenomenological argument	91
7.3	Model	92
7.4	Atoms in a deep lattice	93
7.5	Effects of quenched disorder and dissipation	96
7.6	Proposal for experimental observation	97
7.7	Conclusion	99
	Bibliography	100
	Appendix	
A	Theoretical approaches for evaporative cooling with long-range interactions	119
A.1	Monte Carlo simulation for evaporative cooling	119
A.2	Kinetics of evaporative cooling in 2D	120
A.3	Master equation approach for losses in a quasi-2D trap	122

B	Modeling dissipative dynamics	124
B.1	Mean-field treatment (MF)	125
B.2	Rate equation (RE)	125
C	Phase coherence and correlations in interacting dipoles	127
C.1	Mean-field approach	127
C.2	Cumulant expansion approach and two-time correlation between dipoles	128
C.3	Conditional evolution, entanglement and quantum correlations	129
D	Combining dipole-dipole interaction and motion	131
D.1	Long-range dipole-dipole interaction, force and diffusion	131
D.2	Effect of motion on single-atom fluorescence	134
E	Calculation of Weyl dispersion	138
E.1	Dispersion near Weyl nodes	138
E.2	Excitation dispersion in a deep lattice	139
E.3	Details of disorder averaging.	141

Tables

Table

3.1	Derived parameters from the fit of Eq. (3.1) for the scattering energies shown in Fig. 3.1.	19
-----	---	----

Figures

Figure

- 2.1 Spatial dependence of dipole-dipole interactions. The diagonal parts of the imaginary (f^{zz}) and real (g^{zz}) dipolar interactions between two dipoles are plotted, for three different interparticle spacings. While both types of interactions depend on geometry, they are nonidentical, and the elastic interactions are highly sensitive to the spatial separation and orientation of the particles. The maximum value for imaginary and real interactions for fixed $|\mathbf{r}_{ab}|$ is denoted as f_{\max} and g_{\max} , respectively. The cone illustrates the magic angle, $\theta_m = \arccos(1/\sqrt{3})$, along which the elastic interactions vanish. 12
- 2.2 Typical transitions relevant for dipolar interactions in several AMO systems. a is the optical lattice spacing estimated from experimental realizations [260, 187, 249, 250]. Different choices of internal states allow us to access different dipolar regimes 13
- 2.3 Dicke states for three atoms. $|e\rangle$ and $|g\rangle$ denote the excited and ground state in the individual atom basis. Also indicated are the decay rates under the dissipator $\hat{J}^+ \hat{J}^-$. States in red colors decays at least at rate $N_e \Gamma$, while the decay rate for states in blue (or black) color is $< N_e \Gamma$ (or $=0$), where N_e denotes the number of excitations in the system. 15

- 3.1 (a) Two-dimensional differential scattering cross-section for elastic collisions as a function of the scattering angle. Four collision energies are shown; $E_c = 1$ nK (blue disk), 10 nK (green diamond), 100 nK (red triangle), and 1 μ K (black star). The induced dipole moment is $d = 0.2$ debye and the harmonic frequency of the one-dimensional confinement potential is $\nu = 23$ kHz, The solid lines show the empirical formula Eq. (3.1). (b) Total scattering cross section for elastic collisions (solid line) and reactive processes (dashed line) as a function of the collision energy for an induced dipole moment of $d = 0.2$ debye and a one dimensional confinement of $\nu = 23$ kHz. The ratio of elastic to reactive is indicated at four different collision energies; $E_c = 1$ nK (blue point), 10 nK (green point), 100 nK (red point), and 1 μ K (black point). (c) Number of collisions κ required for thermalization for different differential scattering cross-sections. The magenta solid line shows Eq. (3.10). The purple circles are results from the MC simulations, and are shown with their small statistical error bars. The four symbols (blue disk, green diamond, red triangle, black star) correspond to the same energies as (a). 19
- 3.2 Increase in phase space density vs truncation parameter η for different $\frac{d\lambda(\phi)}{d\phi}$. Here Ω_0 is the initial phase-space density, and the final phase space density, Ω_f , was calculated when the ratio of molecule numbers was $N_f/N_0 = 0.1$. Blue circles: $\frac{d\lambda(\phi)}{d\phi} = \text{const}$; red crosses: $(\frac{d\lambda(\phi)}{d\phi})_{E_c=1\mu\text{K}}$; green squares: $(\frac{d\lambda(\phi)}{d\phi})_{E_c=100\text{nK}}$; black dotted line: critical phase space density Ω_c for quantum degeneracy. 22
- 3.3 Trajectories of evaporation for (a): $(\frac{d\lambda(\phi)}{d\phi})_{E_c=1\mu\text{K}}$ at $\eta \sim 3.4$ and (b): $\frac{d\lambda(\phi)}{d\phi} = \text{const}$ at $\eta \sim 4.3$, under the same initial conditions as in FIG. 3.2. In comparison with (a), it is apparent that in (b) the temperature T drops faster and the phase-space density Ω increases much more rapidly. 23

- 3.4 Comparison of the efficiency of evaporative cooling in two-dimensional (2D) and three-dimensional (3D) harmonic traps. $\ln(\Omega_f/\Omega_0)$'s are calculated at $N_f/N_0 = 0.1$, and $\zeta = 1/200$. Red (blue) line: 3D (2D) harmonic trap from method in Appendix A.2; red squares: 3D harmonic trap from MC simulation; blue disks: 2D harmonic trap from MC simulation; blue (red) dotted line: Ω_c for a 2D (3D) trap. 26
- 3.5 Evaporative cooling trajectories for KRb molecules inside a 2D trap of $2\pi \times 20$ Hz, with scattering cross-sections as computed in FIG. 3.1(b). The initial temperature was ~ 200 nK, with an initial-phase space density $\Omega_0 \sim 0.1\Omega_c$, and $\eta = 3.8$ 27
- 3.6 Heating due to two-body losses in a two-dimensional harmonic trap. Here (a) and (b) show the MC result in a two-dimensional harmonic trap where all molecules are in the lowest band of the lattice potential. The results for (c) and (d) are obtained with the master equation approach. The blue line assumes only 1 band along the lattice direction is populated. The red dashed line (green dots) assumes 2 (3) bands are populated. N_0 is the initial total molecule number. The initial temperature is chosen to be around 800 nK, so that when two bands are included, there are $\sim 25\%$ of molecules on the second band, and when three bands are included, there are $\sim 19\%$ of molecules on the second band and $\sim 6\%$ on the third band. 29
- 3.7 Collisions between molecules in a quasi-2D trap. (a) intra-band collisions, occurring at rate $\tilde{\Gamma}^{(1)}$. (b) inter-band collisions, occurring at rate $\tilde{\Gamma}^{(2)}$ (see Appendix A.3). 30
- 4.1 (a) A 50:50 mixture of fermionic KRb molecules in two rotational states, $|0, 0\rangle$ (red) and $|1, -1\rangle$ (blue), is prepared in a deep 3D lattice, which is suddenly made shallow along one dimension (y). Along y , molecules tunnel with a rate J/\hbar and have a large on-site loss rate Γ_0 because of chemical reactions. (b) In the Zeno regime, $\hbar\Gamma_0 \gg J$, doubly occupied sites are only virtually populated, and the loss occurs at a significantly slower rate $\Gamma_{\text{eff}} \ll \Gamma_0$ for molecules on adjacent sites. For KRb, a multiband analysis of this process is required for all experimental lattice parameters. 35

- 4.2 (a) Measured number loss of $|\downarrow\rangle$ molecules for an axial (transverse) lattice depth of $V_y = 5 E_R$ ($V_\perp = 25 E_R$) (circles) and best fit using a rate equation (RE), Eq. (4.1) (black dashed line). (b) Number loss rate, κ , as a function of Γ_0 (fixing $J \approx 570$ Hz and varying the bare on-site rate via V_\perp). (c) Number loss rate, κ , versus J for fixed $\Gamma_0 \approx 87$ kHz (varying V_y and adjusting V_\perp accordingly). V_y (V_\perp) was varied from 5 to 16 E_R (20 to 40 E_R). Black circles are experimental measurements (error bars represent one standard error). Green short-dashed lines show solutions of the RE Eq. (4.4) using an effective loss rate Γ_{eff} (single-band approximation). The blue long-dashed line shows the multiband RE using $\tilde{\Gamma}_{\text{eff}}$ in Eq. (4.4). The multiband and single-band RE results were obtained by fixing the filling fraction to be 6%, and 25% respectively. Panels (b) and (c) directly manifest the continuous quantum Zeno effect: in (b) the measured loss rate κ decreases with increasing on-site Γ_0 ; in (c) a fit to the experimental data supports $\kappa \propto J^2$, with a χ^2 (sum of the squared fitting errors) several times smaller than for a linear fit. 37
- 4.3 Comparison of experimental loss dynamics for the deepest considered lattice to MF and t-DMRG calculations. (a) Molecule loss vs. time for $V_\perp = 80 E_R$ and $V_y = 5 E_R$ [Identical conventions/conditions to Fig. 4.2(b)]. The MF matches the experimental data better than the RE (experimental fit). (b) Comparison of t-DMRG simulations ($\chi_{\text{MPS}} = 128$, 2000 trajectories) to MF, for two different cases: i) an identical trap for the two spin states with trap frequency $\omega_\downarrow = \omega_\uparrow = 2\pi \times 38$ Hz; and ii) slightly different trap frequencies $\omega_\downarrow = 2\pi \times 38$ Hz, $\omega_\uparrow = 2\pi \times 34.2$ Hz. Shaded areas indicate the standard error of the mean. 42

- 4.4 (a) Number loss rate, κ , as a function of Γ_0 (same data as Fig. 2(b)). (b) Number loss rate, κ , versus J for fixed Γ_0 (same data as Fig. 2(c)). Black circles are experimental measurements. Blue long-dashed and solid red lines show RE and MF solutions, respectively, using $\tilde{\Gamma}_{\text{eff}}$ (multiband model). The shaded area accounts for $\pm 2\%$ variations around the MF estimate of $f \sim 9\%$ arising from the uncertainty in the initial molecule distribution. 43
- 5.1 Arrays of quantum dipoles spontaneously emit and absorb photons at rate Γ . The photons mediate dipolar interactions between dipoles separated by a distance \mathbf{r}_{ab} with both dissipative, $f(\mathbf{r}_{ab})$, and elastic, $g(\mathbf{r}_{ab})$, components. A repumping source at a rate W provides energy to maintain the oscillations and can be implemented using additional internal states that are not shown. A possible implementation can be realized with cold atoms in an optical lattice. 46
- 5.2 (a) Mean-field phase diagram calculated from the order parameter $0 \leq Z \leq 1/\sqrt{8}$. The insets show snapshots of the tips of the Bloch vectors (red points) for dipoles prepared with random initial phases and then evolved to steady-state in both regimes. (b) Quantum phase diagram calculated from $0 \leq Z_Q \leq 1/\sqrt{8}$. (c) The time evolution of the conditional QFI exhibits entanglement (dashed line: single trajectory, solid line: mean value of a few trajectories). Panel (d) shows the steady state QFI vs W/Γ after averaging over many trajectories. The solid line corresponds to the conditional case, and indicates entanglement over the repumping range where synchronization exists. Upon computing the ensemble average one recovers the reduced density matrix which leads to a calculated QFI below the entanglement witness threshold (dashed line). (c) and (d) are shown for $f_{\text{eff}} = 15\Gamma$. For all panels, $\delta_a = g(\mathbf{r}_{ab}) = 0$ and $f(\mathbf{r}_{ab}) = f_{\text{eff}}/N$ 49

- 5.3 Quantum correlations and total correlations. The total and quantum correlations in the steady state are quantified by the mutual information $0 \leq \mathcal{I} \leq 2$ and quantum discord $0 \leq \mathcal{D} \leq 2$. (a) In the synchronized phase, there are nonzero quantum correlations and classical correlations ($\mathcal{I} - \mathcal{D}$), and both show a dependence on W that qualitatively agree with Z_Q . (b) Even in the thermodynamic limit, quantum correlations remain a significant fraction of the total correlations. For both panels, $\delta_a = g(\mathbf{r}_{ab}) = 0$ and $f(\mathbf{r}_{ab}) = f_{\text{eff}}/N$ 54
- 5.4 (a) Spin-spin correlations, Z_Q^d , in linear clusters containing d dipoles at optimal repumping W for power-law couplings $f(\mathbf{r}_{ab}) = \frac{\Gamma}{4} \left(\frac{a}{r_{ab}}\right)^\alpha$ with lattice spacing a . We set $\delta_a = g(\mathbf{r}_{ab}) = 0$ and consider $N = 900$ dipoles arranged in both linear ($D = 1$) and square lattice ($D = 2$) geometries. For $\alpha \lesssim D$ global synchronization is observed and the order parameter is independent on cluster size d . For $D \lesssim \alpha$ the order parameter starts to clearly decay with increasing d . The magenta line ($Z_Q^d = 0.14$) provides an indicative scale of the boundary between global and local synchronization. The white contour lines provide an indication of the decrease of the synchronized domains with increasing α . (b) Pair wise two-time correlation functions in the steady-state are parametrized by $Z_{a,b}(\tau) = A \cos(\nu\tau) \exp(-\gamma\tau)$ where a is chosen as the central dipole of a linear chain of $N = 200$ dipoles. The dipoles are assigned random detunings δ_a distributed uniformly in $[-\Gamma/2, \Gamma/2]$. The dark blue, red, and light blue symbols correspond to $\alpha = 0, 0.65$ and 2 respectively. The histogram of frequencies ν exhibits similar synchronization regimes than those seen in (a). 57

- 5.5 (a) Synchronization in dipole arrays is demonstrated for $N = 12$ dipoles on a line when subjected to incoherent pumping (optimal rate). In this geometry, regardless of the strong angular variation of g with the lattice spacing a (see contours) the order parameter, Z_Q , (normalized by $Z_Q^{\max} = 1/\sqrt{8}$) exhibits a weak dependence on θ and a and reaches a maximum at $\theta = \theta_m$. (b) The order parameter is computed for $N = 16$ dipoles on a line with $\theta = \theta_m$ and $f_{\text{eff}} = \sum_{a,b \neq a} f(\mathbf{r}_{ab})/(N - 1)$ (symbols), and for a system with constant $f(\mathbf{r}_{ab}) = f_{\text{eff}}/N$ and $g(\mathbf{r}_{ab}) = 0$ (dashed line)s. Similar dependence on W is found for these two different systems. Here the order parameter for dipoles is always smaller in the presence of elastic interactions. 58
- 6.1 Scheme. (a) Microscopic models: random-walk model (left) and coherent dipole model (right). In the random-walk model, a photon is randomly scattered by the atoms. Scattering events are characterized by the incident and outgoing wavevector of the photons and their corresponding polarization. In the coherent dipole model, atoms are coupled by dipole-dipole interactions (G_{ab}) and all atoms contribute to the fluorescence. (b) Experimental setup for measuring the fluorescence from a cloud of atoms. An incident laser drives an atomic transition with a spontaneous emission rate Γ . Atoms absorb and emit light. The detectors collect scattered photons at an angle θ measured from the incident beam direction. 65

6.2 CD model: on-resonance intensity. (a) Angular distribution: due to the constructive interference along the forward direction ($\theta = 0$), the intensity is drastically enhanced within a small angular region. (b)-(c) The intensities for three different directions ($\theta = 0, \pi/10, \pi/2$) are shown as a function of atom number, each normalized to the value at $N = 50$. All are calculated for a spherical cloud of fixed size. The right vertical axes label the intensity for $\theta = \pi/2, \pi/10$. In (b) the OD and the density are relatively low (when $N = 500$, $\tau=2, n_0 k_0^{-3}=0.0015$). The transverse intensity increases $\sim N$, while the forward intensity increases $\sim N^2$, showing a collective enhancement for small window of θ around zero. Outside this narrow angular window the enhancement disappears and the intensity becomes almost θ independent as indicated by the identical behavior observed for two different angles, $\theta = \pi/10$ and $\pi/2$. In (c) the OD and density are relatively large (when $N = 500$, $\tau=10, n_0 k_0^{-3}=0.017$). The rate at which the intensity increases with N slows down in both the forward and transverse direction: with $I \sim N^1$ for $\theta = 0$ and $I \sim N^{0.5}$ for $\theta = \pi/2$, respectively. (d) On-resonance intensity as a function of OD: it is highly suppressed at large OD. Here, the intensity is normalized to the corresponding value at $\tau = 25$ for each direction. 69

- 6.3 CD model: collective broadening. (a) FWHM linewidth as a function of OD. At small OD, the FWHM increases linearly with OD, but as OD increases density effects set in, multiple scattering events become relevant and the linewidth dependence on OD is no longer linear. Two different atom numbers are used for the blue ($N=1000$) and black lines ($N=200$), and the OD is varied by changing the cloud size. For the blue line, $n_0 k_0^{-3} = 0.14$ at $\tau=25$, 0.003 at $\tau=2$. For the black line, the density at the same OD is doubled. With smaller density, the linewidth increases to a larger value in the large OD regime. (b) The line shape at small OD values ($\tau=2$, $n_0 k_0^{-3} = 0.002$) for different angles θ (θ is defined in Fig. 6.1(a)) is mainly Lorentzian. Here the intensity is normalized to the on-resonance intensity for each θ . (c) At large OD ($\tau=20$, $n_0 k_0^{-3} = 0.06$), the fluorescence line shape significantly broadens and stops being Lorentzian. The brown dots for $\theta = 0$ show the Lorentzian fit, which fails to describe the line shape. At intermediate θ , a double-peak structure shows up. For all panels, the cloud shape is spherical. 70
- 6.4 CD model: frequency shift. For small density, the shift calculated from the coherent dipole model (blue line) increases linearly with density as predicted by the mean-field theory. However, when density is large, there is a significant deviation from the mean-field result. When motional effects are taken into account (red line, Doppler width = 5Γ , see Sec. 6.4.1), the non linear suppression of the frequency shift with density is less severe. 71

- 6.5 CD model: finite size scaling. (a) The linewidth is calculated for different number of atoms at the same OD ($\tau=4$ for $N=3000$) by varying the density (blue line with circles). From $N = 1000$ to 5000 the linewidth is not obviously changed. In contrast, by keeping the same density ($n_0 k_0^{-3} = 0.0037$ for $N=3000$) while varying the OD (magenta line with triangles), the linewidth keeps changing. (b) The frequency shift is calculated for different number of atoms. By keeping constant density (magenta line with triangles), the frequency shift remains almost constant, while for constant OD (blue line with circles), there is a significant variation of the frequency shift with N . Here the cloud aspect ratio is $R_x : R_y : R_z = 2 : 2 : 1$ [33]. 72
- 6.6 CD model: effect of laser polarization. (a) Intensity distribution in the plane perpendicular to the laser propagation direction, *i.e.*, $\theta = \pi/2$ for all ϕ 's (inset). $\phi = 0$ is the z-direction. Here, the incident laser is polarized along z. The intensity detected along the laser polarization is suppressed compared to other directions. (b) and (c) show the line shape and linewidth of light detected at $\theta = \pi/2, \phi = 0$. (b) At small OD, the FWHM linewidth is below the natural linewidth. (c) As OD increases, the linewidth is collectively broadened due to multiple scattering processes (Fig. 6.3(a)). For all panels, degeneracy in excited levels has been assumed. 73
- 6.7 RW: transformation of Stokes vectors. In the random walk model, a scattering event is determined by two consecutive transformations of local coordinates: $\{\mathbf{e}_3, \mathbf{e}_r, \mathbf{e}_1\} \rightarrow \{\mathbf{e}'_3, \mathbf{e}'_r, \mathbf{e}'_1\}$ via rotation ϕ , and $\{\mathbf{e}'_3, \mathbf{e}'_r, \mathbf{e}'_1\} \rightarrow \{\mathbf{e}''_3, \mathbf{e}''_r, \mathbf{e}''_1\}$ via rotation θ [15]. 75

- 6.8 RW Model. (a) Distribution of on-resonance intensity in the plane $\theta = \pi/2$. Along the direction where single scattering events are forbidden ($\phi = 0$), the light intensity is suppressed. (b) The FWHM linewidth increases linearly with τ_p in a dilute medium. The linewidth along the direction parallel to the laser polarization can drop below Γ for small (purple squares). (c) Lin eshapes for different τ_p s and angles of observation. The line shape is Lorentzian for low τ_p but gets distorted and develops a double-peak structure as the τ_p increases. Here, for all angles, the signal is collected within a small angular region $\delta\theta = 5^\circ$. The intensity is normalized to the value at zero detuning for $\theta = 0$ and $\tau_p=0.3$, and the width of laser beam is 5 times the Gaussian width of the atomic cloud. Here all τ_p are labeled as the value at $\Delta = 0$. 77
- 6.9 Modified frozen dipole model: peak intensity. (a) Collective forward enhancement: forward intensity normalized by the transverse intensity as a function of Doppler width. (b) Intensity detected along different directions at Doppler width $\Delta_D = 6\Gamma$ as a function of atom number for fixed cloud size (when $N = 500$, $\tau=2, n_0 k_0^{-3}=0.0015$). $I \sim N^{1.6}$ for $\theta = 0$, and $I \sim N^{0.7}$ for $\theta = \pi/2$. The right vertical axis labels the intensity for $\theta = \pi/2, \pi/10$ 79
- 6.10 Semi-classical model: single-atom line shape. The excitation line shape is calculated for three different driving strength, each normalized by Ω^2 . The atomic motion is allowed to be one-dimensional and parallel to the laser propagating direction. Here we used $\omega_r = 0.6\Gamma$ (the value of the $^1S_0 \rightarrow ^3P_1$ transition of Sr [108]). 81
- 6.11 Semi-classical model: effect of motion on frequency shift. Two atoms are driven by a pair of counter-propagating lasers, with $\Omega = 0.1\Gamma$, $\omega_r = 0.6\Gamma$. The red dashed line shows the result of semi-classical model where motion is allowed in three dimensions. The blue line shows the result from the modified CD. The center of excitation line shape is calculated at $t = 5/\Gamma$ for different Doppler width, for both models. 82
- 6.12 The short caption 83
- 6.13 The short caption 84

6.14 Forward Scattering. (a) Comparison of forward scattering intensity versus angle using a red and blue probe beam. The inset shows the setup used to block the probe beam. After interacting with the atoms the probe beam is focused using a lens, which also collimates the fluorescence from the atoms. We block the probe beam using a beam stopper, which we translate perpendicular to the probe beam to change the angular range of fluorescence collected by the detector, characterized by the angle (θ) between \hat{x} and the edge of the beam stopper (see Ref. [33]). The measured intensity, $I_{x,0}(\theta)$, for each probe beam is normalized to the intensity at $\theta_{\max} = 7.5$ mRad. The dephasing caused by motion reduces the forward intensity peak for the red transition. (b) Comparison of intensity in the forward direction, I_x , versus intensity in the transverse direction, I_z . Both are varied by changing N . All measurements are made at $\theta = 2$ mRad (arrow in (a)) and normalized to the intensity, $I_{x,0}$, for the atom number used in (a). (c) Linewidth broadening in the forward direction measured by scanning the blue probe beam detuning, Δ , across resonance. Example lineshapes for different optical depths (ODs) are shown in the inset. Two different atom numbers are used, $N = 1.7(2) \times 10^7$ (blue squares) and $N/4$ (cyan triangles). The dashed line represents Γ for reference. All solid curves are based on the full theory of coupled dipoles and the band in (c) is for a $\pm 20\%$ atom number uncertainty. All errorbars are for statistical uncertainties. 85

- 6.15 Transverse Scattering. (a) Linewidth broadening for the blue transition in the transverse direction for \hat{y} -polarization (open squares) and \hat{z} -polarization (open triangles). (b) Intensity ratio, $I_{\text{ypol}}/I_{\text{zpol}}$, of \hat{y} -polarization to \hat{z} -polarization measured in the transverse direction when a blue probe beam is used. For low optical depths single particle scattering is dominant, and for single particle scattering almost zero intensity is predicted for \hat{z} -polarized fluorescence as this polarization points directly into the detector. (c) Linewidth broadening for the red transition in the transverse direction for \hat{y} -polarized light showing a similar trend to the blue transition. This transition is more sensitive to magnetic fields so a large magnetic field is applied to probe only the $m = 0$ to $m' = 0$ transition. All solid curves are based on the full theory of coupled dipoles and the band in (c) is for a $\pm 20\%$ atom number uncertainty. All errorbars are for statistical uncertainties. 87
- 7.1 Weyl quasiparticles in 3D dipolar arrays. (a) Schematics of the 3D lattice potential that traps an array of dipolar particles. The lattice is deep enough to pin the particles, most of which are prepared in the $J = 0$ ground state (blue spheres). Only a few particles are excited to the $J = 1$ states. Dipolar interactions between the $J = 0$ and $J = 1$ states give rise to Weyl excitations. (b) Schematics of dipole mediated interactions: An excited $J = 1$ state of one particle can be transferred to another particle in the $J = 0$ state by dipole-dipole interactions (virtual photon exchange is shown with a yellow wiggly line). Three types of allowed processes include $|00\rangle_i |1\sigma\rangle_j \leftrightarrow |1\sigma\rangle_i |00\rangle_j$, $|00\rangle_i |10\rangle_j \leftrightarrow |1, \pm 1\rangle_i |00\rangle_j$, and $|00\rangle_i |1, \pm 1\rangle_j \leftrightarrow |1, \mp 1\rangle_i |00\rangle_j$ 94

7.2 Weyl quasi-particle dispersion and eigenstates. (a) Brillouin zone for the simple cubic lattice. (b) Dispersion along high-symmetry lines in the absence of magnetic field (all energies are measured in units of $(3/4)\gamma_0/(k_0a)^3$). (c) Dispersion in the presence of magnetic field $B = \gamma_0/(k_0a)^3$ demonstrating the existence of Weyl nodes (red points) with linear quasiparticle dispersion near them. Each node is characterised by the monopole charge ± 1 . In agreement with the fermion doubling theorem [181] (the Nielsen-Ninomiya no-go theorem), there is an even number (six) of Weyl points in the first Brillouin zone. (d) Dispersion in the horizontal $(k_x - k_y)$ plane (shown by blue color in panel (a)) containing the Weyl node near the R point. Quasiparticles in this plane are similar to quasiparticles in graphene and are characterised by a non-trivial Berry phase of π . The arrows show the pseudospin $\langle \hat{\sigma} \rangle$ (the Pauli matrices $\hat{\sigma}_i$ act in the space of the angular-momentum projections $J_z = 0$ and $J_z = -1$). (e) Dispersion along the (yellow in panel (a)) plane consisting of vectors $\mathbf{k} = (\pi + k_d/\sqrt{2}, \pi + k_y, 0.71\pi + k_d/\sqrt{2})$ containing the Weyl point. Color shows the weight of the $|1 - 1\rangle$ state in the quasiparticle eigenstate, and arrows represent the pseudospin $\langle \hat{\sigma} \rangle$. (f) Dispersion along the (green in panel (a)) vertical plane $(k_y - k_z)$ containing the Weyl point near the R point. For each momentum \mathbf{k} the color represents the weight of the $|1 - 1\rangle$ state 95

- 7.3 Effects of disorder and dissipation on Weyl quasiparticles. (a) Real part of the quasiparticle dispersion in the presence of dissipation (including spontaneous emission and collective radiative decay). The parameters of the $J = 1 \rightarrow J = 0$ transition correspond to those of the electronic ${}^3P_0 - {}^3D_1$ levels of bosonic ${}^{88,84}\text{Sr}$ atoms, trapped in a magic optical lattice potential with $a = 206.4\text{nm}$ [187] at unit filling. Momentum \mathbf{k} is measured in units π/a . (b) The upper bound on the inelastic scattering rate estimated from simulating the full quasiparticle spectra including all allowed elastic and inelastic dipolar processes. The dissipation is significantly suppressed near the Weyl node (blue line). In striking contrast, the dissipation is enhanced close to the Γ point (red line) due to the enhanced collective emission (superradiance). (c) Disordered case: Quasiparticle dispersion for a lattice with filling fraction $f = 0.93$ in the limit of small dissipation $k_0a \ll 1$ (the energy is measured in units $\gamma_0/(k_0a)^3$). The line thickness shows the inelastic scattering rate. 97
- 7.4 Observation of Weyl quasiparticles. (a) Momentum-selective Ramsey spectroscopy: interfering Raman beams create an excitation with the angular momentum projection $J_z = -1$ and with translational momentum \mathbf{k} near the Weyl node (see text). After a waiting time t the second pulse is applied to measure the fraction of particles in the $J_z = 0$ angular-momentum state. (b) Six quasimomenta near the Weyl node. (c) The fraction of particles in the $J_z = 0$ state oscillates as a function of time t with the frequency $(E_{\mathbf{k}}^1 - E_{\mathbf{k}}^2)/(2\pi)$, where $E_{\mathbf{k}}^1 - E_{\mathbf{k}}^2$ is the energy splitting between the two branches of the quasiparticle dispersion. (d) The oscillations in the presence of dissipation for $k_0a \sim 0.5$. (e) The oscillations in a 99% randomly filled lattice. (f) The oscillations in a 93% filled lattice. For (c) and (d) a 3D cubic lattice of $100 \times 100 \times 100$ sites was used and we took advantage of the translational symmetry. For (e) and (f) a 3D cubic lattice of $10 \times 10 \times 10$ was used. 98

C.1	Pair-wise two-time correlation functions in the steady-state parametrized by $Z_{1,2}(\tau) = A \exp(-\gamma\tau)$. The correlations are calculated for a pair of dipoles in an ensemble of $N = 70$ dipoles identically coupled with $f(\mathbf{r}_{ab}) = f_{\text{eff}}/N$. The cumulant expansion solution agrees with the full calculation except at $W \ll \Gamma$ where subradiant behavior dominates (purple region) [166].	129
-----	---	-----

Chapter 1

Introduction

1.1 Quantum many-body physics

Atoms and molecules are the building blocks of the objects surrounding us. However, it is somehow amazing that collections of them exhibit behaviors not only drastically different from a single atom or molecule, but also very different between each other. Such many-body behaviors include a kaleidoscope of phenomena, ranging from superconductivity, which promises high performance electronic devices, to light harvesting, which is essential for photosynthesis in green plants. It is then natural to ask, how do these rich phenomena emerge from microscopic rules of quantum mechanics? And perhaps more interestingly, how to engineer materials with certain properties and how to harness the benefits of quantum physics? The understanding of these many-body behaviors has been a long-sought-after goal of physics. Yet with so many degrees of freedom and myriads of ingredients in different systems, it is a challenging task and many open questions remain.

Thanks to impressive experimental advances in the last two decades, systems of ultracold atoms and molecules provide a new avenue for addressing these questions. Experiments nowadays can access and selectively control internal levels of various types of bosonic and fermionic species, trap them in flexible choices of confinement geometries and tune their interaction strength, even with single-atom resolution [26, 143, 74, 121, 190]. In addition, experiments can control the degrees of complexity in the system and separate the target objectives we want to study from the undesired ones.

The power of these tools has been demonstrated in numerous studies that have, for instance,

observed the crossover from a molecular BEC to a BCS superfluid of Cooper pairs [286, 204], the Kibble-Zurek mechanism through a phase transition [138, 177], realized the paradigmatic Bose-Hubbard model in optical lattices and observed the superfluid to Mott insulator quantum phase transition [93, 83]. In those studies, the interaction between atoms is mediated by contact collisions, which are intrinsically short-ranged. Only recently, experimental advances have enabled us to access a variety of atomic, molecular and optical (AMO) systems with long-range interactions, thus opening a window for the exploration of long-range interacting systems, which are ubiquitous in nature but poorly understood. The use of AMO systems to gain a better understanding of long-range interacting physics can not only boost our knowledge of fundamental quantum sciences but also lead to important advances in quantum metrology and technology. This thesis aims to provide a step forward towards reaching this goal. In the remainder of this chapter, the key subjects this thesis revolves around will be briefly highlighted.

1.2 Long-range interactions

In systems such as trapped ions, Rydberg atoms, polar molecules and magnetic atoms, interaction decays with interparticle spacing in a power-law form $V \sim 1/r^\alpha$, with smaller α indicating a longer-ranged interaction. While there have been important developments on the understanding of the nonequilibrium dynamics and equilibrium phases in systems with short-range interactions, long-range interacting systems can exhibit richer but much less understood behaviors. For example, Lieb and Robinson showed that in short-range interacting systems, information can only propagate with a finite speed, and thus quantum correlations only exist within a linear “light-cone” [147]. This behavior has been experimentally confirmed in a one-dimensional array of ultracold bosonic atoms [46]. However, as observed in an experiment with trapped ions that interact with long-range Ising or XY spin-spin interactions, such a bound is violated [206]. A follow-up question is then, if long-range interactions can facilitate entanglement generation and be useful for quantum computation.

For isolated systems with short-range interactions, sufficient disorder can drive the system into

a many-body localized phase, where thermal relaxation is prohibited. It has been conjectured that such localization can not exist when the decay rate of interaction α is smaller than the dimension of the system [176]. However, much is still unclear about the transport properties of systems with long-range interactions.

The observation of many-body effects requires interactions to be stronger than other energy scales, such as loss and heating. This is a particular aspect where long range interactions can bring important opportunities. Let us consider for example the case of two particles sitting at adjacent sites of a lattice. If they interact via short-range interactions, to see each other one of them needs to first tunnel, then interact locally with the other and finally tunnel back. This type of tunneling mediated interactions, known as superexchange interactions, can be very weak \sim nK. Their low energy scales have been an important obstacle to experimentally observing them in the laboratory. On the contrary, if they can interact at long distance via dipolar interactions, no motion is required. This has facilitated their experimental observation as reported in recent experiments using KRb molecules or magnetic atoms such as Cr and Er [278, 10, 61]. The strong dipolar interactions are also experienced by Rydberg atoms, which are becoming an attractive platform for quantum information processing. Dipolar interactions between polar molecules are anisotropic, and consequently can give rise to geometrically frustrated interactions. Those are the underlying mechanism behind exotic states of matter such as spin liquids, which are highly entangled and topologically nontrivial [11]. Moreover, dipolar interactions naturally give rise to spin-orbit coupling (SOC)—a key element for a variety of topological phenomena, such as Majorana fermions and topological insulators [168, 279]. Spin-orbit coupling emerges in dipolar particles because dipolar interactions can couple external angular momentum and internal states.

The fact that dipolar interactions can directly take place between frozen particles also means that they could be a source of undesirable systematic effects in atomic clocks as the clocks become sensitive enough to detect them [153, 45]. Further improving the accuracy of atomic clocks thus demands a thorough knowledge of the underlying many-body dipolar effects. What is more, if frozen dipolar arrays can exhibit rich physics due to the long-range and collective character of

dipolar interactions, then one can anticipate the rich and complex physics that emerges when the dipoles are allowed to move. The study of the interplay between motional and dipolar interactions also constitutes a major part of this thesis.

1.3 Dissipation

To utilize many-body quantum mechanical systems for technological benefits, such as building a powerful quantum computer, it is important to overcome processes that can smear out quantum coherences. Those are in general unavoidable due to the coupling with environment. In AMO systems, the main decoherence mechanisms typically come from two-body or three-body collisions that induce number loss, spontaneous emission that changes internal level of an atom, and heating from light scattering processes. Usually these effects are considered as detrimental since they often result in an exponential decay of coherence. However, it is now appreciated that dissipative processes can also give rise to nontrivial effects and even be used to generate entanglement between particles [56, 148]. In fact, the interplay between dissipation and interactions is far from trivial, especially when the interactions are nonlocal and collective. Superradiance and subradiance are two iconic examples. Superradiance, as will be shown in chapter 5, can drive the system into a robust phase coherent state. Subradiance can maintain long-lived coherence and help to protect interesting quantum states [248, 195, 20]. Understanding how robust phases can emerge as a consequence of such interplay is highly desirable. However, dissipative many-body interacting quantum systems are generically hard to model and understand. In this thesis we present some of the methods developed to deal with several cases relevant to recent experiments.

1.4 Outline of this thesis

In this thesis, comprehensive studies are conducted on non-equilibrium many-body behaviors in long-range interacting systems, especially where the interplay with dissipation is relevant.

Chapter 2 introduces the origin and form of dipole-dipole interactions and their remarkable features, and provides the necessary background for the physics discussed in the following chapters.

The investigation of dipolar physics starts in Chapter 3, which discusses thermalization processes of dipolar molecules, explicitly KRb, confined in a quasi-two-dimensional trap. The main focus of the chapter is to determine possible ways to achieve evaporative cooling of the molecular gas. For efficient evaporation it is important that inelastic collision processes, for KRb molecules mainly coming from chemical reactions, become subdominant. We discuss the competition between elastic and inelastic events and find regimes where cooling to quantum degeneracy could be possible. The calculations presented in this chapter can guide current experiments in their effort to create high-phase-space-density gases of polar molecules.

Chapter 4 studies a different geometry, where molecules are confined in an optical lattice and tunneling along one dimension is allowed. We develop theoretical models to describe the tunneling dynamics in the presence of fast on-site losses. Our calculations reveal the important role played by multiple lattice bands and are capable of reproducing the experimental observations. They explain the suppression of molecule losses as a result of the quantum Zeno effect. Although in this chapter we focused on KRb molecules, the theory presented is expected to be applicable to a variety of other highly dissipative systems.

Alkaline earth atoms have important applications in quantum many-body physics and quantum metrology. They also represent a system where the interplay between long-range dispersive and dissipative interactions is relevant. All the following chapters of this thesis are devoted to explore the collective phenomena that can result from these interactions.

Chapter 5 discusses a possible way to realize a quantum analogue of the phenomenon of synchronization of classical oscillators in an array of incoherently pumped atoms. In this system, macroscopic phase coherence is generated by long-range interactions. Quantum correlations, entanglement, and the spectral properties of atoms in the coherent and incoherent phases are investigated in detail, providing an understanding of the open questions regarding the quantum aspect of synchronization.

Chapter 6 develops theoretical models to study the fluorescence properties of an ensemble of atoms driven by an external laser. Dipole-dipole interaction is shown to collectively affect the

line center and linewidth of the fluorescence spectrum. It is also found that atomic motion can significantly modify the spectral lineshape. We further show that, the theories presented can be applied to successfully model a recent experiment done in ^{88}Sr atoms.

In chapter 7, we show that the same model used to describe the fluorescence in Sr atoms in chapter 6 predicts the emergence of Weyl quasiparticles in a dense array of frozen atoms in a three-dimensional cubic lattice. Weyl excitations possess fascinating topological properties, and remarkably, they are found in this implementation to be robust against dissipation, due to the mechanism of subradiance.

The theoretical approaches developed here are applicable to general long-range interacting systems, such as trapped ions, atoms trapped in photonic crystals, an ensemble of nitrogen vacancy spin impurities in diamond, systems of Rydberg atoms, among others.

Publications summarized in this thesis:

Chapter 3:

Evaporative cooling of reactive polar molecules confined in a two-dimensional geometry

B. Zhu, G. Quémener, A. M. Rey and M. J. Holland, Phys. Rev. A, 88, 063405, 2013.

Chapter 4:

Suppressing the loss of ultracold molecules via the continuous quantum Zeno effect

B. Zhu, B. Gadway, M. Foss-Feig, J. Schachenmayer, M. Wall, K. R. A. Hazzard, B. Yan, S. A. Moses, J. P. Covey, D. S. Jin, J. Ye, M. Holland and A. M. Rey, Phys. Rev. Lett., 112, 070404, 2014.

Chapter 5:

Synchronization of Interacting Quantum Dipoles

B. Zhu, J. Schachenmayer, M. Xu, F. Herrera, J. G. Restrepo, M. J. Holland and A. M. Rey, New J. Phys., 17, 083063, 2015.

Chapter 6:

Light scattering from dense cold atomic media

B. Zhu, J. Cooper, Jun Ye, and A. M. Rey, Phys. Rev. A, 94, 023612, 2016.

Collective atomic scattering and motional effects in a dense coherent medium

S. Bromley, B. Zhu, M. Bishof, X. Zhang, T. Bothwell, J. Schachenmayer, T. L. Nicholson, R. Kaiser, S. F. Yelin, M. D. Lukin, A. M. Rey and J. Ye, Nature Communications, 7, 11039, 2016.

Chapter 7:

Emergent Weyl quasiparticles in three-dimensional dipolar arrays

S. V. Syzranov, M. L. Wall, B. Zhu, V. Gurarie and A. M. Rey, Nature Communications, 7, 13543, 2016.

Chapter 2

Radiating dipoles

2.1 Dipolar interactions: origin and characteristics

The origin of electric dipole-dipole interactions can be formally derived by considering a collection of atoms exposed to an electromagnetic field. Specifically, we consider an ensemble of atoms exhibiting a $J = 0 \rightarrow J' = 1$ transition driven by an electromagnetic field. The Hamiltonian governing this system is [94, 45, 110, 187]

$$\hat{H} = \hat{H}_0 + \hat{V}, \quad (2.1)$$

$$\hat{H}_0 = \hbar\omega_0 \sum_{j,\alpha} \hat{b}_j^{\alpha\dagger} \hat{b}_j^\alpha + \hbar \sum_{\mathbf{k},\epsilon} \omega_{\mathbf{k}} \hat{a}_{\mathbf{k}\epsilon}^\dagger \hat{a}_{\mathbf{k}\epsilon}, \quad (2.2)$$

$$\hat{V} = - \sum_j \hat{\mathbf{D}}_j \cdot \hat{\mathbf{E}}(\mathbf{r}_j), \quad (2.3)$$

$$\hat{\mathbf{D}}_j = \sum_{\alpha} \hat{\mathbf{e}}_{\alpha} d (\hat{b}_j^{\alpha\dagger} + \hat{b}_j^{\alpha}), \quad (2.4)$$

$$\hat{\mathbf{E}}(\mathbf{r}_j) = \sum_{\mathbf{k}\epsilon} g_{\mathbf{k}} \boldsymbol{\epsilon}_{\mathbf{k}} (e^{i\mathbf{k}\cdot\mathbf{r}} \hat{a}_{\mathbf{k}\epsilon} + \text{H.c.}), \quad (2.5)$$

where the notation $|\alpha\rangle$ is used to denote the three different excited levels, and j to label the atoms. For convenience, the Cartesian basis is chosen, $\mathbf{e} = (x, y, z)$, $|\alpha\rangle = |x\rangle, |y\rangle$ or $|z\rangle$. The latter are related to the angular momentum basis by $|x\rangle = -(|+1\rangle - |-1\rangle)/\sqrt{2}$, $|y\rangle = -i(|+1\rangle + |-1\rangle)/\sqrt{2}$ and $|z\rangle = |0\rangle$. $\hat{b}_j^{\alpha\dagger} = |\alpha_j\rangle \langle g_j|$ is the raising operator from the ground state to the state $|\alpha\rangle$ of the j^{th} atom, and d is the atomic dipole moment. ω_0 and $\omega_{\mathbf{k}}$ denote the atomic angular frequency and the photon angular frequencies, respectively. \mathbf{k} (ϵ) is the momentum (polarization) of the photon. ϵ_0 is the vacuum permittivity, and V is the photon quantization volume.

The evolution of the composite system of atoms and photons is described by

$$\frac{d\hat{\rho}_{\text{af}}}{dt} = -\frac{i}{\hbar}[\hat{V}'(t), \hat{\rho}_{\text{af}}], \quad (2.6)$$

$$\hat{V}'(t) = e^{i\hat{H}_0 t/\hbar} \hat{V}(t) e^{-i\hat{H}_0 t/\hbar} \quad (2.7)$$

$$\begin{aligned} &= \sum_{j,\alpha} \sum_{\mathbf{k},\epsilon} g_k d(\hat{\mathbf{e}}_\alpha \cdot \hat{\boldsymbol{\epsilon}}) [\hat{b}_j^{\alpha\dagger} \hat{a}_{\mathbf{k}\epsilon} e^{i\mathbf{k}\cdot\mathbf{r}_j + i(\omega_0 - \omega_k)t} + \hat{b}_j^{\alpha\dagger} \hat{a}_{\mathbf{k}\epsilon}^\dagger e^{-i\mathbf{k}\cdot\mathbf{r}_j + i(\omega_0 + \omega_k)t} \\ &\quad + \hat{b}_j^\alpha \hat{a}_{\mathbf{k}\epsilon} e^{i\mathbf{k}\cdot\mathbf{r}_j - i(\omega_0 + \omega_k)t} + \hat{b}_j^\alpha \hat{a}_{\mathbf{k}\epsilon}^\dagger e^{-i\mathbf{k}\cdot\mathbf{r}_j - i(\omega_0 - \omega_k)t}]. \end{aligned} \quad (2.8)$$

Given the large number of photon modes, the above equation is not very useful. Instead, we look for an equation describing the system of atoms only. To this end, we can formally integrate Eq. (2.6), and obtain

$$\frac{d\hat{\rho}_{\text{af}}}{dt} = -\frac{i}{\hbar} \int_0^t d\tau [\hat{V}'(t - \tau), \hat{\rho}_{\text{af}}(t - \tau)]. \quad (2.9)$$

Substituting this back to Eq. (2.6) leads to

$$\frac{d\hat{\rho}_{\text{af}}}{dt} = -\frac{1}{\hbar^2} \int_0^t d\tau [\hat{V}'(t), [\hat{V}'(t - \tau), \hat{\rho}_{\text{af}}(t - \tau)]]. \quad (2.10)$$

This integro-differential equation gives the density matrix of the composite system via its dependence on all its past history. To further simplify it, we adopt the Born-Markov approximation, which assumes that the correlation between photon modes can be neglected, and that the atom-field correlation time is short compared to the characteristic evolution time of the atomic system. These assumptions are reasonable for many practical applications, considering that the large number of degrees of freedom of the photon field and the fact that the atom-field coupling is too weak to significantly modify the field. In this thesis, we are only interested in cases where these assumptions are valid. Thus we can factorize the density matrix as $\hat{\rho}_{\text{af}}(t - \tau) = \hat{\rho}(t) \otimes |0\rangle\langle 0|$, where we also let the photon field remain in the vacuum state $|0\rangle$, following from the above assumptions. $\hat{\rho}$ is the reduced density matrix of the atomic system, which evolves as

$$\frac{d\hat{\rho}}{dt} = -\frac{1}{\hbar^2} \text{Tr}_f \left[\int_0^\infty d\tau [\hat{V}'(t), [\hat{V}'(t - \tau), \hat{\rho}(t) \otimes |0\rangle\langle 0|]] \right], \quad (2.11)$$

where Tr_f is the trace over the photonic degrees of freedom. Substituting the expression for $V'(t)$ into the above, we obtain

$$\begin{aligned}
\frac{d\rho}{dt} = & -\frac{1}{\hbar^2} \int_0^\infty d\tau \sum_{j,l} \sum_{\mathbf{k},\epsilon} g_k^2 d^2 \sum_{\alpha,\alpha'} (\hat{\mathbf{e}}_\alpha \cdot \hat{\boldsymbol{\epsilon}})(\hat{\mathbf{e}}_{\alpha'} \cdot \hat{\boldsymbol{\epsilon}}) \\
& \times \{ (\hat{b}_j^{\alpha\dagger} \hat{b}_l^{\alpha'} \hat{\rho} - \hat{b}_l^{\alpha'} \hat{\rho} \hat{b}_j^{\alpha\dagger}) e^{i\mathbf{k}\cdot\mathbf{r}_{jl} + i(\omega_0 - \omega_k \tau)} \\
& + (\hat{\rho} \hat{b}_j^{\alpha\dagger} \hat{b}_l^{\alpha'} - \hat{b}_j^{\alpha\dagger} \hat{\rho} \hat{b}_l^{\alpha'}) e^{-i\mathbf{k}\cdot\mathbf{r}_{jl} + i(\omega_0 + \omega_k \tau)} \\
& + (\hat{b}_j^\alpha \hat{b}_l^{\alpha'\dagger} \hat{\rho} - \hat{b}_l^{\alpha'\dagger} \hat{\rho} \hat{b}_j^\alpha) e^{i\mathbf{k}\cdot\mathbf{r}_{jl} - i(\omega_0 + \omega_k \tau)} \\
& + (\hat{\rho} \hat{b}_l^{\alpha'\dagger} \hat{b}_j^\alpha - \hat{b}_j^\alpha \hat{\rho} \hat{b}_l^{\alpha'\dagger}) e^{-i\mathbf{k}\cdot\mathbf{r}_{jl} - i(\omega_0 - \omega_k \tau)} \}, \tag{2.12}
\end{aligned}$$

where $\mathbf{r}_{jl} = \mathbf{r}_j - \mathbf{r}_l$.

The summation over \mathbf{k} can be replaced by an integral $\frac{V}{(2\pi)^3} \int k^2 dk d\Omega$. The angular part of the integral $\int d\Omega$ can be explicitly implemented

$$\int d\Omega^{\pm i\mathbf{k}\cdot\mathbf{r}} \sum_{\epsilon} \sum_{\alpha,\alpha'} (\hat{\mathbf{e}}_\alpha \cdot \hat{\boldsymbol{\epsilon}})(\hat{\mathbf{e}}_{\alpha'} \cdot \hat{\boldsymbol{\epsilon}}) = 4\pi \sum_{\alpha,\alpha'} [A(k)(\hat{\mathbf{e}}_\alpha \cdot \hat{\boldsymbol{\epsilon}})(\hat{\mathbf{e}}_{\alpha'} \cdot \hat{\boldsymbol{\epsilon}}) + B(k)\hat{\mathbf{e}}_\alpha \cdot \hat{\mathbf{e}}_{\alpha'}], \tag{2.13}$$

$$A(k) = -\frac{\sin(kr)}{kr} + 3\frac{\sin(kr)}{(kr)^3} - 3\frac{\cos(kr)}{(kr)^2}, \tag{2.14}$$

$$B(k) = \frac{\sin(kr)}{kr} - \frac{\cos(kr)}{(kr)^3} + \frac{\sin(kr)}{(kr)^2}. \tag{2.15}$$

These seemingly convoluted forms come from the fact that photons have two different polarizations.

The integral over time can be performed using the following relations

$$\int_0^\infty d\tau e^{i(\omega_0 \pm \omega)\tau} = \pi \delta(\omega_k \pm \omega_0) \pm i\text{P.V.} \frac{1}{\omega_k \pm \omega_0}, \tag{2.16}$$

$$\int_0^\infty d\tau e^{-i(\omega_0 \pm \omega)\tau} = \pi \delta(\omega_k \pm \omega_0) \mp i\text{P.V.} \frac{1}{\omega_k \pm \omega_0}. \tag{2.17}$$

where P.V. denotes the principal value. Carrying out the correspondent integrals result in

$$\frac{d\hat{\rho}}{dt} = -\frac{i}{\hbar} [\hat{H}_{\text{dd}}, \hat{\rho}] + \mathcal{L}[\hat{\rho}]. \tag{2.18}$$

In the above expression, the dissipator \mathcal{L} comes from the integration over the Dirac Delta function, which enforces $\omega = \omega_0$. The Hamiltonian part comes from the principal value integral,

which involves $\omega \neq \omega_0$, accounting for the processes involving virtual photons. Explicitly, we have

$$\hat{H}_{\text{dd}} = \hbar \sum_{j,l} \sum_{\alpha,\alpha'} g_{jl}^{\alpha\alpha'} \hat{b}_j^{\alpha\dagger} \hat{b}_l^{\alpha'}, \quad (2.19)$$

$$\mathcal{L}[\hat{\rho}] = \sum_{j,l} \sum_{\alpha,\alpha'} f_{jl}^{\alpha\alpha'} [2\hat{b}_j^{\alpha'} \hat{\rho} \hat{b}_i^{\alpha\dagger} - \{\hat{b}_i^{\alpha\dagger} \hat{b}_j^{\alpha'}, \hat{\rho}\}], \quad (2.20)$$

with dipole-dipole interactions

$$g_{jl}^{\alpha\alpha'} = \text{Re}[G_{jl}^{\alpha\alpha'}], \quad (2.21)$$

$$f_{jl}^{\alpha\alpha'} = \text{Im}[G_{jl}^{\alpha\alpha'}], \quad (2.22)$$

where

$$G_{jl}^{\alpha\alpha'} = \frac{3\Gamma}{4} [a(r_{jl})(\hat{\mathbf{e}}_\alpha \cdot \hat{\mathbf{r}}_{jl})(\hat{\mathbf{e}}_{\alpha'} \cdot \hat{\mathbf{r}}_{jl}) + b(r_{jl})(\hat{\mathbf{e}}_\alpha \cdot \hat{\mathbf{e}}_{\alpha'})], \quad (2.23)$$

$$a(r) = \frac{e^{ik_0 r}}{k_0 r} + 3i \frac{e^{ik_0 r}}{k_0^2 r^2} - 3 \frac{e^{ik_0 r}}{k_0^3 r^3}, \quad (2.24)$$

$$b(r) = -\frac{e^{ik_0 r}}{k_0 r} - i \frac{e^{ik_0 r}}{k_0^2 r^2} + \frac{e^{ik_0 r}}{k_0^3 r^3}. \quad (2.25)$$

In the above equations, $\Gamma = \frac{k_0^3 d^2}{3\pi\hbar\epsilon_0}$ is the spontaneous emission rate, $k_0 = \omega_0/c$ is the wavevector of the dipole transition, and $\hat{\mathbf{e}}_\alpha$ is the dipole polarization direction corresponding to the transition $|g\rangle \rightarrow |\alpha\rangle$. Note that although the above equations were derived for the case of a $J = 0 \rightarrow J' = 1$ transition, the procedure can be generalized straightforwardly to more general dipole transitions.

2.2 Near-field and far-field interactions

In this section we take a closer examination of the dipole-dipole interactions. In addition to the dispersive interactions indicated by the real part of G , the coupling to radiation field results in an imaginary part that represents the dissipative interactions. An illustration of these interactions is shown in Fig. 2.1. The structures and spatial dependence of the dissipative and dispersive interactions are generally very different. For dipole-dipole interactions, Γ sets the dominant energy scale, which depends on the dipole moment, and $1/k_0$ sets the relevant length scale in these interactions. When $k_0 r \ll 1$, namely, when the interparticle spacing is much smaller than the photon wavelength, $g_{jl}^{\alpha\alpha'}$ diverges as $\sim \Gamma/(k_0 r)^3$, while $f_{jl}^{\alpha\alpha'}$ approaches a constant Γ , thus becomes

negligible. Then in this limit the dipolar interactions reduce to the conventional electric dipolar interaction, namely

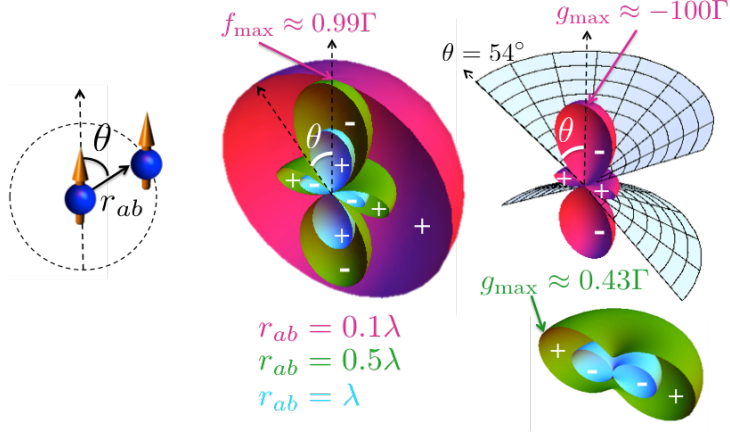


Figure 2.1: Spatial dependence of dipole-dipole interactions. The diagonal parts of the imaginary (f^{zz}) and real (g^{zz}) dipolar interactions between two dipoles are plotted, for three different inter-particle spacings. While both types of interactions depend on geometry, they are nonidentical, and the elastic interactions are highly sensitive to the spatial separation and orientation of the particles. The maximum value for imaginary and real interactions for fixed $|\mathbf{r}_{ab}|$ is denoted as f_{\max} and g_{\max} , respectively. The cone illustrates the magic angle, $\theta_m = \arccos(1/\sqrt{3})$, along which the elastic interactions vanish.

$$\hat{V}_{\text{dd}}(\mathbf{r}) = \sum_{\alpha\alpha'} \frac{d^2}{4\pi\epsilon_0 r^3} [(\hat{\mathbf{e}}_\alpha \cdot \hat{\mathbf{e}}_{\alpha'}) - 3(\hat{\mathbf{e}}_\alpha \cdot \hat{\mathbf{r}})(\hat{\mathbf{e}}_{\alpha'} \cdot \hat{\mathbf{r}})] \hat{b}_j^{\alpha\dagger} \hat{b}_l^{\alpha'}. \quad (2.26)$$

An exemplary system of this regime is ultracold KRb molecules prepared in the lowest two rotational states.

In the opposite limit, $k_0 r \gg 1$, the dominant term in the dipole-dipole interactions is $\propto \frac{e^{ik_0 r}}{r}$, which shares the same behavior as the Green's function of a photon propagating in free space. This is the far-field regime. In fact, it is also possible to modify the form of the interactions by selecting the photon mode to which atoms are coupled. By loading atoms inside a single-mode Fabry–Perot cavity, a collective interaction that does not decay with r can be generated. Tunable power-law long-range interactions can also be engineered by coupling atoms to photonic crystals [69].

In the case where $k_0 r \sim 1$, the near-field and far-field terms $\propto 1/r^3, 1/r^2, 1/r$ are of similar magnitude. Neither the dissipative and dispersive part of the Hamiltonian, nor the near-field and far-field components commute with each other, and thus this case corresponds to an interesting

regime where all terms are relevant. Fig. 2.2 lists the properties of dipole transitions in several experimentally relevant systems. For alkaline earth atoms, such as Sr atoms, it is possible to probe the intermediate regime where the system is affected by the complex interplay between all components of dipole-dipole interactions. While this complexity imposes a challenge to theoretical treatment, it also enables extra control knobs and allows for new phenomena. In a recent experiment, Sr atoms have been loaded into a three-dimensional lattice, and the clock transition ($^1S_0 \rightarrow ^3P_0$) has been probed [38]. Even though the transition matrix element of the transition is ultranarrow ($\Gamma \sim \text{mHz}$), dipolar interactions might play an important role in the future performance of these 3D optical lattice clocks.

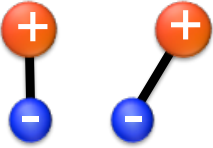

Polar molecules		Alkaline earth atoms	
			
Rotational levels $N=0 \rightarrow N=1$ (KRb)	Vibrational levels $v=0 \rightarrow v=1$ (KRb)	Electronic orbitals $^1S_0 \rightarrow ^3P_0$ (^{87}Sr)	Electronic orbitals $^3P_0 \rightarrow ^3D_1$ (^{87}Sr)
$k_0 a \sim 2 \times 10^{-5}$	$k_0 a \sim 2 \times 10^{-2}$	$k_0 a \sim 3.6$	$k_0 a \sim 0.5$
$d \sim 0.5 \text{Debye}$	$d \sim 0.004 \text{Debye}$	$d \sim 0.001 \text{Debye}$	$d \sim 4 \text{Debye}$

Figure 2.2: Typical transitions relevant for dipolar interactions in several AMO systems. a is the optical lattice spacing estimated from experimental realizations [260, 187, 249, 250]. Different choices of internal states allow us to access different dipolar regimes .

In general, dipole-dipole interactions depend on the orientation of atomic dipoles. The off-diagonal elements in Eq. (2.23), *i.e.*, $\alpha \neq \alpha'$, couple states with different angular momentum projections. This coupling is a quantum analog of the Einstein-de Haas effect [73], and can be also seen as an effective spin-orbit coupling. As will be discussed in Chapter 7, it gives rise to Weyl quasiparticles in a three-dimensional array of dipoles [248].

2.3 Superradiance and subradiance

To illustrate some of the interesting phenomena arising from long-range dipole-dipole interactions, we first consider a simplified case. We include only two levels in the transition, $|g\rangle$ and $|z\rangle$, thus we can define $\hat{\sigma}_j^- = \hat{b}_j^z = |g\rangle\langle z|$. We also consider the case where dipoles are very close to each other $k_0 r \ll 1$ and thus $f_{ij}^{zz} \sim f$. We focus on the dissipative part of the interactions. Then only the second part of Eq. (2.18) is relevant, and the dissipator becomes

$$\mathcal{L}[\hat{\rho}] = f(2\hat{J}^- \hat{\rho} \hat{J}^+ - \hat{J}^+ \hat{J}^- \hat{\rho} - \hat{\rho} \hat{J}^+ \hat{J}^-), \quad (2.27)$$

where $\hat{J}^\pm = \sum_j \hat{\sigma}_j^\pm$ are collective angular momentum operators. Since the dissipator commutes with the total angular momentum J , it is convenient to use a representation in the angular momentum basis $|J, M, \beta\rangle$, where $J = N/2, N/2 - 1, \dots, (N \bmod 2)/2$ is the total angular momentum, $M = -J, -J + 1, \dots, J$ is its projection on the quantization axis, and β is an additional quantum number to label the states with the same J and M . Overall, the total number of states equals 2^N , thus for general $J < N/2$, there are multiple states with the same J and M . The manifold with $J = N/2$ is the symmetrized Dicke states. The above dissipator induces decay only within the same J manifold. An example of three atoms is given in Fig. 2.3, where the decay rates can be explicitly calculated for all states. For states in the symmetrized Dicke manifold, the decay rate can exceed the independent atom spontaneous emission rate. This phenomenon, known as superradiance, was first theoretically predicted by Dicke in 1954 [67]. In fact, the decay rate of symmetrized Dicke states is $\Gamma(J + M)(J - M + 1)$, which is maximal for the state $|N/2, 0\rangle$ [67]. Physically this can be understood from the fact that there are N indistinguishable decay channels, so the decay rate is enhanced by $\sim N$. For states in other manifolds, the individual atomic states are not symmetric, and the decay rates can be even smaller than the rate of independent atoms. These are the so-called subradiant states, which are less affected by the dissipative environment.

Outside the near-field limit, dipole-dipole interactions are not collective, but superradiant and subradiant states still exist, though consisting of a mixture of the above Dicke states and requiring more sophisticated theoretical approaches. Superradiance, which was originally conceived for a

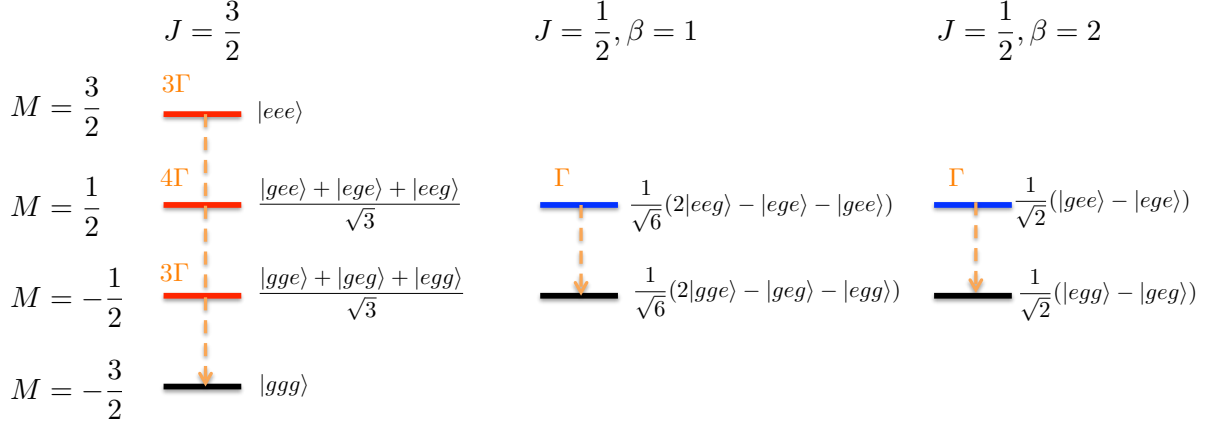


Figure 2.3: Dicke states for three atoms. $|e\rangle$ and $|g\rangle$ denote the excited and ground state in the individual atom basis. Also indicated are the decay rates under the dissipator $\hat{J}^+ \hat{J}^-$. States in red colors decays at least at rate $N_e \Gamma$, while the decay rate for states in blue (or black) color is $< N_e \Gamma$ (or $=0$), where N_e denotes the number of excitations in the system.

small dense sample, can be observed experimentally in large and dilute ensembles. A demonstration of this phenomenon is performed in a recent experiment with bosonic Sr atoms. We show in chapter 6 that using a microscopic theory derived from Eqs. (2.19) and (2.20), we are able to quantitatively describe the experiment. Collective emission has also been observed in various experiments performed using photonic crystal waveguides and in cavity systems [86, 29, 182].

In contrast, subradiant states are usually difficult to prepare or probe in experiments with many atoms. In chapter 7, we propose a protocol to realize subradiant states in a dipolar array, without requiring complicated control of external fields. We also show there, that subradiance stabilizes Weyl quasiparticles.

Chapter 3

Evaporative cooling of reactive polar molecules confined in a two-dimensional geometry

3.1 Introduction

Polar molecules that exhibit strong dipole-dipole interactions have tremendous applications, ranging from quantum many-body physics [253, 14, 136] and quantum information processing [66] to precision measurements [282] and ultracold chemistry [41]. The parameter regime of interest is generally ultralow temperature and high phase-space density, where novel quantum features can emerge. In practice, it turns out to be difficult to cool molecules into the desired regime using standard methods due to their complicated internal level structure. In the past few years, significant experimental progress has been made towards this goal through the demonstration of a method for preparing a gas of fermionic KRb molecules in the lowest electronic, vibrational, and rotational quantum state, with a temperature T at the verge of quantum degeneracy (*i.e.* $T/T_F \sim 1$ where T_F is the Fermi temperature) [179, 189, 180]. From this starting point, one would like to further increase the phase-space density by implementing evaporative cooling—demonstrated to be one of the most useful cooling methods for quantum gases [32, 58, 65].

A fundamental limitation to the effectiveness of evaporative cooling for polar molecules is their fast losses. For KRb molecules, the losses arise mainly from exothermic chemical reactions, *i.e.* $\text{KRb} + \text{KRb} \rightarrow \text{K}_2 + \text{Rb}_2$. In such reactions, molecules prepared in different internal states can undergo barrierless collisions, with a lifetime of only ~ 10 ms [180, 201]. In contrast, identical fermionic KRb molecules at ultra-low temperature are protected by the p -wave barrier, which

potentially results in a much slower reaction rate [180]. However, due to the anisotropic nature of the dipole-dipole interaction, molecules of the correct orientation can be attracted towards each other by experiencing “head-to-tail” collisions. As a result, the p -wave barrier can be greatly suppressed. Such a loss mechanism is further facilitated by the application of a strong external electric field that increases the dipole strength.

Significantly, these obstacles can be overcome by confining the molecules into quasi-two-dimensional traps, which can be generated by a one-dimensional optical lattice. In this case, the adverse collisions can be greatly suppressed and the reaction barrier effectively raised [60, 202, 200]. Furthermore, both the elastic and inelastic collision rates can be tuned by controlling the applied external electric field and the trapping potential. Thus, while most previous experiments implementing evaporative cooling were performed in three-dimensional geometries [123], here we are explicitly interested in focussing on evaporative cooling in two-dimensions, with the anisotropic collisions that arise from the dipolar interaction. A detailed understanding of this situation would be beneficial for future experimental realizations.

Given this motivation, we theoretically investigate evaporative cooling of molecules. We use both Monte Carlo (MC) simulations and models developed on the basis of kinetic theory to study the efficiency of evaporative cooling with parameters applicable to current state-of-the-art KRb experiments. This chapter is structured as follows. In Sec. 3.2 we explore the effect of anisotropic collisions on evaporative cooling. In Sec. 3.3 we consider the effect of reduced trap dimension, *i.e.* two-dimensional rather than three-dimensional traps. In Sec. 3.4 we apply the MC method to determine the optimum evaporative cooling trajectory for KRb molecules. In Sec. 3.5 we discuss the potential anti-evaporation mechanism arising from the energy dependence of the inelastic loss.

3.2 Evaporative cooling with anisotropic collisions

3.2.1 Anisotropic elastic collisions between polar molecules

Evaporative cooling relies on removing particles with above-average energy and redistributing the residual energy among the remaining particles by elastic collisions so that the temperature falls. For polar molecules, the characteristic parameters that encapsulate the elastic scattering process can be dramatically modified by the application of external fields. In the presence of an external electric field, the dipole-dipole interaction between polar molecules can mix different partial waves and give rise to highly-anisotropic scattering. Moreover, for identical fermions, the lowest total angular momentum partial wave that has the correct symmetry is p -wave, so the elastic collisions are anisotropic at ultralow temperature even in the absence of applied fields [87].

Considering current experimental conditions [60], we adopt the differential and total scattering cross-section computed for KRb molecules in two-dimensions at an induced dipole moment $d = 0.2$ debye as a function of the collision energy E_c . FIG. 3.1(a) shows the dependence of differential cross-section on the scattering angle, ϕ , which is the precession angle of the relative momentum during the collision. Scattering is mainly forward (0 or 2π) and backward (π). The peak is more pronounced as the collision energy increases due to the larger contribution of higher partial waves. This differential cross-section is well parametrized by the empirical function

$$\left(\frac{d\lambda(\phi)}{d\phi}\right)_{E_c} = \lambda \left(a(\cos\phi)^{2\alpha} + a'(\cos\phi)^{2\alpha'} \right), \quad (3.1)$$

with a , a' , α and α' constants that are real and positive, and with the total cross-section given by

$$\lambda = \int_0^{2\pi} d\phi \frac{d\lambda(\phi)}{d\phi}. \quad (3.2)$$

The dependence of λ on collision energy is shown in FIG. 3.1(b). Our best parametrization for various scattering energies is given in Table 3.1. Note that at $E_c \sim 1$ nK, the angular dependence of the differential cross-section is well approximated by that of a p -wave collision, since $a \gg a'$ and $\alpha \approx 1$.

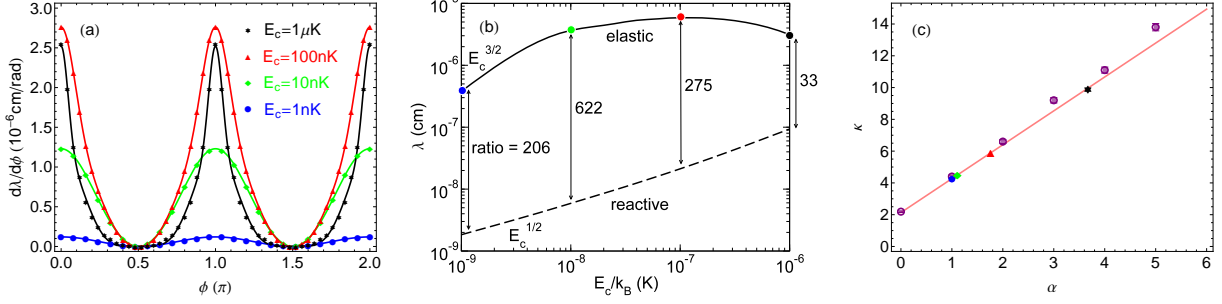


Figure 3.1: (a) Two-dimensional differential scattering cross-section for elastic collisions as a function of the scattering angle. Four collision energies are shown; $E_c = 1$ nK (blue disk), 10 nK (green diamond), 100 nK (red triangle), and $1 \mu\text{K}$ (black star). The induced dipole moment is $d = 0.2$ debye and the harmonic frequency of the one-dimensional confinement potential is $\nu = 23$ kHz. The solid lines show the empirical formula Eq. (3.1). (b) Total scattering cross section for elastic collisions (solid line) and reactive processes (dashed line) as a function of the collision energy for an induced dipole moment of $d = 0.2$ debye and a one dimensional confinement of $\nu = 23$ kHz. The ratio of elastic to reactive is indicated at four different collision energies; $E_c = 1$ nK (blue point), 10 nK (green point), 100 nK (red point), and $1 \mu\text{K}$ (black point). (c) Number of collisions κ required for thermalization for different differential scattering cross-sections. The magenta solid line shows Eq. (3.10). The purple circles are results from the MC simulations, and are shown with their small statistical error bars. The four symbols (blue disk, green diamond, red triangle, black star) correspond to the same energies as (a).

$E_c(\text{nK})$	a	a'	α	α'	$\lambda(10^{-6}\text{cm})$
1	0.31	0.0005	1.00	2.19	0.38
10	0.27	0.06	1.00	2.09	3.67
100	0.24	0.21	1.19	7.03	5.99
1000	0.34	0.40	2.47	26.40	3.42

Table 3.1: Derived parameters from the fit of Eq. (3.1) for the scattering energies shown in Fig. 3.1.

3.2.2 Thermalization rate

The thermalization rate characterizes the timescale needed for a system to redistribute energy after an evaporative cut. To quantitatively investigate the thermalization under anisotropic collisions, we adopt the typical experimental procedure of cross-dimensional thermalization [173, 64]. In order to isolate the effect of anisotropic elastic collisions, we will neglect inelastic collisions completely for these thermalization calculations.

Consider a gas of N molecules in a two-dimensional harmonic trap with a slight initial

imbalance of temperatures along each axis. This initial condition can be prepared in experiment by parametric heating of an equilibrium gas [173]. We define an effective temperature T_i in the i th direction in terms of the total energy E_i by $k_B T_i = E_i/N = \overline{p_i^2}/(2m) + m\omega_i^2 \overline{x_i^2}/2$, where ω_i is the trapping frequency, m is the molecule mass, and $\overline{p_i^2}/(2m)$ and $m\omega_i^2 \overline{x_i^2}$ denote the average kinetic energy and potential energy. We assume that the system is well described by the Boltzmann distribution

$$f_0(\mathbf{x}, \mathbf{p}) = n_0 \exp\left(-\sum_i \left(\frac{p_i^2}{m} + m\omega_i^2 x_i^2\right)/(2k_B T_i)\right), \quad (3.3)$$

where n_0 guarantees normalization, *i.e.*

$$\frac{1}{(2\pi\hbar)^2} \int d^2x d^2p f_0(\mathbf{x}, \mathbf{p}) = N. \quad (3.4)$$

Without loss of generality, we assume $T_y = (1 - \xi)T_x$ with $\xi > 0$. Elastic collisions lead to an exchange of energy between the x and y directions and reduce the relative temperature difference.

The rate of such change is [205]

$$\begin{aligned} \frac{dE_x}{dt} &= Nk_B \frac{dT_x}{dt} = \frac{1}{2m(2\pi\hbar)^4} \int d^2x d^2p_1 d^2p_2 d\phi' \\ &\quad \times f_0(\mathbf{x}, \mathbf{p}_1) f_0(\mathbf{x}, \mathbf{p}_2) |\mathbf{p}_1 - \mathbf{p}_2| \frac{d\lambda(\phi')}{d\phi'} \Delta E_x. \end{aligned} \quad (3.5)$$

This involves the energy change per collision given by

$$\Delta E_x = \frac{1}{4m} |\mathbf{p}_1 - \mathbf{p}_2|^2 (\cos^2 \phi' - \cos^2 \phi), \quad (3.6)$$

where ϕ and ϕ' are the angles between the relative momentum and the total momentum before and after the collision respectively. The period of time it takes to thermalize, τ , can be defined as the $1/e$ decay time of the temperature difference, so that

$$\frac{dT_x}{dt} = -\frac{1}{\tau} (T_x - T_0), \quad (3.7)$$

where $T_0 = (T_x + T_y)/2$ is the temperature at equilibrium. From Eq. (3.5) and Eq. (3.7), we obtain the average number of elastic collisions required for the system to thermalize, κ , in the following way. We begin by defining the collision rate γ

$$\gamma = \frac{\lambda}{m(2\pi\hbar)^4} \int d^2x d^2p_1 d^2p_2 f_0(\mathbf{x}, \mathbf{p}_1) f_0(\mathbf{x}, \mathbf{p}_2) |\mathbf{p}_1 - \mathbf{p}_2|, \quad (3.8)$$

so that $\kappa \equiv \lim_{\xi \rightarrow 0}(\tau\gamma)$, independent of the initial temperature and trapping frequencies [64, 207]. Combining Eq. (3.3)–Eq. (3.8) with the form of the differential cross-sections given in Eq. (3.1) leads to the following result:

$$\kappa = \frac{8}{15\sqrt{\pi}} \left\{ \frac{a}{2\alpha + 2} \frac{\Gamma(\alpha + 1/2)}{\Gamma(\alpha + 1)} + \frac{a'}{2\alpha' + 2} \frac{\Gamma(\alpha' + 1/2)}{\Gamma(\alpha' + 1)} \right\}^{-1}. \quad (3.9)$$

When $a' = 0$ and $\alpha' = 0$, this reduces to the particularly simple expression

$$\kappa = \frac{16}{15}(2\alpha + 2), \quad (3.10)$$

which corresponds to the differential cross-section

$$\frac{d\lambda(\phi)}{d\phi} = a \cos^{2\alpha}\phi. \quad (3.11)$$

In order to interpret these results, for each scattering energy E_c , we calculate κ using Eq. (3.9), and plot the result on the (α, κ) line, as prescribed by Eq. (3.10), with markers (star, square, triangle, diamond, and disk), as shown in FIG. 3.1(c). The use of the linear relationship between α and κ is supported by results obtained from MC simulations, as described in Appendix A.1, utilizing the differential cross-section form of Eq. (3.11) directly (purple circles). The exception is at large α , where the assumption adopted in deriving Eq. (3.9)—namely that of a Boltzman distribution parametrized by an effective temperature—becomes poor when the thermalization is too slow.

The calculations demonstrate a strikingly strong dependence on the anisotropy of the collisions for rethermalization. For $\alpha = 0$ the collisions are isotropic (s -wave like) and $\kappa \approx 2.1$. This compares with $\kappa \approx 4.3$ at $\alpha = 1$, which describes p -wave collisions. For $E_c = 1 \mu\text{K}$ we find $\kappa \approx 9.7$, which is many times that for isotropic collisions, implying a significant increase in the number of collisions required for rethermalization. One may have anticipated this since the differential cross-section is sharply peaked in the forward and backward directions and energy is not efficiently redistributed. Also note that the outcome for the differential cross-section of KRb with $E_c = 1 \text{ nK}$ is very close to that from Eq. (3.10) with $\alpha = 1$, indicating p -wave elastic collisions between identical fermions at ultra-low temperature.

3.2.3 Evaporation with anisotropic collisions

In evaporative cooling experiments, inelastic collisions compete with elastic collisions, and thus a slow thermalization rate gives rise to a reduction in cooling efficiency. In this section, we use MC simulations to quantify the efficiency of evaporative cooling in two ways: by the achieved increase in phase-space density Ω_f/Ω_0 at the expense of losing a certain portion of the molecules in the trap (see FIG. 3.2), and by the time required for the temperature to go down and Ω to increase by a given amount (see FIG. 3.3).

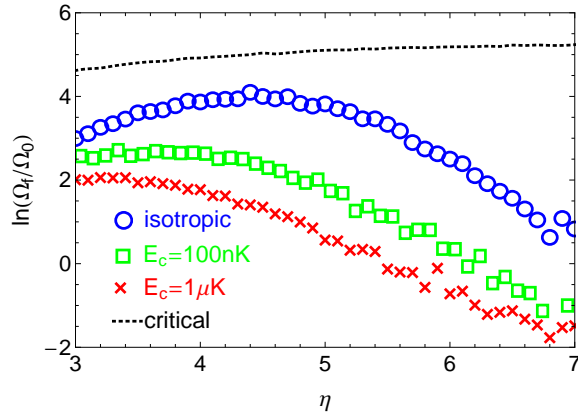


Figure 3.2: Increase in phase space density vs truncation parameter η for different $\frac{d\lambda(\phi)}{d\phi}$. Here Ω_0 is the initial phase-space density, and the final phase space density, Ω_f , was calculated when the ratio of molecule numbers was $N_f/N_0 = 0.1$. Blue circles: $\frac{d\lambda(\phi)}{d\phi} = \text{const}$; red crosses: $(\frac{d\lambda(\phi)}{d\phi})_{E_c=1\mu\text{K}}$; green squares: $(\frac{d\lambda(\phi)}{d\phi})_{E_c=100\text{nK}}$; black dotted line: critical phase space density Ω_c for quantum degeneracy.

In these simulations, we assume an instantaneous removal of all particles with energy greater than a cut-off energy. The cut-off energy, ϵ_t , evolves during the evaporation trajectory with the constraint that a truncation parameter, $\eta = \epsilon_t/\bar{E}$, is kept constant, where \bar{E} is the average energy of the nonequilibrium distribution. The comparison between isotropic and anisotropic collisions is made by calculating the evaporation trajectory for a variety of differential cross-sections, starting with the same initial molecule number. To simplify the comparison, for both elastic and inelastic collisions, we keep the total cross-sections constant while varying the differential cross-section for

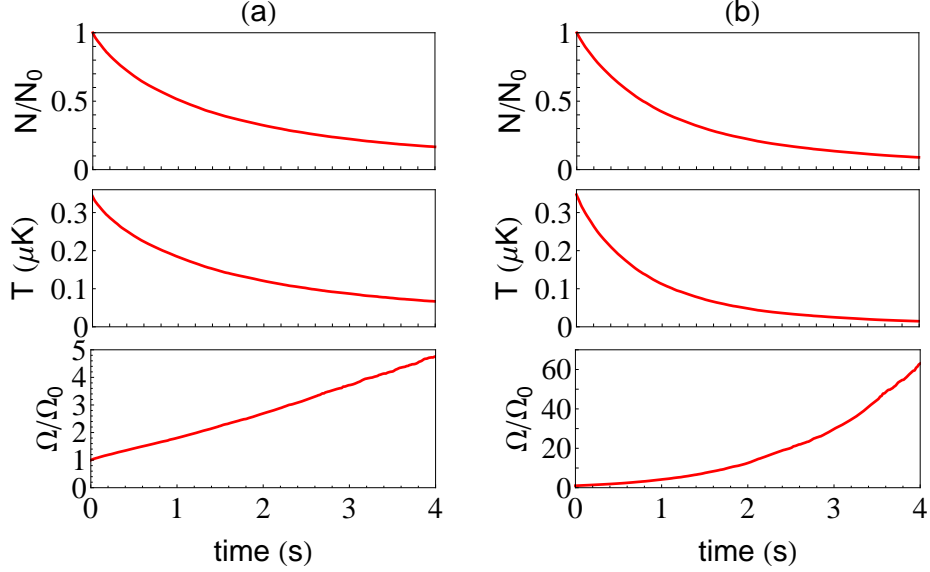


Figure 3.3: Trajectories of evaporation for (a): $(\frac{d\lambda(\phi)}{d\phi})_{E_c=1\mu\text{K}}$ at $\eta \sim 3.4$ and (b): $\frac{d\lambda(\phi)}{d\phi} = \text{const}$ at $\eta \sim 4.3$, under the same initial conditions as in FIG. 3.2. In comparison with (a), it is apparent that in (b) the temperature T drops faster and the phase-space density Ω increases much more rapidly.

elastic scattering. We also assume the cross-sections to be energy independent.

The molecules are initially simulated from a truncated Boltzmann distribution utilizing the cut-off energy [155] ϵ_t :

$$f(\mathbf{x}, \mathbf{p}) = n'_0 \exp\left(-\left(\frac{p^2}{m} + m\omega^2 x^2\right)/(2k_B T)\right) \times \Theta\left(\epsilon_t - \left(\frac{p^2}{2m} + \frac{1}{2}m\omega^2 x^2\right)\right), \quad (3.12)$$

where Θ is the Heaviside function, n'_0 is the normalization, and T is the initial temperature, held fixed for different simulations. Although the energy distribution of the molecules is intrinsically non-equilibrium here, we may assign it a phase-space density, Ω , as that of the corresponding equilibrium distribution that has the same molecule number and average molecule energy.

In FIG. 3.2, Ω is plotted for the case of evaporation trajectories in which 90% of the initial molecules are lost. For anisotropic collisions, we calculate evaporation trajectories for the differential cross-sections for $E_c = 100\text{nK}$ and $E_c = 1\mu\text{K}$ given in the subsection 3.2.2. The results presented in FIG. 3.2 show that the maximum efficiency achievable by varying η is much lower

for anisotropic collisions than that achievable with isotropic collisions. In addition, the maximum efficiency is reached at smaller η . This suggests, for example, that if ϵ_t is set by the trap depth in an experiment, a shallower trap is desirable for evaporating a gas with anisotropic collisions, compared with evaporating a gas with isotropic collisions, at the same temperature and collision rate.

For these calculations, the inelastic to elastic collision rate ratio was held fixed at $\zeta = 1/200$. This was chosen based on typical experimental conditions for KRb molecules (see Sec. 3.4). The value of ζ does not qualitatively change the above comparisons; it only changes the shape of each curve [123], and as one would expect, the maximum efficiency and the corresponding η decreases as ζ increases.

In FIG. 3.3, we plot the time-dependent trajectories of evaporative cooling for isotropic collisions with $\eta = 4.3$, and for anisotropic collisions for $E_c = 1 \mu\text{K}$ with $\eta = 3.4$. These values of η were chosen such that Ω_f/Ω_0 is maximum in FIG. 3.2, and thus most efficient. It is evident from this plot that to reach the same increase in Ω and decrease in T , it takes much shorter time with isotropic collisions (FIG. 3.3(b)). This indicates a lower efficiency with anisotropic collisions, consistent with the results of FIG. 3.2.

3.3 Evaporative cooling in 2D traps

Physics in two-dimensional geometries can often be quite different from that in three-dimensions. Unlike many previous evaporative cooling experiments, KRb molecules need, in general, to be confined in traps with reduced dimensionality to be stable. Such a configuration was also used to evaporate Cs atoms [105]. Here, we study the effect of reduced dimensionality on evaporative cooling by comparing the efficiency in two-dimensional and three-dimensional traps.

The previous section showed that the existence of highly-anisotropic collisions slows down thermalization and decreases the efficiency of evaporative cooling. A calculation analogous to Sec.

3.2.2 but for a three-dimensional harmonic trap gives

$$\kappa = \frac{5}{6}(2\alpha + 3), \quad (3.13)$$

which implies $\kappa = 2.5$ when $\alpha = 0$ (isotropic collisions). This result may suggest a potentially faster thermalization rate and more efficient evaporation in a two-dimensional harmonic trap when compared with a three-dimensional harmonic trap with everything else held fixed. However, such a conclusion based solely on Eq. (3.13) would be premature, since the density of states depends on the dimensionality. Specifically, it was found for the comparison between quadratic potentials and linear potentials in three dimensions that changing the density of states can also change the evaporative cooling efficiency [123].

To incorporate such differences, we use MC simulation and a truncated-Boltzmann (TB) method based on kinetic theory (see Appendix A.2) to calculate the evaporation trajectories. Here, we consider harmonic traps and isotropic energy-independent collisions in order to isolate the effect of dimensionality. Following a similar procedure to that of the previous section, we calculate $\ln(\Omega_f/\Omega_0)$ at fixed N_f/N_0 , under equivalent initial conditions for both types of traps. As shown in FIG. 3.4, both the MC and TB approaches show a lower achievable increase in the phase-space density for a two-dimensional harmonic trap. This suggests that evaporative cooling is intrinsically less efficient in two-dimensional traps. The discrepancy between MC and TB, which increases for smaller η , is caused by the discrepancy between the form of the energy distributions, which for TB is constrained. At smaller η , the truncated Boltzmann distribution deviates significantly from the actual distribution of molecules, as calculated in MC.

3.4 Evaporative cooling of KRb molecules

In a quasi-two-dimensional trap, the elastic and reactive collisions between KRb molecules both depend on both the strength of the external electric field and the confinement induced by the lattice. Under current trapping conditions in experiments, a favorable ratio between the elastic and reactive processes can be reached at a moderate electric field [60, 201]. We show in FIG. 3.1(b)

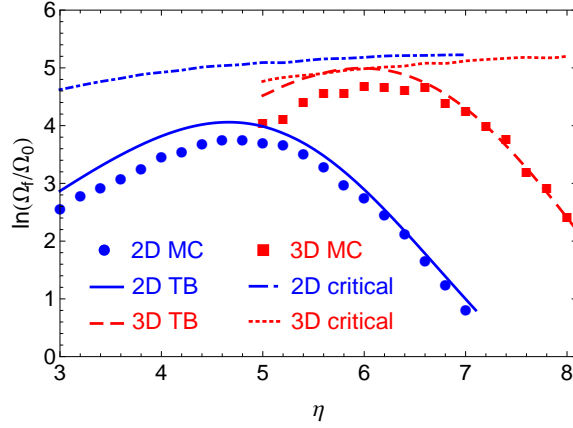


Figure 3.4: Comparison of the efficiency of evaporative cooling in two-dimensional (2D) and three-dimensional (3D) harmonic traps. $\ln(\Omega_f/\Omega_0)$'s are calculated at $N_f/N_0 = 0.1$, and $\zeta = 1/200$. Red (blue) line: 3D (2D) harmonic trap from method in Appendix A.2; red squares: 3D harmonic trap from MC simulation; blue disks: 2D harmonic trap from MC simulation; blue (red) dotted line: Ω_c for a 2D (3D) trap.

the total scattering cross-section for the elastic process and reactive process of KRb molecules at $d = 0.2$ debye with the confinement along the lattice direction given by $\nu = 23$ kHz. In the ultracold regime, the elastic cross-section scales as $E_c^{3/2}$, while the reactive cross-section scales as $E_c^{1/2}$ [146]. Furthermore, elastic processes are found to be generally faster than reactive processes, supporting the potential for successful evaporative cooling [200] while the large elastic cross-section favors fast rethermalization.

The quantitative knowledge of the elastic and reactive collisions between KRb molecules allows us to apply MC simulation with realistic experimental parameters. In FIG. 3.5, we show evaporation trajectories in a $2\pi \times 20$ Hz two-dimensional gaussian trap. For this simulation, we have assumed the instantaneous removal of energetic molecules above the cut, as in Sec. 3.2.3 and Sec. 3.3. We also assume that the inelastic losses are only due to the reactive collisions that are discussed above. The initial temperature was chosen to be within the accessible regime of experiments. The results show that a considerable increase in phase-space density can be achieved via evaporative cooling. We note that there are further experimental effects that can in principle reduce the achieved phase-space density increase from that calculated here, such as the finite rate

of removing energetic molecules and other sources of loss and heating. On the other hand, progress towards realizing deeper lattices (*i.e.*, $\nu > 23$ kHz), can potentially reduce ζ and thereby enhance the cooling efficiency.

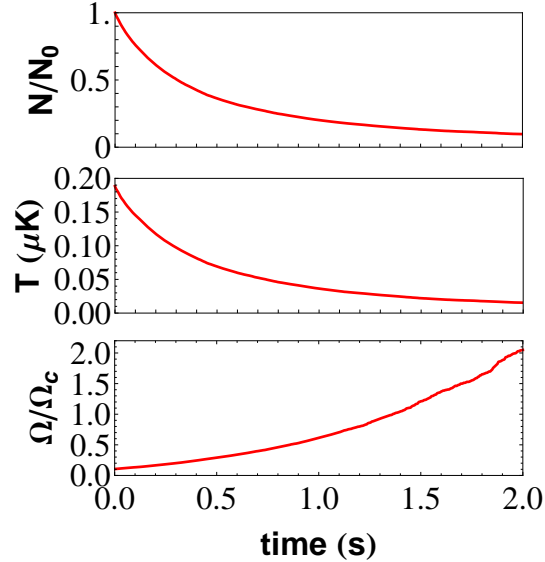


Figure 3.5: Evaporative cooling trajectories for KRb molecules inside a 2D trap of $2\pi \times 20$ Hz, with scattering cross-sections as computed in FIG. 3.1(b). The initial temperature was ~ 200 nK, with an initial-phase space density $\Omega_0 \sim 0.1\Omega_c$, and $\eta = 3.8$.

3.5 Anti-evaporation in quasi-2D

Fast inelastic collisions are disadvantageous for evaporative cooling, since they not only reduce the molecule number, but can also cause heating known as “anti-evaporation” [180]. Since the ability to identify the relative importance of different heating mechanisms is important in the design of experiments, in this section we quantitatively investigate heating due to two-body inelastic collisions.

Anti-evaporation arises from the fact that inelastic collisions are more frequent in the high density region of the trap (density-selection). Molecules there have on average total energies that are less than the ensemble average. Thus one may anticipate evaporative heating rather than evaporative cooling to occur. In competition with this, however, is the effect that the inelastic

collision cross-section is dependent on the collision energy, *i.e.*, molecules with energies higher than the average are more likely to engage in a reactive collision and be removed (velocity-selection). In three-dimensional harmonic traps, the density-selection mechanism wins over the velocity-selection mechanism and consequently there is net heating caused by p -wave two-body losses [180]. In two-dimensional trapping potentials, however, this is not necessarily true as we now show.

We consider a two-dimensional harmonic trap and assume a Boltzmann distribution as given in Eq. (3.3), for which the number loss rate is

$$\frac{dN}{dt} = 2 \int d^2x d^2p_1 d^2p_2 \lambda(E_{\text{rel}}) v_{\text{rel}} f_0(\mathbf{x}, \mathbf{p}_1) f_0(\mathbf{x}, \mathbf{p}_2), \quad (3.14)$$

and the corresponding energy loss is

$$\frac{dE}{dt} = \int d^2x d^2p_1 d^2p_2 \lambda(E_{\text{rel}}) v_{\text{rel}} f_0(\mathbf{x}, \mathbf{p}_1) f_0(\mathbf{x}, \mathbf{p}_2) (E_1 + E_2), \quad (3.15)$$

where E_{rel} and v_{rel} are the relative energy and velocity between the two colliding molecules, and $E_1 + E_2$ is the total energy. From Eq. (3.14) and Eq. (3.15), with $\lambda(E_{\text{rel}}) \propto E^{1/2}$ for p -wave collisions (Sec. 3.4), which dominates for ultracold identical fermionic KRb molecules [60], one can derive the energy loss per molecule, which is given by

$$\frac{dE}{dN} = 2k_B T. \quad (3.16)$$

This is precisely equal to the average energy per molecule. Thus we have a remarkable result that there is no net heating or cooling in a pure two-dimensional harmonic trap due to reactive loss. In contrast, a similar argument leads to heating for three-dimensional traps, as shown in Ref. [180] (heating rate there ~ 100 nK/s).

However, we emphasize that Eq. (3.14) to Eq. (3.16) only takes into account the two-body inelastic collisions and assumes a Boltzmann distribution, which implies sufficiently fast rethermalization. Note that at zero electric field, the elastic collisions that lead to thermalization are infrequent and can generally be neglected in experiments with KRb molecules [180], thus a Boltzmann distribution is not guaranteed.

To study possible effects caused by the deviation from a Boltzmann distribution during the evolution, we use MC simulations to calculate the molecule loss and temperature change in a two-dimensional harmonic trap, assuming only two-body inelastic processes between molecules. The results are plotted in FIGs. 3.6(a) and (b) respectively. The reactive collision rate is taken from FIG. 3.1 (b). The heating rate is found to be very small, illustrating a drastically different quantitative behavior from that seen in three-dimensional traps.

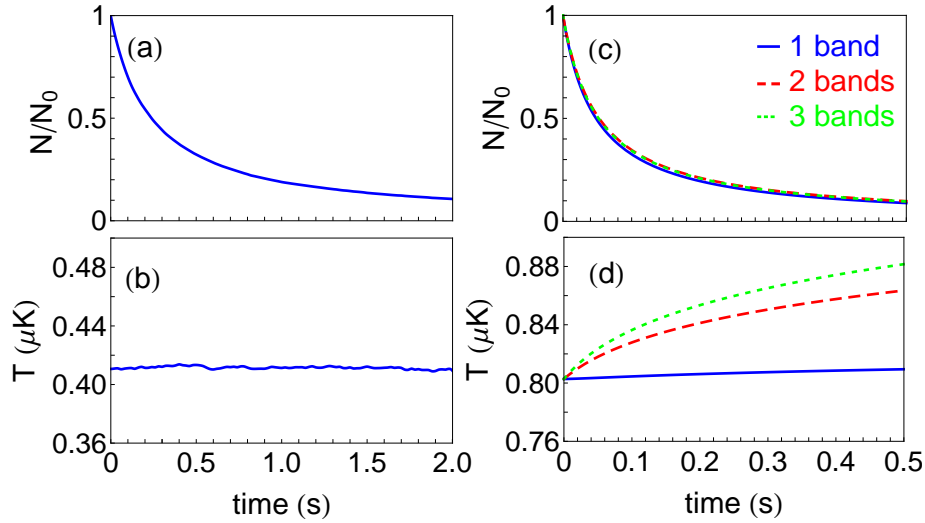


Figure 3.6: Heating due to two-body losses in a two-dimensional harmonic trap. Here (a) and (b) show the MC result in a two-dimensional harmonic trap where all molecules are in the lowest band of the lattice potential. The results for (c) and (d) are obtained with the master equation approach. The blue line assumes only 1 band along the lattice direction is populated. The red dashed line (green dots) assumes 2 (3) bands are populated. N_0 is the initial total molecule number. The initial temperature is chosen to be around 800 nK, so that when two bands are included, there are $\sim 25\%$ of molecules on the second band, and when three bands are included, there are $\sim 19\%$ of molecules on the second band and $\sim 6\%$ on the third band.

The periodic array of two-dimensional pancake traps for confining KRb molecules is generated by a one-dimensional optical lattice [60]. This forms energy bands separated by $\sim \hbar\omega_z$, where $\omega_z = 2\pi\nu$ and ν is the frequency of the harmonic approximation of the lattice potential. When the temperature is sufficiently low, the longitudinal degree-of-freedom along the lattice axis is effectively frozen out and one may consider solely the lowest band. However, as the temperature increases,

higher bands can be populated. For example, at $T \sim 800$ nK in a lattice of $\nu = 23$ kHz, about 25% of molecules occupy higher bands.

With multiband population, collisions between molecules can occur as inter-band or intra-band, as shown in FIG. 3.7. The inter-band collisions involve additional degrees-of-freedom along the longitudinal direction (see FIG. 3.7(b)), and thus do not satisfy the assumptions leading to Eq. (3.16) and can give rise to anti-evaporation heating [180].

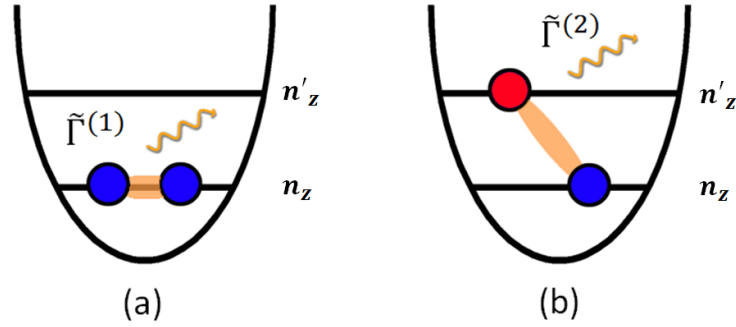


Figure 3.7: Collisions between molecules in a quasi-2D trap. (a) intra-band collisions, occurring at rate $\tilde{\Gamma}^{(1)}$. (b) inter-band collisions, occurring at rate $\tilde{\Gamma}^{(2)}$ (see Appendix A.3).

We adopt a many-body Hamiltonian to describe these p -wave inelastic collisions [119, 243, 162]

$$\hat{H}_p = \frac{3\pi b_p^3 \hbar^2}{m} \int d^3r [(\nabla \hat{\Psi}^\dagger(\mathbf{r})) \hat{\Psi}^\dagger(\mathbf{r}) - \hat{\Psi}^\dagger(\mathbf{r})(\nabla \hat{\Psi}^\dagger(\mathbf{r}))] \cdot [(\nabla \hat{\Psi}(\mathbf{r})) \hat{\Psi}(\mathbf{r}) - \hat{\Psi}(\mathbf{r})(\nabla \hat{\Psi}(\mathbf{r}))], \quad (3.17)$$

where $\hat{\Psi}(\mathbf{r})$ is a fermionic field operator that annihilates a molecule at position \mathbf{r} , and b_p^3 is the inelastic p -wave scattering volume. The value of b_p for KRb molecules can be found from the reactive cross-section calculated in the previous section. In a trap with transverse confinement ω_r and longitudinal confinement ω_z , the field operator can be expanded in the basis of non-interacting harmonic oscillator eigenstates ϕ_n^r and ϕ_n^z as:

$$\hat{\Psi}(\mathbf{r}) = \sum_{\mathbf{n}} \hat{c}_{\mathbf{n}} \phi_{n_x}^r(x) \phi_{n_y}^r(y) \phi_{n_z}^z(z), \quad (3.18)$$

where $\mathbf{n} = (n_x, n_y, n_z)$ enumerates the mode number along each dimension, and $\hat{c}_{\mathbf{n}}$ annihilates a fermion in mode \mathbf{n} .

Considering elastic collisions to be negligible, we assume there is no change of modes during the losses, *i.e.*, a molecule initially in mode \mathbf{n} remains in mode \mathbf{n} . With such an assumption, each molecule can be labeled with its mode indices, and for identical fermions, there are no two molecules with the same indices. The two-body losses can then be accounted for by jump operators $\hat{A}_{\mathbf{n},\mathbf{m}} = \sqrt{\Gamma_{\mathbf{n},\mathbf{m}}}\hat{c}_{\mathbf{n}}\hat{c}_{\mathbf{m}}$, which remove two molecules in mode \mathbf{n} and \mathbf{m} at a rate $\Gamma_{\mathbf{n},\mathbf{m}}$ determined by the corresponding p -wave two-body inelastic collisions Eq. (3.17) (see Appendix A.3 for details). When $n_z = m_z$, these correspond to the intra-band collisions (FIG. 3.7(a)); when $n_z \neq m_z$, these correspond to the inter-band collisions (FIG. 3.7(b)).

The dynamics can then be described by the quantum master equation

$$\frac{d\hat{\rho}}{dt} = \frac{1}{2} \sum_{\mathbf{n},\mathbf{m}} (2\hat{A}_{\mathbf{n},\mathbf{m}}\hat{\rho}\hat{A}_{\mathbf{n},\mathbf{m}}^\dagger - \hat{A}_{\mathbf{n},\mathbf{m}}^\dagger\hat{A}_{\mathbf{n},\mathbf{m}}\hat{\rho} - \hat{\rho}\hat{A}_{\mathbf{n},\mathbf{m}}^\dagger\hat{A}_{\mathbf{n},\mathbf{m}}). \quad (3.19)$$

Since we have assumed that the molecules do not change modes during evolution, in order to solve Eq.(6.1), we can use $\hat{\rho} = \prod_i \sum_{\mathbf{n}} \rho_{\mathbf{n},\mathbf{n}}^i \delta(\mathbf{n} - \mathbf{n}^i) |\mathbf{n}\rangle \langle \mathbf{n}|$, where $i = 1, 2, 3 \dots N$ represents the i th molecule that initially is in mode \mathbf{n}^i , N is the initial total number of molecules. Since the quantum jumps here correspond to the reactive loss of pairs of molecules, the off-diagonal coherence terms have been dropped. The relevant equation of motion under these assumptions is

$$\frac{d\rho_{\mathbf{n}^i, \mathbf{n}^i}^i}{dt} = -\rho_{\mathbf{n}^i, \mathbf{n}^i}^i \sum_{j \neq i} \Gamma_{\mathbf{n}^i, \mathbf{m}^j} \rho_{\mathbf{m}^j, \mathbf{m}^j}^j. \quad (3.20)$$

The total molecule number at time t is thus

$$N(t) = \sum_i \rho_{\mathbf{n}^i, \mathbf{n}^i}^i(t), \quad (3.21)$$

and the average temperature can be found from

$$T(t) = \frac{1}{N(t)k_B} \sum_i \hbar\omega_r (n_x^i + n_y^i) \rho_{\mathbf{n}^i, \mathbf{n}^i}^i(t). \quad (3.22)$$

Furthermore, the initial population in different bands can be determined by

$$\frac{N^\alpha}{N} = \frac{e^{-(1/2 + \alpha\hbar\omega_z)/k_B T}}{\sum_\alpha e^{-(1/2 + \alpha\hbar\omega_z)/k_B T}}, \quad (3.23)$$

where $\alpha = 0, 1, \dots$ is the band index. For the initial condition, the density matrix is simulated such that N^α molecules are assigned to band index $n_z^i = \alpha$, and the transverse modes n_x^i, n_y^i are randomly generated from a Boltzmann distribution with given initial temperature T . The final result is averaged over many different simulations. In order to show the effect of including different number of bands, we assume a cut-off in the highest band index. In our calculation, if a total of n_{max} bands are taken into account, the population of the lower $n_{max} - 2$ bands is determined according to Eq. (3.23). All of the remainder molecules are assigned to the highest populated band, $n_{max} - 1$.

In FIG. 3.6(c) and (d), we show the result with temperature $T = 800$ nK and lattice frequency $\nu = 23$ kHz, which are typical for KRb experiments. While the small amount of multiband population does not lead to a significant change in the loss rate for molecules (FIG. 3.6(c)), there can nevertheless be significant heating. In consequence, it is necessary to greatly suppress the population outside the lowest band for evaporative cooling experiments to be effectively performed in quasi-two-dimensional geometries when reactive loss of the form considered here is present.

3.6 Conclusion

Motivated by recent experiments of KRb molecules, we have applied MC simulation methods and semianalytical approaches to perform a detailed study of evaporative cooling properties in two-dimensional traps with anisotropic collisions. We have quantitatively analyzed the dependence of the thermalization rate on the anisotropy of the elastic collisions. Specifically, for our calculations of the differential and total scattering cross-section for KRb molecules confined in a quasi-two-dimensional trap, we were able to investigate the efficiency of evaporative cooling for the practical parameter regime of recent experiments. The dipole-dipole interactions resulted in highly anisotropic elastic collisions which were disadvantageous for evaporative cooling when compared with isotropic collisions.

The reduced dimension of the trapping potential further decreased the efficiency of evaporative cooling when compared with conventional evaporation procedures for three-dimensional traps. Nevertheless, we showed that the phase space density of KRb molecules can potentially be increased

using evaporative cooling with parameters that are accessible under current experimental conditions. Although this could be limited by further complicated real-world experimental details that we have not considered, it is also the case that future experimental progress in increasing the ratio between the elastic and inelastic collision rates could lead to more efficient evaporative cooling of KRb molecules.

We also developed theoretical models to investigate the anti-evaporation induced by two-body losses. Our results highlighted the distinctions between the evaporation processes in two-dimensional and three-dimensional geometries through the role of multiband excitations in a quasi-two-dimensional trap. We point out that the importance of multiband physics has also been addressed in recent literature [233, 161, 267].

Chapter 4

Suppressing the loss of ultracold molecules via the continuous quantum Zeno effect

Fast inelastic two-body losses, induced for example by the exothermic chemical reactions discussed in the previous chapter for KRb molecules, impose a severe limit on molecule lifetimes [188, 180, 59]. For the use of ultracold molecules as a quantum resource for the exploration of rich physical phenomena, it is crucial to find appropriate means to overcome losses. Recent experiments with KRb molecules [278] have reported an inhibition of losses when the molecules are confined in an array of one-dimensional tubes with a superimposed axial optical lattice along the tubes (Fig. 4.1). Similar loss suppression by strong dissipation was previously observed in bosonic Feshbach molecules [244]. Extending the molecules' lifetime over timescales much longer than those determined by tunneling opens a path for the exploration of itinerant magnetism and other many-body phenomena arising from the interplay between dipolar interactions and motion, even in these highly reactive systems.

In Chapter 3, we have shown that free KRb molecules react rapidly. In a lattice, the two-body inelastic collision rates are larger than all other lattice energy scales, including the band separation energy. Consequently, this system is an example of a strongly correlated system that defies simple treatment in terms of single-particle physics. As such, description of the loss suppression based on the assumption that inelastic interactions do not affect the single-particle wave-functions is incorrect [161]. Evidence of this issue was reported in Ref. [278] where a heuristic “single-band” treatment of the losses was found to significantly overestimate the molecule filling fraction f .

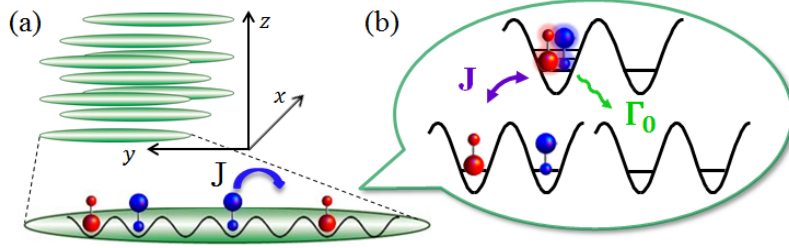


Figure 4.1: (a) A 50:50 mixture of fermionic KRb molecules in two rotational states, $|0,0\rangle$ (red) and $|1,-1\rangle$ (blue), is prepared in a deep 3D lattice, which is suddenly made shallow along one dimension (y). Along y , molecules tunnel with a rate J/\hbar and have a large on-site loss rate Γ_0 because of chemical reactions. (b) In the Zeno regime, $\hbar\Gamma_0 \gg J$, doubly occupied sites are only virtually populated, and the loss occurs at a significantly slower rate $\Gamma_{\text{eff}} \ll \Gamma_0$ for molecules on adjacent sites. For KRb, a multiband analysis of this process is required for all experimental lattice parameters.

Here, we develop a theoretical description of the dissipative dynamics that non-perturbatively includes three dimensional multi-band effects. Our analysis allows us to attribute the observed loss suppression to the continuous quantum Zeno effect [170, 109, 76, 99, 82] – a suppression of coherent transitions due to strong dissipation – and to generalize previous single-band treatments [82, 16] to the strongly dissipative regime. We perform systematic measurements of the KRb lifetime under controlled and reproducible lattice conditions that allow us to validate the calculations. The observed dependence of the loss rate on lattice parameters is consistent with Ref. [278] and is fully reproduced by the multiband theory. Moreover, the inclusion of multiple bands reduces the determined filling f by a factor of ~ 5 , giving results consistent with the filling predicted by Ramsey spectroscopy measurements of molecules pinned in a 3D lattice and prepared under similar initial conditions [278, 100].

The multiband calculations are first applied to derive a simple rate equation (RE) for two-body losses, which assumes instantaneous redistribution of molecules between collision events. We show that the RE can describe the measured dissipative dynamics fairly well over a broad range of lattice parameters, but fails for the deepest lattice configurations. We develop a simple and unified theory capable of describing the loss dynamics in **all** parameter regimes based on a mean-

field (MF) approximation of the many-body master equation. We validate the MF formulation by comparing it to a numerically exact time-dependent density matrix renormalization group method (t-DMRG) [259, 55, 266], which we combine with a quantum trajectory technique [39, 172, 72]. The MF, t-DMRG, and experimentally observed loss dynamics quantitatively agree.

4.1 Experiment with KRb molecules

The experiment begins by loading $\sim 10^4$ fermionic KRb ro-vibrational ground-state molecules, $|N = 0, m_N = 0\rangle$, into the lowest band of a deep 3D cubic optical lattice with lattice constant $a = 532$ nm. Here, N is the principal rotational quantum number and m_N is the projection onto the quantization axis, which in our case is determined by an external magnetic field angled 45° between the x and y lattice directions. We next apply a $\pi/2$ microwave pulse to rotationally excite half of the molecules to $|N = 1, m_N = -1\rangle$. We consider $|0, 0\rangle$ and $|1, -1\rangle$ as $|\downarrow\rangle$ and $|\uparrow\rangle$ components of a pseudo-spin 1/2 system. We choose the lattice polarizations so that the tensor AC polarizabilities of $|0, 0\rangle$ and $|1, -1\rangle$ are similar [178]. However, a residual differential AC Stark shift introduces single-particle dephasing that results in a spin-coherence time for the entire sample of ~ 1 ms. This dephasing allows us to prepare an incoherent 50:50 spin mixture of $|\downarrow\rangle$ and $|\uparrow\rangle$ by holding the molecules in the deep lattice for 50 ms. Losses are then initiated by quickly ramping down the lattice depth in the y direction (within 1 ms) to allow tunneling. We measure the number of remaining molecules $|\downarrow\rangle$, i.e., $N_\downarrow(t)$, as a function of the subsequent holding time in the lattice.

We experimentally determine the initial loss rate κ by fitting $N_\downarrow(t)$ to the solution of a two-body loss RE of the form

$$\frac{dN_\downarrow}{dt} = -\frac{\kappa}{N_\downarrow(0)} [N_\downarrow(t)]^2, \quad (4.1)$$

with $N_\downarrow(0)$ the initial number of $|\downarrow\rangle$ molecules. A typical experimental fit is shown in Fig. 4.2(a). To avoid the saturation of the losses that originates from the finite number of molecules per tube (~ 6 per tube on average), which cannot be captured by the RE, we fit only up to times when $\sim 25\%$ of the molecules are lost.

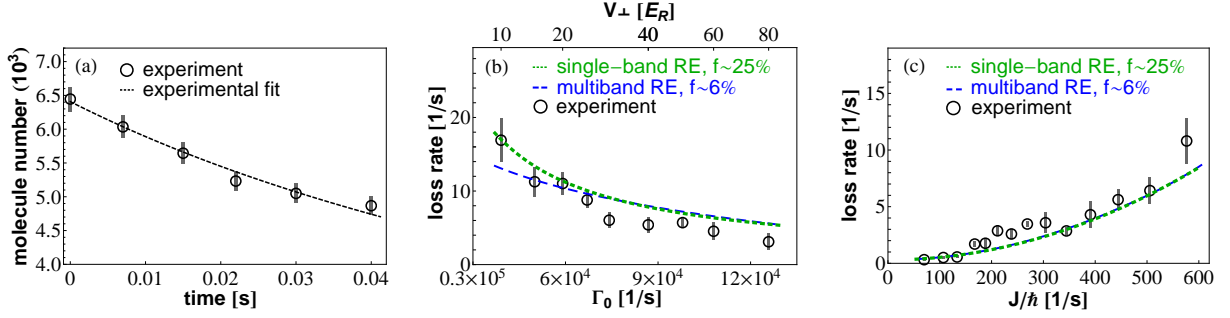


Figure 4.2: (a) Measured number loss of $|\downarrow\rangle$ molecules for an axial (transverse) lattice depth of $V_y = 5 E_R$ ($V_\perp = 25 E_R$) (circles) and best fit using a rate equation (RE), Eq. (4.1) (black dashed line). (b) Number loss rate, κ , as a function of Γ_0 (fixing $J \approx 570$ Hz and varying the bare on-site rate via V_\perp). (c) Number loss rate, κ , versus J for fixed $\Gamma_0 \approx 87$ kHz (varying V_y and adjusting V_\perp accordingly). V_y (V_\perp) was varied from 5 to 16 E_R (20 to 40 E_R). Black circles are experimental measurements (error bars represent one standard error). Green short-dashed lines show solutions of the RE Eq. (4.4) using an effective loss rate Γ_{eff} (single-band approximation). The blue long-dashed line shows the multiband RE using $\tilde{\Gamma}_{\text{eff}}$ in Eq. (4.4). The multiband and single-band RE results were obtained by fixing the filling fraction to be 6%, and 25% respectively. Panels (b) and (c) directly manifest the continuous quantum Zeno effect: in (b) the measured loss rate κ decreases with increasing on-site Γ_0 ; in (c) a fit to the experimental data supports $\kappa \propto J^2$, with a χ^2 (sum of the squared fitting errors) several times smaller than for a linear fit.

The loss rate κ in general depends on the tunneling rate J/\hbar and the on-site “bare” loss rate Γ_0 . If a single-band approximation is used, the on-site bare loss rate Γ_0 is given by [82]

$$\Gamma_0 = \beta^{(3D)} \int |W(\mathbf{x})|^4 d^3\mathbf{x}, \quad (4.2)$$

where $W(\mathbf{x})$ is the lowest-band single-particle 3D Wannier orbital. The two-body loss rate coefficient for molecules in $|0, 0\rangle$ and $|1, -1\rangle$, $\beta^{(3D)}$, was measured to be $\beta^{(3D)} = 9.0(4) \times 10^{-10} \text{ cm}^3 \text{ s}^{-1}$ [278].

To experimentally extract the dependence of κ on Γ_0 and the single-particle hopping energy J , we perform similar measurements to those reported in Ref. [278]. However, here we ensure reproducibility of the initial conditions to fix f for all lattice conditions. To measure the Γ_0 -dependence we set $V_y = 5 E_R$, which fixes J , and then tune Γ_0 by modifying V_\perp [Fig. 4.2(b)]. Here, $E_R = \hbar^2 \pi^2 / 2ma^2$ is the recoil energy and m is the KRb mass. To study the J -dependence, we vary V_y while simultaneously adjusting V_\perp to keep Γ_0 fixed [Fig. 4.2(c)]. The loss rate κ is found to depend quadratically on J for fixed Γ_0 and to decrease with increasing Γ_0 for fixed J . This scaling

is consistent with the continuous quantum Zeno effect, as we now explain.

4.2 Theoretical description

4.2.1 Single-band rate equation

A simple way to understand the loss suppression is to consider two opposite spin particles in a double well, $|\uparrow, \downarrow\rangle$. Left and right sides in this notation represent left and right wells [Fig. 4.1(b)]. When two molecules occupy the same site the singlet component decays with rate Γ_0 , while the decay of the triplet component is suppressed by the centrifugal barrier in odd partial-wave channels [59]. Consequently, the loss rate is determined by $J_s = \sqrt{2}J$, which is the tunneling computed after projecting the initial wavefunction into the singlet state $|s\rangle = (|\uparrow, \downarrow\rangle - |\downarrow, \uparrow\rangle)/\sqrt{2}$.

When $\hbar\Gamma_0 \gg J_s$, second-order perturbation theory can be applied and gives a net $|\downarrow\rangle$ loss rate of $4\Gamma_{\text{eff}}$ with $\Gamma_{\text{eff}} = \frac{2(J/\hbar)^2}{\Gamma_0}$. This loss rate can be connected to number loss dynamics with a RE, $\frac{dn_{j\downarrow}}{dt} = -4q\Gamma_{\text{eff}}n_{j+1\uparrow}n_{j\downarrow}$, where $n_{j\downarrow}$ is the number of $|\downarrow\rangle$ molecules at site j and q is the number of nearest neighbor lattice sites ($q = 2$ for tunneling along the tube direction) [16]. Assuming a uniform distribution, the 50:50 mixture implies $n_{j+1\uparrow} = n_{j\downarrow} = n_{\downarrow}$ and

$$\frac{dn_{\downarrow}}{dt} = -8\Gamma_{\text{eff}}[n_{\downarrow}(t)]^2 \quad \text{or} \quad (4.3)$$

$$\frac{dN_{\downarrow}}{dt} = -\frac{\kappa_{SB}}{N_{\downarrow}(0)}[N_{\downarrow}(t)]^2, \quad (4.4)$$

where $\kappa_{SB} = 8\Gamma_{\text{eff}}n_{\downarrow}(0)$. All parameters are known except the filling fraction $f = 2n_{\downarrow}(0)$. The RE assumes that the loss rate depends only on the **average** density. This assumption is valid when the redistribution of density after a loss process occurs faster than the typical time between losses ($J \gg \Gamma_{\text{eff}}$)¹.

This simplified single-band model qualitatively reproduces the measured dependence of κ on lattice parameters [green-short-dashed line in Figs. 4.2(b)-(c)]. However, since Γ_0 is larger than the band gap (e.g., 4 times larger for a $V_y = 5 E_R$ and $V_{\perp} = 40 E_R$ lattice), this single-band theory is

¹ Note: Although a transition dipole matrix element exists between $|\uparrow\rangle$ and $|\downarrow\rangle$, we neglect dipolar interactions because of the lack of spin coherence in our 50:50 mixture

known to be inadequate. Moreover, in order to fit the experiment, the single-band theory requires $f \approx 25\%$, which is known to be inconsistent with estimates of the filling $f \lesssim 10\%$ from Ramsey spectroscopy procedures [100, 49]. Resolution of this discrepancy requires including multiple single-particle bands, which are admixed by strong two-body losses.

4.2.2 Multiband rate equation

A single-band model overestimates Γ_0 , predicting it to be larger than the band gap. Incorporating higher bands decreases Γ_0 and hence decreases the f estimated from experiment (since the effective loss rate is inversely proportional to Γ_0). We extract a renormalized effective loss rate by numerically computing the loss of two molecules trapped in a double well along y . We expand the non-Hermitian Hamiltonian $\hat{H} = \hat{H}_0 - i\hbar\beta^{(3D)}\delta_{\text{reg}}(\mathbf{r})/2$, where $\delta_{\text{reg}}(\mathbf{r}) = \delta(\mathbf{r})(\partial/\partial r)r$ is a regularized pseudopotential [104] and \hat{H}_0 the single-particle Hamiltonian, in the 3D Wannier function basis. This model accounts for interaction-mediated band excitations in all three dimensions. We initialize the system with two molecules in the singlet $|s\rangle$ and infer the effective loss rate by fitting the norm decay to $\exp(-4\tilde{\Gamma}_{\text{eff}}t)$. Convergence is achieved with 6 bands in each dimension.

Surprisingly, as shown in Figs. 4.2(b–c), both effective loss rates Γ_{eff} and $\tilde{\Gamma}_{\text{eff}}$ scale similarly with Γ_0 and J . This similarity explains why qualitative experimental signatures of Zeno suppression expected from a single-band model survive even though such a model is invalid. However, the multiband $\tilde{\Gamma}_{\text{eff}}$ is ~ 5 times larger than Γ_{eff} . Once these effective loss rates are calculated, the only free parameter to fit the experimental measurements is the filling f , which was fixed to be the same for all data shown in Figs. 4.2(b–c). The ~ 5 times faster loss rate from the multiband model leads to a ~ 5 times smaller filling fraction of $f = 6\%$ [Figs. 4.2(b–c), blue-long-dashed line] compared to the grossly overestimated 25% extracted using Γ_{eff} [Figs. 4.2(b–c) green-short-dashed lines]. The inadequacy of the single-band model to extract the correct filling fraction, and the success of the multiband model, are key results of this work.

4.2.3 Mean-field and DMRG

The RE, with parameters extracted from the multiband model, describes the experimental observations fairly well at intermediate V_{\perp} , but deviates from them for the largest V_{\perp} . We attribute these deviations to the suppression of tunneling at the cloud's edges due to the energy mismatch between adjacent sites in the harmonic potential generated by the lattice beams. By inhibiting transport, this effect invalidates the assumption that molecules are redistributed rapidly between loss events, and therefore the losses are not determined exclusively by the average density but depend on the detailed dynamical redistribution of molecules.

Although this redistribution is absent from the RE, it can be accounted for by solving a master equation with a density matrix, $\hat{\rho}$, projected into the states with at most one molecule per site after adiabatic elimination of doubly occupied states. We keep terms up to order Γ_{eff} [82], and we simultaneously account for multiband effects by replacing the single-band Γ_{eff} by the renormalized loss rate extracted from the multiband double well solution, obtaining

$$\frac{d}{dt}\hat{\rho} = -\frac{i}{\hbar}[\hat{H}_0, \hat{\rho}] + \mathcal{L}\hat{\rho}. \quad (4.5)$$

Here $\hat{H}_0 = -J \sum_{j,\sigma} (\hat{c}_{j\sigma}^{\dagger} \hat{c}_{j+1\sigma} + h.c.) + \sum_{j,\sigma} V_j^{\sigma} \hat{c}_{j\sigma}^{\dagger} \hat{c}_{j\sigma}$, $\mathcal{L}\hat{\rho} = \frac{1}{2} \sum_j \left[2\hat{A}_j \hat{\rho} \hat{A}_j^{\dagger} - \hat{\rho} \hat{A}_j^{\dagger} \hat{A}_j - \hat{A}_j^{\dagger} \hat{A}_j \hat{\rho} \right]^2$, and $V_j^{\sigma} = \frac{1}{2} m \omega_{\sigma}^2 j^2 a^2$ is the parabolic trapping potential felt by molecules in state σ at site j . The average trap frequency $(\omega_{\uparrow} + \omega_{\downarrow})/2$ varies between $\approx 2\pi \times (15 - 40)$ Hz for the experimental range of V_{\perp} . The σ -dependence is due to residual differential AC Stark shifts between the two rotational states. \mathcal{L} is a Lindblad superoperator that accounts for losses, and the jump operators are $\hat{A}_j = \sqrt{2\tilde{\Gamma}_{\text{eff}}}$ $\left[(\hat{c}_{j\uparrow} \hat{c}_{j+1\downarrow} + \hat{c}_{j\uparrow} \hat{c}_{j-1\downarrow}) - (\hat{c}_{j\downarrow} \hat{c}_{j+1\uparrow} + \hat{c}_{j\downarrow} \hat{c}_{j-1\uparrow}) \right]$. We have checked the validity of the renormalized single-band model by confirming that it reproduces the dynamics of the multiband problem for the case of two molecules in four wells.

To solve Eq. (B.1) we map the hardcore fermions onto hardcore spin-1/2 bosons [255], and then use a mean-field ansatz $\hat{\rho} = \prod_j \tilde{\rho}_j$ with $\tilde{\rho}_j \equiv \sum_{\alpha,\beta=\{\uparrow,\downarrow,0\}} \rho_j^{\alpha,\beta} |\alpha\rangle\langle\beta|$. Here, $\tilde{\rho}_j$ is the reduced projected density matrix at site j , and $\uparrow, \downarrow, 0$ label the three possible local states of spin up, down,

² Note: The sums run over all lattice sites, operators acting outside the bounds are implicitly ignored.

and the vacuum, respectively. This ansatz leads to closed equations of motion for $\rho_j^{\alpha,\beta}$ [see Appendix B]. Due to the rapid dephasing of spin coherence resulting from $\omega_\uparrow \neq \omega_\downarrow$, we set $\rho_j^{\sigma,\sigma' \neq \sigma} = 0$, which simplifies the equations further. Although the MF treatment predicts no coherent tunneling for a pure Fock state, we initiate it by assuming non-zero particle/hole coherence $|\rho_j^{\sigma,0}| = 1/2$.

Fig. 4.3(a) shows the dynamics for the largest V_\perp , where the coherent tunneling is strongly suppressed by the large parabolic potential $\omega_{\uparrow/\downarrow}$. We see that the dynamics is poorly described by the RE, and the MF solution better describes the data. Admittedly, the MF assumption is an extreme approximation precluding entanglement between parts of the system. In order to test its validity, we also solve Eq. (B.1) numerically by combining t-DMRG algorithms [259, 55, 266] with a stochastic sampling over quantum trajectories [39, 172, 72, 220]. The results, shown in Fig. 4.3(b), are converged in the matrix product state dimension χ_{MPS} and are therefore numerically exact. The differential stark shift for the lattice parameters of Fig. 4.3 ($\omega_\uparrow/\omega_\downarrow \sim 0.9$) gives rise to an effective spatially dependent magnetic field that disrupts spin correlations generated during the dynamics. In this case the data, t-DMRG, and MF (which explicitly ignores spin-correlations) agree up to the times used to extract loss rates from the data, when the contrast has decayed by $\sim 20\%$. However, in the absence of a differential Stark shift ($\omega_\downarrow = \omega_\uparrow$), we note that the density calculated from t-DMRG saturates at a higher value than predicted by the MF theory, which we attribute to the growth of spin correlations in the absence of dephasing [77].

4.3 Comparison with experiment measurement

4.3.1 Mean-field vs. experiment

With the validity of the MF established, we use it to model the experiment. In the MF calculation, we assume that molecules are initially uniformly distributed within a shell with inner (outer) radius of 20 (50) lattice sites. The shell distribution is expected because molecules are created from a Mott insulator of Rb and a band insulator of K. Assuming only sites with one Rb and one K can yield molecules during STIRAP [188, 49], sites in the trap center initially doubly

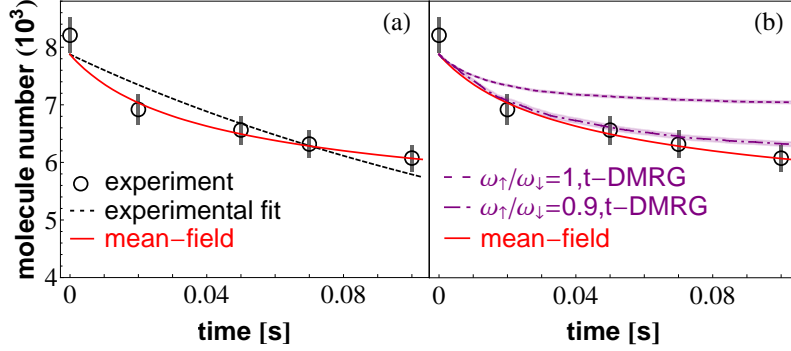


Figure 4.3: Comparison of experimental loss dynamics for the deepest considered lattice to MF and t-DMRG calculations. (a) Molecule loss vs. time for $V_\perp = 80 E_R$ and $V_y = 5 E_R$ [Identical conventions/conditions to Fig. 4.2(b)]. The MF matches the experimental data better than the RE (experimental fit). (b) Comparison of t-DMRG simulations ($\chi_{\text{MPS}} = 128$, 2000 trajectories) to MF, for two different cases: i) an identical trap for the two spin states with trap frequency $\omega_\downarrow = \omega_\uparrow = 2\pi \times 38$ Hz; and ii) slightly different trap frequencies $\omega_\downarrow = 2\pi \times 38$ Hz, $\omega_\uparrow = 2\pi \times 34.2$ Hz. Shaded areas indicate the standard error of the mean.

occupied by Rb atoms are lost [188]. We then average over random initial configurations, since the experiments measure an ensemble of 1D tubes. Figures 4.4(a-b) show the MF results (red line), where we used $f = 9\%$ to match the experiment. This is slightly larger than that from the multiband RE (dashed blue line in Figures 4.4), $f = 6\%$, since the RE overestimates the loss rate by assuming instantaneous redistribution of the molecules.

Since the molecule distribution in the experiment is known only approximately, we vary the shell width and find that the estimated MF filling fraction that best fits the experimental loss has a range $f \sim 9 \pm 2\%$. The MF accounts better for the dependence of the loss rate on V_\perp . Remaining deviations between MF and experiment are seen only for the shallowest V_\perp , where the transverse tunneling rate is only three times smaller than the axial one, which may indicate the breakdown of 1D dynamics.

4.4 Conclusion

The understanding of the underlying physical mechanism responsible for the loss suppression in KRb opens the path for laboratory explorations of iconic models of quantum magnetism com-

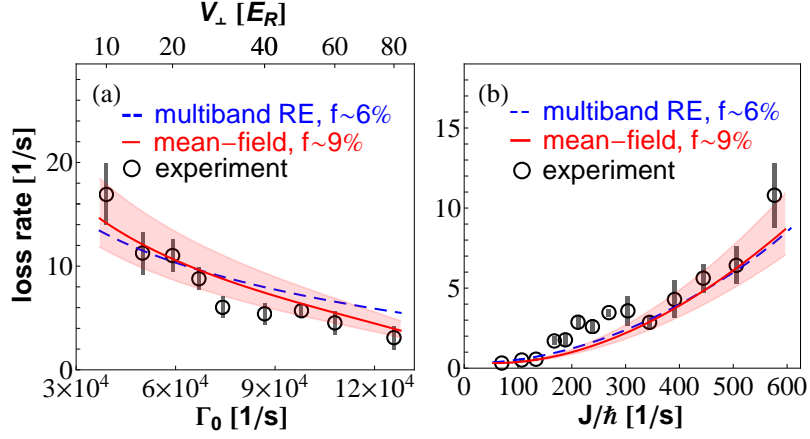


Figure 4.4: (a) Number loss rate, κ , as a function of Γ_0 (same data as Fig. 2(b)). (b) Number loss rate, κ , versus J for fixed Γ_0 (same data as Fig. 2(c)). Black circles are experimental measurements. Blue long-dashed and solid red lines show RE and MF solutions, respectively, using $\tilde{\Gamma}_{\text{eff}}$ (multiband model). The shaded area accounts for $\pm 2\%$ variations around the MF estimate of $f \sim 9\%$ arising from the uncertainty in the initial molecule distribution.

binning motional and spin degrees of freedom, previously believed to be inaccessible due to losses. These include the extended t - J model, predicted to exhibit itinerant ferromagnetism, d -wave superfluidity [90, 129], and topological phases [136, 13]. Our findings also extend to other dissipative systems, such as alkaline earth atoms [152, 23, 252, 149] and other chemically reactive molecular species [285].

Chapter 5

Synchronization of Interacting Quantum Dipoles

5.1 Introduction

Arrays of synchronized oscillators [197] are ubiquitous in biological [277, 236], physical [52] and engineering [210] systems and are a resource for technological advances [145]. Although there has been significant progress in the study of synchronization in classical systems [8], the understanding of the same phenomena in the quantum realm remains limited. A major obstacle so far is the general problem of the exponential scaling of the Hilbert space with system size which makes calculations dealing with quantum arrays very challenging. In fact, current investigations have been limited to the exact treatment of arrays of a small number of coupled quantum oscillators [262, 226, 283, 163, 85, 84, 199, 3, 106, 261, 159], and large ensembles at the mean field level or by including quantum corrections perturbatively [154, 140, 141]. Highly symmetric situations with collective coupling mediated, for example, by a cavity mode [9, 273, 160], have also been studied.

Ensembles of radiating dipoles are a natural platform to study quantum synchronization, where coherence can be generated from an incoherent source. One might regard laser systems, where radiation is amplified by the stimulated emission of photons, as a prototypical example. However, lasing is fundamentally a distinct phenomenon from quantum synchronization. This can be seen from the fact that lasing is possible even in the absence of coupling between the atomic dipoles, as is clear in the single atom laser [164], or in atomic beam lasers where only one atom is present in the cavity at any given time. A more relevant situation is the quantum synchronization that takes place in the context of superradiance [94, 158]. It has recently been understood that,

in contrast to lasers, steady-state superradiance can produce spectrally pure light [94, 158, 29, 166, 96, 272, 241, 97] without stimulated emission. So far this has been demonstrated using a cavity mode as a communication channel that spatially selects an optical mode and enhances the coupling (through the cavity finesse). A more generic and relevant scenario, with great potential and applicability, is the emergence of spontaneous macroscopic quantum synchronization in radiating dipole arrays without a cavity but naturally coupled by the intrinsic anisotropic and long-range dipolar interactions. This is the situation considered in this chapter.

Here we demonstrate that in the presence of an incoherent repumping source, dipole induced cooperative emission can dominate over spatial inhomogeneities and quantum fluctuations and lead to a resilient steady-state that exhibits macroscopic quantum phase coherence and intrinsic quantum correlations. An iconic example of a macroscopic coherent state is a Bose-Einstein condensate, achieved in ultra-cold gases at thermal equilibrium. In our case, however, the macroscopic order is reached in the steady-state of an interacting and driven-dissipative system. Moreover, the cooperative behavior can be detected by measuring the spectral purity of the emitted radiation. We note that in clear distinction to previous studies [106, 154, 262, 3, 261, 141], our proposal does not rely on an external coherent source or externally generated nonlinearities to seed the collective phase. In our model synchronization emerges as a spontaneously broken symmetry driven by incoherent processes in naturally coupled dipole arrays. As we show, and somewhat counterintuitively, an incoherent drive is sufficient to generate phase coherence in these systems.

Specifically, the systems we consider are dense arrays of frozen quantum dipoles modeled as quantized two-level systems. By dense arrays of frozen dipoles we mean arrays separated by a distance much closer than the wavelength of the emitted photons and with motional degrees of freedom evolving at a much slower rate than their internal dynamics (Fig. 5.1). These conditions can be readily satisfied in a variety of quantum systems found in atomic, molecular and optical physics (e.g., Rydberg gases [257, 1, 5], alkali vapors [122], alkaline-earth atoms [187], and polar molecules [278]), chemistry (e.g., J-aggregates of dye molecules [28, 192, 234]), and biology (e.g., light-harvesting complexes [193, 222]). In cold vapors, one possible way to freeze the motion and

tightly trap the particles is via an optical lattice potential (Fig. 5.1). In this case a sub-optical-wavelength transition must be used in order to reach the tight-packing regime [278, 187].

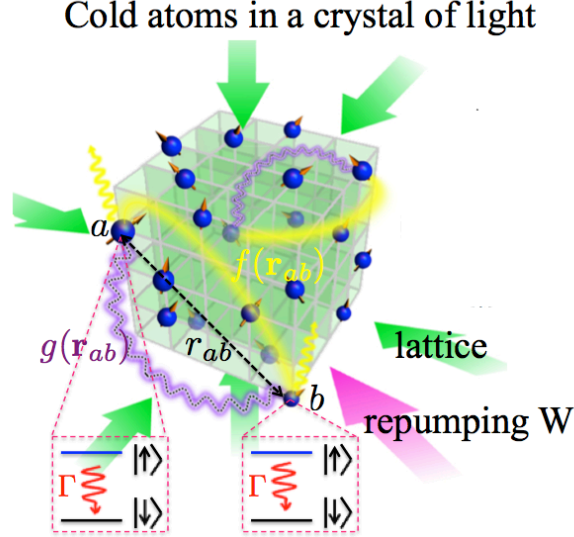


Figure 5.1: Arrays of quantum dipoles spontaneously emit and absorb photons at rate Γ . The photons mediate dipolar interactions between dipoles separated by a distance \mathbf{r}_{ab} with both dissipative, $f(\mathbf{r}_{ab})$, and elastic, $g(\mathbf{r}_{ab})$, components. A repumping source at a rate W provides energy to maintain the oscillations and can be implemented using additional internal states that are not shown. A possible implementation can be realized with cold atoms in an optical lattice.

To fully understand synchronization in the complex dipolar system, we analyze each of the ingredients that compete and affect synchronization in a step-by-step procedure: the interplay between repumping and collective emission, inhomogeneity in the coupling constants, quantum correlations, and the competition between elastic and inelastic interactions. This chapter is organized as follows: In Sec. 5.2 we introduce the system in consideration and the master equation we use to describe the dynamics. In Sec. 5.3 we first provide a simple mean-field description and discuss connections to the classical Kuramoto model—the iconic model used to describe synchronization in non-linear coupled oscillators. In Sec. 5.4 we discuss the phase diagram for the quantum system assuming collective (all-to-all) coupling in the absence of inhomogeneity and elastic interactions, and compare it with the mean-field solution. For this exactly solvable case we are able to explicitly quantify the entanglement and correlations present in the steady state. In Sec. 5.6 we study how

inhomogeneity in the inelastic couplings affects synchronization and focus on the case of power-law decaying interactions. In Sec. 5.5 we study the emergence of quantum synchronization in radiating dipoles taking the full long-range and anisotropic dipolar interactions into account. Specifically, we consider a one dimensional geometry, where both the elastic and inelastic interactions can vary significantly across the dipoles and can be easily adjusted. In Sec. 5.7 we discuss experimental implementations of our model, and in Sec. 5.8 we provide a conclusion and an outlook.

5.2 Dipole-dipole interaction and master equation

In this work we consider arrays of quantum dipoles with two accessible levels, which we denote as $|\downarrow\rangle$ and $|\uparrow\rangle$. The interactions between two dipoles a and b , can be explicitly written as

$$\begin{aligned} g(\mathbf{r}_{ab}) &= -\frac{3\Gamma}{2} \left\{ \sin^2 \theta \frac{\cos \zeta_{ab}}{\zeta_{ab}} + (3 \cos^2 \theta - 1) \left[\frac{\cos \zeta_{ab}}{(\zeta_{ab})^3} + \frac{\sin \zeta_{ab}}{(\zeta_{ab})^2} \right] \right\}, \\ f(\mathbf{r}_{ab}) &= \frac{3\Gamma}{2} \left\{ \sin^2 \theta \frac{\sin \zeta_{ab}}{\zeta_{ab}} + (3 \cos^2 \theta - 1) \left[\frac{\sin \zeta_{ab}}{(\zeta_{ab})^3} - \frac{\cos \zeta_{ab}}{(\zeta_{ab})^2} \right] \right\}. \end{aligned}$$

In the above, $\zeta_{ab} = k_0 |\mathbf{r}_{ab}|$. Both $g(\mathbf{r}_{ab})$ and $f(\mathbf{r}_{ab})$ depend on the dipoles' separation, $|\mathbf{r}_{ab}|$, and the angle θ between the mean dipole moment and the vector joining the dipoles. As noted in Chapter 2, when $\zeta_{ab} \ll 1$, the elastic g interactions with a strong angular variation are dominant except close to the magic angle $\theta_m = \arccos(1/\sqrt{3})$, at which they are greatly suppressed¹. In contrast, $f(\mathbf{r}_{ab})$ is almost isotropic in the near-field regime.

The spatially uniform behavior of $f(\mathbf{r}_{ab})$ at short distance is what gives rise to cooperative effects and superradiant emission [94]. Under generic conditions, however, superradiance is a transient effect that substantially limits the lifetime of dipole excitations. To compensate for the fast decay here we add an incoherent repumping driving term at a rate W . This term is needed to generate a synchronized steady state where long-lasting coherence persists. An incoherent repumping drive is commonly used in laser systems to maintain population inversion. It can be implemented

¹ For generic cases, the pathological divergence of $g(\mathbf{r})$ at $\mathbf{r} = 0$ can be removed by introducing an additional term into the expression of $g(\mathbf{r}_{ab})$, $-\frac{4\pi}{3k^3} \delta(\mathbf{r}_{ab})$ [175, 43]. This gives rise to the so called Lorentz-Lorentz shift [80]. For the discrete arrays we consider in this work, there is always a cut-off distance and thus no divergence. For example, in the suggested implementation using Sr atoms that is discussed in Sec. 5.7, the cut-off distance is determined by the optical lattice spacing.

by coherently driving, at a rate Ω , the $|\downarrow\rangle$ state to an excited level that spontaneously decays, at a rate $\gamma \gg \Omega$, to the state $|\uparrow\rangle$ [224]. Due to the fast depletion of the excited state, it can be adiabatically eliminated and thus the net process is just an incoherent transfer of population from $|\downarrow\rangle$ to $|\uparrow\rangle$ at a rate $W = \Omega^2/\gamma$.

The evolution of N dipoles is modeled by a quantum master equation for the reduced density matrix $\hat{\rho}$ of the dipoles [94]:

$$\frac{d\hat{\rho}}{dt} = -\frac{i}{\hbar}[\hat{H}_0, \hat{\rho}] + \mathcal{L}_f[\hat{\rho}] + \mathcal{L}_W[\hat{\rho}], \quad (5.1)$$

$$\hat{H}_0 = \frac{\hbar}{2} \sum_{a=1}^N \left[\delta_a \hat{\sigma}_a^z + \sum_{b=1, b \neq a}^N g(\mathbf{r}_{ab}) \hat{\sigma}_a^+ \hat{\sigma}_b^- \right], \quad (5.2)$$

$$\mathcal{L}_f[\hat{\rho}] = \frac{1}{2} \sum_{a,b} f(\mathbf{r}_{ab}) (2\hat{\sigma}_b^- \hat{\rho} \hat{\sigma}_a^+ - \hat{\sigma}_a^+ \hat{\sigma}_b^- \hat{\rho} - \hat{\rho} \hat{\sigma}_a^+ \hat{\sigma}_b^-), \quad (5.3)$$

$$\mathcal{L}_W[\hat{\rho}] = \frac{W}{2} \sum_a (2\hat{\sigma}_a^+ \hat{\rho} \hat{\sigma}_a^- - \hat{\sigma}_a^- \hat{\sigma}_a^+ \hat{\rho} - \hat{\rho} \hat{\sigma}_a^- \hat{\sigma}_a^+). \quad (5.4)$$

The Hamiltonian \hat{H}_0 generates the coherent evolution of the dipole array where $\hat{\sigma}_a^{(+,-,z)}$ are the Pauli spin operators for dipole a , δ_a denotes its oscillation frequency in the rotating frame defined by the mean frequency of the dipole ensemble, and \hbar is the reduced Planck constant. The Lindblad operator functionals, $\mathcal{L}_{f,W}$, describe the inelastic photon emission and incoherent repumping processes, respectively.

5.3 Mean-field treatment and connection to the Kuramoto model

To obtain a qualitative picture of how synchronization can happen among the dipoles, we first perform a mean-field treatment and show the close connection between our quantum model and the prototype models for classical synchronization. The mean-field approach assumes uncorrelated dipoles, i.e., $\hat{\rho} = \bigotimes_a \hat{\rho}_a$, where each $\hat{\rho}_a = \sum_{\sigma, \sigma' = \uparrow, \downarrow} \rho_a^{\sigma, \sigma'} |\sigma\rangle \langle \sigma'|$ is a 2×2 matrix in the pseudospin $1/2$ basis $\{|\uparrow\rangle, |\downarrow\rangle\}$. The components of the single-dipole density matrix, $\hat{\rho}_a$, can be visualized as a Bloch vector $\{S_a^x(t) \cos \phi_a(t), S_a^x(t) \sin \phi_a(t), S_a^z(t)\} = (1/2)\{\rho_a^{\uparrow\downarrow} + \rho_a^{\downarrow\uparrow}, -i(\rho_a^{\uparrow\downarrow} - \rho_a^{\downarrow\uparrow}), \rho_a^{\uparrow\uparrow} - \rho_a^{\downarrow\downarrow}\}$ (Fig. 5.2). The mean-field solution yields a system of coupled nonlinear differential equations for $\rho_a^{\sigma, \sigma'}$. For each $a = 1, 2, \dots, N$ the parameters evolve as

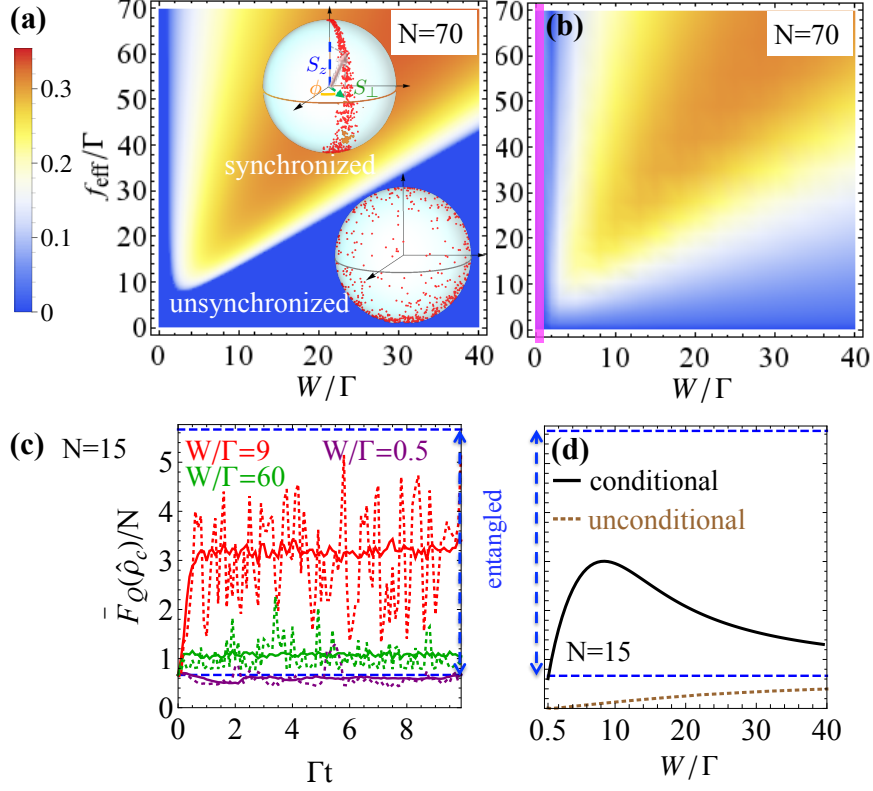


Figure 5.2: (a) Mean-field phase diagram calculated from the order parameter $0 \leq Z \leq 1/\sqrt{8}$. The insets show snapshots of the tips of the Bloch vectors (red points) for dipoles prepared with random initial phases and then evolved to steady-state in both regimes. (b) Quantum phase diagram calculated from $0 \leq Z_Q \leq 1/\sqrt{8}$. (c) The time evolution of the conditional QFI exhibits entanglement (dashed line: single trajectory, solid line: mean value of a few trajectories). Panel (d) shows the steady state QFI vs W/Γ after averaging over many trajectories. The solid line corresponds to the conditional case, and indicates entanglement over the repumping range where synchronization exists. Upon computing the ensemble average one recovers the reduced density matrix which leads to a calculated QFI below the entanglement witness threshold (dashed line). (c) and (d) are shown for $f_{\text{eff}} = 15\Gamma$. For all panels, $\delta_a = g(\mathbf{r}_{ab}) = 0$ and $f(\mathbf{r}_{ab}) = f_{\text{eff}}/N$.

$$\begin{aligned} \frac{dS_a^z(t)}{dt} &= -S_a^\perp(t) \sum_{b \neq a} S_b^\perp(t) \left[f(\mathbf{r}_{ab}) \cos[\delta\phi_{ba}] - g(\mathbf{r}_{ab}) \sin[\delta\phi_{ba}] \right] \\ &\quad - \Gamma \left[\frac{1}{2} + S_a^z(t) \right] + W \left[\frac{1}{2} - S_a^z(t) \right], \end{aligned} \quad (5.5)$$

$$\frac{dS_a^\perp(t)}{dt} = -S_a^z(t) \sum_{b \neq a} S_b^\perp(t) \left[g(\mathbf{r}_{ab}) \sin[\delta\phi_{ba}] - f(\mathbf{r}_{ab}) \cos[\delta\phi_{ba}] \right] - \frac{\Gamma + W}{2} S_a^\perp(t), \quad (5.6)$$

$$\frac{d\phi_a}{dt} = \delta_a + \sum_{b=1, b \neq a}^N S_a^z \frac{S_b^\perp}{S_a^\perp} \left[g(\mathbf{r}_{ab}) \cos[\delta\phi_{ba}] + f(\mathbf{r}_{ab}) \sin[\delta\phi_{ba}] \right], \quad (5.7)$$

where $\delta\phi_{ba}(t) = \phi_b(t) - \phi_a(t)$. The term proportional to $f(\mathbf{r}_{ab})$ in Eq. (5.7) that contains the sine function can be identified with a similar term in the Kuramoto model (KM) [130]:

$$\frac{d\phi_a}{dt} = \delta_a + K \sum_{b=1}^N \sin[\delta\phi_{ba}], \quad (5.8)$$

where K , the coupling strength per oscillator, must be large enough and positive for synchronization to occur. The term proportional to $g(\mathbf{r}_{ab})$ that contains the cosine function appears in the Sakaguchi-Kuramoto model [216]—a more general but similar synchronization model to the KM. Compared to the basic KM, the situation here is more complex. This is due to the fact that in Eq. (5.7) the coupling constants are nonuniform and effectively time-dependent, since $S_a^\perp(t)$ and $S_a^z(t)$ are dynamic variables.

To investigate whether the mean-field model admits spontaneous synchronization we consider first the simplified case where $\delta_a = 0$ for all dipoles, impose $g(\mathbf{r}_{ab}) = 0$ for all pairs, and assume a constant collective decay rate $Nf(\mathbf{r}_{ab}) \equiv f_{\text{eff}}$. We define a global order parameter Z as $Z e^{i\Phi} = \frac{1}{N} \sum_a S_a^\perp e^{i\phi_a}$ and look for a solution in which Z is time-independent and synchronized oscillators possess a collective frequency $\bar{\omega}$, and thus a macroscopic phase $\Phi = \bar{\omega}t$. These conditions lead to two equations for the order parameter Z and the collective frequency $\bar{\omega}$ (see C.1):

$$\bar{\omega} = 0, \quad (5.9)$$

$$Z = \frac{\sqrt{f_{\text{eff}}(W - \Gamma) - (W + \Gamma)^2}}{\sqrt{2}f_{\text{eff}}}. \quad (5.10)$$

The solution is shown in Fig. 5.2(a). The insets show the phase distribution in the steady-state for an array of oscillators initially prepared with a random distribution of phases for two different values of the repump rate W . For a slow repumping rate (bottom inset), the system remains unsynchronized. As the repumping rate is increased beyond a threshold value, the system enters a synchronized state, as can be seen by the appearance of phase locking and the resulting narrow phase spread (top inset). This can be explained by the fact that one necessary condition for synchronization in the KM is $K > 0$, which translates to the requirement $S_a^z > 0$ on average in our model and thus the need to have sufficiently large repump rate. In the limit $f_{\text{eff}} \gg \Gamma$ (e.g., for large

N), maximum synchronization is achieved at $W_{\text{opt}} = f_{\text{eff}}/2$, where the order parameter Z reaches a maximum value $Z_{\text{max}} \approx \sqrt{1/8}$. For this optimal condition for synchronization the quantum dipoles are ordered with the same phase and radiate with atomic inversion $S_a^z \approx 1/4$. Note that the maximum order parameter is smaller than $1/2$ even when fully synchronized because of this required finite value of the atomic inversion. One intriguing aspect is that repumping, which is the process that builds up synchronization, is itself an incoherent process. It is crucial that repumping does not preserve the norm of the collective Bloch vector, allowing it to extend or contract. For large $W > W_{\text{opt}}$, Z decreases again reflecting a suppression of synchronization. In this limit the dipoles are repumped so fast that they are all driven to the $|\uparrow\rangle$ state ($S_a^z \rightarrow 1/2$ and $S_a^\perp \rightarrow 0$) and phase coherence between them cannot build up.

The cases of a heterogeneous distribution of δ_a 's can be treated at the mean-field level in a simple way. The results, summarized in the C.1, are qualitatively similar. In general, the inclusion of a finite spread Δ in δ_a decreases the value of the order parameter Z . For instance, if δ_a is sampled from a Lorentzian distribution $p(\delta_a) = \Delta/[\pi(\Delta^2 + \delta_a^2)]$,

$$Z = \frac{\sqrt{f_{\text{eff}}P - Q^2 + 2\Delta^2 - 2\Delta\sqrt{\Delta^2 + f_{\text{eff}}P}}}{\sqrt{2}f_{\text{eff}}}, \quad (5.11)$$

where $Q = \Gamma + W$ and $P = W - \Gamma$. Optimal synchronization is obtained at a smaller repumping rate, $W_{\text{opt}} \approx f_{\text{eff}}/2 - \Delta/\sqrt{2}$. We note that for given f_{eff} and W , synchronization is destroyed (that is, $Z = 0$) at $\Delta_c = (Q^2 - f_{\text{eff}}P)/(2Q)$.

For the case with finite $g(\mathbf{r}_{ab}) \neq 0$, Eq. (5.7) predicts dephasing caused by different $g(\mathbf{r}_{ab}) \neq 0$, and a global rotation that does not affect synchronization if all $g(\mathbf{r}_{ab})$ are identical [see C.1]. However, the mean-field ansatz is not appropriate for treating the case where elastic interactions are present since it neglects quantum entanglement between dipoles. The case with finite $g(\mathbf{r}_{ab})$ will be discussed in Sec. 5.6 by exactly solving the many-body problem.

5.4 Quantum synchronization for the collective system

In the simplified case where $\delta_a = 0$ for all dipoles, $g(\mathbf{r}_{ab}) = 0$ for all pairs, and a constant collective decay rate $Nf(\mathbf{r}_{ab}) \equiv f_{\text{eff}}$, it is possible to exactly solve Eq. (5.1), *i.e.*, the full quantum dynamics, even for many particles, allowing us to benchmark the validity of the mean-field solution. This is due to the invariance of the master equation under individual dipole permutations that reduces the scaling of the Liouville space from exponential, 4^N , to polynomial, of order N^3 [275].

5.4.1 Phase Diagram

Quantum fluctuations can lead to phase diffusion and to decay of single particle coherences in the steady-state (it is possible for $\langle \hat{\sigma}_a^+ \rangle \rightarrow 0$ even in a synchronized state), so Z cannot be used as a measure of synchronization in a beyond mean-field treatment. However, phase locking in quantum mechanics can be quantified by the degree of spin-spin correlations Z_Q , defined by $Z_Q^2 \equiv \overline{\langle \hat{\sigma}_a^+ \hat{\sigma}_b^- \rangle}$, where the bar indicates an average over all pairs of different dipoles a and b . For an unsynchronized state Z_Q is 0 and for a completely synchronized state Z_Q is $Z_Q^{\text{max}} = 1/\sqrt{8}$ [166, 29]. The corresponding phase diagram, shown in Fig. 5.2(b), closely resembles the mean-field one.

To demonstrate that Z_Q can be used to quantify the emergence of quantum synchronization, regardless of the inherent non-equilibrium and dissipative character of our system, we have also computed pairwise two-time correlation functions (see Appendix C.2). The decay rate of these correlations encodes information about the spectral coherence of the emitted radiation. The range of W/Γ values where the emitted light is maximally coherent agrees with the regime where the system is optimally synchronized according to Z_Q . Moreover, we have also confirmed the moderate importance of higher order correlations in the synchronized steady-state by comparing the exact solution with a cumulant expansion calculation (which includes lowest order corrections to the mean-field result). We find the cumulant expansion agrees well with the exact solution (see Appendix C.2). The only limit where there are important deviations is at very weak pumping $W \ll \Gamma$ where the system favors subradiant emission arising from strong atom-atom correlations

[indicated by the purple region in Fig. 5.2(b)] [275].

5.4.2 Quantum correlations and entanglement

The robust macroscopic quantum coherence exhibited by the synchronized state leads to the natural question of whether or not entanglement can be present in the steady-state even in this dissipative environment. Most previous studies that attempted to address this question have been limited to small systems [84, 141, 159, 160] and focused on the entanglement between a pair of synchronized oscillators. Here, to determine the non-separability of the many-body steady-state, we compute the average of the quantum Fisher information (QFI) and use it as an entanglement witness [237, 107]. Any N particle state with $(N^2 + 2N)/3 \geq \bar{F}_Q(\hat{\rho}) > 2N/3$ is entangled (non-separable) and a quantum resource for phase estimation (see Appendix C.3 for details).

Due to dissipation, the density matrix of the system is reduced to a mixed state, as obtained from Eq. (5.1), which describes the dynamics of the system after a statistical average over many experimental trials. However, the evolution of the system for an individual experimental realization can be quite different. We consider a **Gedanken** experiment in which one monitors the system evolution and keeps a measurement record of the emitted photons. The evolution of the system is then conditioned on the measurement record [40, 198]. This type of conditional evolution has been widely studied in quantum optics and utilized together with quantum feedback control in examples such as the optimal generation of spin squeezed states (See Refs. [251, 98]). It should be emphasized that the conditional evolution based on the measurement record gives a quantum trajectory that should not be regarded simply as a numerical tool to allow the efficient assembly of ensemble averages. Each quantum trajectory is a potentially realizable physical outcome (even if hard to perform in practice) as allowed by the quantum dynamics of the open quantum system under consideration.

We calculate $\bar{F}_Q(\hat{\rho}_c)$ (with the c in $\hat{\rho}_c$ meaning conditional) for each conditional trajectory and in Fig. 5.2(d) we show its average over a sufficiently large set of trajectories at steady state (see Appendix C.3). For this conditional evolution we observe entanglement in a parameter regime that

correlates with $Z_Q > 0$ [see Fig. 5.2(c) and (d)]. On the other hand, if we discard the information present in the measurement record, by using the ensemble averaged ρ obtained from directly solving Eq. (5.1), and then computing $F_Q(\hat{\rho})$, the QFI falls below the entanglement witness threshold [see Fig. 5.2(d)].

To differentiate quantum effects from classical ones, we further calculate the quantum discord \mathcal{D} [see Appendix C], which can be considered as a measure of quantum correlation more general than entanglement and more robust in a dissipative environment [186, 54]. Separable states with nonzero \mathcal{D} are intrinsically nonclassical, since local measurements performed on a subsystem inevitably disturb the whole system [186, 171]. We measure classical correlations of the steady state by the difference between the mutual information \mathcal{I} [see Appendix C] and \mathcal{D} . We find the mixed steady-state contains nonzero quantum correlations in the synchronized regime Fig. 5.3(a). Moreover we observed that although both \mathcal{D} and Z_Q exhibit a similar dependence with pumping rate W , they do not exactly peak at the same value [3].

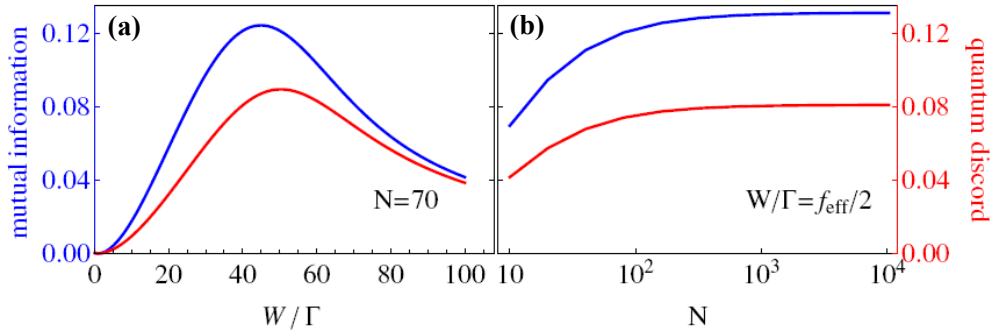


Figure 5.3: Quantum correlations and total correlations. The total and quantum correlations in the steady state are quantified by the mutual information $0 \leq \mathcal{I} \leq 2$ and quantum discord $0 \leq \mathcal{D} \leq 2$. (a) In the synchronized phase, there are nonzero quantum correlations and classical correlations ($\mathcal{I} - \mathcal{D}$), and both show a dependence on W that qualitatively agree with Z_Q . (b) Even in the thermodynamic limit, quantum correlations remain a significant fraction of the total correlations. For both panels, $\delta_a = g(\mathbf{r}_{ab}) = 0$ and $f(\mathbf{r}_{ab}) = f_{\text{eff}}/N$.

Although the existence of a nonzero \mathcal{D} has been reported to exist in several quantum synchronization studies [159, 171], we want to emphasize that those have been always limited to small systems. To our knowledge our calculations are the first to consider \mathcal{D} in macroscopic samples. In

Fig. 5.3(b) we show the dependence of \mathcal{D} with system size. Our calculation shows that quantum correlations remain a significant fraction of \mathcal{I} even in the thermodynamic limit.

5.5 Synchronization with finite-range interactions

Up to this point we have only considered all-to-all interactions; now we consider the effect of finite range interactions on synchronization. In the dipole array both $f(\mathbf{r}_{ab})$ and $g(\mathbf{r}_{ab})$ are nontrivial functions of \mathbf{r}_{ab} and contain terms decaying as a power-law with distance, $\propto 1/|\mathbf{r}_{ab}|^\alpha$ with $\alpha = 1, 2, 3$. Instead of dealing with all these terms together, to gain insight on how spatial inhomogeneities affect quantum synchronization, we first study a simpler case assuming a power-law cooperative decay $f(\mathbf{r}_{ab}) \propto |\mathbf{r}_{ab}|^{-\alpha}$, with the exponent α as a variable parameter and set both $g(\mathbf{r}_{ab}) = 0$ and $\delta_a = 0$.

In the classical regime [53, 238, 50, 256], analytical calculations and numerical simulations considering arrays of oscillators interacting via power law interactions on a one-dimensional lattice had identified $\alpha_c = 3/2$ as the critical value of the power law exponent below which long-range phase order is possible [50]. For $\alpha < \alpha_c$, a transition to a state in which a finite fraction of the oscillators is entrained takes place for a sufficiently strong but finite coupling strength in the large system limit. Generalizations of these results to oscillators in D dimensions [50] have also identified three different regimes for synchronization: perfect phase ordering for $\alpha \leq D$, entrainment with long-range phase order for $\alpha < 3D/2$ and a crossover to exponential decay of correlations at $\alpha = (3D + 1)/2$. Reference [256] has also suggested that in the regime $\alpha > D$ global synchronization is absent but local synchronization persists for arbitrary weak coupling with a slowly decaying order parameter.

To quantify the effect of finite-range interactions on synchronization in the quantum regime we compute spin-spin correlations within linear clusters that contain d dipoles, $(Z_Q^d)^2 \equiv \overline{\langle \hat{\sigma}_a^+ \hat{\sigma}_b^- \rangle}_d$, using a cumulant expansion method as described in Appendix B. Here the bar followed by a subscript d indicates an average over the pairs of different dipoles a and b contained in a linear cluster of size d . The linear clusters start at the central spin as shown in Fig. 5.4. We have confirmed that the cumulant expansion method reproduces well the correlation functions by performing direct

comparisons with the exact solution (see Appendix B). Fig. 5.4(a) shows the behavior of Z_Q^d as a function of cluster size d and power-law decay exponent α in arrays of dimension $D = 1$ and 2. Clear global synchronization with an order parameter Z_Q^d independent of d is observed for $\alpha \lesssim D$. For $0 < \alpha \lesssim D/2$, the local order parameter Z_Q^d is almost independent of α and d and the system behaves almost like the all-to-all system. For $D/2 \lesssim \alpha \lesssim D$ synchronization remains global and almost independent of d , but the order parameter slowly decreases with α . For $\alpha \gtrsim D$, synchronization becomes local and correlations quickly decrease with cluster size. The magenta contour provides an indicative scale of the boundary between global and local synchronization. The white contour lines also provide information about the decrease of the order parameter with increasing α and d . We observe that, as in the classical case, $\alpha \sim D$ roughly marks the transition between global and local synchronization, although a more quantitative comparison would require far larger systems.

An alternative way to characterize domain formation and the fact that it can persist even when there is a variation in the local detunings, $\delta_a \neq 0$, is to examine pairwise two-time correlation functions, $Z_{a,b}(\tau) \equiv \lim_{t \rightarrow \infty} \langle (\hat{\sigma}_a^+(t + \tau) + \hat{\sigma}_b^+(t + \tau))(\hat{\sigma}_a^-(t) + \hat{\sigma}_b^-(t)) \rangle$, which can be related to the emission spectrum of the pair of atoms [40]. The oscillations in $Z_{a,b}(\tau)$ encode information about the relative precession rate between different dipoles. By parameterizing $Z_{a,b}(\tau)$ as $Z_{a,b}(\tau) = A \cos(\nu_{ab}\tau) \exp(-\gamma\tau)$ we can extract the relative precession frequency ν_{ab} between dipoles a and b , where entrainment of dipoles a and b corresponds to $\nu_{ab} = 0$. To explore the entrainment of dipole pairs in our system, we assign random detunings distributed uniformly in $[-\Gamma/2, \Gamma/2]$ to a linear chain of $N = 200$ dipoles and calculate ν_{ab} for $b = 1, 2, \dots, 100$ with $a = 101$ corresponding to the central dipole in the chain. Synchronization regimes similar to those shown in Fig. 5.4(a) are observed for this $D = 1$ system, which we illustrate in Fig. 5.4(b) by plotting a histogram (top panel) and the distribution of frequencies ν (bottom panel) for three values of α . For global coupling, $\alpha = 0$ (dark blue symbols), all the dipoles become entrained with each other ($\nu = 0$), indicating complete synchronization; for $\alpha = 0.65$ (red symbols) dipoles split into entrained ($\nu = 0$) and drifting ($\nu \neq 0$) groups. While not all dipoles are entrained, the entrained dipoles are distributed

along the whole array, and thus synchronization is still global; and for $\alpha = 2$ (light blue symbols) the majority of dipoles are not entrained. These observations of relative precession frequencies between pairs of oscillators are consistent with the regimes obtained from the order parameter plotted in Fig. 5.4(a).

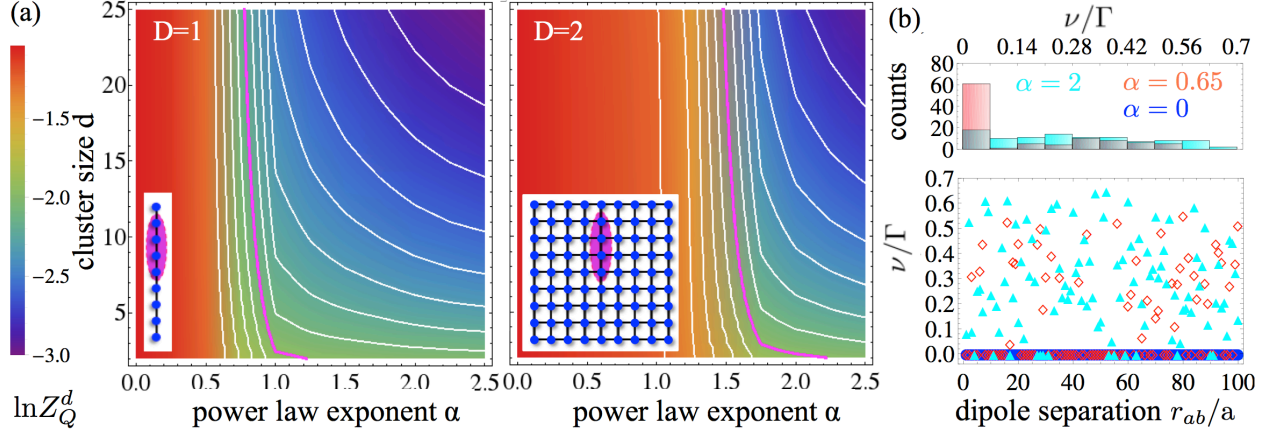


Figure 5.4: (a) Spin-spin correlations, Z_Q^d , in linear clusters containing d dipoles at optimal repumping W for power-law couplings $f(\mathbf{r}_{ab}) = \frac{\Gamma}{4} \left(\frac{a}{r_{ab}}\right)^\alpha$ with lattice spacing a . We set $\delta_a = g(\mathbf{r}_{ab}) = 0$ and consider $N = 900$ dipoles arranged in both linear ($D = 1$) and square lattice ($D = 2$) geometries. For $\alpha \lesssim D$ global synchronization is observed and the order parameter is independent on cluster size d . For $D \lesssim \alpha$ the order parameter starts to clearly decay with increasing d . The magenta line ($Z_Q^d = 0.14$) provides an indicative scale of the boundary between global and local synchronization. The white contour lines provide an indication of the decrease of the synchronized domains with increasing α . (b) Pair wise two-time correlation functions in the steady-state are parametrized by $Z_{a,b}(\tau) = A \cos(\nu\tau) \exp(-\gamma\tau)$ where a is chosen as the central dipole of a linear chain of $N = 200$ dipoles. The dipoles are assigned random detunings δ_a distributed uniformly in $[-\Gamma/2, \Gamma/2]$. The dark blue, red, and light blue symbols correspond to $\alpha = 0, 0.65$ and 2 respectively. The histogram of frequencies ν exhibits similar synchronization regimes than those seen in (a).

5.6 Synchronization of dipoles with elastic interactions

We now treat the full problem of radiating quantum dipoles incorporating elastic interactions $g(\mathbf{r}_{ab})$ and the intricate competition of spatially-dependent and anisotropic couplings [both $g(\mathbf{r}_{ab})$ and $f(\mathbf{r}_{ab})$ have terms with power law dependence $\alpha = 1, 2, 3$ on distance] (Fig. 2.1). We solve the full master equation without any approximation [40] for systems of up to twenty dipoles in a chain using the actual spatial dependence of both $f(\mathbf{r}_{ab})$ and $g(\mathbf{r}_{ab})$, and set $\delta_a = 0$. We observe a robust

synchronized state that exists in a wide parameter space. As long as $f_{\text{eff}} \equiv N \overline{f(\mathbf{r}_{ab})}$ is large enough, we find that synchronization takes place and is only weakly affected by substantial differences in $g(\mathbf{r}_{ab})$, e.g., variations in the dipole array that modify $g(\mathbf{r}_{ab})$ by two orders of magnitude only decrease the order parameter by a factor of two (Fig. 5.5) in the steady state. This is in striking

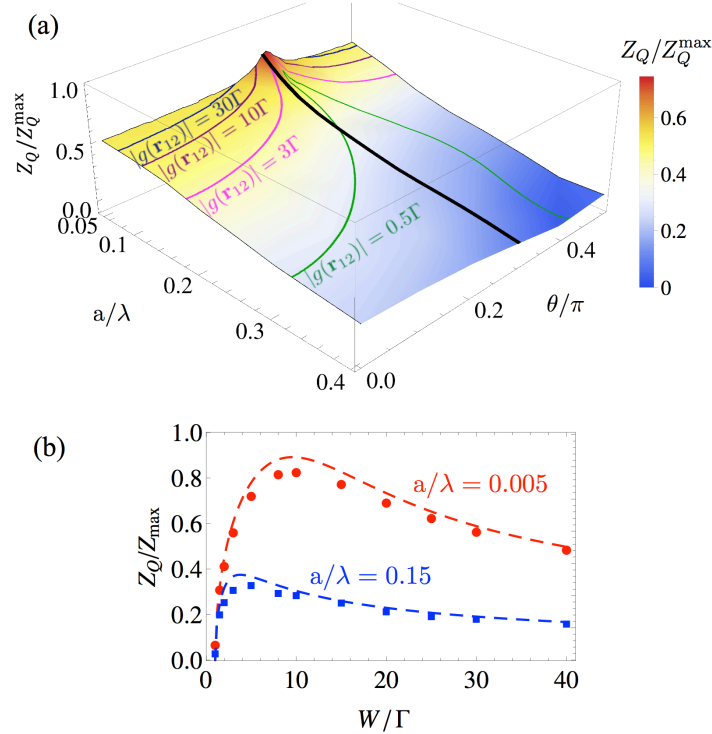


Figure 5.5: (a) Synchronization in dipole arrays is demonstrated for $N = 12$ dipoles on a line when subjected to incoherent pumping (optimal rate). In this geometry, regardless of the strong angular variation of g with the lattice spacing a (see contours) the order parameter, Z_Q , (normalized by $Z_Q^{\text{max}} = 1/\sqrt{8}$) exhibits a weak dependence on θ and a and reaches a maximum at $\theta = \theta_m$. (b) The order parameter is computed for $N = 16$ dipoles on a line with $\theta = \theta_m$ and $f_{\text{eff}} = \sum_{a,b \neq a} f(\mathbf{r}_{ab}) / (N - 1)$ (symbols), and for a system with constant $f(\mathbf{r}_{ab}) = f_{\text{eff}}/N$ and $g(\mathbf{r}_{ab}) = 0$ (dashed line)s. Similar dependence on W is found for these two different systems. Here the order parameter for dipoles is always smaller in the presence of elastic interactions.

contrast to the situation in a system without dissipation, where the elastic interaction is known to generate entanglement between spins and to cause a decay of the order parameter during time evolution [157].

For the orientation $\theta_m = \arccos(1/\sqrt{3})$, the order parameter reaches a significant fraction of Z_Q^{max} , indicating the emergence of macroscopic spontaneous synchronization of the radiating

quantum dipole array (Fig. 5.5). To further emphasize the relevant role played by the inelastic term, in Fig. 5.5(b) we compare a solution of the master equation [Eq. (5.1)] for two cases: a system of coupled dipoles arranged in a 1D chain and oriented at the magic angle (symbols) and an array of identically coupled dipoles with the same f_{eff} but experiencing only inelastic interactions [$g(\mathbf{r}_{ab}) = 0$, dashed lines]. The calculated order parameters agree well for the two different cases. The similar behavior demonstrates that in spite of the complex geometry of the dipolar interactions, the capability of the dipole system to synchronize can be characterized to great extent by the quantity f_{eff} .

5.7 Experimental implementation

Our calculations above demonstrate the potential for synchronization in a dense array of dipoles. The flexible and precise control exhibited by ultracold atomic systems make them ideal platforms to experimentally investigate the synchronization phenomenon predicted here. Atomic systems operate with a large number of quantum oscillators and also allow for the tunability of the interaction parameters over a broad range.

One possible set-up to observe synchronization consists of arrays of ultracold ^{87}Sr atoms prepared in two electronic internal states that form the two-level system. The $|\downarrow\rangle$ could then correspond to the long-lived $5s5p\ ^3P_0$ state, with an intercombination line narrower than $10^{-3}\ \text{s}^{-1}$. This is the state used to operate the most precise atomic clocks [27]. The $|\uparrow\rangle$ could correspond to the $5s4d\ ^3D_1$ state with a natural linewidth $\Gamma = 290 \times 10^3\ \text{s}^{-1}$. Both states can be trapped in an optical lattice at the magic wavelength $a = 0.2\ \mu\text{m}$ [187], that generates the same trapping potential for both states minimizing Stark shifts and inhomogeneities in the coupling constants. The dipole-dipole interactions are mediated by photons at the wavelength $\lambda = 2.6\ \mu\text{m}$ and thus, as shown in Fig. 5.5, the ratio $a/\lambda < 0.08$ falls in the parameter regime where dipoles can be synchronized.

By changing the angle between the laser beams used to form the lattice potential, the lattice spacing can be varied allowing tunability of the interaction strength between dipoles. The incoher-

ent pumping can be realized by coherently transferring the $5s5p\ ^3P_0$ population to one or several appropriate intermediate states that decay rapidly to the $5s4d\ ^3D_1$ state [167]. An example would be the $4d5p\ ^3P_1$ state [217].

The polarization of the dipoles can be oriented in an arbitrary direction by an electromagnetic field. Although all the dipoles cannot be oriented at the magic angle in a 3D geometry, one may still suppress the elastic interactions by dynamical decoupling techniques adopted from NMR [71]. Those have been already demonstrated in ultracold polar molecule systems [278]. Another possibility is to use a spatial configuration of external fields that induces an ‘averaging out’ of the dominant elastic interactions [184]. Moreover, by slightly departing from the magic-wavelength condition, the dipoles can be subjected to onsite inhomogeneities that generate different detunings δ_a .

The phase synchronization can be probed by measuring Z_Q , which experimentally can be directly obtained from the fluorescence intensity. As suggested in Sec. 5.5, phase locking can also be extracted from two-point correlations which can be determined by analyzing the fluorescence spectrum [167].

An intriguing but also more speculative and less controllable realization of our quantum dipole model is the case of fluorescent organic molecules. A possible two-level configuration in those systems consists of a vibrational level of the ground electronic potential chosen as $|\downarrow\rangle$ and the lowest vibronic level of the first excited potential chosen as $|\uparrow\rangle$. Incoherent pumping can be realized by driving an optical transition to a higher excited vibronic level $|\phi\rangle$ in the first excited potential, which decays on picosecond timescales to the state $|\uparrow\rangle$ via non-radiative transitions [127]. Typical values of the fluorescence wavelength λ_f and lifetime τ_f for organic chromophores under a variety of environmental conditions put these systems in a regime of near optimal synchronization. For instance, pseudoisocyanine chloride (PIC) and merocyanine derivatives commonly used in organic light-emitting diodes (LED) [68, 17, 120, 6] typically form low-dimensional molecular aggregates in liquid solution with a $\approx 0.5 - 2.0\ \text{\AA}$, and ratios a/λ_f on the order of 10^{-3} . The typical fluorescence decay rate for these organic chromophores is $\Gamma \sim 0.1 - 1\ \text{GHz}$ [127]. In order to achieve $W/\Gamma = 1$ and enter the synchronized phase, the required pumping laser intensity is $I_W \sim 1 - 10\ \text{kW/cm}^2$,

which is lower than the theoretical lasing threshold intensities $I_{\text{th}} \sim 0.1 - 1 \text{ MW/cm}^2$ of dye lasers [127]. Therefore, it should be feasible to achieve steady state synchronization of organic dipoles via incoherent optical driving.

5.8 Conclusion

We have demonstrated that a system of radiating quantum dipoles can be synchronized in the presence of repumping. Our analytic mean-field approach provides a direct analogy between synchronization of quantum dipoles and synchronization of classical phase oscillators. Using exact solutions of the master equation and a cumulant expansion approach, we determined the necessary conditions for synchronization, and the entanglement properties in the steady state of macroscopic ensembles under different measurement protocols. We also analyzed the effect of finite-range interactions in large arrays. To our knowledge those have been previously explored only in the classical regime. These calculations, although restricted to $g(\mathbf{r}_{ab}) = 0$, emphasize how the interplay between incoherent repumping and cooperative dipole decay can give rise to robust quantum synchronization. For treating the general case of dense packed dipoles, we numerically solved the master equation exactly for up to twenty dipoles, and studied the effect of elastic interactions. The one dimensional geometry chosen allows us to tune the dipolar interactions across a wide range of parameters by simply adjusting the spacing and polarization angle, and investigate the competing roles of the elastic and inelastic interactions. One dimensional systems are amenable for theoretical investigation since they help us to minimize finite size effects. They can be implemented in current experiments using ultra-cold gases and are relevant for the suggested implementation using organic molecules. There are several organic species such as PIC molecules [17] that are known to form quasi-one dimensional arrays both as single crystals and in liquid solution. These systems are typically modelled as 1D arrays of two-level dipoles with energetic disorder to match spectroscopic data [75]. For this configuration, we found synchronization in the presence of a large variation of elastic interactions. We expect that in more general geometries, similar degree of synchronization could be achieved provided the collective dissipative coupling f_{eff} dominates over the elastic pair-

wise couplings, $g(\mathbf{r}_{ab})$. These conditions might be easier to be satisfied in higher dimensional dense packed dipolar arrays given the anisotropic character of the elastic terms which fluctuate both in sign and magnitude across the array. In higher dimensions, geometric effect becomes more important. Nevertheless, whether or not spontaneous synchronization in dipole arrays can be observed under more generic high dimensional geometries remains an open question.

Our results show that the intrinsic macroscopic coherence of the superradiant steady state is inherently resilient to single particle decoherence, spatial inhomogeneities, and noisy environmental effects. This observation could have relevant application to the development of low-threshold organic lasers, highly efficient solar cells, materials with enhanced chemical reactivity, as well as ultra-precise quantum devices, where these effects are anticipated to play an important role. Moreover, since quantum synchronization is imprinted in the spectral purity of the emitted radiation [166], the generated light may potentially serve as a direct diagnostic tool of quantum coherences in generic systems beyond cold gases such as organic molecules.

Chapter 6

Light scattering from dense cold atomic media

6.1 Introduction

Light-matter interactions are fundamental for the control and manipulation of quantum systems. Thoroughly understanding them can lead to significant advancements in quantum technologies, quantum simulations, quantum information processing and precision measurements [124, 51, 62, 69, 24, 118, 25]. Over the past decades, cold atom experiments have provided a clean and tunable platform for studying light-matter interactions in microscopic systems where rich quantum effects emerge, such as superradiance and subradiance, electromagnetically induced transparency, and non-classical states of light [30, 95, 214, 191, 34]. However, in spite of intensive theoretical and experimental efforts over the years, long-standing open questions still remain regarding the propagation of light through a coherent medium, especially when it consists of large and dense ensembles of scatterers [110, 142, 213, 113, 223, 242, 22, 122, 232, 112, 231, 185, 115, 111, 114, 7, 31]. In fact, by studying small systems where analytical solutions are obtainable, it has been realized that atom-atom interactions can significantly modify the spectral characteristics of the emitted light. These effects yet need to be understood in large systems [187, 158, 281, 284, 19] where finite size effects and boundary conditions become irrelevant. The situation is even more complicated when the coupling with atomic motion is non-negligible [18, 144]. It is timely to develop theories capable of addressing these questions, given the rapid developments on cold atom experiments and nanophotonic systems. The experiments are entering strongly coupled regimes, where atom-atom and atom-photon interactions need to be treated simultaneously and sometimes fully microscopi-

cally [187, 116, 88].

A widely adopted approach to describe light scattering consists of integrating out the atomic degrees of freedom and treating the atoms just as random scatterers with prescribed polarizability [63, 258, 134, 36]. While this approach can successfully capture some classical properties of the scattered light, it does not fully treat the roles of atom-atom interactions and atomic motion [131, 133, 227, 132]. An alternative route consists of tracing over the photonic degrees of freedom. In this case the virtual exchange of photons induces dispersive and dissipative dipole-dipole interactions between atoms, which can be accounted for by a master equation formulation [110, 142]. This approach has been used to study systems of tightly localized atoms where the dynamics only takes place in the atomic internal degrees of freedom. It has been shown to successfully capture quantum effects in light scattering [242, 48, 280, 22, 21, 240]. However, due to the computational complexity, it has been often restricted to weak excitation and small samples [169, 165, 281, 284], and a direct comparison with experiments containing a large number of atoms has been accomplished only recently [33, 212]. In general, most theories have not properly accounted for atomic motional effects and atomic interactions on the same footing and many open questions in light scattering processes remain.

Here, we present a unifying theoretical framework based on a coherent dipole (CD) model (see Fig. 6.1(a)) to study the light scattering from cold atoms with possible residual motion. In the low intensity and slow motion regime, we use the CD to investigate the collective effects in the light scattered by a large cloud and show the interplay of optical depth (OD) and density. These results are compared with the random walk (RW) model (see Fig. 6.1(a)) that only accounts for incoherent scattering and thus ignores coherent dipolar interaction effects. To address the role of atomic motion, we perform different levels of generalization of the CD model. With these modified models, we show that atomic motion not only reduces phase coherence and collective effects, but also impacts the line shape and line center of the spectral emission lines via photon recoils. Motivated by a recent experiment at JILA (see Fig. 6.1(b)) [33], we focus our discussions on a $J = 0 \rightarrow J' = 1$ transition, but the methods presented here can be extended to more complicated level structures

without much difficulty.

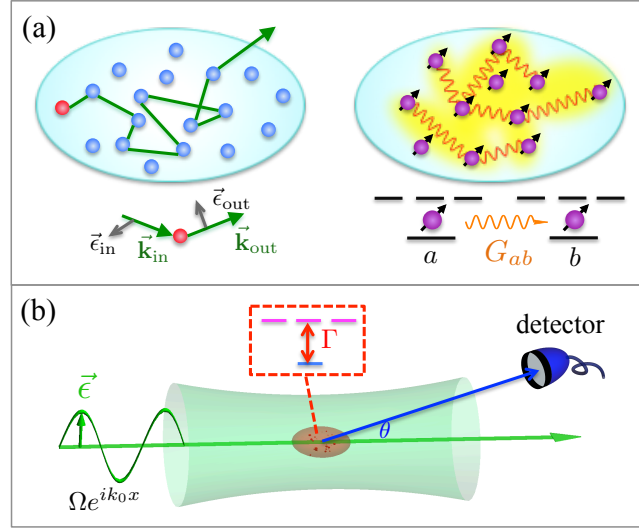


Figure 6.1: Scheme. (a) Microscopic models: random-walk model (left) and coherent dipole model (right). In the random-walk model, a photon is randomly scattered by the atoms. Scattering events are characterized by the incident and outgoing wavevector of the photons and their corresponding polarization. In the coherent dipole model, atoms are coupled by dipole-dipole interactions (G_{ab}) and all atoms contribute to the fluorescence. (b) Experimental setup for measuring the fluorescence from a cloud of atoms. An incident laser drives an atomic transition with a spontaneous emission rate Γ . Atoms absorb and emit light. The detectors collect scattered photons at an angle θ measured from the incident beam direction.

This chapter is organized as follows. In Sec. 6.2, we provide the mathematical description of the CD model, which treats atoms as coupled, spatially fixed dipoles sharing a single excitation. Its predictions on the collective properties of the emitted light such as the light polarization and density dependence of the line shape and peak intensity are discussed. In Sec. 6.3, we introduce the RW model and compare its predictions on the linewidth and peak intensity of the scattered light to the ones obtained from the CD model. Those comparisons allow us to explore the role of phase coherence in the atom-light interaction. In Sec. 6.4, we present extended models to study motional effects on atomic emission. We first include motion in the CD model by assuming that its leading contributions comes from Doppler shifts. Those are accounted for in the frozen model approximation when we introduce local random detunings for atoms sampled from a Maxwell-Boltzmann distribution. Then we go beyond the frozen model approximation and explicitly include

atomic motion by means of a semi-classical approach. This treatment also allow us to go beyond the low excitation regime. In Sec. 6.5, we apply the CD model to a recent experiment measuring the fluorescence from an ensemble of ^{88}Sr atoms. We finish in Sec. 6.6 with conclusions and outlook.

6.2 Coherent dipole model

6.2.1 Equations of motion for coherent dipoles

As derived in chapter 2, for an ensemble of N atoms with internal dipole transition $J = 0 \rightarrow J' = 1$, the master equation is

$$\begin{aligned}
i\frac{d\hat{\rho}}{dt} = & -\sum_{i,\alpha} \Delta^\alpha [\hat{b}_i^{\alpha\dagger} \hat{b}_i^\alpha, \hat{\rho}] + \sum_{i,\alpha} \Omega^\alpha [(e^{i\mathbf{k}_0 \cdot \mathbf{r}_i} \hat{b}_i^{\alpha\dagger} + \text{H.c.}), \hat{\rho}] \\
& + \sum_{i \neq j, \alpha, \alpha'} g_{i,j}^{\alpha\alpha'} [\hat{b}_i^{\alpha\dagger} \hat{b}_j^{\alpha'}, \hat{\rho}] \\
& + \sum_{i,j,\alpha,\alpha'} f_{i,j}^{\alpha\alpha'} (2\hat{b}_j^{\alpha'} \hat{\rho} \hat{b}_i^{\alpha\dagger} - \{\hat{b}_i^{\alpha\dagger} \hat{b}_j^{\alpha'}, \hat{\rho}\}),
\end{aligned} \tag{6.1}$$

where we have added the term describing the effect of an external driving laser with polarization α , wavevector \mathbf{k}_0 , and Rabi frequency Ω^α . The Hamiltonian is written in the rotating frame of the laser, with Δ^α denoting the detuning between the laser and the transition $|0\rangle \rightarrow |\alpha\rangle$. The dipole-dipole interactions include both the far-field ($1/r$) and near-field ($1/r^2, 1/r^3$) contributions. The terms described by $f_{i,j}^{\alpha\alpha'}$ encapsulate collective dissipative process responsible for the superradiant emission in a dense sample. The terms described by $g_{i,j}^{\alpha\alpha'}$ account for elastic interactions between atoms which can give rise to coherent dynamical evolution. These elastic interactions compete with and can even destroy the superradiant emission [79, 284].

When the atoms' thermal velocity v satisfies $k_0 v \ll \Gamma$, atoms can be assumed to be frozen during the radiation process. Moreover, in the weak driving regime, $\Omega \ll \Gamma$, to an excellent approximation, the master equation dynamics can be captured by the $3N$ linear equations describing the atomic coherences $b_j^\alpha = \langle \hat{b}_j^\alpha \rangle$ of an excitation propagating through the ground state atomic

medium. The corresponding steady state solution can be found from:

$$b_j^\alpha = \frac{\Omega^\alpha \delta_{\alpha,\gamma} e^{i\mathbf{k}_0 \cdot \mathbf{r}_j / 2}}{\Delta^\alpha + i\Gamma/2} + \sum_{n \neq j, \alpha'} \frac{G_{jn}^{\alpha\alpha'}}{\Delta^\alpha + i\Gamma/2} b_n^{\alpha'}, \quad (6.2)$$

where we have specified the polarization of the driving laser to be along γ . For obtaining Eq. (6.2), we have assumed there is only one excitation in the system, and ignored multi-atom coherences (see Appendix D.1). This assumption is justified in the weak driving field regime [21, 234]. The fluorescence intensity measured at the position \mathbf{r}_s in the far-field can be obtained by the summation [110]

$$I(\mathbf{r}_s) \propto \sum_{jn} e^{-i\mathbf{k}_s \cdot \mathbf{r}_{jn}} \sum_{\alpha, \alpha'} (\delta_{\alpha, \alpha'} - \hat{\mathbf{r}}_s^\alpha \hat{\mathbf{r}}_s^{\alpha'}) b_j^{\alpha'} b_n^{\alpha*}, \quad (6.3)$$

where $b_n^{\alpha*}$ is the complex conjugate of b_n^α , and $\mathbf{r}_{jn} = \mathbf{r}_j - \mathbf{r}_n$.

6.2.2 Collective effects in fluorescence

For dilute samples the dipolar interactions are weak, $\mathcal{G} \equiv \sum_{i \neq j, \alpha, \alpha'} |G_{ij}^{\alpha\alpha'}| / (N\Gamma) \ll 1$, and Eq. (6.2) can be solved perturbatively using \mathcal{G} as the expansion parameter, $b_j^\alpha = b_j^{\alpha,0} + b_j^{\alpha,1} + b_j^{\alpha,2} + \dots$, ($b_j^{\alpha,n} \propto \mathcal{G}^n$) which results in

$$b_j^{\alpha,n} = \sum_{\substack{l_1 \neq j \\ l_2 \neq l_1 \\ \dots l_n \neq l_{n-1} \\ \alpha_1, \alpha_2 \dots \alpha_n}} \frac{G_{jl_1}^{\alpha\alpha_1} G_{l_1 l_2}^{\alpha_1 \alpha_2} \dots G_{l_{n-1} l_n}^{\alpha_{n-1} \alpha_n} \Omega^\gamma \delta_{\alpha_n, \gamma} e^{i\mathbf{k}_0 \cdot \mathbf{r}_{l_n}}}{i^n (\Delta^\alpha + i\frac{\Gamma}{2})(\Delta^{\alpha_1} + i\frac{\Gamma}{2}) \dots (\Delta^{\alpha_n} + i\frac{\Gamma}{2})}. \quad (6.4)$$

In the expansion, terms of order n account for n^{th} order scattering events. For simplicity, in the following we assume the atomic sample has a spherical shape, with density distribution $n(r) = n_0 e^{-r^2/2R^2}$, unless otherwise specified. However, the conclusions can be generalized to other geometries. Here, $n_0 = \frac{N}{2\pi\sqrt{2\pi}R^3}$ is the peak density.

To the zeroth order, the atomic response is driven by the external field only and is not modified by the scattered light:

$$b_j^{\alpha,0} = \frac{\Omega^\alpha \delta_{\alpha,\gamma} e^{i\mathbf{k}_0 \cdot \mathbf{r}_j}}{\Delta^\alpha + i\Gamma/2}. \quad (6.5)$$

Substituting it into Eq. (6.3), the intensity of scattered light is

$$I \propto N + N^2 e^{-|\mathbf{k}_s - \mathbf{k}_0|^2 R^2}. \quad (6.6)$$

There are two contributions to the intensity, the first term $\propto N$ represents the incoherent contribution, and the second term $\propto N^2$ is the collective emission resulting from coherent scattering processes [223, 33]. The phase coherence is restricted to a narrow angular region around the incident laser direction, with $\delta\theta \sim 1/k_0 R$. The enhanced emission arises from the constructive interference of the radiation from N dipoles [21]. Along other directions, the random distribution of atom positions randomizes the phases of the emitted light, smearing out the phase coherence after averaging over the whole sample [33].

Including first order corrections, the intensity of the scattered light is given by

$$I(r_s) \propto \frac{N\Omega^2}{(\Delta - \Gamma\Re[\overline{G}])^2 + (\Gamma + 2\Gamma\Im[\overline{G}])^2/4}, \quad (6.7)$$

for transverse directions, where we have denoted $\Omega = \Omega^\gamma$ and $\Delta = \Delta^\gamma$, and

$$\overline{G} = \sum_{i \neq j} G_{ij}^{\gamma\gamma} e^{-i\mathbf{k}_0 \cdot \mathbf{r}_{ij}} / (N\Gamma). \quad (6.8)$$

For the forward direction, the intensity has the same form, except that the factor N is replaced by N^2 , due to the phase coherence. Therefore, the line shape of the scattered light is Lorentzian, with its line center frequency shifted by the elastic interactions [211, 211], and the linewidth broadened by the radiative interactions. If we temporarily neglect the effect of polarization, when the atom-atom separation is large, the dipole-dipole interaction is dominated by far-field terms, *i.e.*, $G_{ij}^{\gamma\gamma} \sim -\frac{3\Gamma}{4}(1 - \hat{\mathbf{r}}_{ij}^\gamma \cdot \hat{\mathbf{r}}_{ij}^\gamma) \frac{e^{ik_0 r_{ij}}}{k_0 r_{ij}}$. In this limit analytical expressions for the linewidth broadening $\overline{\Gamma}$, and density shift, $\overline{\Delta}$, can be obtained: $\overline{\Gamma} = 2\Gamma\Im[\overline{G}] = 3N\Gamma/(8k_0^2 R^2) = \frac{\tau}{4}\Gamma$, with $\tau = \frac{3N}{2k_0^2 R^2}$ being the OD of the sample, and $\overline{\Delta} = \Gamma\Re[\overline{G}] = -\Gamma n_0 k_0^{-3}/4\sqrt{2\pi}$. Therefore, while the collectively broadened linewidth depends on the OD of the atomic cloud, the frequency shift depends on the density.

In a dense medium dipolar interactions are strong, $\mathcal{G} \gtrsim 1$, higher order scattering events become important, and the interplay between the radiative interactions and elastic interactions becomes non-negligible. As a consequence the above perturbative analysis is no longer applicable.

In Fig. 6.2 and Fig. 6.3, we show the numerical solution of Eq. (6.2), which takes into account all the scattering orders. As shown in Fig. 6.2(a), most of the scattered light is distributed

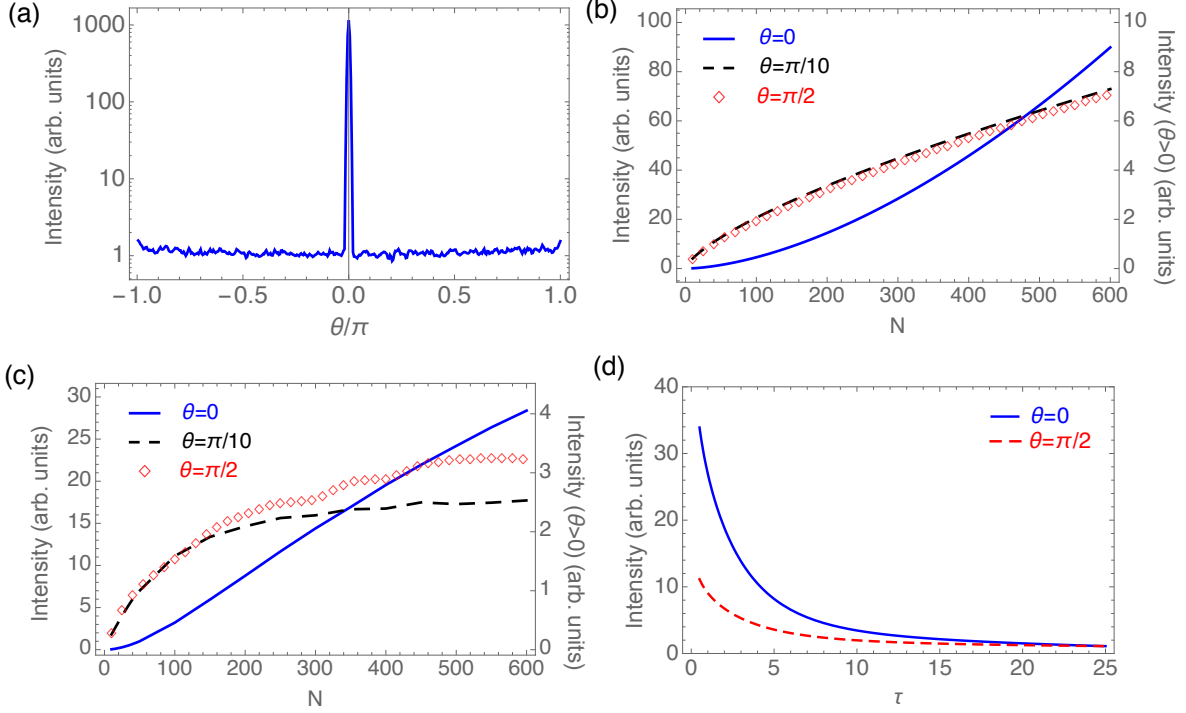


Figure 6.2: CD model: on-resonance intensity. (a) Angular distribution: due to the constructive interference along the forward direction ($\theta = 0$), the intensity is drastically enhanced within a small angular region. (b)-(c) The intensities for three different directions ($\theta = 0, \pi/10, \pi/2$) are shown as a function of atom number, each normalized to the value at $N = 50$. All are calculated for a spherical cloud of fixed size. The right vertical axes label the intensity for $\theta = \pi/2, \pi/10$. In (b) the OD and the density are relatively low (when $N = 500$, $\tau=2, n_0 k_0^{-3}=0.0015$). The transverse intensity increases $\sim N$, while the forward intensity increases $\sim N^2$, showing a collective enhancement for small window of θ around zero. Outside this narrow angular window the enhancement disappears and the intensity becomes almost θ independent as indicated by the identical behavior observed for two different angles, $\theta = \pi/10$ and $\pi/2$. In (c) the OD and density are relatively large (when $N = 500$, $\tau=10$, $n_0 k_0^{-3}=0.017$). The rate at which the intensity increases with N slows down in both the forward and transverse direction: with $I \sim N^1$ for $\theta = 0$ and $I \sim N^{0.5}$ for $\theta = \pi/2$, respectively. (d) On-resonance intensity as a function of OD: it is highly suppressed at large OD. Here, the intensity is normalized to the corresponding value at $\tau = 25$ for each direction.

within a narrow peak around the forward direction (laser direction). Outside this narrow region fluorescence is almost uniformly distributed among other directions¹. The forward emission is

¹ Note: Around the $\theta = \pi$ direction there is a small enhancement ~ 2 due to the coherent backward scattering [134].

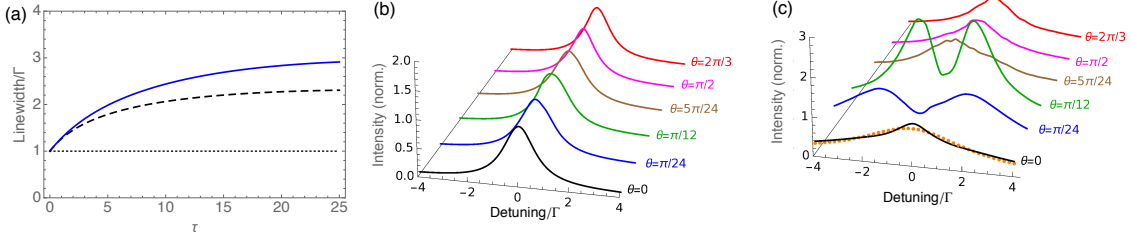


Figure 6.3: CD model: collective broadening. (a) FWHM linewidth as a function of OD. At small OD, the FWHM increases linearly with OD, but as OD increases density effects set in, multiple scattering events become relevant and the linewidth dependence on OD is no longer linear. Two different atom numbers are used for the blue ($N=1000$) and black lines ($N=200$), and the OD is varied by changing the cloud size. For the blue line, $n_0 k_0^{-3} = 0.14$ at $\tau=25$, 0.003 at $\tau=2$. For the black line, the density at the same OD is doubled. With smaller density, the linewidth increases to a larger value in the large OD regime. (b) The line shape at small OD values ($\tau=2$, $n_0 k_0^{-3} = 0.002$) for different angles θ (θ is defined in Fig. 6.1(a)) is mainly Lorentzian. Here the intensity is normalized to the on-resonance intensity for each θ . (c) At large OD ($\tau=20$, $n_0 k_0^{-3} = 0.06$), the fluorescence line shape significantly broadens and stops being Lorentzian. The brown dots for $\theta = 0$ show the Lorentzian fit, which fails to describe the line shape. At intermediate θ , a double-peak structure shows up. For all panels, the cloud shape is spherical.

collectively enhanced. For low OD it increases as $\sim N^2$ (Fig. 6.2 (b)) while the transverse intensity increases as $\sim N$.

Dipolar interactions tend to suppress the rate at which the intensity grows with N (Fig. 6.2(c)). This can be qualitatively understood from Eq. (6.7), which predicts that the intensity is reduced as OD increases. Despite the fact that the perturbative analysis is only valid in the weak interaction limit, this tendency remains and becomes more pronounced in the large OD regime as shown by the numerical solution presented in Fig. 6.2(d). Broadly speaking, multiple scattering events tend to suppress collective behavior [112, 135]. Similar physics is also observed in the behavior of the linewidth. At small OD, the FWHM linewidth increases linearly with OD (Fig. 6.3(a)) and the line shape is well described by a Lorentzian (Fig. 6.3(b)), as expected from Eq. (6.7). However, when OD is large and the density is high, in addition to a significant broadening, the line shape becomes non-Lorentzian (Fig. 6.3(c)) and the FWHM increases slowly with OD (Fig. 6.3(a)). To further illustrate this, in Fig. 6.3(a) we plot the FWHM for the same OD but with smaller density (by using a larger atom number). The figure shows that the linewidth indeed keeps increasing

until saturation at a larger value of OD. Another interesting feature is the double-peak structure observed only at intermediate angles θ , which arises from the interplay between the stimulated photon emission driven by the probe field and the scattered photons emitted via dipolar exchange processes (Fig. 6.3(c)).

The drastic modifications of the perturbative expectations from multiple scattering are also present in the frequency shift of the scattered light. From a mean-field point of view, the linecenter of scattered light is shifted according to the Lorentz-Lorenz shift $\pi n_0 k_0^{-3} \Gamma$ [80]. As shown by the numerical calculation in Fig. 6.4 (blue line), at small density, the frequency shift is indeed linear with $n_0 k_0^{-3}$, but as density increases, the shift is quickly suppressed [112]. For atom density $\sim 5 \times 10^{13} \text{cm}^{-3}$ (reached for example in cold ^{87}Rb atom experiments [12]), the calculated density shift is approximately a factor of two lower than the mean-field prediction.

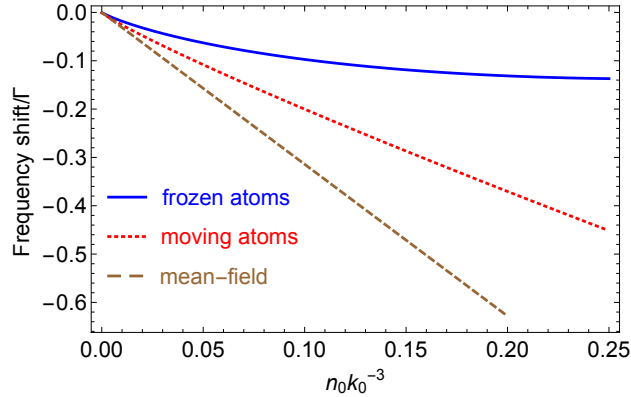


Figure 6.4: CD model: frequency shift. For small density, the shift calculated from the coherent dipole model (blue line) increases linearly with density as predicted by the mean-field theory. However, when density is large, there is a significant deviation from the mean-field result. When motional effects are taken into account (red line, Doppler width = 5Γ , see Sec. 6.4.1), the non linear suppression of the frequency shift with density is less severe.

The interplay between the imaginary and real part of the dipole-dipole interaction has to be carefully accounted for to compare numerical simulations with experimental measurements by doing finite size scaling. For typical computation resources the numerical solution of Eq. (6.2) is limited to $\sim 10^4$ atoms. On the other hand experiments usually operate with ensembles of tens of millions of atoms. To theoretically model these large systems a proper rescaling in the cloud size is

necessary. Equation (6.7) implies that in order to characterize the effect of radiative interactions one should aim to match the experimental OD, which scales as $\sim N^{1/2}$. On the other hand, to properly reproduce the effect of elastic interactions it is better to match the dimensionless number $n_0 k_0^{-3}$, which scales as $N^{1/3}$. Therefore, there exist two different ways of rescaling the cloud size, either by keeping the same OD or the same density. In Fig. 6.5 we show the effect of finite N for a moderate range of atom numbers. Indeed, except from small deviations seen at very low atom

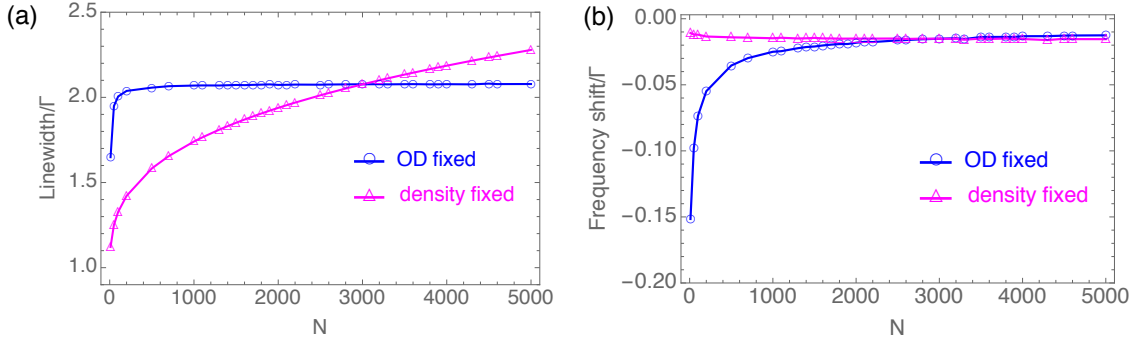


Figure 6.5: CD model: finite size scaling. (a) The linewidth is calculated for different number of atoms at the same OD ($\tau=4$ for $N=3000$) by varying the density (blue line with circles). From $N = 1000$ to 5000 the linewidth is not obviously changed. In contrast, by keeping the same density ($n_0 k_0^{-3} = 0.0037$ for $N=3000$) while varying the OD (magenta line with triangles), the linewidth keeps changing. (b) The frequency shift is calculated for different number of atoms. By keeping constant density (magenta line with triangles), the frequency shift remains almost constant, while for constant OD (blue line with circles), there is a significant variation of the frequency shift with N . Here the cloud aspect ratio is $R_x : R_y : R_z = 2 : 2 : 1$ [33].

number (< 1000), the linewidth broadening can be well captured by keeping the OD constant, while the frequency shift is well described by using a constant density. In contrast, if a constant OD is used to compute the frequency shift, the result would considerably overestimate the shift, e.g., by a factor of 10 when the N in numerical simulation is 1/100 the atom number in experiment. The interplay of multiple scattering and density effects is more prominent for larger N values. To deal with the OD vs density scaling issues in comparing with experiments the most appropriate rescaling procedure that we found is the following: when computing the linewidth or peak intensity, the theory is rescaled accordingly with the experimental OD. However, the actual OD value is not exactly matched to the experimental one but to a slightly modified value, $\tilde{\tau} = \eta\tau$ to account for

density effects [33]. For a moderate window of τ values, for example achieved experimentally by letting the cloud expand for different times, η should be kept fixed. For the frequency shift the theory should be rescaled according to density.

6.2.3 Anisotropic features of scattered light

For independent atoms radiation along the polarization of the driving laser is forbidden. However, dipole-dipole interactions can generate polarization components different to the driven ones if the atoms exhibit internal level structure, e.g., degenerate Zeeman levels in the excited state. This is the case of a $J = 0 \rightarrow J' = 1$ transition, where, as shown in Fig. 6.6, the fluorescence emitted along the laser polarization direction (z -direction, $\theta = \pi/2$) is nonzero. It is, however,

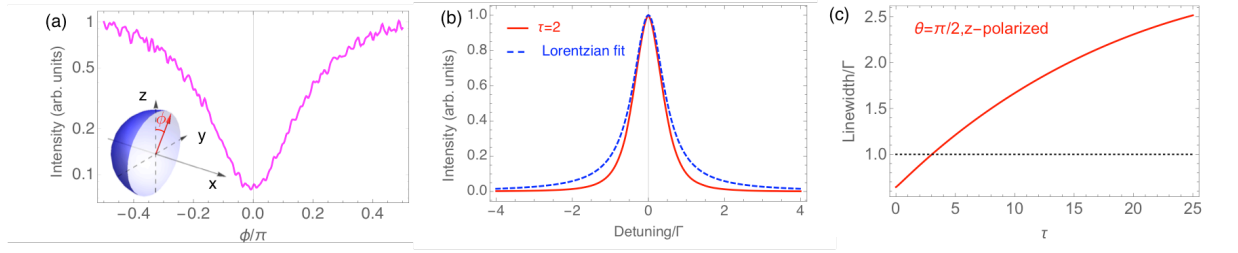


Figure 6.6: CD model: effect of laser polarization. (a) Intensity distribution in the plane perpendicular to the laser propagation direction, *i.e.*, $\theta = \pi/2$ for all ϕ 's (inset). $\phi = 0$ is the z -direction. Here, the incident laser is polarized along z . The intensity detected along the laser polarization is suppressed compared to other directions. (b) and (c) show the line shape and linewidth of light detected at $\theta = \pi/2, \phi = 0$. (b) At small OD, the FWHM linewidth is below the natural linewidth. (c) As OD increases, the linewidth is collectively broadened due to multiple scattering processes (Fig. 6.3(a)). For all panels, degeneracy in excited levels has been assumed.

much weaker than the intensity emitted along other directions. On the contrary, for two-level transitions the polarization of the scattered light is conserved and thus the emission parallel to the laser polarization is completely suppressed. The strong dependence of the scattered light on polarization and atomic internal structure is most relevant along the transverse direction. Along the forward direction those effects are irrelevant, as verified by our numerical simulations. From Eq. (6.4), the lowest order contribution to the intensity detected along the laser polarization direction comes from the first order scattering processes, thus $I \propto \frac{1}{(\Delta^2 + \Gamma^2/4)^2}$, which lead to a “subradiant”

line shape (*i.e.* the full width at half maximum (FWHM), $\bar{\Gamma}_{\text{FWHM}} = \sqrt{\sqrt{2} - 1}\Gamma < \Gamma$, is smaller than the one for independent particles). The analytic result agrees perfectly with the numerical simulation at low OD (Fig. 6.6(b)). As the OD increases and interactions become stronger, higher order scattering contributions lead to a collective broadening (linewidth larger than Γ) even along this “single dipole forbidden” direction, as shown in Fig. (6.6 (c)).

6.3 Random walk model

In this section we use the random walk model to investigate the role of incoherent scattering processes in collective emission. We focus on the low-intensity regime. Classically, light transport in a disordered medium can be described by a sequence of random scattering events experienced by a photon (see Fig. 6.1(a)) [134, 133, 135]. The expected number of scattering events is roughly given by $(\tau_p)^2$, where τ_p is the peak optical depth, which depends on detuning Δ as $3N/[k_0^2 R^2(1+4\Delta^2/\Gamma^2)]$. For simplicity here we also assume a spherical cloud. The transmission of light is given by $e^{-\tau_p}$ [44]². For the $J = 0 \rightarrow J' = 1$ transition (degenerated $J' = 1$ states), the differential scattering cross section that defines a scattering event is given by [134, 135]

$$\frac{d\sigma}{d\Omega}(\mathbf{k}_{\text{in}}, \boldsymbol{\epsilon}_{\text{in}} \rightarrow \mathbf{k}_{\text{out}}, \boldsymbol{\epsilon}_{\text{out}}) = \frac{3\sigma_0}{8\pi} |\boldsymbol{\epsilon}_{\text{in}}^* \cdot \boldsymbol{\epsilon}_{\text{out}}|^2, \quad (6.9)$$

where $\mathbf{k}_{\text{in,out}}$ is the incident/scattered wavevector, $\boldsymbol{\epsilon}_{\text{in,out}}$ is the polarization of the incident/scattered photon [134, 135, 203] and $\sigma_0 = 3\lambda^2/[2\pi(1 + 4\Delta^2/\Gamma^2)]$, with λ the wavelength of the driving laser.

To simulate the polarization dependent scattering events as dictated by Eq. (6.9), it is convenient to use the Stokes-Mueller formalism [103]. A photon in a given state of polarization can be

² Note: For a cloud with a Gaussian distribution, the size of the incident laser beam needs to be taken into account, since a broad beam experiences fewer scattering events at the edge of the cloud and the actual optical depth depends on the transverse coordinates. The finite beamsizes is not taken into account in the CD presented here. In RW we choose the beamsizes to be 5 times the Gaussian width of the cloud.

described by a Stokes vector [35]

$$\mathbf{S} = \begin{pmatrix} S_0 \\ S_1 \\ S_2 \\ S_3 \end{pmatrix} = \begin{pmatrix} \overline{|E_l|^2} + \overline{|E_r|^2} \\ \overline{|E_l|^2} - \overline{|E_r|^2} \\ \overline{E_l^* E_r} + \overline{E_l E_r^*} \\ i(\overline{E_l^* E_r} - \overline{E_l E_r^*}) \end{pmatrix}, \quad (6.10)$$

where E_l , E_r are the electric field components projected onto the two orthogonal axis \hat{e}_l and \hat{e}_r in the plane perpendicular to the wavevector \mathbf{k} . For example, $\mathbf{S} = (1, 1, 0, 0)$ represents a photon linearly polarized along the reference axis \hat{e}_l . A scattering event $\mathbf{k}_{\text{in}}, \boldsymbol{\epsilon}_{\text{in}} \rightarrow \mathbf{k}_{\text{out}}, \boldsymbol{\epsilon}_{\text{out}}$ can be determined by two angles: θ and ϕ [see Fig. 6.7]. The change of polarization can be obtained from the transformation $\mathbf{S}'' = M(\theta)\mathcal{R}(\phi)\mathbf{S}^{\text{in}}$, where \mathbf{S}^{in} is the incident Stokes vector, \mathbf{S}'' is defined with respect to the axis \hat{e}_l'', \hat{e}_r'' and \hat{e}_3'' , and then $\mathbf{S}^{\text{out}} = \mathcal{R}(\psi)\mathbf{S}''$ transforming back to the original frame \hat{e}_l, \hat{e}_r and \hat{e}_3 [15], with \mathbf{S}^{out} the scattered Stokes vectors. The scattering matrix that we use, M , is the scattering matrix that describes Rayleigh scattering [103, 135]. It is given by

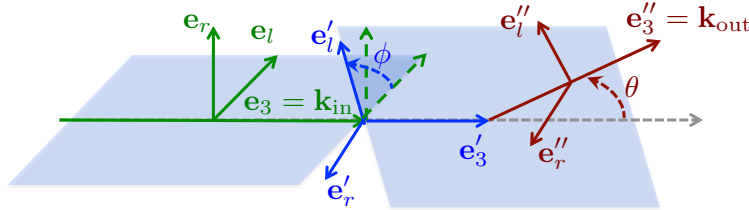


Figure 6.7: RW: transformation of Stokes vectors. In the random walk model, a scattering event is determined by two consecutive transformations of local coordinates: $\{\mathbf{e}_3, \mathbf{e}_r, \mathbf{e}_l\} \rightarrow \{\mathbf{e}_3', \mathbf{e}_r', \mathbf{e}_l'\}$ via rotation ϕ , and $\{\mathbf{e}_3', \mathbf{e}_r', \mathbf{e}_l'\} \rightarrow \{\mathbf{e}_3'', \mathbf{e}_r'', \mathbf{e}_l''\}$ via rotation θ [15].

$$M(\theta) = \frac{3}{4} \begin{pmatrix} \cos^2\theta + 1 & \cos^2\theta - 1 & 0 & 0 \\ \cos^2\theta - 1 & \cos^2\theta + 1 & 0 & 0 \\ 0 & 0 & 2\cos\theta & 0 \\ 0 & 0 & 0 & 2\cos\theta \end{pmatrix}. \quad (6.11)$$

The matrix, $\mathcal{R}(\phi)$, is the rotation matrix that rotates the incident axis \hat{e}_r to \hat{e}_r' (perpendicular to the scattering plane),

$$\mathcal{R}(\phi) = \begin{pmatrix} 1 & 0 & 0 & 0 \\ 0 & \cos(2\phi) & \sin(2\phi) & 0 \\ 0 & -\sin(2\phi) & \cos(2\phi) & 0 \\ 0 & 0 & 0 & 1 \end{pmatrix} \quad (6.12)$$

and $\mathcal{R}(\psi)$ is the rotation matrix that transforms the coordinate system \hat{e}'_l, \hat{e}'_r and \hat{e}'_3 back to the original coordinate system \hat{e}_l, \hat{e}_r and \hat{e}_3 , and can be found from θ and ϕ . The polarization of the photons is encoded in the Stokes vector. The probability of a scattering event can be directly calculated from S''_0/S_0^{in} . Complete trajectories of the photons can be found from Monte Carlo sampling of scattering events. As the phase information of photon is not kept in this approach, it is more suitable for describing classical media or hot atoms where phase coherence is not important.

The polarization of the incident photon is randomized after multiple scattering events. Since the intensity detected along the polarization direction of the incident photon requires at least two scattering events, it is suppressed compared to other directions but nonzero (Fig. 6.8(a)) and the linewidth at small τ_p also drops below the natural linewidth (Fig. 6.8(c)) along this direction. For the other directions, the intensity distribution is roughly homogeneous and does not exhibit the collective enhancement along the forward direction observed in the coherent dipole model. The FWHM linewidth for different directions increases linearly with OD up to a moderate value of OD (see Fig. 6.8(b)), and displays a polarization dependence similar to the prediction of CD. Under this classical treatment more scattering processes are expected to occur with increasing τ_p and those processes tend to inhibit the transmission of light. As the scattering becomes more frequent, forward scattering decreases and more light is scattered backwards [133]. Since τ_p is maximum at resonance, $\Delta = 0$, the linewidth develops a “double-peak” profile as the medium becomes denser (Fig. 6.8(c)). Before the distortion in line shape develops, the FWHM linewidth also linearly increases with τ_p . We note that a similar “double-peak” structure also appears in the coherent dipole model. However, there, it only happens at specific small angles (see Fig. 6.3(c)), and never happens along the forward direction, where the stimulated photon emission dominates or the

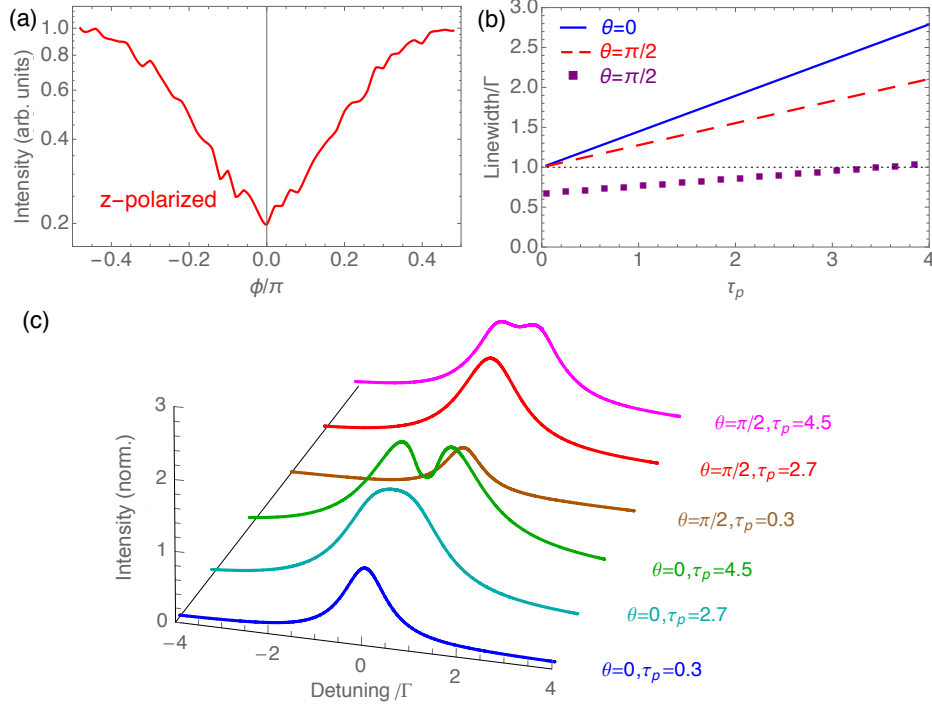


Figure 6.8: RW Model. (a) Distribution of on-resonance intensity in the plane $\theta = \pi/2$. Along the direction where single scattering events are forbidden ($\phi = 0$), the light intensity is suppressed. (b) The FWHM linewidth increases linearly with τ_p in a dilute medium. The linewidth along the direction parallel to the laser polarization can drop below Γ for small (purple squares). (c) Lineshapes for different τ_p s and angles of observation. The line shape is Lorentzian for low τ_p but gets distorted and develops a double-peak structure as the τ_p increases. Here, for all angles, the signal is collected within a small angular region $\delta\theta = 5^\circ$. The intensity is normalized to the value at zero detuning for $\theta = 0$ and $\tau_p=0.3$, and the width of laser beam is 5 times the Gaussian width of the atomic cloud. Here all τ_p are labeled as the value at $\Delta = 0$.

transverse direction, where the photons scattered via dipolar exchange dominate. We attribute the appearance of the “double-peak” structure to the interplay between these two types of emission. In summary, despite of the fact that the RW model does not include coherent emission mechanisms, it is able to reproduce the collective broadening observed with increasing optical depth and the sub-natural linewidth present in the direction parallel to the laser polarization at relatively small optical depths. The RW model on the other hand ignores coherent elastic dipolar interactions and thus does not predict a density shift.

6.4 Role of atomic motion

An assumption made in Sec. 6.2 is that the position of the atoms remains fixed. This assumption is only valid when atoms move at a rate slower than the radiative decay rate. When motion is significantly faster, e.g. hot atomic clouds, the coherence during radiation is smeared out and classical approaches, such as the RW model, are usually satisfactory [258, 36] to describe collective light emission. However, many experiments operate in an intermediate regime where coherences cannot be totally disregarded and it is not a good approximation to treat atoms as frozen. For example, for the $^1S_0 \rightarrow ^3P_1$ transition of ^{88}Sr atoms, the Doppler broadening at $\sim 1 \mu\text{K}$, $\Delta_D \approx 6\Gamma$, and recoil frequency $\omega_r = \hbar k_0^2/2m \approx 0.6\Gamma$, both comparable to the natural linewidth [108, 254]. Consequently for a proper description of light scattering one needs to account for both photon coherences and atomic motion on an equal footing. Below we present two approximate ways to accomplish this:

6.4.1 Modified frozen dipole model

In this section, we discuss a simple way to include the effects of atomic motion on light scattering via a modified CD model. For a single atom, to leading order, a major modification from motion in the emitted light intensity is the Doppler shift, a velocity dependent modification of the effective laser detuning experienced by an atom (see Appendix D.2). We include this effect in the many-body system by introducing random detunings for each atom, *i.e.*, $\Delta \rightarrow \Delta + \delta\nu$, and by sampling them according to a Maxwell-Boltzmann distribution $P(\delta\nu) = \frac{1}{\sqrt{2\pi}\tilde{\Delta}_D} \exp\left(-\frac{\delta\nu^2}{2\tilde{\Delta}_D^2}\right)$ that accounts for the Doppler shifts [112]. Here $\tilde{\Delta}_D = \Delta_D/\sqrt{8\ln 2}$. We denote this approximation as the modified frozen dipole model. The random detunings modify atomic coherences as (for simplicity we assume a single beam illumination):

$$b_j = \frac{\Omega e^{i\mathbf{k}_0 \cdot \mathbf{r}_j}}{(\Delta - \delta\nu_j) + i\Gamma/2}. \quad (6.13)$$

Using Eq. (6.13), the intensity along a generic direction becomes

$$I_{\text{incoh}} = \frac{1}{\sqrt{2\pi}\tilde{\Delta}_D} \int d\delta\nu_j |b_j|^2 e^{-\delta\nu_j^2/2\tilde{\Delta}_D^2}. \quad (6.14)$$

On the other hand, the coherent scattering in the forward direction which takes into account pairwise atomic contributions, becomes

$$I_{\text{coh}} = \frac{1}{2\pi\tilde{\Delta}_D^2} \int d\delta\nu_j d\delta\nu_{j'} b_j b_{j'}^* e^{-\delta\nu_j^2/2\tilde{\Delta}_D^2} e^{-\delta\nu_{j'}^2/2\tilde{\Delta}_D^2}. \quad (6.15)$$

The on-resonance enhancement factor is thus

$$\frac{I_{\text{coh}}}{I_{\text{incoh}}} = \frac{\sqrt{\frac{\pi}{2}} e^{\frac{8\tilde{\Delta}_D^2}{\Gamma^2}} \text{erfc}\left(\frac{1}{2\sqrt{2}\tilde{\Delta}_D/\Gamma}\right)}{2\tilde{\Delta}_D/\Gamma}, \quad (6.16)$$

where erfc is the complementary error function. This induces an exponential suppression of the forward interference that depends on $\tilde{\Delta}_D/\Gamma$ [33], as shown in Fig. 6.9(a).

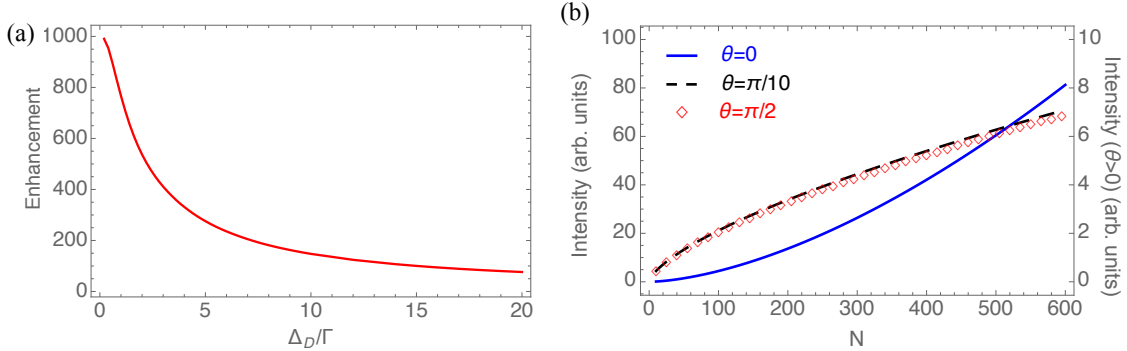


Figure 6.9: Modified frozen dipole model: peak intensity. (a) Collective forward enhancement: forward intensity normalized by the transverse intensity as a function of Doppler width. (b) Intensity detected along different directions at Doppler width $\Delta_D = 6\Gamma$ as a function of atom number for fixed cloud size (when $N = 500$, $\tau=2, n_0 k_0^{-3}=0.0015$). $I \sim N^{1.6}$ for $\theta = 0$, and $I \sim N^{0.7}$ for $\theta = \pi/2$. The right vertical axis labels the intensity for $\theta = \pi/2, \pi/10$.

The reduced light scattering probability, on the other hand, competes with dephasing since it suppresses multiple scattering, and as a consequence promotes collective enhancement. Effectively, it brings the system closer to the small OD regime (Fig. 6.2(b)). The motion induced suppression of multi-scattering processes is also signaled in the frequency shift (Fig. 6.4) [112, 114], which keeps increasing until a larger value of density in the presence of motion.

6.4.2 Semi-classical approach

Laser light mediated forces on atoms are a fundamental concept in atomic physics and lay the foundations of laser trapping and cooling [196, 44]. They can be accounted for at the semiclassical level by explicitly including the position \mathbf{r}_i and the momentum \mathbf{p}_i degrees of freedom of the atoms, and solving for their dynamics while feeding those back into the quantum dynamics of the internal degrees of freedom. An explicit description of this procedure is presented below.

For simplicity we will assume a two-level transition. This condition is achievable in experiments, for example, by applying a large magnetic field to split apart ($|\Delta^\alpha - \Delta^\gamma| \gg \mathcal{G}\Gamma$) the excited state levels and thus energetically suppressing population of the ones not directly driven by the laser. For driving the atoms we will consider the case of two counter-propagating lasers with wavevector $\pm\mathbf{k}_0$, propagating along x , and Rabi frequency Ω . The internal atomic variables evolve according to (see Appendix D.1)

$$\frac{db_j}{dt} = i\Omega \cos(\mathbf{k}_0 \cdot \mathbf{r}_j) s_j - \left(\frac{\Gamma}{2} + i\Delta\right) b_j + i \sum_{l \neq j} s_j b_l (g_{jl} - i f_{jl}), \quad (6.17)$$

$$\begin{aligned} \frac{ds_j}{dt} = & 2i\Omega \cos(\mathbf{k}_0 \cdot \mathbf{r}_j) (b_j - \text{H.c.}) - \Gamma s_j \\ & - 2i \sum_{l \neq j} (g_{jl} - i f_{jl}) b_j^* b_l + 2i \sum_{l \neq j} (g_{jl} + i f_{jl}) b_l^* b_j, \end{aligned} \quad (6.18)$$

where $\Delta = \Delta^\alpha$, and the last terms describe the effect of dipole-dipole interactions $g(r)$ and $f(r)$ (see Appendix D.1). In general the position of atoms can also change with time as

$$\frac{d\mathbf{r}_j}{dt} = \frac{\mathbf{p}_j}{m}, \quad (6.19)$$

so the response to the local driving field and dipole-dipole interactions in Eq. (6.17) and Eq. (6.18) change accordingly. The momentum changes not only due to the force exerted by the driving laser, but also the long-range forces $\mathbf{g}_{jl} = -\nabla g_{jl}$ and $\mathbf{f}_{jl} = -\nabla f_{jl}$, which originate from the dispersive and dissipative dipole-dipole interaction, respectively (see Appendix D.1), and depend

on the instantaneous atomic coherences and positions:

$$\begin{aligned} \frac{d\mathbf{p}_j}{dt} = & -2\hbar\mathbf{k}_0\Omega\sin(\mathbf{k}_0 \cdot \mathbf{r}_i)\Re\{b_i(t)\} \\ & + \sum_{l \neq j} [\mathbf{g}_{jl}(b_j b_l^* + \text{H.c.}) - i\mathbf{f}_{jl}(b_j b_l^* - \text{H.c.})]. \end{aligned} \quad (6.20)$$

The atomic coherence and external motion are now coupled together, so Eq. (6.17)~Eq. (6.20) need to be solved simultaneously to obtain the dynamics. In deriving Eq. (6.20), we have ignored the role of momentum diffusion (see Appendix D.1). We have verified in our numerical simulations that it can be safely ignored for the parameters of interest presented in this work.

From previous sections, it has been shown that except for a narrow cone around the forward direction, the fluorescence intensity is $I(\mathbf{r}_s) \propto \sum_i s_i$ (also see Appendix D.2). Since we expect motion to further reduce the effect of coherence, we will focus on the transverse scattering, and compute $\sum_i s_i$. Fig. 6.10 shows the line shape of a single atom for different Ω calculated from the semi-classical approach.

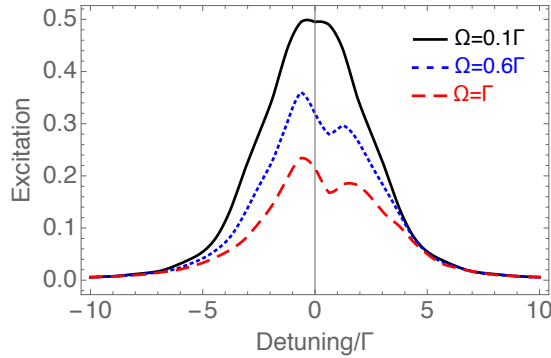


Figure 6.10: Semi-classical model: single-atom line shape. The excitation line shape is calculated for three different driving strength, each normalized by Ω^2 . The atomic motion is allowed to be one-dimensional and parallel to the laser propagating direction. Here we used $\omega_r = 0.6\Gamma$ (the value of the $^1S_0 \rightarrow ^3P_1$ transition of Sr [108]).

As a result of atomic motion, the laser-atom system is not in a stationary state. We show the results for driving time $t = 5/\Gamma$. When $\Omega \ll \Gamma$, the line shape is a Voigt profile with the Doppler width determined by the velocity. When $\Omega \sim \Gamma$, there is a distortion in the line shape, with more intensity at $\Delta < 0$. This is because for $\Delta < 0$ the laser force decelerates the atom, while for $\Delta > 0$

the atom is heated up. With reduced/increased velocity, the atom is on average more/less excited, resulting in a distorted line shape. The center of the line is therefore shifted to the red.

Motion can significantly modify the interactions between atoms [57]. We study the effect of motion on the frequency shift in Fig. 6.11. Dipolar induced frequency shifts were previously discussed in Sec. 6.2. Since we focus on low driving fields, again we neglect momentum diffusion in these calculations. The calculations show that unless Δ_D is very small, atomic motion leads to a fast suppression of the frequency shift. Only when $\Delta_D \ll \Gamma$, the frequency can be increased by motion and this is the regime where the modified frozen dipole model is qualitatively valid; recall, it predicts always an increase of density shift with Doppler broadening. We note that at $\Delta_D \rightarrow 0$ the frequency shift obtained using the modified frozen dipole model, is slightly smaller than that one obtained from the semi-classical approach. This is a consequence of the distortion caused by laser cooling/heating which additionally shifts the spectral line. For $\Delta_D \gtrsim \Gamma$ motion needs to be properly accounted for and the modified frozen dipole model is not reliable.

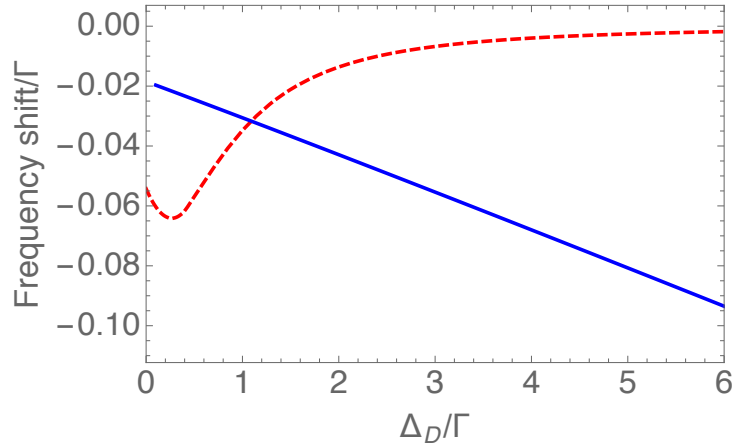


Figure 6.11: Semi-classical model: effect of motion on frequency shift. Two atoms are driven by a pair of counter-propagating lasers, with $\Omega = 0.1\Gamma$, $\omega_r = 0.6\Gamma$. The red dashed line shows the result of semi-classical model where motion is allowed in three dimensions. The blue line shows the result from the modified CD. The center of excitation line shape is calculated at $t = 5/\Gamma$ for different Doppler width, for both models.

6.5 Comparison with experiment

In this section, we describe an experiment that measures the collective emission from coherently driven ultracold ^{88}Sr atoms. ^{88}Sr atoms have both a strong $^1S_0-^1P_1$ blue transition ($\lambda = 461$ nm) and a spin-forbidden weak $^1S_0-^3P_1$ red transition ($\lambda = 689$ nm), with a strict 4-level geometry (Fig. 6.12(a)). When the atoms are cooled to a temperature of ~ 1 μK , Doppler broadening at 461 nm is about 55 kHz, which is almost three orders of magnitude smaller than the blue transition natural linewidth, $\Gamma = 32$ MHz. To an excellent approximation atomic motion is negligible for atomic coherence prepared by the 461 nm light. To the contrary, the red transition with a natural linewidth $\Gamma = 7.5$ kHz is strongly affected by atomic motion. By comparing the behaviors of the same atomic ensemble observed at these two different wavelengths (Fig. 6.12(b)) we can thus collect clear signatures of motional effects on coherent scattering and dipolar coupling[112, 132].

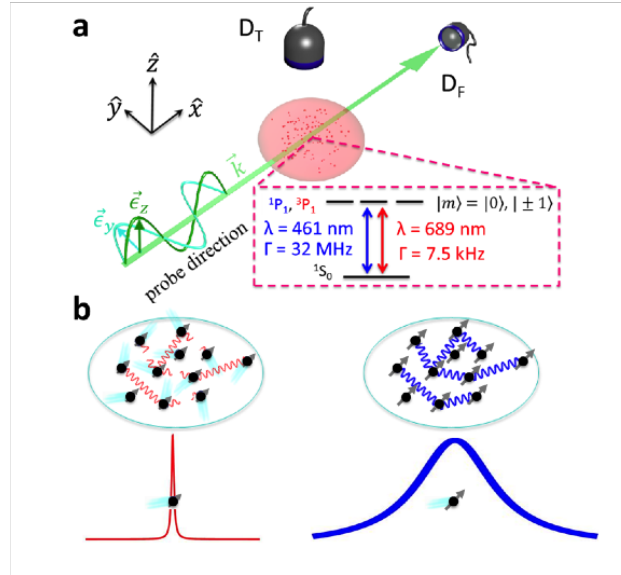


Figure 6.12: (a) The experimental scheme and concept. We weakly excite the strontium atoms with a linearly polarized probe beam and measure the fluorescence with two detectors, one in the forward direction, \hat{x} , and the other almost in the perpendicular direction, \hat{z} . We probe two different $J = 0$ to $J' = 1$ transitions. The first transition is a $^1S_0-^1P_1$ blue transition with a natural linewidth of $\Gamma = 32$ MHz and the second is a $^1S_0-^3P_1$ red transition with $\Gamma = 7.5$ kHz. (b) In the coherent dipole model photons are shared between atoms. When the Doppler broadened linewidth becomes comparable to the natural linewidth, dephasing must be considered. At our $\sim 1\mu\text{K}$ temperatures the Doppler broadening is ≈ 40 kHz meaning motional effects are important only for the red transition.

We use the experimental scheme shown in Fig. 6.12(a) to perform a comprehensive set of measurements of fluorescence intensity emitted by a dense sample of ^{88}Sr atoms. The sample is released from the trap and then illuminated with a weak probe laser. We vary the atomic density, cloud geometry, observation direction, and polarization state of the laser field, and we report the system characteristics using three key parameters: the peak scattered intensity, the linewidth broadening, and the line center shift. For example, along the forward and transverse directions we observe different values of intensity and linewidth broadening, as well as their dependence on light polarization (see Fig. 6.13). We also observe motional effects on the red transition in contrast to the same measurements on the blue transition.

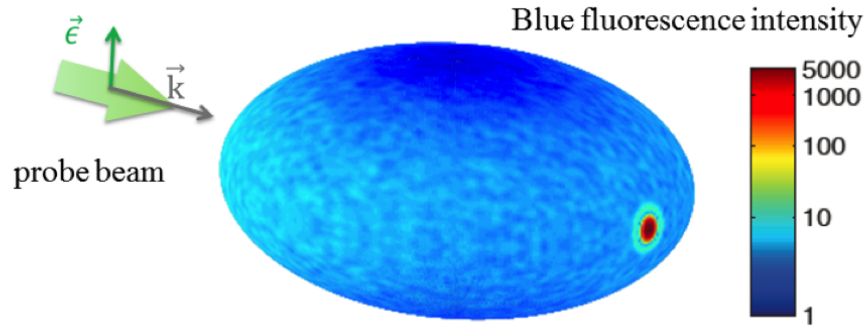


Figure 6.13: The 3D intensity distribution predicted for a blue probe beam. The coupled-dipole model predicts a strong 10^3 enhancement of the forward intensity compared to other directions and a finite fluorescence along a direction parallel to the incident polarization. The speckled pattern is due to randomly positioned atoms and can be removed by averaging over multiple atom configurations.

In the experiment, up to 20 million ^{88}Sr atoms are cooled to $\sim 1 \mu\text{K}$ in a two-stage magneto-optical trap (MOT), the first based on the blue transition and the second on the red transition. The atomic cloud is then released from the MOT and allowed to expand for a variable time of flight (TOF), which allows us to control its optical depth and density. They are subsequently illuminated for $50(100) \mu\text{s}$ with a large size probe beam resonant with the blue (red) transition (Fig. 6.14(a)). The resulting scattered light is measured with two detectors far away from the cloud (see Fig. 6.12 (a)). One detector is along the forward direction \hat{x} (detector D_F), and the other transverse direction

\hat{z} (detector D_T , offset by $\sim 10^\circ$). For a short TOF, the atomic cloud is anisotropic and has an approximately Gaussian distribution with an aspect ratio of $R_x : R_y : R_z = 2 : 2 : 1$, where $R_{\{x,y,z\}}$ are r.m.s radii.

The coherent effect manifests itself most clearly in the forward direction (Fig. 6.14). To

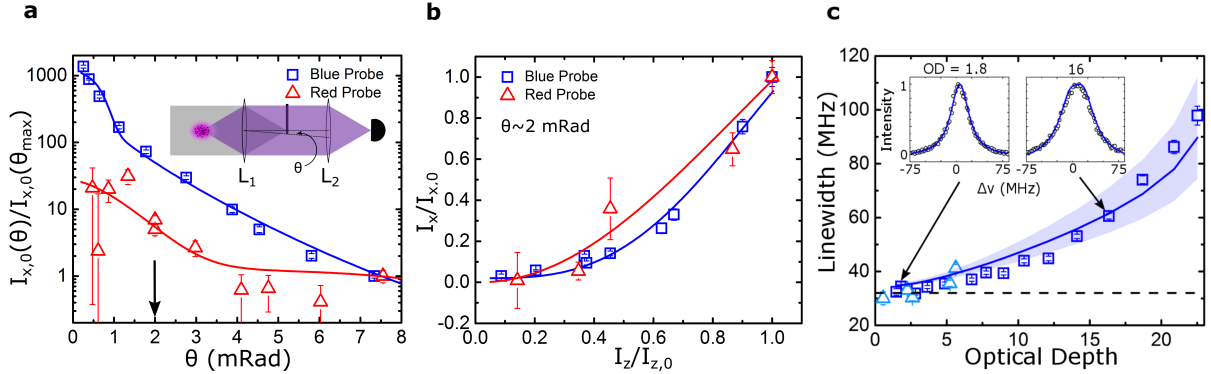


Figure 6.14: Forward Scattering. (a) Comparison of forward scattering intensity versus angle using a red and blue probe beam. The inset shows the setup used to block the probe beam. After interacting with the atoms the probe beam is focused using a lens, which also collimates the fluorescence from the atoms. We block the probe beam using a beam stopper, which we translate perpendicular to the probe beam to change the angular range of fluorescence collected by the detector, characterized by the angle (θ) between \hat{x} and the edge of the beam stopper (see Ref. [33]). The measured intensity, $I_{x,0}(\theta)$, for each probe beam is normalized to the intensity at $\theta_{\max} = 7.5$ mRad. The dephasing caused by motion reduces the forward intensity peak for the red transition. (b) Comparison of intensity in the forward direction, I_x , versus intensity in the transverse direction, I_z . Both are varied by changing N . All measurements are made at $\theta = 2$ mRad (arrow in (a)) and normalized to the intensity, $I_{x,0}$, for the atom number used in (a). (c) Linewidth broadening in the forward direction measured by scanning the blue probe beam detuning, Δ , across resonance. Example lineshapes for different optical depths (ODs) are shown in the inset. Two different atom numbers are used, $N = 1.7(2) \times 10^7$ (blue squares) and $N/4$ (cyan triangles). The dashed line represents Γ for reference. All solid curves are based on the full theory of coupled dipoles and the band in (c) is for a $\pm 20\%$ atom number uncertainty. All errorbars are for statistical uncertainties.

separate the forward fluorescence from the probe beam, we focus the probe with a lens (L_1) after it has passed through the atomic cloud and then block it with a beam stopping blade, which can be translated perpendicular to the probe beam (Fig. 6.14(a) inset). The same lens (L_1) also collimates the atomic fluorescence so that it can be imaged onto D_F . The position of the beam stopper can be used to vary the angular range of collected fluorescence, characterized by the angle (θ) between \hat{x} and the edge of the beam stopper (See Ref. [33]). Using the maximum atom number available in

the experiment, the measured intensity $I_{x,0}(\theta)$ is normalized to that collected at $\theta_{\max} = 7.5$ mRad. Both the blue (square) and red (triangle) transition results are displayed in Fig. 6.14(a). For the blue transition a thousand-fold enhancement of the normalized intensity is observed for $\theta < 0.5$ mRad. We note that this enhancement as a function of θ far exceeds the diffraction effect by the beam stopper. The latter effect becomes significant only when $\theta \lesssim 0.1$ mRad, and is also suppressed in our differential measurement scheme which compares measurements with and without atoms. The enhancement is also present for the red transition, but it is reduced by nearly two-orders of magnitude at small θ due to the motional effect. On the other hand, the wider angular area of enhancement is attributed to the longer wavelength of the red transition. The forward intensity strongly depends on the atom number. Fig. 6.14(b) shows measurements of the forward intensity I_x versus the transverse intensity I_z at a fixed $\theta = 2$ mRad for different atom numbers. The intensities are normalized to those obtained at the peak atom number as used in Fig. 6.14(a). To the first order approximation, the transverse fluorescence intensity scales linearly with the atom number. Hence, the forward intensity of both the blue and red transitions scales approximately with the atom number squared. These observations are consistent with the conclusions obtained in Sec. 6.2. The solid lines in Figs. 6.14(a) and (b) represent the full solution of the CD model, which agree with experiment for both transitions.

In the forward direction we have also investigated the linewidth broadening of the blue transition as a function of the atomic OD. By scanning the probe frequency across resonance we extract the fluorescence linewidth, which is found to be determined primarily by the OD of the cloud (open squares in Fig. 6.14(c)). For the range of $0 < OD < 20$ the lineshape is Lorentzian (see insets); however, the observed lineshape starts to flatten at the center for $OD > 20$. We have also varied the atom number by a factor of four, and to an excellent approximation the linewidth data is observed to collapse to the same curve when plotted as a function of OD (open triangles). It is also evident that the scaling of the linewidth vs. OD turns nonlinear at large values of OD. The experimental data falls within the shaded area in Fig. 6.14(c), which represents the full solution of CD model with a 20% uncertainty in the experimental atom number.

For independent emitters the forward fluorescence should have no dependence on the probe beam polarization; however, the transverse fluorescence (along \hat{z}) should be highly sensitive to the probe polarization, and it is even classically forbidden if the probe is \hat{z} -polarized. However, multiple scattering processes with dipolar interactions can completely modify this picture by redistributing the atomic population in the three excited magnetic states and thus scrambling the polarization of the emitted fluorescence, with an intensity that increases with increasing OD. Consequently, even for a \hat{z} -polarized probe there should be a finite emission along \hat{z} . This is consistent with the theoretical prediction of the CD model, as shown in Fig. 6.13. The experimental investigation of the fluorescence properties along the transverse direction is summarized in Fig. 6.15. Under the same

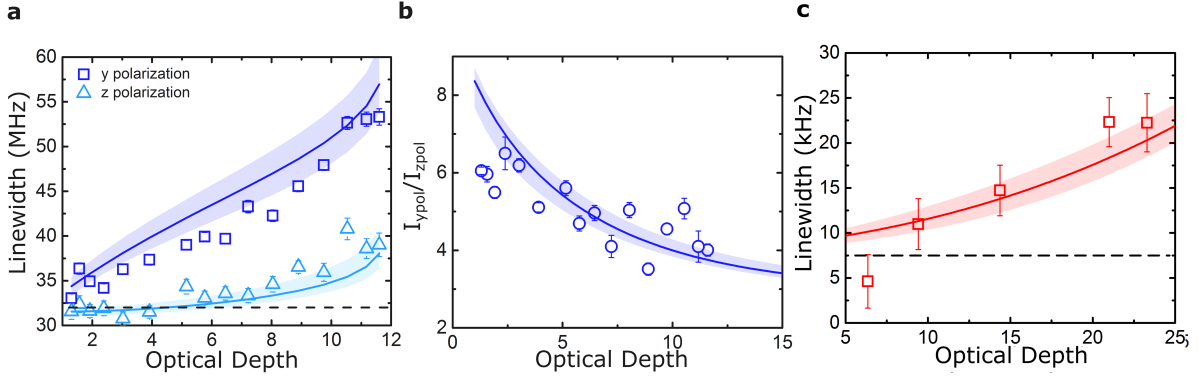


Figure 6.15: Transverse Scattering. (a) Linewidth broadening for the blue transition in the transverse direction for \hat{y} -polarization (open squares) and \hat{z} -polarization (open triangles). (b) Intensity ratio, I_{ypol}/I_{zpol} , of \hat{y} -polarization to \hat{z} -polarization measured in the transverse direction when a blue probe beam is used. For low optical depths single particle scattering is dominant, and for single particle scattering almost zero intensity is predicted for \hat{z} -polarized fluorescence as this polarization points directly into the detector. (c) Linewidth broadening for the red transition in the transverse direction for \hat{y} -polarized light showing a similar trend to the blue transition. This transition is more sensitive to magnetic fields so a large magnetic field is applied to probe only the $m = 0$ to $m' = 0$ transition. All solid curves are based on the full theory of coupled dipoles and the band in (c) is for a $\pm 20\%$ atom number uncertainty. All errorbars are for statistical uncertainties.

OD along \hat{z} , the \hat{y} -polarized probe beam (square) gives rise to a much more broadened lineshape for the blue transition than the \hat{z} -polarized probe beam does (triangle), as shown in Fig. 6.15(a). Meanwhile, the peak intensity ratio of I_{ypol}/I_{zpol} decreases significantly with an increasing OD, indicating the rapidly rising fluorescence with a \hat{z} -polarized probe when OD increases (Fig. 6.15(b)).

For both intensity and linewidth broadening observed in the transverse direction, under either \hat{y} or \hat{z} probe polarization, the full solution of the CD model (shown as shaded areas in both Fig. 6.15(a) and (b)) reproduces well the experimental results on $^1S_0-^1P_1$.

For the red transition, the existence of Doppler broadening requires the lineshape data to be fitted to a Voigt profile. With the Doppler linewidth Δ_D fixed from the thermal velocity measured in free expansion, the Voigt profile determines the line center as well as the Lorentzian linewidth with the Gaussian linewidth determined by the temperature. Fig. 6.15(c) displays the Lorentzian linewidth obtained with a \hat{y} -polarized red probe showing a strong increase of the linewidth with OD. Taking into account motional dephasing (see Sec. 6.4.1), the transverse broadening for $^1S_0-^3P_1$ is also well reproduced as shown in Fig. 6.15(c).

6.6 Conclusion

We theoretically studied the propagation of light through a cold atomic medium. We presented two different microscopic models, the “coherent dipole model” and the “random walk model”, and analyzed how the light polarization, optical depth and density affect the linewidth broadening, intensity and line center shift of the emitted light. We showed that the random walk model, which neglects photonic phase coherence, can fairly capture the collective broadening (narrowing) of the emission linewidth but on the other hand does not predict a density shift. Due to the limitation of computation capacity, the numerical simulation of CD is usually restricted to $\sim 10^4$ atoms, which is much smaller than that in some cold atom experiments [95, 12]. Nevertheless, the understanding of the underlying physics allowed us to perform an appropriate rescaling in the cloud size to compare with experiments. We further developed generalized models that explicitly take into account motional effects. We showed that atomic motion can lead to drastic dephasing and reduction in the collective effects, together with a distortion in the line shape. While the modified frozen dipole model predicts a monotonic increase of the density shift with increasing motion, the semiclassical model, which properly accounts for recoil effects, predicts that this behavior only holds at slow motion $\Delta_D \ll \Gamma$. Instead, as atoms move faster, motional effects start to become dominant, the

cloud expands and the frequency shift decreases. We show, as an explicit example, an experiment done with ^{88}Sr atoms [33], and apply the CD model to explain all the experiment observations for the strong transition, where motional effects are weak. The modified frozen dipole model is also shown to capture the fluorescence intensity and linewidth broadening measured for the weak transition, where motional effects are significant. None of the presented theoretical models, however, can explain the large density shift measured in the $^1\text{S}_0 \rightarrow ^3\text{P}_1$ transition of ^{88}Sr atoms [108]. It will be intriguing to determine what are the actual physical processes that cause this large shift.

Chapter 7

Emergent Weyl excitations in systems of polar particles

7.1 Introduction

Recent predictions [263, 37] and experimental observations [276, 156, 151] of Weyl semimetals in solid state systems have instigated intensive studies of their properties, such as non-local electrodynamics and chiral anomaly [194], topologically protected Fermi arcs on the surfaces [263, 276, 156], non-Anderson disorder-driven transitions [78, 91, 246, 245, 219, 174, 125] and unusual dependencies of transport properties on doping and temperature [218, 228, 209]. In parallel, enormous research efforts are now directed at finding Weyl excitations in new systems. A promising platform for exploring Weyl physics is tunable and fully controllable ultracold atomic gases [139, 117, 4, 70, 81, 150]. However, henceforth proposed cold-atom realisations of Weyl quasiparticles have focussed mostly on non-interacting systems, and all have required implementations of externally imposed spin-orbit coupling through laser assisted tunneling schemes [139, 117, 4, 70, 81], other optical means [271, 89, 225], or external rotating fields [150].

In this chapter we demonstrate that excitations with Weyl dispersion generically emerge in three-dimensional (3D) arrays of dipolar particles in the presence of a weak magnetic field, as a result of the dipole-interactions-induced transitions between their internal angular-momentum $J = 0$ and $J = 1$ states. These excitations exhibit the same single-particle physics as Weyl fermions [265] but, similarly to other non-fermionic Weyl excitations [151], their many-particle properties are expected to be different, opening alternative research directions, new functionalities and applications beyond those accessible with solid-state systems [276, 156].

We also show that, experimentally such excitations can be observed, for instance, in trapped alkaline-earth atoms (AEAs) in a 3D optical lattice with lattice spacings smaller than the wavelength of the electronic $J = 0 \rightarrow J = 1$ transition. The simple and unique internal structure of these atoms has already lead to record levels of precision and accuracy in atomic clocks [27]. Taking advantage of the well developed spectroscopic tools to interrogate and manipulate AEAs, we propose to probe the Weyl quasiparticle dispersion and non-trivial chirality by means of momentum-resolved Ramsey spectroscopy. Our proposal opens a path for a feasible experimental realisation of Weyl quasiparticles in clean and controllable atomic systems. Moreover, it lays the groundwork for the yet unexplored regime of topologically protected sensing, owing to the topological robustness of Weyl quasiparticles that could be used to push the stability and accuracy of optical-lattice AEA-based clocks.

7.2 Phenomenological argument

We assume that the system has long-lived excitations (quasiparticles) with (integer) angular momentum \mathbf{J} . Due to the translational invariance, the (quasi)momentum \mathbf{k} is a good quantum number. In the long-wave limit the effective quasiparticle Hamiltonian is insensitive to the details of the potential of the periodic lattice that the particles may be placed in. To preserve rotation and inversion symmetries in the absence of magnetic field the Hamiltonian has to be an even function of $(\mathbf{k} \cdot \hat{\mathbf{J}})$ and a function of $|\mathbf{k}|$ and $\hat{\mathbf{J}}^2$. In the presence of a sufficiently weak uniform magnetic field, $\boldsymbol{\omega}$, that creates a perturbation $-\boldsymbol{\omega} \cdot \hat{\mathbf{J}}$ independent of \mathbf{k} in the limit $\mathbf{k} \rightarrow 0$, the most generic form of the quasiparticle Hamiltonian is given by

$$\hat{h}(\mathbf{k}, \mathbf{J}) = F \left[|\mathbf{k}|, (\mathbf{k} \cdot \hat{\mathbf{J}})^2, \hat{\mathbf{J}}^2 \right] - \boldsymbol{\omega} \cdot \hat{\mathbf{J}}, \quad (7.1)$$

where F is an arbitrary function of three arguments.

The small quasimomentum \mathbf{k} can be measured from any high-symmetry point in the Brillouin zone characterised by an isotropic dispersion $\xi_{\mathbf{k}} = \xi(|\mathbf{k}|)$ of non-interacting particles in the limit $\mathbf{k} \rightarrow 0$.

For the particular case of $J = 1$, the Hamiltonian (7.1) has nodes at momenta $\mathbf{K} \parallel \boldsymbol{\omega}$, such that $F(|\mathbf{K}|, |\mathbf{K}|^2, 2) \pm \omega = F(|\mathbf{K}|, 0, 2)$, corresponding to two intersecting branches with angular momentum projections $J_z = 0$ and $J_z = 1$ or $J_z = -1$ on the direction of magnetic field. We note that such nodes always exist for weak magnetic fields and Hamiltonians that are regular as a function of \mathbf{k} .

The excitation Hamiltonian near a node is obtained by expanding the function F in small momentum $\mathbf{p} = \mathbf{k} - \mathbf{K}$. For a 3D system, it has Weyl dispersion of the form (see Appendix E)

$$\hat{h}_{\text{eff}}(\mathbf{p}) = \zeta(\mathbf{p}) + v_{\perp} \hat{\sigma}_x p_x + v_{\perp} \hat{\sigma}_y p_y + v_{\parallel} \hat{\sigma}_z p_z \quad (7.2)$$

with Pauli matrices $\hat{\sigma}_i$ acting in the space of the respective two angular-momentum projections.

7.3 Model

In what follows we confirm the above phenomenological argument by microscopic calculations for a 3D system of dipolar particles described by the Hamiltonian

$$\hat{H} = \sum_i \hat{H}_0(\mathbf{r}_i) + \frac{1}{2} \sum_{i,j} \hat{H}_{\text{dip}}(\hat{\mathbf{d}}_i, \hat{\mathbf{d}}_j, \mathbf{r}_i - \mathbf{r}_j), \quad (7.3)$$

where $\hat{\mathbf{d}}_i$ is the dipole moment operator of the i -th particle, and

$$\hat{H}_0(\mathbf{r}_i) = -\frac{\hat{\nabla}_i^2}{2m} + U(\mathbf{r}_i) + B_J \hat{\mathbf{J}}_i^2 - \hat{\mathbf{J}}_i \cdot \mathbf{B} \quad (7.4)$$

is the single-particle Hamiltonian that includes the particle kinetic energy $-\frac{\hat{\nabla}_i^2}{2m}$ (hereinafter $\hbar = 1$), the periodic potential $U(\mathbf{r}_i)$ of the lattice that the system may be placed in, the energy $B_J \hat{\mathbf{J}}_i^2$ of internal levels with $\hat{\mathbf{J}}_i$ being the angular momentum of the i -th particle, and the interaction $-\hat{\mathbf{J}}_i \cdot \mathbf{B}$ with magnetic field (measured in units of the gyromagnetic ratio) that splits the $J = 1$ levels.

The most generic form of the dipole-dipole interaction, which accounts for retardation effects, is given by ¹

$$\hat{H}_{\text{dip}}(\hat{\mathbf{d}}_i, \hat{\mathbf{d}}_j, \mathbf{r}) = a(r)(\hat{\mathbf{r}} \cdot \hat{\mathbf{d}}_i)(\hat{\mathbf{r}} \cdot \hat{\mathbf{d}}_j) + b(r)\hat{\mathbf{d}}_i \cdot \hat{\mathbf{d}}_j \quad (7.5)$$

¹ See chapter 2. $\hat{\mathbf{d}} = \sum_{\sigma} \hat{e}_{\sigma} d(b_i^{\sigma\dagger} + b_i^{\sigma})$. Terms like $b_i^{\sigma\dagger} b_j^{\sigma\dagger}$ and $b_i^{\sigma} b_j^{\sigma}$ do not play an role, since they are energetically suppressed. See Appendix E.2 for further explanation.

where $\hat{\mathbf{r}} = \mathbf{r}/r$; $a(r) = \frac{3\gamma_0}{4d^2} [y_2(k_0r) - ij_2(k_0r)]$ and $b(r) = \frac{3\gamma_0}{4d^2} \sum_{n=0}^1 (-1)^n [y_n(k_0r) - ij_n(k_0r)]/(k_0r)$ for $r \neq 0$, with y_n and j_n being the n -th-order spherical Bessel functions of the second and first kind respectively and k_0 the wavevector of the $J = 0$ to $J = 1$ transition. The terms proportional to y_n describe elastic interactions between dipoles a distance r apart, while the terms with j_n account for the inelastic collective photon emission (radiation). In this chapter we use γ_0 to denote the natural linewidth of the transition to distinguish it from the high symmetry point Γ . If the dipoles are much closer to one another than the wavelength of the dipole transition, $k_0r \ll 1$, retardation effects can be ignored, and one recovers the more familiar form of the dipolar interactions, $a(r) \propto -3/r^3$, $b(r) \propto 1/r^3$, common for NMR solid-state systems [47], polar molecules [278] and Rydberg atoms [264, 208].

We note that the above phenomenological derivation of the dispersion of Weyl-type quasiparticles carries over straightforwardly to other dimensions. For example, a 2D system of dipolar particles with an in-plane magnetic field hosts 2D Dirac excitations with the dispersion of monolayer graphene [183]. We emphasise that such 2D excitations are distinct from the 2D ‘‘chiron’’ excitations [247] that exist in a perpendicular magnetic field and resemble electrons in bilayer graphene.

7.4 Atoms in a deep lattice

While the above phenomenological argument demonstrates the existence of Weyl quasiparticles in a generic 3D system of dipolar particles in magnetic field, below we focus on the experimentally important case of particles pinned in a deep unit-filled cubic lattice (Fig. 7.1 (a)) with small lattice spacing a ; $ak_0 \ll 1$.

We assume that all particles are initially prepared in the $J_i = 0$ state and that the energy B_J of internal levels significantly exceeds the interaction strength (usually in dipolar gases [278, 187] $|\hat{H}_{\text{dip}}|/B_J \lesssim 10^{-6}$), leading to the conservation of the number of sites excited to the $J = 1$ state to a good accuracy (cf. Appendix E).

If an excitation with the angular momentum $J = 1$ is created on site i , the dipole-dipole

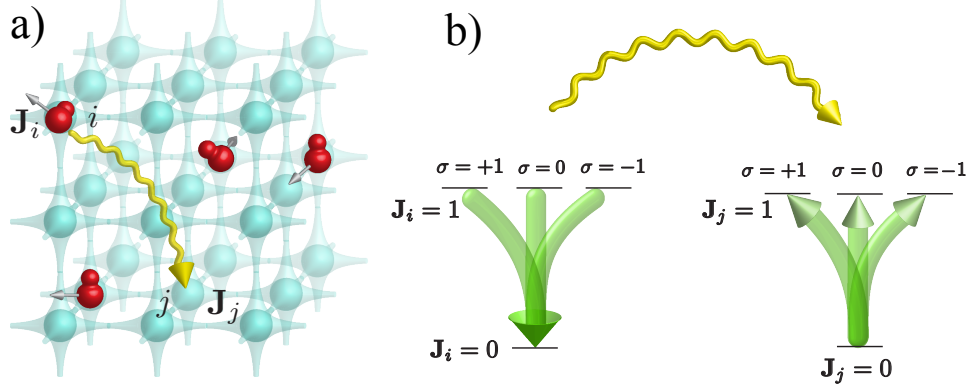


Figure 7.1: Weyl quasiparticles in 3D dipolar arrays. (a) Schematics of the 3D lattice potential that traps an array of dipolar particles. The lattice is deep enough to pin the particles, most of which are prepared in the $J = 0$ ground state (blue spheres). Only a few particles are excited to the $J = 1$ states. Dipolar interactions between the $J = 0$ and $J = 1$ states give rise to Weyl excitations. (b) Schematics of dipole mediated interactions: An excited $J = 1$ state of one particle can be transferred to another particle in the $J = 0$ state by dipole-dipole interactions (virtual photon exchange is shown with a yellow wiggly line). Three types of allowed processes include $|00\rangle_i |1\sigma\rangle_j \leftrightarrow |1\sigma\rangle_i |00\rangle_j$, $|00\rangle_i |10\rangle_j \leftrightarrow |1, \pm 1\rangle_i |00\rangle_j$, and $|00\rangle_i |1, \pm 1\rangle_j \leftrightarrow |1, \mp 1\rangle_i |00\rangle_j$.

interaction can transfer it to another site j , possibly changing the projection of the angular momentum on the direction of the magnetic field; $|1\sigma\rangle_i \rightarrow |1\sigma'\rangle_j$. The quasiparticles in the system are thus hard-core bosons corresponding to the angular momentum-degrees of freedom that hop from site to site as described by the effective Hamiltonian (see Appendix E for a detailed derivation)

$$\hat{H}_{\text{lat}} = \sum_{i,j,\sigma,\sigma'} M_{ij}^{\sigma\sigma'} \hat{b}_{i\sigma}^\dagger \hat{b}_{j\sigma'} = \sum_{\sigma\sigma'\mathbf{k}} M_{\mathbf{k}}^{\sigma\sigma'} \hat{b}_{\sigma,\mathbf{k}}^\dagger \hat{b}_{\sigma',\mathbf{k}}, \quad (7.6)$$

$$M_{ij}^{\sigma\sigma'} = \langle 1\sigma |_i \langle 00 |_j \hat{H}_{\text{dip}} (\hat{\mathbf{d}}_i, \hat{\mathbf{d}}_j, \mathbf{r}_i - \mathbf{r}_j) | 00 \rangle_i | 1\sigma' \rangle_j - \sigma \delta_{\sigma\sigma'} \delta_{ij} B. \quad (7.7)$$

Due to the translational invariance, the single-excitation Hamiltonian can be diagonalised in the basis of momentum states \mathbf{k} , with the results shown in Figs. 7.2a,c. In accordance with the above general phenomenological argument, for $B \neq 0$ the dispersion has Weyl nodes (six in the first Brillouin zone, Figs. 7.2a,c).

To demonstrate the chiral nature of Weyl quasiparticles we show in Figs. 7.2d,e,f the pseudospins $\langle \hat{\sigma} \rangle$ (with the Pauli matrices $\hat{\sigma}_i$ acting in the space of the $J_z = -1$ and $J_z = 0$ angular-

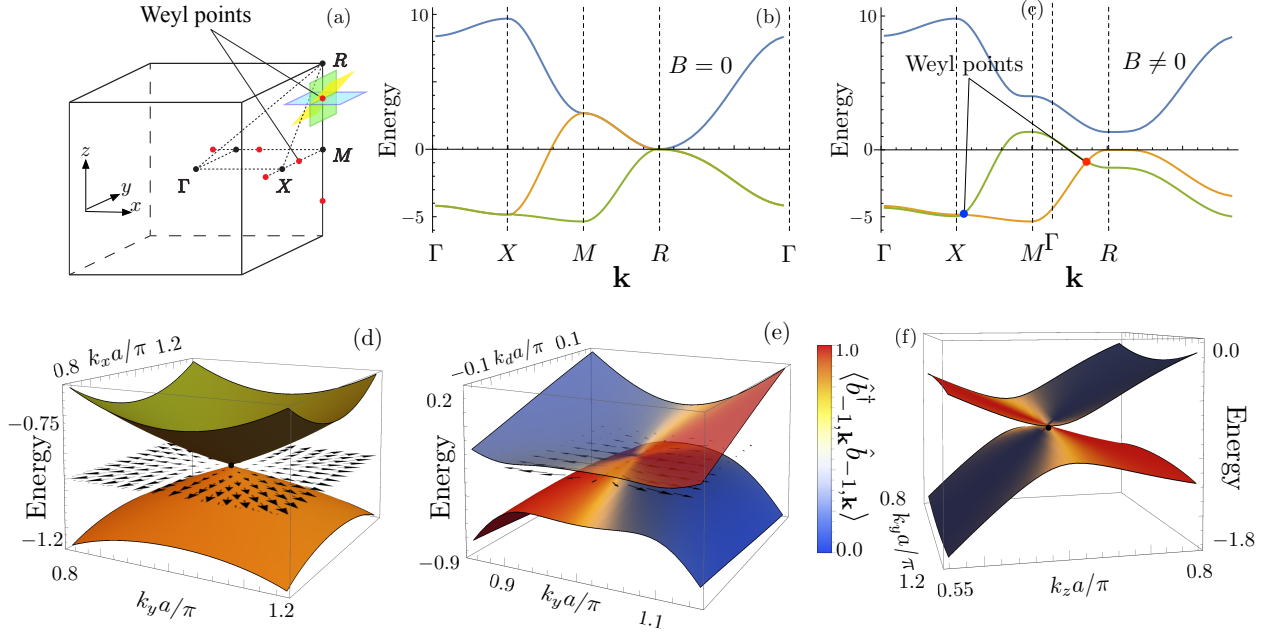


Figure 7.2: Weyl quasi-particle dispersion and eigenstates. (a) Brillouin zone for the simple cubic lattice. (b) Dispersion along high-symmetry lines in the absence of magnetic field (all energies are measured in units of $(3/4)\gamma_0/(k_0a)^3$). (c) Dispersion in the presence of magnetic field $B = \gamma_0/(k_0a)^3$ demonstrating the existence of Weyl nodes (red points) with linear quasiparticle dispersion near them. Each node is characterised by the monopole charge ± 1 . In agreement with the fermion doubling theorem [181] (the Nielsen-Ninomiya no-go theorem), there is an even number (six) of Weyl points in the first Brillouin zone. (d) Dispersion in the horizontal ($k_x - k_y$) plane (shown by blue color in panel (a)) containing the Weyl node near the R point. Quasiparticles in this plane are similar to quasiparticles in graphene and are characterised by a non-trivial Berry phase of π . The arrows show the pseudospin $\langle \hat{\sigma} \rangle$ (the Pauli matrices $\hat{\sigma}_i$ act in the space of the angular-momentum projections $J_z = 0$ and $J_z = -1$). (e) Dispersion along the (yellow in panel (a)) plane consisting of vectors $\mathbf{k} = (\pi + k_d/\sqrt{2}, \pi + k_y, 0.71\pi + k_d/\sqrt{2})$ containing the Weyl point. Color shows the weight of the $|1-1\rangle$ state in the quasiparticle eigenstate, and arrows represent the pseudospin $\langle \hat{\sigma} \rangle$. (f) Dispersion along the (green in panel (a)) vertical plane ($k_y - k_z$) containing the Weyl point near the R point. For each momentum \mathbf{k} the color represents the weight of the $|1-1\rangle$ state.

momentum projections) for the eigenstates with momenta \mathbf{k} in the horizontal ($p_z = 0$), tilted ($p_z = p_x$), and vertical ($p_x = 0$) planes (Fig. 7.2 (a)) that contain a Weyl node. Excitations in these planes are equivalent to quasiparticles in graphene, the 2D counterpart of a Weyl semimetal, and are characterised by the non-trivial Berry phase π . Figs. 7.2d,e,f demonstrate that the pseudospins $\hat{\sigma}$ of these states are linked to their momenta \mathbf{p} , measured from the Weyl node, in agreement with the effective Hamiltonian (7.2).

7.5 Effects of quenched disorder and dissipation

In general, quasiparticles in interacting systems have finite lifetimes due to elastic and inelastic scattering processes. Indeed, deep optical lattices under consideration are usually not completely filled by particles and thus inherently disordered due to the randomness of the particle distribution. Also, spontaneous and dipolar collective emission from the internal $J = 1$ levels to the ground state can lead to the decay of the excitations.

To analyse the effects of dissipation in a unit-filled lattice we compute numerically the quasiparticle dispersion for retarded dipolar interactions, Eq. (7.5), with parameters of the $J = 1$ to $J = 0$ transition of the electronic ${}^3P_0 - {}^3D_1$ levels of bosonic ${}^{88,84}\text{Sr}$ atoms trapped in a magic optical lattice with $a = 206.4\text{nm}$ considered in Ref. [187]. The wavelength and the dipole moment for this transition are $2.6\mu\text{m}$ and $d = 4.03\text{D}$, leading to the linewidth $\gamma_0 = 290 \times 10^3\text{s}^{-1}$ and the dissipation parameter $ak_0 \sim 0.5$. Albeit quasiparticle damping in this regime is rather strong, it is significantly suppressed (by more than three orders of magnitude) near the Weyl nodes, as our simulations show, Fig. 7.3 (a) (b). Our results indicate that the quasiparticle scattering in such a system would be dominated by quenched disorder rather than by collective radiative decay or spontaneous emission.

To account for the effects of disorder we evaluate numerically the quasiparticle dispersion for a lattice filling of 93%. This filling fraction could be achieved by preparing a cold bosonic Mott insulator using moderate atom numbers that allow one to suppress doubly occupied states at the trap centre. Mott insulators have already been realised with bosonic AEs in the ground 1S_0 state [239, 235]. These atoms can be excited to the desired 3P_0 state by laser pulses [2].

As our simulations demonstrate, the characteristic energy scales of Weyl excitations significantly exceed the elastic scattering rate, demonstrating that the excitations could be conveniently observed in current experiments.

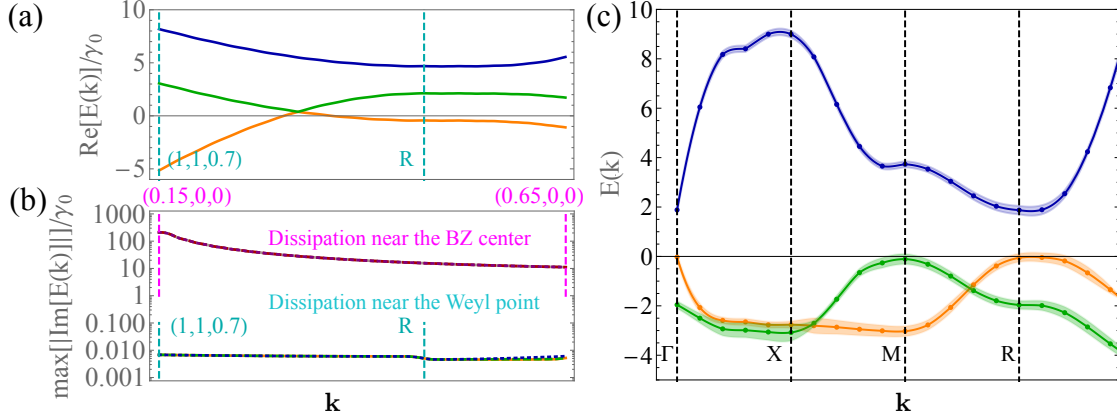


Figure 7.3: Effects of disorder and dissipation on Weyl quasiparticles. (a) Real part of the quasiparticle dispersion in the presence of dissipation (including spontaneous emission and collective radiative decay). The parameters of the $J = 1 \rightarrow J = 0$ transition correspond to those of the electronic ${}^3P_0 - {}^3D_1$ levels of bosonic ${}^{88,84}\text{Sr}$ atoms, trapped in a magic optical lattice potential with $a = 206.4\text{nm}$ [187] at unit filling. Momentum \mathbf{k} is measured in units π/a . (b) The upper bound on the inelastic scattering rate estimated from simulating the full quasiparticle spectra including all allowed elastic and inelastic dipolar processes. The dissipation is significantly suppressed near the Weyl node (blue line). In striking contrast, the dissipation is enhanced close to the Γ point (red line) due to the enhanced collective emission (superradiance). (c) Disordered case: Quasiparticle dispersion for a lattice with filling fraction $f = 0.93$ in the limit of small dissipation $k_0a \ll 1$ (the energy is measured in units $\gamma_0/(k_0a)^3$). The line thickness shows the inelastic scattering rate.

7.6 Proposal for experimental observation

For probing the Weyl character of the excitations we propose a Ramsey protocol illustrated in Fig. 7.4 (a). After preparing a Mott insulator of particles in the $J = 0$ state, a pulse of interfering Raman beams is used to create excitations in the $|1, -1\rangle$ angular-momentum state with translational momentum \mathbf{k} . Here we consider the case when \mathbf{k} is set to be close to the Weyl point with intersecting $J_z = 0$ and $J_z = -1$ branches. For the proposed ${}^3P_0 - {}^3D_1$ electronic levels in Sr, two intermediate states $|e\rangle, |e'\rangle$ could be used to create the Raman pulses, imparting a net momentum to the atoms proportional to $\mathbf{k} = \mathbf{k}_1 + \mathbf{k}_2 + \mathbf{k}_3$ (see Fig. 7.4 (a)). A possible excitation level scheme consists on using $5s6s {}^3S_1$ and $5s6p {}^3P_1$ as the intermediate $|e\rangle$ and $|e'\rangle$ levels respectively. After a waiting time t , another pulse is applied to measure the fraction of particles in the $J_z = 0$ angular-momentum state. Because of the interference of the two branches, this fraction oscillates with the frequency

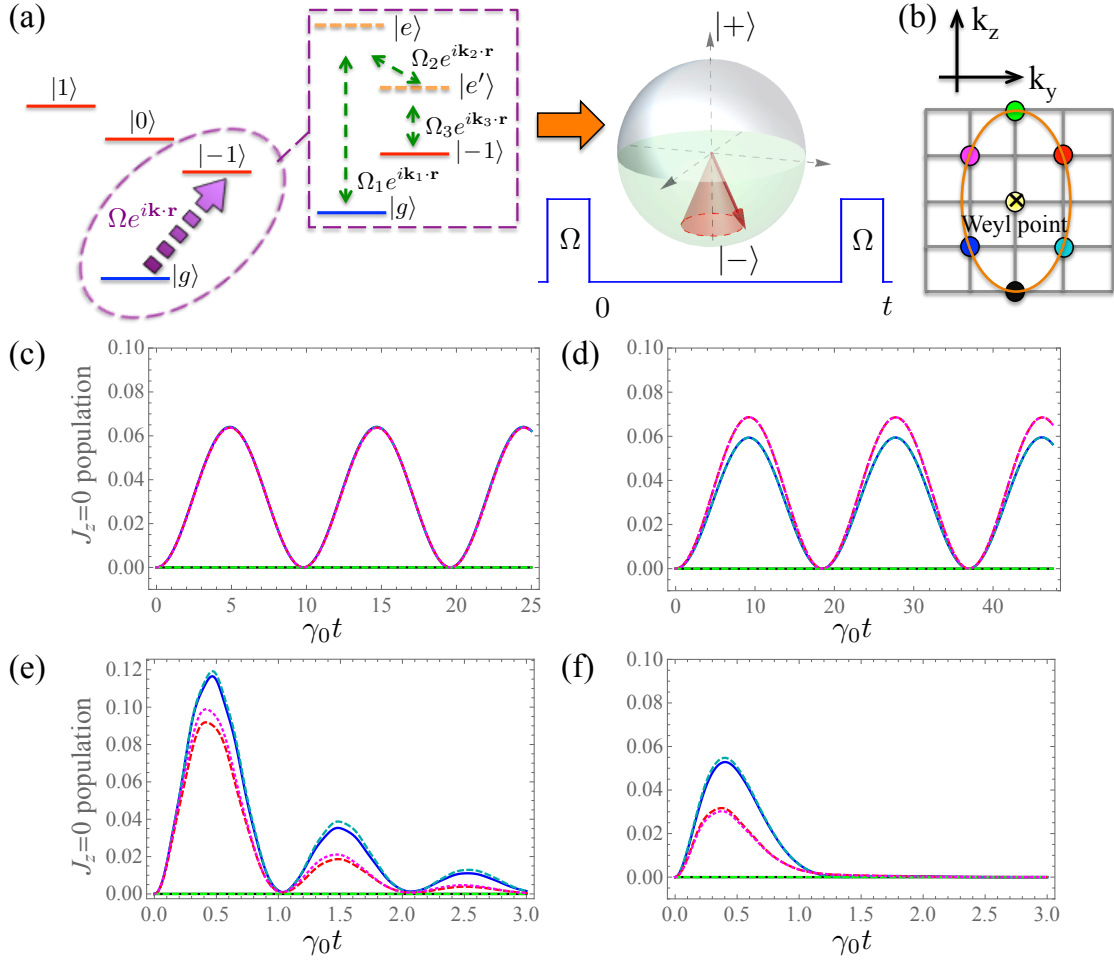


Figure 7.4: Observation of Weyl quasiparticles. (a) Momentum-selective Ramsey spectroscopy: interfering Raman beams create an excitation with the angular momentum projection $J_z = -1$ and with translational momentum \mathbf{k} near the Weyl node (see text). After a waiting time t the second pulse is applied to measure the fraction of particles in the $J_z = 0$ angular-momentum state. (b) Six quasimomenta near the Weyl node. (c) The fraction of particles in the $J_z = 0$ state oscillates as a function of time t with the frequency $(E_{\mathbf{k}}^1 - E_{\mathbf{k}}^2)/(2\pi)$, where $E_{\mathbf{k}}^1 - E_{\mathbf{k}}^2$ is the energy splitting between the two branches of the quasiparticle dispersion. (d) The oscillations in the presence of dissipation for $k_0 a \sim 0.5$. (e) The oscillations in a 99% randomly filled lattice. (f) The oscillations in a 93% filled lattice. For (c) and (d) a 3D cubic lattice of $100 \times 100 \times 100$ sites was used and we took advantage of the translational symmetry. For (e) and (f) a 3D cubic lattice of $10 \times 10 \times 10$ was used.

$(E_{\mathbf{k}}^1 - E_{\mathbf{k}}^2)/(2\pi)$, where the energy splitting $E_{\mathbf{k}}^1 - E_{\mathbf{k}}^2$ between the two branches is linear in \mathbf{k} and vanishes near the Weyl node.

Another signature of the Weyl node is the strong dependency of the amplitude of such oscillations on momentum \mathbf{k} near the node, as the amplitude is determined by the projection of

the Bloch vector on \hat{k}_z (the magnetic field direction).

In Fig. 7.4 (c-f) we show the fraction of particles in the $J_z = 0$ state as a function of time at the end of the above described Ramsey protocol, for the six different quasi-momenta in the $k_z - k_y$ plane near the Weyl point indicated in Fig. 7.4 (b). Panel (c) shows the dynamics for an ideal unit filled lattice in the dissipationless limit $k_0 a \ll 1$. Panel (d) shows the dynamics in the presence of dissipation for the experimentally relevant scenario discussed above. The population dynamics in disordered systems is shown in panels (e) and (f) for 99% and 93% filled lattices respectively. Quasiparticles scattering on empty sites in a disordered system leads to the decay of the oscillations.

7.7 Conclusion

We demonstrated that Weyl quasiparticles generically emerge in 3D systems of polar particles in magnetic field. This opens intriguing prospects of observing chiral anomaly, non-local electrodynamics, non-Anderson disorder-driven transitions, and other fascinating phenomena in the realm of fully controllable atomic systems. We showed that observing Weyl excitations is currently possible in arrays of AEA in 3D lattices, in particular, using the $^3P_0 - ^3D_1$ levels of bosonic Sr atoms. Other experimentally convenient schemes, that deserve further exploration, include using metastable levels of Sr or Yb atoms that can be trapped in magic lattices with spacings smaller than the wavelength [215] or arrays of polar molecules with the rotational levels dressed to avoid the splitting of $J = 1$ levels in the presence of hyperfine interactions [278]. The long lifetimes and the topological character of Weyl excitations in interacting dipolar systems also open new possibilities for implementing optical-lattice clocks with sensing capabilities beyond those of non-interacting systems.

Bibliography

- [1] K. Afrousheh, P. Bohlouli-Zanjani, D. Vagale, A. Mugford, M. Fedorov, and J. D. D. Martin. Spectroscopic observation of resonant electric dipole-dipole interactions between cold rydberg atoms. Phys. Rev. Lett., 93:233001, 2004.
- [2] Tomoya Akatsuka, Masao Takamoto, and Hidetoshi Katori. Optical lattice clocks with non-interacting bosons and fermions. Nature, 4:954–959, 2008.
- [3] V. Ameri, M. Eghbali-Arani, A. Mari, A. Farace, F. Kheirandish, V. Giovannetti, and R. Fazio. Mutual information as an order parameter for quantum synchronization. Phys. Rev. A, 91:012301, Jan 2015.
- [4] Brandon M. Anderson, Gediminas Juzeliūnas, Victor M. Galitski, and I. B. Spielman. Synthetic 3D spin-orbit coupling. Phys. Rev. Lett., 108:235301, 2012.
- [5] W. R. Anderson, J. R. Veale, and T. F. Gallagher. Resonant dipole-dipole energy transfer in a nearly frozen rydberg gas. Phys. Rev. Lett., 80:249–252, 1998.
- [6] P. F. Aramendia et al. The photophysics of merocyanine 540. A comparative study in ethanol and in liposomes. Photochem. Photobiol., 48:187, 1988.
- [7] Michelle O. Araújo, Ivor Krešić, Robin Kaiser, and William Guerin. Superradiance in a large and dilute cloud of cold atoms in the linear-optics regime. Phys. Rev. Lett., 117:073002, Aug 2016.
- [8] Alex Arenas, Albert Diaz-Guilera, Jurgen Kurths, Yamir Moreno, and Changsong Zhou. Synchronization in complex networks. Physics Reports, 469(3):93–153, 2008.
- [9] Mahmood Bagheri, Menno Poot, Linran Fan, Florian Marquardt, and Hong X. Tang. Photonic cavity synchronization of nanomechanical oscillators. Phys. Rev. Lett., 111:213902, 2013.
- [10] Simon Baier, MJ Mark, Daniel Petter, Kiyotaka Aikawa, Lauriane Chomaz, Zi Cai, M Baranov, P Zoller, and F Ferlaino. Extended bose-hubbard models with ultracold magnetic atoms. Science, 352(6282):201–205, 2016.
- [11] Leon Balents. Spin liquids in frustrated magnets. Nature, 464(7286):199–208, 2010.
- [12] S. Balik, A. L. Win, M. D. Havey, I. M. Sokolov, and D. V. Kupriyanov. Near-resonance light scattering from a high-density ultracold atomic ^{87}rb gas. Phys. Rev. A, 87:053817, May 2013.

- [13] M. A. Baranov, Klaus Osterloh, and M. Lewenstein. Fractional quantum Hall states in ultracold rapidly rotating dipolar Fermi gases. Phys. Rev. Lett., 94:070404, Feb 2005.
- [14] MA Baranov, M Dalmonte, G Pupillo, and P Zoller. Condensed matter theory of dipolar quantum gases. Chemical Reviews, 112(9):5012–5061, 2012.
- [15] Sebastian Bartel and Andreas H. Hielscher. Monte carlo simulations of the diffuse backscattering mueller matrix for highly scattering media. Appl. Opt., 39(10):1580–1588, Apr 2000.
- [16] Stefan K. Baur and Erich J. Mueller. Two-body recombination in a quantum-mechanical lattice gas: Entropy generation and probing of short-range magnetic correlations. Phys. Rev. A, 82:023626, Aug 2010). (We note that in this reference there is a factor of 2 missing on the right hand side of Eq. (13).
- [17] H. V. Berlepsch et al. Structure of J-Aggregates of Pseudoisocyanine Dye in Aqueous Solution. J. Phys. Chem. B, 104:8792, 2000.
- [18] P. R. Berman. Resonant interaction between identical atoms including recoil. Phys. Rev. A, 55:4466–4476, Jun 1997.
- [19] Robert J Bettles, Simon A Gardiner, and Charles S Adams. Cooperative ordering in lattices of interacting two-level dipoles. Physical Review A, 92(6):063822, 2015.
- [20] Robert J Bettles, Jiří Minář, Igor Lesanovsky, Charles S Adams, and Beatriz Olmos. Topological properties of a dense atomic lattice gas. arXiv preprint arXiv:1703.03351, 2017.
- [21] T. Bienaimé, R. Bachelard, J. Chabé, M.T. Rouabah, L. Bellando, Ph.W. Courteille, N. Piovella, and R. Kaiser. Interplay between radiation pressure force and scattered light intensity in the cooperative scattering by cold atoms. Journal of Modern Optics, 61(1):18–24, 2014.
- [22] Tom Bienaimé, Nicola Piovella, and Robin Kaiser. Controlled dicke subradiance from a large cloud of two-level systems. Phys. Rev. Lett., 108:123602, Mar 2012.
- [23] M. Bishof, M. J. Martin, M. D. Swallows, C. Benko, Y. Lin, G. Quémener, A. M. Rey, and J. Ye. Inelastic collisions and density-dependent excitation suppression in a ^{87}Sr optical lattice clock. Phys. Rev. A, 84:052716, 2011.
- [24] Immanuel Bloch. Ultracold quantum gases in optical lattices. Nature Physics, 1(1):23–30, 2005.
- [25] Immanuel Bloch, Jean Dalibard, and Sylvain Nascimbène. Quantum simulations with ultracold quantum gases. Nature Physics, 8(4):267–276, 2012.
- [26] Immanuel Bloch, Jean Dalibard, and Wilhelm Zwerger. Many-body physics with ultracold gases. Rev. Mod. Phys., 80:885–964, Jul 2008.
- [27] B. J. Bloom, T. L. Nicholson, J. R. Williams, S. L. Campbell, M. Bishof, X. Zhang, W. Zhang, S. L. Bromley, and J. Ye. An optical lattice clock with accuracy and stability at the 10-18 level. Nature, 506:71, 2014.
- [28] S. De Boer and D. A. Wiersma. Dephasing-induced damping of superradiant emission in j-aggregates. Chemical Physics Letters, 165:45, 1990.

- [29] Justin G Bohnet, Zilong Chen, Joshua M Weiner, Dominic Meiser, Murray J Holland, and James K Thompson. A steady-state superradiant laser with less than one intracavity photon. Nature, 484(7392):78–81, 2012.
- [30] Justin G Bohnet, Zilong Chen, Joshua M Weiner, Dominic Meiser, Murray J Holland, and James K Thompson. A steady-state superradiant laser with less than one intracavity photon. Nature, 484(7392):78–81, 2012.
- [31] P. C. Bons, R. de Haas, D. de Jong, A. Groot, and P. van der Straten. Quantum enhancement of the index of refraction in a bose-einstein condensate. Phys. Rev. Lett., 116:173602, Apr 2016.
- [32] C. C. Bradley, C. A. Sackett, J. J. Tollett, and R. G. Hulet. Evidence of bose-einstein condensation in an atomic gas with attractive interactions. Phys. Rev. Lett., 75:1687–1690, Aug 1995.
- [33] Sarah L Bromley, Bihui Zhu, Michael Bishof, Xibo Zhang, Tobias Bothwell, Johannes Schachenmayer, Travis L Nicholson, Robin Kaiser, Susanne F Yelin, Mikhail D Lukin, et al. Collective atomic scattering and motional effects in a dense coherent medium. Nature communications, 7:11039, 2016.
- [34] Daniel WC Brooks, Thierry Botter, Sydney Schreppler, Thomas P Purdy, Nathan Brahms, and Dan M Stamper-Kurn. Non-classical light generated by quantum-noise-driven cavity optomechanics. Nature, 488(7412):476–480, 2012.
- [35] C. Brosseau. Fundamentals of polarized light: a statistical optics approach. Wiley-interscience publication. John Wiley, 1998.
- [36] W. Brown and K. Mortensen. Scattering in Polymeric and Colloidal Systems. Gordon and Breach, New York, 2000.
- [37] A. A. Burkov and Leon Balents. Weyl semimetal in a topological insulator multilayer. Phys. Rev. Lett., 107:127205, 2011.
- [38] SL Campbell, RB Hutson, GE Marti, A Goban, N Darkwah Oppong, RL McNally, L Sonderhouse, JM Robinson, W Zhang, BJ Bloom, et al. A fermi-degenerate three-dimensional optical lattice clock. arXiv preprint arXiv:1702.01210, 2017.
- [39] Howard Carmichael. An Open Systems Approach to Quantum Optics, Lectures Presented at the Université Libre de Bruxelles. Lecture Notes in Physics monographs. Springer, 1991.
- [40] Howard J Carmichael. Statistical methods in quantum optics, volume 2. Springer, 1999.
- [41] Lincoln D. Carr, David DeMille, Roman V. Krems, and Jun Ye. Cold and ultracold molecules: Science, technology and applications. New J. Phys., 11:055049, 2009.
- [42] Y Castin, H Wallis, and Jean Dalibard. Limit of doppler cooling. JOSA B, 6(11):2046–2057, 1989.
- [43] Yvan Castin and Klaus Mølmer. Maxwell-bloch equations: A unified view of nonlinear optics and nonlinear atom optics. Phys. Rev. A, 51:R3426–R3428, May 1995.

- [44] Julien Chabé, Mohamed-Taha Rouabah, Louis Bellando, Tom Bienaimé, Nicola Piovella, Romain Bachelard, and Robin Kaiser. Coherent and incoherent multiple scattering. Phys. Rev. A, 89:043833, Apr 2014.
- [45] D. E. Chang, Jun Ye, and M. D. Lukin. Controlling dipole-dipole frequency shifts in a lattice-based optical atomic clock. Phys. Rev. A, 69:023810, Feb 2004.
- [46] Marc Cheneau, Peter Barmettler, Dario Poletti, Manuel Endres, Peter Schauß, Takeshi Fukuhara, Christian Gross, Immanuel Bloch, Corinna Kollath, and Stefan Kuhr. Light-cone-like spreading of correlations in a quantum many-body system. Nature, 481(7382):484–487, 2012.
- [47] Lilian Childress. Diamond dynamics under control. Science, 345:1247, 2015.
- [48] L Chomaz, L Corman, T Yefsah, R Desbuquois, and J Dalibard. Absorption imaging of a quasi-two-dimensional gas: a multiple scattering analysis. New Journal of Physics, 14(5):055001, 2012.
- [49] Amodsen Chotia, Brian Neyenhuis, Steven A. Moses, Bo Yan, Jacob P. Covey, Michael Foss-Feig, Ana Maria Rey, Deborah S. Jin, and Jun Ye. Long-lived dipolar molecules and Feshbach molecules in a 3D optical lattice. Phys. Rev. Lett., 108:080405, Feb 2012.
- [50] Debanjan Chowdhury and M. C. Cross. Synchronization of oscillators with long-range power law interactions. Phys. Rev. E, 82:016205, Jul 2010.
- [51] J. I. Cirac, P. Zoller, H. J. Kimble, and H. Mabuchi. Quantum state transfer and entanglement distribution among distant nodes in a quantum network. Phys. Rev. Lett., 78:3221–3224, Apr 1997.
- [52] M. C. Cross. Improving the frequency precision of oscillators by synchronization. Phys. Rev. E, 85:046214, Apr 2012.
- [53] Hiroaki Daido. Lower critical dimension for populations of oscillators with randomly distributed frequencies: A renormalization-group analysis. Phys. Rev. Lett., 61:231–234, Jul 1988.
- [54] Borivoje Dakić, Yannick Ole Lipp, Xiaosong Ma, Martin Ringbauer, Sebastian Kropatschek, Stefanie Barz, Tomasz Paterek, Vlatko Vedral, Anton Zeilinger, Časlav Brukner, et al. Quantum discord as resource for remote state preparation. Nature Physics, 8(9):666–670, 2012.
- [55] A J Daley, C Kollath, U Schollwöck, and G Vidal. Time-dependent density-matrix renormalization-group using adaptive effective hilbert spaces. J. Stat. Mech. Theor. Exp., page P04005, 2004.
- [56] Emanuele G. Dalla Torre, Johannes Otterbach, Eugene Demler, Vladan Vuletic, and Mikhail D. Lukin. Dissipative preparation of spin squeezed atomic ensembles in a steady state. Phys. Rev. Lett., 110:120402, Mar 2013.
- [57] François Damanet, Daniel Braun, and John Martin. Master equation for collective spontaneous emission with quantized atomic motion. Phys. Rev. A, 93:022124, Feb 2016.

- [58] K. B. Davis, M. O. Mewes, M. R. Andrews, N. J. van Druten, D. S. Durfee, D. M. Kurn, and W. Ketterle. Bose-einstein condensation in a gas of sodium atoms. Phys. Rev. Lett., 75:3969–3973, Nov 1995.
- [59] MHG De Miranda, A Chotia, B Neyenhuis, D Wang, G Quéméner, S Ospelkaus, JL Bohn, J Ye, and D. S. Jin. Controlling the quantum stereodynamics of ultracold bimolecular reactions. Nature Phys., 7(6):502–507, 2011.
- [60] MHG de Miranda, A. Chotia, B. Neyenhuis, D. Wang, G. Quéméner, S. Ospelkaus, JL Bohn, J. Ye, and DS Jin. Controlling the quantum stereodynamics of ultracold bimolecular reactions. Nature Physics, 7(6):502–507, 2011.
- [61] Aurelie De Paz, Arijit Sharma, Amodsen Chotia, Etienne Marechal, JH Huckans, Paolo Pedri, Luis Santos, Olivier Gorceix, Laurent Vernac, and Bruno Laburthe-Tolra. Nonequilibrium quantum magnetism in a dipolar lattice gas. Physical review letters, 111(18):185305, 2013.
- [62] Hugues De Riedmatten, Mikael Afzelius, Matthias U Staudt, Christoph Simon, and Nicolas Gisin. A solid-state light–matter interface at the single-photon level. Nature, 456(7223):773–777, 2008.
- [63] Pedro de Vries, David V. van Coevorden, and Ad Lagendijk. Point scatterers for classical waves. Rev. Mod. Phys., 70:447–466, Apr 1998.
- [64] B. DeMarco, J. L. Bohn, J. P. Burke, M. Holland, and D. S. Jin. Measurement of p -wave threshold law using evaporatively cooled fermionic atoms. Phys. Rev. Lett., 82:4208–4211, May 1999.
- [65] B. DeMarco and DS Jin. Onset of fermi degeneracy in a trapped atomic gas. Science, 285(5434):1703–1706, 1999.
- [66] D. DeMille. Quantum computation with trapped polar molecules. Phys. Rev. Lett., 88:067901, Jan 2002.
- [67] RH Dicke. Coherence in spontaneous radiation processes. Physical Review, 93(1):99, 1954.
- [68] H. P. Dorn and A. Muller. Temperature dependence of the fluorescence lifetime and quantum yield of pseudoisocyanine monomers. Chem. Phys. Lett., 130:426, 1986.
- [69] James S Douglas, H Habibian, C-L Hung, AV Gorshkov, H Jeff Kimble, and Darrick E Chang. Quantum many-body models with cold atoms coupled to photonic crystals. Nature Photonics, 9(5):326–331, 2015.
- [70] Tena Dubček, Colin J. Kennedy, Ling Lu, Wolfgang Ketterle, Marin Soljačić, and Hrvoje Buljan. Weyl points in three-dimensional optical lattices: Synthetic magnetic monopoles in momentum space. Phys. Rev. Lett., 114:225301, 2015.
- [71] M. J. Duer. Solid-State NMR Spectroscopy Principles and Applications. Vol I. Blackwell Science, 2002.
- [72] R. Dum, A. S. Parkins, P. Zoller, and C. W. Gardiner. Monte Carlo simulation of master equations in quantum optics for vacuum, thermal, and squeezed reservoirs. Phys. Rev. A, 46(7):4382–4396, October 1992.

- [73] A Einstein and WJ De Haas. Experimenteller nachweis der ampereschen molekularströme., Deutsche Physikalische Gesellschaft, Verhandlungen, 17:152–170, 1915.
- [74] Manuel Endres, Hannes Bernien, Alexander Keesling, Harry Levine, Eric R. Anschuetz, Alexandre Krajenbrink, Crystal Senko, Vladan Vuletic, Markus Greiner, and Mikhail D. Lukin. Atom-by-atom assembly of defect-free one-dimensional cold atom arrays. Science, 354(6315):1024–1027, 2016.
- [75] Henk Fidder, Jasper Knoester, and Douwe A. Wiersma. Optical properties of disordered molecular aggregates: A numerical study. The Journal of Chemical Physics, 95(11):7880–7890, 1991.
- [76] M. C. Fischer, B. Gutiérrez-Medina, and M. G. Raizen. Observation of the quantum zeno and anti-zeno effects in an unstable system. Phys. Rev. Lett., 87:040402, Jul 2001.
- [77] M. Foss-Feig, A. J. Daley, J. K. Thompson, and A. M. Rey. Steady-state many-body entanglement of hot reactive fermions. Phys. Rev. Lett., 109:230501, 2012.
- [78] E. Fradkin. Critical behavior of disordered degenerate semiconductors. I. models, symmetries, and formalism. Phys. Rev. B, 33:3257, 1986.
- [79] R. Friedberg, S.R. Hartmann, and J.T. Manassah. Limited superradiant damping of small samples. Physics Letters A, 40(5):365 – 366, 1972.
- [80] R. Friedberg, S.R. Hartmann, and J.T. Manassah. Frequency shifts in emission and absorption by resonant systems of two-level atoms. Physics Reports, 7(3):101 – 179, 1973.
- [81] Sriram Ganeshan and S. Das Sarma. Constructing a Weyl semimetal by stacking one-dimensional topological phases. Phys. Rev. B, 91:125438, 2015.
- [82] Juan José García-Ripoll, S Dürr, N Syassen, DM Bauer, M Lettner, G Rempe, and JI Cirac. Dissipation-induced hard-core boson gas in an optical lattice. New J. Phys., 11(1):013053, 2009.
- [83] Nathan Gemelke, Xibo Zhang, Chen-Lung Hung, and Cheng Chin. In situ observation of incompressible mott-insulating domains in ultracold atomic gases. Nature, 460(7258):995–998, 2009.
- [84] G. L. Giorgi, F. Plastina, G. Francica, and R. Zambrini. Spontaneous synchronization and quantum correlation dynamics of open spin systems. Phys. Rev. A, 88:042115, 2013.
- [85] Gian Luca Giorgi, Fernando Galve, Gonzalo Manzano, Pere Colet, and Roberta Zambrini. Quantum correlations and mutual synchronization. Phys. Rev. A, 85:052101, 2012.
- [86] A. Goban, C.-L. Hung, J. D. Hood, S.-P. Yu, J. A. Muniz, O. Painter, and H. J. Kimble. Superradiance for atoms trapped along a photonic crystal waveguide. Phys. Rev. Lett., 115:063601, Aug 2015.
- [87] Malkhaz R. Gochitashvili, Roman Ya. Kezerashvili, and Ramaz A. Lomsadze. Excitation of meinel and the first negative band system at the collision of electrons and protons with the nitrogen molecule. Phys. Rev. A, 82:022702, Aug 2010.

- [88] E. A. Goldschmidt, T. Boulier, R. C. Brown, S. B. Koller, J. T. Young, A. V. Gorshkov, S. L. Rolston, and J. V. Porto. Anomalous broadening in driven dissipative rydberg systems. Phys. Rev. Lett., 116:113001, Mar 2016.
- [89] Ming Gong, Sumanta Tewari, and Chuanwei Zhang. Bcs-bec crossover and topological phase transition in 3d spin-orbit coupled degenerate fermi gases. Phys. Rev. Lett., 107(19):195303, 2011.
- [90] AV Gorshkov, M Hermele, V Gurarie, C Xu, PS Julienne, J Ye, P Zoller, E Demler, MD Lukin, and AM Rey. Two-orbital SU (N) magnetism with ultracold alkaline-earth atoms. Nature Phys., 6(4):289–295, 2010.
- [91] Pallab Goswami and Sudip Chakravarty. Quantum criticality between topological and band insulators in 3+1 dimensions. Phys. Rev. Lett., 107:196803, 2011.
- [92] Daniel Greif, Thomas Uehlinger, Gregor Jotzu, Leticia Tarruell, and Tilman Esslinger. Short-range quantum magnetism of ultracold fermions in an optical lattice. Science, 340(6138):1307–1310, 2013.
- [93] Markus Greiner, Olaf Mandel, Tilman Esslinger, Theodor W Hänsch, and Immanuel Bloch. Quantum phase transition from a superfluid to a mott insulator in a gas of ultracold atoms. nature, 415(6867):39–44, 2002.
- [94] Michel Gross and Serge Haroche. Superradiance: an essay on the theory of collective spontaneous emission. Physics Reports, 93(5):301–396, 1982.
- [95] William Guerin, Michelle O. Araújo, and Robin Kaiser. Subradiance in a large cloud of cold atoms. Phys. Rev. Lett., 116:083601, Feb 2016.
- [96] Fritz Haake, Mikhail I. Kolobov, Claude Fabre, Elisabeth Giacobino, and Serge Reynaud. Superradiant laser. Phys. Rev. Lett., 71:995–998, Aug 1993.
- [97] Fritz Haake, Mikhail I. Kolobov, Carsten Seeger, Claude Fabre, Elisabeth Giacobino, and Serge Reynaud. Quantum noise reduction in stationary superradiance. Phys. Rev. A, 54:1625–1637, Aug 1996.
- [98] Klemens Hammerer, Anders S. Sørensen, and Eugene S. Polzik. Quantum interface between light and atomic ensembles. Rev. Mod. Phys., 82:1041–1093, Apr 2010.
- [99] Y.-J. Han, Y.-H. Chan, W. Yi, A. J. Daley, S. Diehl, P. Zoller, and L.-M. Duan. Stabilization of the p -wave superfluid state in an optical lattice. Phys. Rev. Lett., 103:070404, Aug 2009.
- [100] Kaden R A Hazzard, Salvatore R Manmana, Michael Foss-Feig, and Ana Maria Rey. Far-from-equilibrium quantum magnetism with ultracold polar molecules. Phys. Rev. Lett., 110(7):075301, 2013.
- [101] Kathrin Henschel, Johannes Majer, Jörg Schmiedmayer, and Helmut Ritsch. Cavity qed with an ultracold ensemble on a chip: Prospects for strong magnetic coupling at finite temperatures. Phys. Rev. A, 82:033810, Sep 2010.
- [102] M. J. Holland, B. DeMarco, and D. S. Jin. Evaporative cooling of a two-component degenerate fermi gas. Phys. Rev. A, 61:053610, Apr 2000.

- [103] J.W. Hovenier, C.V.M. Mee, and H. Domke. Transfer of Polarized Light in Planetary Atmospheres: Basic Concepts and Practical Methods. Astrophysics and Space Science Library. Springer, 2004.
- [104] Kerson Huang and C. N. Yang. Quantum-mechanical many-body problem with hard-sphere interaction. Phys. Rev., 105:767–775, Feb 1957.
- [105] Chen-Lung Hung, Xibo Zhang, Nathan Gemelke, and Cheng Chin. Accelerating evaporative cooling of atoms into bose-einstein condensation in optical traps. Physical Review A, 78(1):011604, 2008.
- [106] Michael R. Hush, Weibin Li, Sam Genway, Igor Lesanovsky, and Andrew D. Armour. Spin correlations as a probe of quantum synchronization in trapped-ion phonon lasers. Phys. Rev. A, 91:061401, Jun 2015.
- [107] Philipp Hyllus, Wiesław Laskowski, Roland Krischek, Christian Schwemmer, Witlef Wieczorek, Harald Weinfurter, Luca Pezzé, and Augusto Smerzi. Fisher information and multi-particle entanglement. Phys. Rev. A, 85:022321, Feb 2012.
- [108] Tetsuya Ido, Thomas H. Loftus, Martin M. Boyd, Andrew D. Ludlow, Kevin W. Holman, and Jun Ye. Precision spectroscopy and density-dependent frequency shifts in ultracold Sr. Phys. Rev. Lett., 94:153001, Apr 2005.
- [109] Wayne M. Itano, D. J. Heinzen, J. J. Bollinger, and D. J. Wineland. Quantum Zeno effect. Phys. Rev. A, 41:2295–2300, Mar 1990.
- [110] Daniel F. V. James. Frequency shifts in spontaneous emission from two interacting atoms. Phys. Rev. A, 47:1336–1346, Feb 1993.
- [111] Juha Javanainen and Janne Ruostekoski. Light propagation beyond the mean-field theory of standard optics. Optics Express, 24(2):993–1001, 2016.
- [112] Juha Javanainen, Janne Ruostekoski, Yi Li, and Sung-Mi Yoo. Shifts of a resonance line in a dense atomic sample. Phys. Rev. Lett., 112:113603, Mar 2014.
- [113] Juha Javanainen, Janne Ruostekoski, Bjarne Vestergaard, and Matthew R. Francis. One-dimensional modeling of light propagation in dense and degenerate samples. Phys. Rev. A, 59:649–666, Jan 1999.
- [114] S. D. Jenkins, J. Ruostekoski, J. Javanainen, R. Bourgain, S. Jennewein, Y. R. P. Sortais, and A. Browaeys. Optical resonance shifts in the fluorescence of thermal and cold atomic gases. Phys. Rev. Lett., 116:183601, May 2016.
- [115] S. Jennewein, M. Besbes, N. J. Schilder, S. D. Jenkins, C. Sauvan, J. Ruostekoski, J.-J. Greffet, Y. R. P. Sortais, and A. Browaeys. Coherent scattering of near-resonant light by a dense microscopic cold atomic cloud. Phys. Rev. Lett., 116:233601, Jun 2016.
- [116] S. Jennewein, Y. R. P. Sortais, J.-J. Greffet, and A. Browaeys. Propagation of light through small clouds of cold interacting atoms. Phys. Rev. A, 94:053828, Nov 2016.
- [117] Jian-Hua Jiang. Tunable topological Weyl semimetal from simple-cubic lattices with staggered fluxes. Phys. Rev. A, 85:033640, 2012.

- [118] Gregor Jotzu, Michael Messer, Rémi Desbuquois, Martin Lebrat, Thomas Uehlinger, Daniel Greif, and Tilman Esslinger. Experimental realization of the topological haldane model with ultracold fermions. Nature, 515(7526):237–240, 2014.
- [119] K. Kanjilal and D. Blume. Nondivergent pseudopotential treatment of spin-polarized fermions under one- and three-dimensional harmonic confinement. Phys. Rev. A, 70:042709, Oct 2004.
- [120] N. Kato et al. Determination of a merocyanine J-aggregate structure and the significant contribution of the electric dipole interaction to the exciton band wavelength. Phys. Rev. Lett., 94:136404, 2005.
- [121] A. M. Kaufman, B. J. Lester, C. M. Reynolds, M. L. Wall, M. Foss-Feig, K. R. A. Hazzard, A. M. Rey, and C. A. Regal. Two-particle quantum interference in tunnel-coupled optical tweezers. Science, 345(6194):306–309, 2014.
- [122] J. Keaveney, A. Sargsyan, U. Krohn, I. G. Hughes, D. Sarkisyan, and C. S. Adams. Cooperative lamb shift in an atomic vapor layer of nanometer thickness. Phys. Rev. Lett., 108:173601, 2012.
- [123] W. Ketterle and N.J.V. Druten. Evaporative cooling of trapped atoms. Advances in atomic, molecular, and optical physics, 37:181–236, 1996.
- [124] H Jeff Kimble. The quantum internet. Nature, 453(7198):1023–1030, 2008.
- [125] Koji Kobayashi, Tomi Ohtsuki, Ken-Ichiro Imura, and Igor F. Herbut. Density of states scaling at the semimetal to metal transition in three dimensional topological insulators. Phys. Rev. Lett., 112:016402, 2014.
- [126] Michael Köhl, Henning Moritz, Thilo Stöferle, Kenneth Günter, and Tilman Esslinger. Fermionic atoms in a three dimensional optical lattice: Observing Fermi surfaces, dynamics, and interactions. Phys. Rev. Lett., 94:080403, Mar 2005.
- [127] G Kranzelbinder and G Leising. Organic solid-state lasers. Rep. Prog. Phys., 63:729, 2000.
- [128] Ryogo Kubo. Generalized cumulant expansion method. Journal of the Physical Society of Japan, 17(7):1100–1120, 1962.
- [129] Kevin A. Kuns, Ana Maria Rey, and Alexey V. Gorshkov. d -wave superfluidity in optical lattices of ultracold polar molecules. Phys. Rev. A, 84:063639, Dec 2011.
- [130] Yoshiki Kuramoto. Chemical oscillations, waves, and turbulence. Courier Dover Publications, 2003.
- [131] G. Labeyrie, F. de Tomasi, J.-C. Bernard, C. A. Müller, C. Miniatura, and R. Kaiser. Coherent backscattering of light by cold atoms. Phys. Rev. Lett., 83:5266–5269, Dec 1999.
- [132] G. Labeyrie, D. Delande, R. Kaiser, and C. Miniatura. Light transport in cold atoms and thermal decoherence. Phys. Rev. Lett., 97:013004, Jul 2006.
- [133] G. Labeyrie, D. Delande, C.A. Mller, C. Miniatura, and R. Kaiser. Multiple scattering of light in a resonant medium. Optics Communications, 243(16):157 – 164, 2004. Ultra Cold Atoms and Degenerate Quantum Gases.

- [134] Guillaume Labeyrie, Dominique Delande, Cord A. Müller, Christian Miniatura, and Robin Kaiser. Coherent backscattering of light by an inhomogeneous cloud of cold atoms. Phys. Rev. A, 67:033814, Mar 2003.
- [135] Ad Lagendijk and Bart A Van Tiggelen. Resonant multiple scattering of light. Physics Reports, 270(3):143–215, 1996.
- [136] T. Lahaye, C. Menotti, L. Santos, M. Lewenstein, and T. Pfau. The physics of dipolar bosonic quantum gases. Rep. Prog. Phys., 72(12):126401, 2009.
- [137] Juan Francisco Lam and Paul R. Berman. Effect of recoil in resonance fluorescence. Phys. Rev. A, 14:1683–1688, Nov 1976.
- [138] Giacomo Lamporesi, Simone Donadello, Simone Serafini, Franco Dalfovo, and Gabriele Ferrari. Spontaneous creation of kibble-zurek solitons in a bose-einstein condensate. Nature Physics, 9(10):656–660, 2013.
- [139] Z. Lan, N. Goldman, A. Bermudez, W. Lu, and P. Öhberg. Dirac-Weyl fermions with arbitrary spin in two-dimensional optical superlattices. Phys. Rev. B, 84:165115, 2011.
- [140] Tony E. Lee, Ching-Kit Chan, and Shenshen Wang. Entanglement tongue and quantum synchronization of disordered oscillators. Phys. Rev. E, 89:022913, 2014.
- [141] Tony E. Lee and H. R. Sadeghpour. Quantum synchronization of quantum van der pol oscillators with trapped ions. Phys. Rev. Lett., 111:234101, 2013.
- [142] R. H. Lehmburg. Radiation from an n -atom system. i. general formalism. Phys. Rev. A, 2:883–888, Sep 1970.
- [143] Maciej Lewenstein, Anna Sanpera, Veronica Ahufinger, Bogdan Damski, Aditi Sen(De), and Ujjwal Sen. Ultracold atomic gases in optical lattices: mimicking condensed matter physics and beyond. Advances in Physics, 56(2):243–379, 2007.
- [144] Qiong Li, DZ Xu, CY Cai, and CP Sun. Recoil effects of a motional scatterer on single-photon scattering in one dimension. Scientific reports, 3:3144, 2013.
- [145] Qun Li and Daniela Rus. Global clock synchronization in sensor networks. Computers, IEEE Transactions on, 55(2):214–226, 2006.
- [146] Z. Li, S. V. Alyabyshev, and R. V. Krems. Ultracold inelastic collisions in two dimensions. Phys. Rev. Lett., 100:073202, Feb 2008.
- [147] Elliott H Lieb and Derek W Robinson. The finite group velocity of quantum spin systems. In Statistical Mechanics, pages 425–431. Springer, 1972.
- [148] Y Lin, JP Gaebler, F Reiter, TR Tan, R Bowler, AS Sørensen, D Leibfried, and DJ Wineland. Dissipative production of a maximally entangled steady state of two quantum bits. Nature, 504(7480):415–418, 2013.
- [149] Ch. Lisdat, J. S. R. Vellore Winfred, T. Middelmann, F. Riehle, and U. Sterr. Collisional losses, decoherence, and frequency shifts in optical lattice clocks with bosons. Phys. Rev. Lett., 103:090801, 2009.

- [150] Bo Liu, Xiaopeng Li, Lan Yin, and W. Vincent Liu. Weyl superfluidity in a three-dimensional dipolar Fermi gas. *Phys. Rev. Lett.*, 114:045302, 2015.
- [151] Ling Lu, Zhiyu Wang, Dexin Ye, Lixin Ran, Liang Fu, John D. Joannopoulos, and Marin Soljačić. Experimental observation of Weyl points. *Science*, 349:622, 2015.
- [152] A. D. Ludlow, N. D. Lemke, J. A. Sherman, C. W. Oates, G. Quéméner, J. von Stecher, and A. M. Rey. Cold-collision-shift cancellation and inelastic scattering in a yb optical lattice clock. *Phys. Rev. A*, 84:052724, 2011.
- [153] Andrew D. Ludlow, Martin M. Boyd, Jun Ye, E. Peik, and P. O. Schmidt. Optical atomic clocks. *Rev. Mod. Phys.*, 87:637–701, Jun 2015.
- [154] Max Ludwig and Florian Marquardt. Quantum many-body dynamics in optomechanical arrays. *Phys. Rev. Lett.*, 111:073603, 2013.
- [155] O. J. Luiten, M. W. Reynolds, and J. T. M. Walraven. Kinetic theory of the evaporative cooling of a trapped gas. *Phys. Rev. A*, 53:381–389, Jan 1996.
- [156] B. Q. Lv, H. M. Weng, B. B. Fu, X. P. Wang, H. Miao, J. Ma, P. Richard, X. C. Huang, L. X. Zhao, G. F. Chen, Z. Fang, X. Dai, T. Qian, and H. Ding. Experimental discovery of Weyl semimetal TaAs. *Phys. Rev. X*, 5:031013, 2015.
- [157] Jian Ma, Xiaoguang Wang, C.P. Sun, and Franco Nori. Quantum spin squeezing. *Physics Reports*, 509(23):89 – 165, 2011.
- [158] Thomas Maier, Sebastian Kraemer, Laurin Ostermann, and Helmut Ritsch. A superradiant clock laser on a magic wavelength optical lattice. *Opt. Express*, 22(11):13269–13279, Jun 2014.
- [159] Gonzalo Manzano, Fernando Galve, Gian Luca Giorgi, Emilio Hernandez-Garcia, and Roberta Zambrini. Synchronization, quantum correlations and entanglement in oscillator networks. *Sci. Rep.*, 3:1439, 2013.
- [160] A. Mari, A. Farace, N. Didier, V. Giovannetti, and R. Fazio. Measures of quantum synchronization in continuous variable systems. *Phys. Rev. Lett.*, 111:103605, Sep 2013.
- [161] M. J. Mark, E. Haller, K. Lauber, J. G. Danzl, A. J. Daley, and H.-C. Nägerl. Precision measurements on a tunable mott insulator of ultracold atoms. *Phys. Rev. Lett.*, 107:175301, Oct 2011.
- [162] M. J. Martin, M. Bishof, M. D. Swallows, X. Zhang, C. Benko, J. von Stecher, A. V. Gorshkov, A. M. Rey, and Jun Ye. A quantum many-body spin system in an optical lattice clock. *Science*, 341(6146):632–636, 2013.
- [163] Matthew H. Matheny, Matt Grau, Luis G. Villanueva, Rassul B. Karabalin, M. C. Cross, and Michael L. Roukes. Phase synchronization of two anharmonic nanomechanical oscillators. *Phys. Rev. Lett.*, 112:014101, 2014.
- [164] Jason McKeever, Andreea Boca, A David Boozer, Joseph R Buck, and H Jeff Kimble. Experimental realization of a one-atom laser in the regime of strong coupling. *Nature*, 425(6955):268–271, 2003.

- [165] Z. Meir, O. Schwartz, E. Shahmoon, D. Oron, and R. Ozeri. Cooperative lamb shift in a mesoscopic atomic array. Phys. Rev. Lett., 113:193002, 2014.
- [166] D. Meiser and M. J. Holland. Steady-state superradiance with alkaline-earth-metal atoms. Phys. Rev. A, 81:033847, Mar 2010.
- [167] D. Meiser, Jun Ye, D. R. Carlson, and M. J. Holland. Prospects for a millihertz-linewidth laser. Phys. Rev. Lett., 102:163601, Apr 2009.
- [168] Andrea Micheli, GK Brennen, and Peter Zoller. A toolbox for lattice-spin models with polar molecules. Nature Physics, 2(5):341–347, 2006.
- [169] Yevhen Miroshnychenko, Uffe V. Poulsen, and Klaus Mølmer. Directional emission of single photons from small atomic samples. Phys. Rev. A, 87:023821, Feb 2013.
- [170] B. Misra and E. C. G Sudarshan. The Zeno’s paradox in quantum theory. J. Math. Phys., 18:756–763, 1977.
- [171] Kavan Modi, Aharon Brodutch, Hugo Cable, Tomasz Paterek, and Vlatko Vedral. The classical-quantum boundary for correlations: Discord and related measures. Rev. Mod. Phys., 84:1655–1707, Nov 2012.
- [172] Klaus Mølmer, Yvan Castin, and Jean Dalibard. Monte Carlo wave-function method in quantum optics. J. Opt. Soc. Am. B, 10(3):524–538, 1993.
- [173] C. R. Monroe, E. A. Cornell, C. A. Sackett, C. J. Myatt, and C. E. Wieman. Measurement of cs-cs elastic scattering at $T = 30 \mu\text{k}$. Phys. Rev. Lett., 70:414–417, Jan 1993.
- [174] Eun-Gook Moon and Yong Baek Kim. Non-Fermi liquid in Dirac semi-metals, 2014. arXiv:1409.0573.
- [175] Olivier Morice, Yvan Castin, and Jean Dalibard. Refractive index of a dilute bose gas. Phys. Rev. A, 51:3896–3901, May 1995.
- [176] Rahul Nandkishore and David A Huse. Many-body localization and thermalization in quantum statistical mechanics. Annu. Rev. Condens. Matter Phys., 6(1):15–38, 2015.
- [177] Nir Navon, Alexander L Gaunt, Robert P Smith, and Zoran Hadzibabic. Critical dynamics of spontaneous symmetry breaking in a homogeneous bose gas. Science, 347(6218):167–170, 2015.
- [178] B. Neyenhuis, B. Yan, S. A. Moses, J. P. Covey, A. Chotia, A. Petrov, S. Kotochigova, J. Ye, and D. S. Jin. Anisotropic polarizability of ultracold polar KRb molecules. Phys. Rev. Lett., 109(23):230403, DEC 4 2012.
- [179] K.-K. Ni, S. Ospelkaus, M. H. G. de Miranda, A. Pe’er, B. Neyenhuis, J. J. Zirbel, S. Kotochigova, P. S. Julienne, D. S. Jin, and J. Ye. A high phase-space-density gas of polar molecules. Science, 322(5899):231–235, OCT 10 2008.
- [180] K-K Ni, S Ospelkaus, D Wang, G Quéméner, B Neyenhuis, MHG De Miranda, JL Bohn, J Ye, and D. S. Jin. Dipolar collisions of polar molecules in the quantum regime. Nature, 464(7293):1324–1328, 2010.

- [181] H. B. Nielsen and M. Ninomiya. Absence of neutrinos on a lattice (I). Proof by homotopy theory. Nucl. Phys. B, 185:20, 1981.
- [182] Matthew A Norcia, Matthew N Winchester, Julia RK Cline, and James K Thompson. Superradiance on the millihertz linewidth strontium clock transition. Science advances, 2(10):e1601231, 2016.
- [183] K. S. Novoselov, A. K. Geim, S. V. Morozov, D. Jiang, Y. Zhang, S. V. Dubonos, I. V. Grigorieva, and A. A. Firsov. Electric field effect in atomically thin carbon films. Science, 306(5696):666–669, 2004.
- [184] D. O’Dell, S. Giovanazzi, G. Kurizki, and V. M. Akulin. Bose-einstein condensates with $1/r$ interatomic attraction: Electromagnetically induced “gravity”. Phys. Rev. Lett., 84:5687–5690, Jun 2000.
- [185] RG Olave, AL Win, K Kemp, SJ Roof, S Balik, MD Havey, IM Sokolov, and DV Kupriyanov. Optical manipulation of light scattering in cold atomic rubidium. From Atomic to Mesoscale: The Role of Quantum Coherence in Systems of Various Complexities. Edited by S. A. Malinovskaya and I. Novikova. Published by World Scientific Publishing Co. Pte. Ltd., 2015. ISBN# 9789814678704, pp. 39–59, 1:39–59, 2015.
- [186] Harold Ollivier and Wojciech H. Zurek. Quantum discord: A measure of the quantumness of correlations. Phys. Rev. Lett., 88:017901, 2001.
- [187] B. Olmos, D. Yu, Y. Singh, F. Schreck, K. Bongs, and I. Lesanovsky. Long-range interacting many-body systems with alkaline-earth-metal atoms. Phys. Rev. Lett., 110:143602, 2013.
- [188] S Ospelkaus, K-K Ni, D Wang, MHG De Miranda, B Neyenhuis, G Quéméner, PS Julienne, JL Bohn, D. S. Jin, and J Ye. Quantum-state controlled chemical reactions of ultracold potassium-rubidium molecules. Science, 327(5967):853–857, 2010.
- [189] S. Ospelkaus, K.K. Ni, MHG De Miranda, B. Neyenhuis, D. Wang, S. Kotochigova, PS Julienne, DS Jin, and J. Ye. Ultracold polar molecules near quantum degeneracy. Faraday Discussions, 142:351–359, 2009.
- [190] Herwig Ott. Single atom detection in ultracold quantum gases: a review of current progress. Reports on Progress in Physics, 79(5):054401, 2016.
- [191] Alexei Ourjoumtsev, Alexander Kubanek, Markus Koch, Christian Sames, Pepijn WH Pinkse, Gerhard Rempe, and Karim Murr. Observation of squeezed light from one atom excited with two photons. Nature, 474(7353):623–626, 2011.
- [192] Serdar Ozelik and Daniel L. Akins. Extremely low excitation threshold, superradiant, molecular aggregate lasing system. Applied Physics Letters, 71(21):3057–3059, 1997.
- [193] Gitt Panitchayangkoon, Dugan Hayes, Kelly A. Fransted, Justin R. Caram, Elad Harel, Jianzhong Wen, Robert E. Blankenship, and Gregory S. Engel. Long-lived quantum coherence in photosynthetic complexes at physiological temperature. Proceedings of the National Academy of Sciences, 107(29):12766–12770, 2010.

- [194] S. A. Parameswaran, T. Grover, D. A. Abanin, D. A. Pesin, and A. Vishwanath. Probing the chiral anomaly with nonlocal transport in three-dimensional topological semimetals. Phys. Rev. X, 4:031035, 2014.
- [195] Janos Perczel, Johannes Borregaard, Darrick Chang, Hannes Pichler, Susanne F Yelin, Peter Zoller, and Mikhail D Lukin. Topological quantum optics in two-dimensional atomic arrays. arXiv preprint arXiv:1703.04849, 2017.
- [196] William D. Phillips. Nobel lecture: Laser cooling and trapping of neutral atoms. Rev. Mod. Phys., 70:721–741, Jul 1998.
- [197] A. Pikovsky, M. Rosenblum, and J. Kurths. Synchronization: A Universal Concept in Nonlinear Sciences. Cambridge Nonlinear Science Series. Cambridge University Press, 2003.
- [198] M. B. Plenio and P. L. Knight. The quantum-jump approach to dissipative dynamics in quantum optics. Rev. Mod. Phys., 70:101–144, Jan 1998.
- [199] Haibo Qiu, Bruno Julia-Diaz, Miguel Angel Garcia-March, and Artur Polls. Measure synchronization in quantum many-body systems. Phys. Rev. A, 90:033603, 2014.
- [200] Goulven Quéméner and John L. Bohn. Electric field suppression of ultracold confined chemical reactions. Phys. Rev. A, 81:060701, Jun 2010.
- [201] Goulven Quéméner and John L. Bohn. Strong dependence of ultracold chemical rates on electric dipole moments. Phys. Rev. A, 81:022702, Feb 2010.
- [202] Goulven Quéméner and John L. Bohn. Dynamics of ultracold molecules in confined geometry and electric field. Phys. Rev. A, 83:012705, Jan 2011.
- [203] Milun J. Raković, George W. Kattawar, Mehrübe Mehrübeoğlu, Brent D. Cameron, Lihong V. Wang, Sohi Rastegar, and Gerard L. Coté. Light backscattering polarization patterns from turbid media: theory and experiment. Appl. Opt., 38(15):3399–3408, May 1999.
- [204] C. A. Regal, M. Greiner, and D. S. Jin. Observation of resonance condensation of fermionic atom pairs. Phys. Rev. Lett., 92:040403, Jan 2004.
- [205] F. Reif. Fundamentals of statistical and thermal physics. McGraw-Hill series in fundamentals of physics. McGraw-Hill, 1965.
- [206] Philip Richerme, Zhe-Xuan Gong, Aaron Lee, Crystal Senko, Jacob Smith, Michael Foss-Feig, Spyridon Michalakis, Alexey V Gorshkov, and Christopher Monroe. Non-local propagation of correlations in quantum systems with long-range interactions. Nature, 511(7508):198–201, 2014.
- [207] J. L. Roberts, N. R. Claussen, James P. Burke, Chris H. Greene, E. A. Cornell, and C. E. Wieman. Resonant magnetic field control of elastic scattering in cold ^{85}rb . Phys. Rev. Lett., 81:5109–5112, Dec 1998.
- [208] F. Robicheaux, J. V. Hernandez, T. Topcu, and L. D. Noordam. Simulation of coherent interactions between Rydberg atoms. Phys. Rev. A, 70:042703, 2004.
- [209] Ya. I. Rodionov and S. V. Syzranov. Conductivity of a Weyl semimetal with donor and acceptor impurities. Phys. Rev. B, 91:195107, 2015.

- [210] Martin Rohden, Andreas Sorge, Marc Timme, and Dirk Witthaut. Self-organized synchronization in decentralized power grids. Phys. Rev. Lett., 109:064101, 2012.
- [211] Ralf Röhlsberger, Kai Schlage, Balaram Sahoo, Sebastien Couet, and Rudolf Ruffer. Collective lamb shift in single-photon superradiance. Science, 328(5983):1248–1251, 2010.
- [212] S. J. Roof, K. J. Kemp, M. D. Havey, and I. M. Sokolov. Observation of single-photon superradiance and the cooperative lamb shift in an extended sample of cold atoms. Phys. Rev. Lett., 117:073003, Aug 2016.
- [213] Janne Ruostekoski and Juha Javanainen. Quantum field theory of cooperative atom response: Low light intensity. Phys. Rev. A, 55:513–526, Jan 1997.
- [214] Amir H Safavi-Naeini, TP Mayer Alegre, Jasper Chan, Matt Eichenfield, Martin Winger, Qiang Lin, Jeffrey T Hill, DE Chang, and Oskar Painter. Electromagnetically induced transparency and slow light with optomechanics. Nature, 472(7341):69–73, 2011.
- [215] M. S. Safronova, Z. Zuhrianda, U. I. Safronova, and Charles W. Clark. The magic road to precision, 2015. arXiv:1507.06570.
- [216] Hidetsugu Sakaguchi and Yoshiki Kuramoto. A soluble active rotator model showing phase transitions via mutual entertainment. Progress of Theoretical Physics, 76(3):576–581, 1986.
- [217] J. E. Sansonetti and G. Nave. Wavelengths, transition probabilities, and energy levels for the spectrum of neutral strontium (sri). Journal of Physical and Chemical Reference Data, 39(3):-, 2010.
- [218] S. Das Sarma, E. H. Hwang, and Hongki Min. Carrier screening, transport, and relaxation in 3D Dirac semimetals. Phys. Rev. B, 91:035201, 2015.
- [219] Bjoern Sbierski, Gregor Pohl, Emil J. Bergholtz, and Piet W. Brouwer. Quantum transport of disordered Weyl semimetals at the nodal point. Phys. Rev. Lett., 113:026602, 2014.
- [220] J. Schachenmayer, L. Pollet, M. Troyer, and A. J. Daley. Spontaneous emission and thermalization of cold bosons in optical lattices. Phys. Rev. A, 89:011601, Jan 2014.
- [221] U Schneider, L Hackermüller, S Will, Th Best, Immanuel Bloch, TA Costi, RW Helmes, D Rasch, and A Rosch. Metallic and insulating phases of repulsively interacting fermions in a 3D optical lattice. Science, 322(5907):1520–1525, 2008.
- [222] Gregory D. Scholes, Graham R. Fleming, Alexandra Olaya-Castro, and Rienk van Grondelle. Lessons from nature about solar light harvesting. Nat Chem, 3:763–774, 2011.
- [223] Marlan O. Scully, Edward S. Fry, C. H. Raymond Ooi, and Krzysztof Wódkiewicz. Directed spontaneous emission from an extended ensemble of n atoms: Timing is everything. Phys. Rev. Lett., 96:010501, Jan 2006.
- [224] M.O. Scully and S. Zubairy. Quantum Optics. Cambridge University Press, 1997.
- [225] Kangjun Seo, Li Han, and CAR Sá de Melo. Emergence of majorana and dirac particles in ultracold fermions via tunable interactions, spin-orbit effects, and zeeman fields. Phys. Rev. Lett., 109(10):105303, 2012.

- [226] Seung-Bo Shim, Matthias Imboden, and Pritiraj Mohanty. Synchronized oscillation in coupled nanomechanical oscillators. Science, 316(5821):95–99, 2007.
- [227] O. Sigwarth, G. Labeyrie, T. Jonckheere, D. Delande, R. Kaiser, and C. Miniatura. Magnetic field enhanced coherence length in cold atomic gases. Phys. Rev. Lett., 93:143906, Sep 2004.
- [228] Brian Skinner. Coulomb disorder in three-dimensional Dirac systems. Phys. Rev. B, 90:060202, 2014.
- [229] A. M. Smith and K. Burnett. Effect of long-range collisions between atoms on laser cooling. J. Opt. Soc. Am. B, 8(8):1592–1611, Aug 1991.
- [230] A. M. Smith and K. Burnett. Effect of diffusion on laser cooling of atoms with long-range collisions. J. Opt. Soc. Am. B, 9(8):1240–1255, Aug 1992.
- [231] IM Sokolov. Light transmission of the dense and cold atomic ensembles. Laser Physics, 25(6):065202, 2015.
- [232] IM Sokolov, AS Kuraptsev, DV Kupriyanov, MD Havey, and S Balik. A scaling law for light scattering from dense and cold atomic ensembles. Journal of Modern Optics, 60(1):50–56, 2013.
- [233] Parvis Soltan-Panahi, Dirk-Sören Lühmann, Julian Struck, Patrick Windpassinger, and Klaus Sengstock. Quantum phase transition to unconventional multi-orbital superfluidity in optical lattices. Nature Physics, 8(1):71–75, 2011.
- [234] Frank C. Spano and Shaul Mukamel. Superradiance in molecular aggregates. The Journal of Chemical Physics, 91(2):683–700, 1989.
- [235] S. Stellmer, F. Schreck, and T. C. Killian. Degenerate Quantum Gases of Strontium. In K. W. Madison et al., editor, Annual Review of Cold Atoms and Molecules, volume 2, pages 1–80. World Scientific Publishing Co, March 2014.
- [236] M Steriade. Synchronized activities of coupled oscillators in the cerebral cortex and thalamus at different levels of vigilance. Cerebral Cortex, 7(6):583–604, 1997.
- [237] Helmut Strobel, Wolfgang Muessel, Daniel Linnemann, Tilman Zibold, David B. Hume, Luca Pezz, Augusto Smerzi, and Markus K. Oberthaler. Fisher information and entanglement of non-gaussian spin states. Science, 345(6195):424–427, 2014.
- [238] S H Strogatz and R E Mirollo. Collective synchronisation in lattices of nonlinear oscillators with randomness. Journal of Physics A: Mathematical and General, 21(13):L699, 1988.
- [239] S. Sugawa, Y. Takasu, K. Enomoto, and Y. Takahashi. Ultracold ytterbium: Generation, many-body physics, and molecules. In K. W. Madison et al., editor, Annual Review of Cold Atoms and Molecules, volume 1, pages 3–51. World Scientific Publishing Co, March 2013.
- [240] R. T. Sutherland and F. Robicheaux. Coherent forward broadening in cold atom clouds. Phys. Rev. A, 93:023407, Feb 2016.
- [241] A. Svedberg, L. Hgberg, and R. Nilsson. Observation of superradiant laser action in spark discharges in air at atmospheric pressure. Applied Physics Letters, 12(3):102–104, 1968.

- [242] Anatoly A. Svidzinsky, Jun-Tao Chang, and Marlan O. Scully. Cooperative spontaneous emission of n atoms: Many-body eigenstates, the effect of virtual lamb shift processes, and analogy with radiation of n classical oscillators. Phys. Rev. A, 81:053821, May 2010.
- [243] Matthew D Swallows, Michael Bishof, Yige Lin, Sebastian Blatt, Michael J Martin, Ana Maria Rey, and Jun Ye. Suppression of collisional shifts in a strongly interacting lattice clock. science, 331(6020):1043–1046, 2011.
- [244] N Syassen, DM Bauer, M Lettner, T Volz, D Dietze, J.J. García-Ripoll, JI Cirac, G Rempe, and S Dürr. Strong dissipation inhibits losses and induces correlations in cold molecular gases. Science, 320(5881):1329–1331, 2008.
- [245] S. V. Syzranov, V. Gurarie, and L. Radzihovsky. Unconventional localisation transition in high dimensions. Phys. Rev. B, 91:035133, 2015.
- [246] S. V. Syzranov, L. Radzihovsky, and V. Gurarie. Critical transport in weakly disordered semiconductors and semimetals. Phys. Rev. Lett., 114:166601, 2015.
- [247] Sergey V. Syzranov, Michael L. Wall, Victor Gurarie, and Ana Maria Rey. Spin-orbital dynamics in a system of polar molecules. Nature Comm., 5:5391, 2014.
- [248] Sergey V Syzranov, Michael L Wall, Bihui Zhu, Victor Gurarie, and Ana Maria Rey. Emergent weyl excitations in systems of polar particles. Nature Communications, 7, 2016.
- [249] Masao Takamoto, Feng-Lei Hong, Ryoichi Higashi, and Hidetoshi Katori. An optical lattice clock. Nature, 435(7040):321–324, 2005.
- [250] Private communication with Michael L. Wall.
- [251] L. K. Thomsen, S. Mancini, and H. M. Wiseman. Spin squeezing via quantum feedback. Phys. Rev. A, 65:061801, Jun 2002.
- [252] A. Traverso, R. Chakraborty, Y. N. Martinez de Escobar, P. G. Mickelson, S. B. Nagel, M. Yan, and T. C. Killian. Inelastic and elastic collision rates for triplet states of ultracold strontium. Phys. Rev. A, 79:060702, 2009.
- [253] C Trefzger, C Menotti, B Capogrosso-Sansone, and M Lewenstein. Ultracold dipolar gases in optical lattices. Journal of Physics B: Atomic, Molecular and Optical Physics, 44(19):193001, 2011.
- [254] M. Trippenbach, Bo Gao, J. Cooper, and K. Burnett. Slow collisions between identical atoms in a laser field: The spectrum of redistributed light. Phys. Rev. A, 45:6555–6569, May 1992.
- [255] Hirokazu Tsunetsugu, Manfred Sigrist, and Kazuo Ueda. The ground-state phase diagram of the one-dimensional kondo lattice model. Rev. Mod. Phys., 69:809–864, 1997.
- [256] Nariya Uchida. Many-body theory of synchronization by long-range interactions. Phys. Rev. Lett., 106:064101, Feb 2011.
- [257] C. S. E. van Ditzhuijzen, A. F. Koenderink, J. V. Hernández, F. Robicheaux, L. D. Noordam, and H. B. vanLindenvandenHeuvell. Spatially resolved observation of dipole-dipole interaction between rydberg atoms. Phys. Rev. Lett., 100:243201, Jun 2008.

- [258] M. C. W. van Rossum and Th. M. Nieuwenhuizen. Multiple scattering of classical waves: microscopy, mesoscopy, and diffusion. Rev. Mod. Phys., 71:313–371, Jan 1999.
- [259] Guifré Vidal. Efficient simulation of one-dimensional quantum many-body systems. Phys. Rev. Lett., 93(4):040502, Jul 2004.
- [260] ML Wall, KRA Hazzard, and AM Rey. Quantum magnetism with ultracold molecules. From Atomic to Mesoscale: The Role of Quantum Coherence in Systems of Various Complexities. Edited by MALINOVS KAYA SVETLANA A ET AL. Published by World Scientific Publishing Co. Pte. Ltd., 2015. ISBN# 9789814678704, pp. 3-37, 1:3–37, 2015.
- [261] Stefan Walter, Andreas Nunnenkamp, and Christoph Bruder. Quantum synchronization of a driven self-sustained oscillator. Phys. Rev. Lett., 112:094102, Mar 2014.
- [262] Stefan Walter, Andreas Nunnenkamp, and Christoph Bruder. Quantum synchronization of two van der pol oscillators. Annalen der Physik, 527(1-2):131–138, 2015.
- [263] Xiangang Wan, Ari M. Turner, Ashvin Vishwanath, and Sergey Y. Savrasov. Topological semimetal and Fermi-arc surface states in the electronic structure of pyrochlore iridates. Phys. Rev. B, 83:205101, 2011.
- [264] T. M. Weber, M. Höning, T. Niederprüm, T. Manthey, O. Thomas, V. Guarrera, M. Fleischhauer, G. Barontini, and H. Ott. Mesoscopic Rydberg-blockaded ensembles in the superatom regime and beyond. Nat. Phys., 11:157, 2015.
- [265] Hermann Weyl. Elektron und Gravitation. I. Zeitschrift für Physik, 56:330, 1929.
- [266] Steven R. White and Adrian E. Feiguin. Real-time evolution using the density matrix renormalization group. Phys. Rev. Lett., 93(7):076401, Aug 2004.
- [267] Sebastian Will, Thorsten Best, Ulrich Schneider, Lucia Hackermüller, Dirk-Sören Lühmann, and Immanuel Bloch. Time-resolved observation of coherent multi-body interactions in quantum phase revivals. Nature, 465(7295):197–201, 2010.
- [268] H. M. Wiseman and G. J. Milburn. Interpretation of quantum jump and diffusion processes illustrated on the bloch sphere. Phys. Rev. A, 47:1652–1666, Mar 1993.
- [269] Huang Wu, Ennio Arimondo, and Christopher J. Foot. Dynamics of evaporative cooling for bose-einstein condensation. Phys. Rev. A, 56:560–569, Jul 1997.
- [270] Huang Wu and Christopher J Foot. Direct simulation of evaporative cooling. Journal of Physics B: Atomic, Molecular and Optical Physics, 29(8):L321, 1996.
- [271] Liu Xia-Ji, Hu Hui, and Pu Han. Three-dimensional spinorbit coupled fermi gases: Fuldeferrell pairing, majorana fermions, weyl fermions, and gapless topological superfluidity. Chinese Physics B, 24(5):050502, 2015.
- [272] Luo Xizhang, Zou Joujia, Qiu Bingshen, and Lin Yikun. A very short opfir superradiant laser. International Journal of Infrared and Millimeter Waves, 10(2):237–249, 1989.
- [273] M. Xu, D. A. Tieri, E. C. Fine, J. K. Thompson, and M. J. Holland. Synchronization of two ensembles of atoms. Phys. Rev. Lett., 113:154101, 2014.

- [274] Minghui Xu and M. J. Holland. Conditional ramsey spectroscopy with synchronized atoms. Phys. Rev. Lett., 114:103601, Mar 2015.
- [275] Minghui Xu, D. A. Tieri, and M. J. Holland. Simulating open quantum systems by applying $su(4)$ to quantum master equations. Phys. Rev. A, 87:062101, Jun 2013.
- [276] Su-Yang Xu, Ilya Belopolski, Nasser Alidoust, Madhab Neupane, Guang Bian, Chenglong Zhang, Raman Sankar, Guoqing Chang, Zhujun Yuan, Chi-Cheng Lee, Shin-Ming Huang, Hao Zheng, Jie Ma, Daniel S. Sanchez, BaoKai Wang, Arun Bansil, Fangcheng Chou, Pavel P. Shibayev, Hsin Lin, Shuang Jia, and M. Zahid Hasan. Discovery of a Weyl fermion semimetal and topological Fermi arcs. Science, 349:613, 2015.
- [277] Shun Yamaguchi, Hiromi Isejima, Takuya Matsuo, Ryusuke Okura, Kazuhiro Yagita, Masaki Kobayashi, and Hitoshi Okamura. Synchronization of cellular clocks in the suprachiasmatic nucleus. Science, 302(5649):1408–1412, 2003.
- [278] Bo Yan, Steven A Moses, Bryce Gadway, Jacob P Covey, Kaden RA Hazzard, Ana Maria Rey, Deborah S Jin, and Jun Ye. Observation of dipolar spin-exchange interactions with lattice-confined polar molecules. Nature, 501(7468):521–525, 2013.
- [279] N. Y. Yao, A. V. Gorshkov, C. R. Laumann, A. M. Läuchli, J. Ye, and M. D. Lukin. Realizing fractional chern insulators in dipolar spin systems. Phys. Rev. Lett., 110:185302, Apr 2013.
- [280] Deshui Yu. Single-photon emitter based on an ensemble of lattice-trapped interacting atoms. Phys. Rev. A, 89:063809, Jun 2014.
- [281] Deshui Yu. Properties of far-field fluorescence from an ensemble of interacting sr atoms. Journal of Modern Optics, 63(5):428–442, 2016.
- [282] T. Zelevinsky, S. Kotochigova, and Jun Ye. Precision test of mass-ratio variations with lattice-confined ultracold molecules. Phys. Rev. Lett., 100:043201, Jan 2008.
- [283] Mian Zhang, Gustavo S. Wiederhecker, Sasikanth Manipatruni, Arthur Barnard, Paul McEuen, and Michal Lipson. Synchronization of micromechanical oscillators using light. Phys. Rev. Lett., 109:233906, 2012.
- [284] Bihui Zhu, Johannes Schachenmayer, Minghui Xu, F Herrera, Juan G Restrepo, Murray J Holland, and Ana Maria Rey. Synchronization of interacting quantum dipoles. New Journal of Physics, 17(8):083063, 2015.
- [285] Piotr S. Żuchowski and Jeremy M. Hutson. Reactions of ultracold alkali-metal dimers. Phys. Rev. A, 81:060703, Jun 2010.
- [286] M. W. Zwierlein, C. A. Stan, C. H. Schunck, S. M. F. Raupach, A. J. Kerman, and W. Ketterle. Condensation of pairs of fermionic atoms near a feshbach resonance. Phys. Rev. Lett., 92:120403, Mar 2004.

Appendix A

Theoretical approaches for evaporative cooling with long-range interactions

A.1 Monte Carlo simulation for evaporative cooling

With its stochastic nature, the Monte Carlo method is capable of simulating the individual collisions that are intrinsic to evaporative cooling phenomena [270, 64, 269], and this leads to a flexible algorithm in which it is easy to incorporate a variety of different conditions in a straightforward way. The detailed simulation algorithm consists mainly of the following steps:

1. Preparation of an ensemble of particles with coordinates and velocities generated from a given probability distribution, e.g. an initial equilibrium Boltzmann distribution.
2. Evolution of the particles between collisions that follows the classical Hamilton's equations of motion, *i.e.*

$$\begin{aligned}\frac{d\mathbf{x}}{dt} &= \mathbf{v}, \\ \frac{d\mathbf{v}}{dt} &= -\nabla V(\mathbf{x}),\end{aligned}\tag{A.1}$$

where $V(\mathbf{x})$ is the external potential. The time step is chosen to be both small enough to guarantee numerical convergence for the computed trajectory, as well as much less than the time between adjacent collision events.

3. Checking every pair of particles to decide if there is a collision. Since we are interested in two-body collisions, the collision events are determined by the distance between particles. This distance is characterized by the scattering length a_s . In three-dimensional collisions, there is a collision cross-section with units of area, $\sigma = \pi a_s^2$. In two-dimensional collisions, there is an

analogous cross-section with units of length, $\lambda = 2a_s$.

4. Changing the state of the pair of particles if they collide. For an elastic collision event, the velocities after collisions are determined from the conservation of total momentum and energy. The scattering angle is simulated from a probability distribution determined by the differential cross-section. For instance, in two-dimensional s -wave scattering, the outgoing angles ϕ are uniformly distributed in the interval $[0, 2\pi)$, while for p -wave scattering, the distribution of the outgoing angles follows the distribution $\cos^2 \phi$. In three-dimensional isotropic scattering, there are two random angles: an azimuthal angle ϕ uniformly distributed in the interval $[0, 2\pi)$ and a polar angle θ from uniformly distributed according to $\cos \theta$. The non-uniform distribution of the scattering angles does not affect the collision rate that is determined by the total cross-section, but the rate of redistributing energies does vary. For an inelastic collision event corresponding to two-body reactive collisions, the two particles are lost from the trap after the collision, and thus deleted from the simulation when such processes occur.

5. Averaging over many initial samples and trajectories. The physical quantities such as the total number of particles, temperature, collision rate and phase space density can be computed statistically from the simulation ensemble.

A.2 Kinetics of evaporative cooling in 2D

An alternative algorithm which is partially analytic can be derived by assuming that in the process of evaporative cooling, the energetic particles can be efficiently removed from the trap. The system is assumed to follow a truncated Boltzmann distribution $f(\mathbf{x}, \mathbf{p})$ (Eq. 3.12), with a cut-off energy ϵ_t [155, 102], meaning that there is no particle with energy $E > \epsilon_t$. Then similar to the description of an equilibrium ensemble, the measured quantities of the system can be expressed by averaging over this distribution function. For example, the collision rate is

$$\begin{aligned} \gamma = & \frac{\lambda \Lambda^2}{m} \int_{\epsilon_1, \epsilon_2} d^2x d^2p_1 d^2p_2 \\ & \times f(\mathbf{x}, \mathbf{p}_1) f(\mathbf{x}, \mathbf{p}_2) |\mathbf{p}_1 - \mathbf{p}_2|, \end{aligned} \quad (\text{A.2})$$

in which $\Lambda = 1/(2\pi\hbar)^2$, $\epsilon_{1,2} = p_{1,2}^2/2m + V(\mathbf{x}_{1,2})$ are the energies of the incident particles. For simplicity, here we have assumed isotropic energy-independant elastic and inelastic collisions, so λ in Eq. (A.2) is constant. We also assume the two-body inelastic collisions happen rate $\zeta\gamma$. During forced evaporative cooling, ϵ_t decreases with time, so does the temperature T , and the distribution function $f = f(\mathbf{x}, \mathbf{p})$. As a result, the evolution of the system from t to t' can be modeled via three steps: the change due to f when ϵ_t decreases to ϵ'_t (dN_1, dE_1), the change due to evaporation (dN_2, dE_2), and the change due to the inelastic losses (dN_3, dE_3). These can be represented by the following equations:

$$dN_1 = \Lambda \int_{\epsilon=\epsilon'_t}^{\epsilon_t} d^2x d^2p f, \quad (\text{A.3})$$

$$dE_1 = \Lambda \int_{\epsilon=\epsilon'_t}^{\epsilon_t} d^2x d^2p \epsilon f, \quad (\text{A.4})$$

$$\frac{dN_2}{dt} = \frac{\lambda\Lambda^2}{m} \int_{\Sigma} d^2x d^2p_1 d^2p_2 d\phi' f_1 f_2 |\mathbf{p}_1 - \mathbf{p}_2|, \quad (\text{A.5})$$

$$\frac{dE_2}{dt} = \frac{\lambda\Lambda^2}{m} \int_{\Sigma} d^2x d^2p_1 d^2p_2 d\phi' s f_1 f_2 |\mathbf{p}_1 - \mathbf{p}_2| \epsilon_4, \quad (\text{A.6})$$

$$\frac{dN_3}{dt} = \zeta \frac{\lambda\Lambda^2}{m} \int_{\Sigma'} d^2x d^2p_1 d^2p_2 f_1 f_2 |\mathbf{p}_1 - \mathbf{p}_2|, \quad (\text{A.7})$$

$$\frac{dE_3}{dt} = \zeta \frac{\lambda\Lambda^2}{m} \int_{\Sigma'} d^2x d^2p_1 d^2p_2 (\epsilon_1 + \epsilon_2) f_1 f_2 |\mathbf{p}_1 - \mathbf{p}_2|, \quad (\text{A.8})$$

where f_1, f_2 are the distribution function for each of the two colliding particles, ϕ' specifies the scattering angle, $\epsilon = \epsilon(\mathbf{x}, \mathbf{p})$ is the energy of a particle and is a function of the coordinate and momentum of the particles, ϵ_3 and ϵ_4 are energies after collision, which are determined once $\mathbf{p}_1, \mathbf{p}_2$ and ϕ' are known, and $\Sigma = \{\epsilon_1, \epsilon_2, \epsilon_3 < \epsilon'_t, \epsilon_4 > \epsilon'_t\}$ and $\Sigma' = \{\epsilon_1, \epsilon_2 < \epsilon'_t\}$ specify the integration region. These contributions add up to give the total changes: $N(t') = N(t) - dN_1 - dN_2 - dN_3$ and $E(t') = E(t) - dE_1 - dE_2 - dE_3$. The new temperature $T(t')$ is found from

$$N(t') = \Lambda^2 \int_0^{\epsilon'_t} d^2x d^2p f(\mathbf{x}, \mathbf{p}), \quad (\text{A.9})$$

$$E(t') = \Lambda^2 \int_0^{\epsilon'_t} d^2x d^2p f(\mathbf{x}, \mathbf{p}) \epsilon. \quad (\text{A.10})$$

Then the trajectory of evaporative cooling in two-dimensional traps can be solved from the above equations. Similar calculations also apply to three-dimensional harmonic traps, and the results are equivalent to solving the rate equations following the method developed by Walraven *et al.*, as long as the truncated Boltzmann distribution is a good approximation [155].

A.3 Master equation approach for losses in a quasi-2D trap

Represented in the basis of harmonic oscillator eigenstates, the rate coefficients $\Gamma_{\mathbf{n},\mathbf{m}}$ defined in the jump operators in Sec. 3.5 can be written explicitly for intraband collisions ($n_z = m_z$, FIG. 3.7(a)) [162]

$$\begin{aligned}
\Gamma_{\mathbf{n},\mathbf{m}} &= \tilde{\Gamma}^{(1)} \\
&= \frac{3\sqrt{2\pi}b_p^3\sqrt{\omega_r\omega_z}}{(a_{\text{ho}}^r)^3} Is(n_z, m_z, n_z, m_z) \\
&\quad \times \sum_{\sigma \neq \sigma'} Is(n_\sigma, m_\sigma, n_\sigma, m_\sigma) Ip(n_{\sigma'}, m_{\sigma'}, n_{\sigma'}, m_{\sigma'}),
\end{aligned} \tag{A.11}$$

and for interband collisions ($n_z \neq m_z$, FIG. 3.7(b))

$$\begin{aligned}
\Gamma_{\mathbf{n},\mathbf{m}} &= \tilde{\Gamma}^{(2)} \\
&= \frac{3\sqrt{2\pi}b_p^3\sqrt{\omega_r\omega_z}}{(a_{\text{ho}}^r)^3} \sum_{\sigma_1 \neq \sigma_2 \neq \sigma_3} \frac{\omega_{\sigma_2}}{\omega_r} Is(n_{\sigma_1}, m_{\sigma_1}, n_{\sigma_1}, m_{\sigma_1}) \\
&\quad \times Ip(n_{\sigma_2}, m_{\sigma_2}, n_{\sigma_2}, m_{\sigma_2}) Is(n_{\sigma_3}, m_{\sigma_3}, n_{\sigma_3}, m_{\sigma_3}),
\end{aligned} \tag{A.12}$$

where $\sigma, \sigma' = \{x, y\}$, $\sigma_1, \sigma_2, \sigma_3 = \{x, y, z\}$, $a_{\text{ho}}^r = \sqrt{\hbar/m\omega_r}$,

$$Is(n, m, p, q) = \int du \frac{e^{-2u^2} H_n(u) H_m(u) H_p(u) H_q(u)}{\pi \sqrt{2^{n+m+p+q} n! m! p! q!}}, \quad (\text{A.13})$$

$$\begin{aligned} Ip(n, m, p, q) = & \int du \frac{e^{-2u^2}}{\pi \sqrt{2^{n+m+p+q} n! m! p! q!}} \\ & \times [\partial H_n(u) H_m(u) - H_n(u) \partial H_m(u)] \\ & \times [\partial H_p(u) H_q(u) - H_p(u) \partial H_q(u)], \end{aligned} \quad (\text{A.14})$$

and H_n, H_m, H_p, H_q are Hermite polynomials.

Appendix B

Modeling dissipative dynamics

We model the dissipative dynamics by means of a master equation for the density operator $\hat{\rho}$:

$$\frac{d}{dt}\hat{\rho} = -\frac{i}{\hbar}[\hat{H}_0, \hat{\rho}] + \mathcal{L}\hat{\rho}, \quad (\text{B.1})$$

with \hat{H}_0 describing the unitary evolution and $\mathcal{L}\hat{\rho} = \frac{1}{2}\sum_j(\hat{\rho}\hat{C}_j^\dagger\hat{C}_j + \hat{C}_j^\dagger\hat{C}_j\hat{\rho} - 2\hat{C}_j\hat{\rho}\hat{C}_j^\dagger)$ accounting for dissipation. In a 1D tube with a superimposed lattice potential, $\hat{H}_0 = -J\sum_{j,\sigma}(\hat{c}_{j\sigma}^\dagger\hat{c}_{j+1\sigma} + h.c.) + \hat{V}_{\text{trap}}$, where J represents the hopping of molecules between sites, and \hat{V}_{trap} represents the parabolic trapping potential. The two-body losses that occur between KRb molecules are described by jump operators $\hat{C}_j = \sqrt{\Gamma_0}\hat{c}_{j\uparrow}\hat{c}_{j\downarrow}$, which destroy a pair of molecules in different rotational states ($|\uparrow\rangle$ or $|\downarrow\rangle$) at the same site j , and Γ_0 is the on-site loss rate. In the regime $\Gamma_0 \gg J/\hbar$, the doubly occupied states can be adiabatically eliminated [82], projecting the Hilbert space to states with at most one molecules per site. As a result, the jump operators \hat{C}_j are replaced by $\hat{A}_j = \sqrt{2\Gamma_{\text{eff}}}\left[(\hat{c}_{j\uparrow}\hat{c}_{j+1\downarrow} + \hat{c}_{j\uparrow}\hat{c}_{j-1\downarrow}) - (\hat{c}_{j\downarrow}\hat{c}_{j+1\uparrow} + \hat{c}_{j\downarrow}\hat{c}_{j-1\uparrow})\right]$, and $\Gamma_{\text{eff}} = 2(J/\hbar)^2/\Gamma_0$. These new jump operators \hat{A}_j effectively remove spin singlet states formed in neighboring sites, and account for second order tunneling processes. Even within the reduced space, the above master equation is generally difficult to solve for experimentally relevant lattice sizes. In 1D, however, various numerical techniques can be applied. In the following we provide the details of the numerical methods utilized in this paper for solving the above master equation.

B.1 Mean-field treatment (MF)

The above master equation can be significantly simplified by adopting a MF ansatz that allows for efficient numerical treatment of realistic system sizes. Under this ansatz, $\hat{\rho} = \prod_j \tilde{\rho}_j$ with $\tilde{\rho}_j \equiv \sum_{\alpha,\beta=\{\uparrow,\downarrow,0\}} \rho_j^{\alpha,\beta} |\alpha\rangle\langle\beta|$. $\uparrow, \downarrow, 0$ label the three possible local states of spin up, spin down, and the vacuum, respectively. Solving the master equation reduces to solving a set of coupled and non-linear differential equations for $\rho_j^{\alpha,\beta}$:

$$\frac{d\rho_j^{\sigma\sigma}}{dt} = \frac{i}{\hbar} J \sum_l (\rho_l^{\sigma 0} \rho_j^{0\sigma} - \rho_l^{0\sigma} \rho_j^{\sigma 0}) + 2\Gamma_{\text{eff}} \sum_l (\rho_l^{\sigma'\sigma} \rho_j^{\sigma\sigma'} + \rho_l^{\sigma\sigma'} \rho_j^{\sigma'\sigma}) - 4\Gamma_{\text{eff}} \sum_l \rho_l^{\sigma'\sigma'} \rho_j^{\sigma\sigma}, \quad (\text{B.2})$$

$$\frac{d\rho_j^{\sigma\sigma'}}{dt} = \frac{i}{\hbar} (\Omega_\sigma - \Omega_{\sigma'}) j^2 \rho_j^{\sigma\sigma'} + \frac{i}{\hbar} J \sum_l (\rho_l^{\sigma 0} \rho_j^{0\sigma'} - \rho_l^{0\sigma'} \rho_j^{\sigma 0}) + 2\Gamma_{\text{eff}} \sum_l \sum_\alpha (\rho_l^{\sigma\sigma'} \rho_j^{\alpha\alpha} - \rho_l^{\alpha\alpha} \rho_j^{\sigma\sigma'}), \quad (\text{B.3})$$

$$\frac{d\rho_j^{0\sigma}}{dt} = \frac{i}{\hbar} \Omega_\sigma j^2 \rho_j^{0\sigma} + \frac{i}{\hbar} J \sum_l \left(\sum_\alpha \rho_l^{0\alpha} \rho_j^{\alpha\sigma} - \rho_l^{0\sigma} \rho_j^{00} \right) + 2\Gamma_{\text{eff}} \sum_l (\rho_l^{\sigma'\sigma} \rho_j^{0\sigma'} - \rho_l^{\sigma'\sigma'} \rho_j^{0\sigma}), \quad (\text{B.4})$$

$$\frac{d\rho_j^{\sigma 0}}{dt} = -\frac{i}{\hbar} \Omega_\sigma j^2 \rho_j^{\sigma 0} + \frac{i}{\hbar} J \sum_l (\rho_l^{\sigma 0} \rho_j^{00} - \sum_\alpha \rho_l^{\alpha 0} \rho_j^{\sigma\alpha}) + 2\Gamma_{\text{eff}} \sum_l (\rho_l^{\sigma\sigma'} \rho_j^{\sigma'0} - \rho_l^{\sigma'\sigma'} \rho_j^{\sigma 0}), \quad (\text{B.5})$$

$$\frac{d\rho_j^{00}}{dt} = \frac{i}{\hbar} J \sum_l \sum_\alpha (\rho_l^{0\alpha} \rho_j^{\alpha 0} - \rho_l^{\alpha 0} \rho_j^{0\alpha}) + 4\Gamma_{\text{eff}} \sum_l \sum_{\alpha \neq \alpha'} \sum_{\beta \neq \beta'} (-1)^{\delta_{\alpha\beta}} \rho_l^{\alpha\beta} \rho_j^{\alpha'\beta'}, \quad (\text{B.6})$$

where $\sigma, \alpha, \alpha', \beta, \beta' \in \{\uparrow, \downarrow\}$, $\sigma \neq \sigma'$, the summation of l is over the nearest neighbors of j , and $\Omega_{\uparrow(\downarrow)} = \frac{1}{2} m \omega_{\uparrow(\downarrow)}^2 a^2$ with a the lattice spacing. In deriving the above Eqs. (B.2)-(B.6), we have neglected terms such as $\hat{n}_{j\sigma} \hat{c}_{j+1\sigma'}^\dagger \hat{c}_{j-1\sigma'} \hat{\rho}$ and $\hat{c}_{j+1\sigma}^\dagger \hat{c}_{j\sigma} \hat{c}_{j\sigma'}^\dagger \hat{c}_{j-1\sigma'} \hat{\rho}$ in $\mathcal{L}\hat{\rho}$, which correspond to the correlated hopping processes involving three sites. We have performed calculations to confirm the contributions from these terms are small for the systems we treat in this paper.

B.2 Rate equation (RE)

A further simplification can be obtained by neglecting the dynamical redistribution of molecules and the effect of inhomogeneity, as well as coherences. This is equivalent to dropping the unitary evolution terms in Eqs. (B.2)-(B.6), and setting all off-diagonal terms of the density matrix $\tilde{\rho}_j$ to 0. With these approximations, for a 50:50 mixture of molecules, $\rho_j^{\uparrow\uparrow} = n_\uparrow = \rho_{j+1}^{\downarrow\downarrow} = n_\downarrow$, Eq. (B.2)

simplifies to

$$\frac{dn_{\downarrow}}{dt} = -8\Gamma_{\text{eff}}[n_{\downarrow}(t)]^2, \quad (\text{B.7})$$

which is the same as the RE Eq. (3) in the main text. The RE gives a fairly good understanding of the loss dynamics at short times, as discussed in the main text. However, a quantitative estimate of the filling fraction requires going beyond these approximations. This can be accomplished by using the MF treatment.

Appendix C

Phase coherence and correlations in interacting dipoles

C.1 Mean-field approach

The mean-field ansatz, $\hat{\rho} = \bigotimes_a \hat{\rho}_a$, reduces the dynamics to $3N$ coupled nonlinear differential equations presented in the main text. In the most generic case we define local order parameters to take into account the effect of the inhomogeneous couplings:

$$X_a e^{i\Phi} = \sum_{b \neq a} f(\mathbf{r}_{ab}) S_b^\perp e^{i\phi_b}, \quad Y_a e^{i\Phi} = \sum_{b \neq a} g(\mathbf{r}_{ab}) S_b^\perp e^{i\phi_b}.$$

If the local order parameters vary slowly over the system size, and can be approximated to be the same for all dipoles one can define $X_a \approx f_{\text{eff}} Z$, $Y_a \approx g_{\text{eff}} Z$, where the global order parameter Z is defined as $Z e^{i\Phi} = \frac{1}{N} \sum_a S_a^\perp e^{i\phi_a}$ and the effective couplings are given by $f_{\text{eff}} = \sum_a \sum_{b \neq a} f(\mathbf{r}_{ab}) / (N - 1)$ and $g_{\text{eff}} = \sum_a \sum_{b \neq a} g(\mathbf{r}_{ab}) / (N - 1)$.

The steady-state solution $\dot{Z} = 0$, $\Phi = \bar{\omega} t$ leads to two self-consistent equations for the order parameter Z and the collective frequency $\bar{\omega}$

$$Z = \sum_a^N \frac{ZP[f_{\text{eff}}Q + 2g_{\text{eff}}(\delta_a + \bar{\omega})]}{NQ[4(\delta_a + \bar{\omega})^2 + (2f_{\text{eff}}^2 Z^2 + 2g_{\text{eff}}^2 Z^2 + Q^2)]}, \quad (\text{C.1})$$

$$0 = \sum_a^N \frac{ZP[g_{\text{eff}}Q - 2f_{\text{eff}}(\delta_a + \bar{\omega})]}{NQ[4(\delta_a + \bar{\omega})^2 + (2f_{\text{eff}}^2 Z^2 + 2g_{\text{eff}}^2 Z^2 + Q^2)]}, \quad (\text{C.2})$$

which can be evaluated in the $N \rightarrow \infty$ limit as integrals when the detunings δ_a have a known distribution.

We note that in this treatment, when $g(\mathbf{r}_{ab}) \neq 0$, the elastic couplings simply induce a global frequency shift $\bar{\omega} = g_{\text{eff}}Q / (2f_{\text{eff}})$ that can be eliminated by moving to a rotating frame. However, as

discussed in the main text the role of elastic interactions is not just to introduce a simple rotation. In fact the elastic terms tend to generate entanglement and correlations which can not be capture by a simple mean-field treatment. Therefore the applicability of the mean-field solution is restricted to regimes where elastic interactions are highly suppressed.

C.2 Cumulant expansion approach and two-time correlation between dipoles

The cumulant expansion method is a useful theoretical tool for including correlation effects beyond the mean-field approximation [166, 274, 101]. We keep two-point correlations such as $\langle \hat{\sigma}_a^{+, -, z} \hat{\sigma}_b^{+, -, z} \rangle$, but factorize three-point correlations and higher [128]:

$$\begin{aligned} \langle \hat{\sigma}_a^\alpha \hat{\sigma}_b^\beta \hat{\sigma}_c^\gamma \rangle &= \langle \hat{\sigma}_a^\alpha \hat{\sigma}_b^\beta \rangle \langle \hat{\sigma}_c^\gamma \rangle + \langle \hat{\sigma}_a^\alpha \rangle \langle \hat{\sigma}_b^\beta \hat{\sigma}_c^\gamma \rangle + \langle \hat{\sigma}_a^\alpha \hat{\sigma}_c^\gamma \rangle \langle \hat{\sigma}_b^\beta \rangle \\ &\quad - 2 \langle \hat{\sigma}_a^\alpha \rangle \langle \hat{\sigma}_b^\beta \rangle \langle \hat{\sigma}_c^\gamma \rangle. \end{aligned} \quad (\text{C.3})$$

This factorization closes the set of dynamical equations of motion for all single particle observables $\langle \hat{\sigma}_a^{+, -, z} \rangle$ and equal time two-point correlations. Two-time correlation functions can be computed by solving [40]:

$$\begin{aligned} \frac{d\langle \hat{\sigma}_a^+(t+\tau) \hat{\sigma}_b^-(t) \rangle}{d\tau} &= - \left[i\delta_a + \frac{\Gamma + W}{2} \right] \langle \hat{\sigma}_a^+(t+\tau) \hat{\sigma}_b^-(t) \rangle \\ &\quad + \frac{1}{2} f_{ab} \langle \hat{\sigma}_a^z(t) \rangle \langle \hat{\sigma}_b^+(t+\tau) \hat{\sigma}_b^-(t) \rangle \\ &\quad + \frac{1}{2} \sum_{j \neq a, b} f_{aj} \langle \hat{\sigma}_a^z(t) \rangle \langle \hat{\sigma}_j^+(t+\tau) \hat{\sigma}_b^-(t) \rangle, \end{aligned}$$

where we have introduced the approximation $\langle \hat{\sigma}_a^z(t+\tau) \hat{\sigma}_j^+(t+\tau) \hat{\sigma}_b^-(t) \rangle \approx \langle \hat{\sigma}_a^z(t) \rangle \langle \hat{\sigma}_j^+(t+\tau) \hat{\sigma}_b^-(t) \rangle$. Comparisons with exact numerical solutions show that the cumulant expansion captures well the steady-state behavior for inhomogeneous couplings $f(\mathbf{r}_{ab})$, provided the elastic couplings $g(\mathbf{r}_{ab})$ are sufficiently small. In Fig. C.1 we compute the pair-wise two-time correlation function, $Z_{a,b}(\tau) \equiv \lim_{t \rightarrow \infty} \langle (\hat{\sigma}_a^+(t+\tau) + \hat{\sigma}_b^+(t+\tau)) (\hat{\sigma}_a^-(t) + \hat{\sigma}_b^-(t)) \rangle$, using both the cumulant expansion and the exact solution. The decay rate of these correlations, $Z_{a,b}(\tau) = A e^{-\tau\gamma}$, encodes information about the spectral coherence of the emitted radiation (note that here $\nu = 0$). The result shows that Γ/γ exhibits the same dependence on W/Γ as Z_Q .

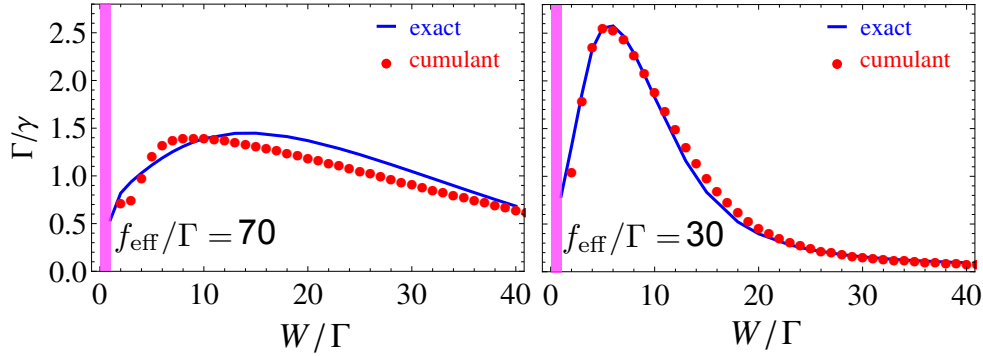


Figure C.1: Pair-wise two-time correlation functions in the steady-state parametrized by $Z_{1,2}(\tau) = A \exp(-\gamma\tau)$. The correlations are calculated for a pair of dipoles in an ensemble of $N = 70$ dipoles identically coupled with $f(\mathbf{r}_{ab}) = f_{\text{eff}}/N$. The cumulant expansion solution agrees with the full calculation except at $W \ll \Gamma$ where subradiant behavior dominates (purple region) [166].

C.3 Conditional evolution, entanglement and quantum correlations

An individual experimental realization can be considered as a single trajectory, whose evolution can be quite different from the ensemble averaged solution of the master equation. Tracking the evolution of an individual trajectory is equivalent to performing continuous measurements that collect the record of the emitted photons, for example homodyne measurements. The conditional evolution of the system subject to continuous measurements can be modeled by the method of quantum state diffusion [40, 268]. For a single run the state of the system remains pure, $\hat{\rho}_c = |\psi\rangle\langle\psi|$, but the average over many trials reduces the system into a mixed state and recovers the density matrix obtained from the master equation.

To probe the entanglement of the dipoles, in Fig. 2 we calculate the average quantum Fisher information for each individual trajectory [107, 237]

$$\overline{F}_Q(\hat{\rho}_c) = \frac{1}{3}(F_Q(\hat{\rho}_c; \hat{J}_x) + F_Q(\hat{\rho}_c; \hat{J}_y) + F_Q(\hat{\rho}_c; \hat{J}_z)),$$

where $F_Q(\hat{\rho}_c; \hat{\mathcal{H}}) = 4(\langle\psi|\hat{\mathcal{H}}^2|\psi\rangle - \langle\psi|\hat{\mathcal{H}}|\psi\rangle^2)$, and $\hat{J}_{x,y,z}$ are collective angular momentum operators.

States with zero entanglement can still be nonclassical. Two systems are correlated if they share information with each other. The total amount of correlation can be quantified by the quan-

tum mutual information $\mathcal{I} = \mathcal{S}_A + \mathcal{S}_B - \mathcal{S}_{AB}$, where \mathcal{S}_i is the von Neumann entropy of the subsystem $i \in \{A, B, AB\}$ (AB is the total system spanned by A and B together), $\mathcal{S}_i = -\text{Tr}[\hat{\rho}_i \log_2 \hat{\rho}_i]$, with $\hat{\rho}_i$ the reduced density matrix of the subsystem i . A value varying between 0 and 2 is obtained when A and B are pure states or maximally correlated respectively. The mutual information can be separated into a classical and a quantum part. The classical part is $\mathcal{J}_{B|A} = \max\{\mathcal{S}_B - \mathcal{S}_{B|A}\}$. Here $\mathcal{S}_{B|A}$ is the von Neumann entropy of subsystem B conditioned on the measurement performed on A and \max represents maximum value obtainable over all local measurements on A . The quantum part, known as the quantum discord, $\mathcal{D}_{B|A} = \mathcal{I} - \mathcal{J}_{B|A}$, measures the amount of correlations that exceed the classical part and characterizes the “quantumness” of the system [171]. A state with nonzero quantum discord behaves in a way intrinsically non-classical, since a local measurement performed on one of its subsystems can disturb the whole system. In order to calculate $\mathcal{J}_{B|A}$, we consider a set of von Neumann measurements $\hat{\Pi}_{k=1,2}^A = \frac{1}{2}(1 \pm \vec{n}_k \cdot \vec{\sigma}^A)$ with $|\vec{n}_k|^2 = 1$, made on the subsystem A and minimize the corresponding conditional entropy $\mathcal{S}_{B|A} = \sum_{k=1}^2 \text{Tr}[p_k S(\hat{\rho}_{B|\Pi_k^A})]$, where $p_k = \text{Tr}[\hat{\Pi}_k^A \hat{\rho}]$, $\hat{\rho}_{B|\Pi_k^A} = \text{Tr}_A[\hat{\Pi}_k^A \hat{\rho}] / p_k$ [171]. In Fig. 2(e) we calculate the mutual information from \mathcal{I} and the quantum discord from \mathcal{D} using as subsystems A and B a pair of dipoles, a and b respectively.

Appendix D

Combining dipole-dipole interaction and motion

D.1 Long-range dipole-dipole interaction, force and diffusion

In Chapter 2, we presented a derivation of dipole-dipole interactions based on a direct factorization of the atomic and photonic density matrices. Here we adopt an alternative approach, and derive the form of dipole-dipole interactions and the corresponding forces for two-level moving atoms, with $\omega_a = k_0 c$ the frequency of transition and \mathbf{d} the dipole moment. We include motion in the dipolar coupling after eliminating the electromagnetic vacuum modes. The Hamiltonian, including the atoms and free-space electromagnetic field is

$$\begin{aligned}
 H = & \hbar\omega_a \sum_j \hat{b}_j^\dagger \hat{b}_j + \sum_{\mathbf{k}, \epsilon} \omega_k \hat{a}_{\mathbf{k}\epsilon}^\dagger \hat{a}_{\mathbf{k}\epsilon} - \sum_j \sum_{\mathbf{k}, \epsilon} g_k \\
 & \times (\mathbf{d} \cdot \hat{\epsilon}_{\mathbf{k}}) [(e^{i\mathbf{k} \cdot \mathbf{r}_j} \hat{a}_{\mathbf{k}\epsilon} + \text{H.c.}) (\hat{b}_j^\dagger + \text{H.c.})].
 \end{aligned} \tag{D.1}$$

The atomic dipoles and the field modes evolve according to

$$\frac{d\hat{a}_{\mathbf{k}\epsilon}}{dt} = -i\omega_k \hat{a}_{\mathbf{k}\epsilon} + \frac{i}{\hbar} \sum_j g_k (\mathbf{d}_j \cdot \epsilon_{\mathbf{k}}) [e^{-i\mathbf{k} \cdot \mathbf{r}_j} (\hat{b}_j + \text{H.c.})], \tag{D.2}$$

$$\frac{d\hat{b}_j}{dt} = -i\omega_a \hat{b}_j + i \sum_{\mathbf{k}, \epsilon} \frac{g_k}{\hbar} (\mathbf{d}_j \cdot \hat{\epsilon}_{\mathbf{k}}) [e^{i\mathbf{k} \cdot \mathbf{r}_j} \hat{a}_{\mathbf{k}\epsilon} \hat{s}_j + \text{H.c.}], \tag{D.3}$$

$$\begin{aligned}
 \frac{d\hat{s}_j}{dt} = & -i \sum_{\mathbf{k}, \epsilon} \frac{g_k}{\hbar} (\mathbf{d}_j \cdot \hat{\epsilon}_{\mathbf{k}}) [e^{i\mathbf{k} \cdot \mathbf{r}_j} \hat{a}_{\mathbf{k}\epsilon} \hat{b}_j^\dagger - e^{-i\mathbf{k} \cdot \mathbf{r}_j} \hat{a}_{\mathbf{k}\epsilon}^\dagger \hat{b}_j \\
 & - e^{i\mathbf{k} \cdot \mathbf{r}_j} \hat{a}_{\mathbf{k}\epsilon} \hat{b}_j + e^{-i\mathbf{k} \cdot \mathbf{r}_j} \hat{a}_{\mathbf{k}\epsilon}^\dagger \hat{b}_j^\dagger],
 \end{aligned} \tag{D.4}$$

where $\hat{s}_j = \hat{b}_j^\dagger \hat{b}_j - \hat{b}_j \hat{b}_j^\dagger$, and $s_j = \langle \hat{s}_j \rangle$ gives the inversion of the j^{th} atom. We have assumed that internal operators commute with external operators, and neglected the diffusion of the atomic wavepacket. Eq. (D.2) can be formally integrated to obtain

$$\begin{aligned} \hat{a}_{\mathbf{k}\epsilon}(t) &= \hat{a}_{\mathbf{k}\epsilon}(0) - i \sum_j \frac{g_k}{\hbar} (\mathbf{d}_j \cdot \hat{\epsilon}_{\mathbf{k}}) \int dt' e^{i\mathbf{k}\cdot\mathbf{r}_j + i\omega_k(t'-t)} \\ &\quad \times (\hat{b}_j + \text{H.c.}). \end{aligned} \quad (\text{D.5})$$

Assuming the external motion is much slower than the internal dynamics relevant inside the integral, so that $\mathbf{r}_j(t') \approx \mathbf{r}_j(t)$, and the interaction between atoms and the field modes is weak so that $\hat{b}_j(t') \approx \hat{b}_j(t) e^{-i\omega_a(t'-t)}$. Substituting Eq. (D.5) into Eq. (D.3), we obtain the equation for the quantum averaged quantities

$$\begin{aligned} \frac{d\hat{b}_j}{dt} &= -i\omega_a \hat{b}_j + \hat{s}_j \sum_l \sum_{\mathbf{k}, \epsilon} \frac{g_k^2}{\hbar^2} (\mathbf{d}_j \cdot \hat{\epsilon}_{\mathbf{k}}) (\mathbf{d}_l \cdot \hat{\epsilon}_{\mathbf{k}}) \\ &\quad \times \left\{ e^{i\mathbf{k}\cdot\mathbf{r}_{jl}} [\hat{b}_l^\dagger (\pi\delta(\omega_k + \omega_a) - i\text{P} \frac{1}{\omega_k + \omega_a}) \right. \\ &\quad \left. + \hat{b}_l (\pi\delta(\omega_k - \omega_a) - i\text{P} \frac{1}{\omega_k - \omega_a})] \right. \\ &\quad \left. - e^{-i\mathbf{k}\cdot\mathbf{r}_{jl}} [\hat{b}_l^\dagger (\pi\delta(\omega_k - \omega_a) + i\text{P} \frac{1}{\omega_k - \omega_a}) \right. \\ &\quad \left. + \hat{b}_l (\pi\delta(\omega_k + \omega_a) + i\text{P} \frac{1}{\omega_k + \omega_a})] \right\}, \end{aligned} \quad (\text{D.6})$$

where we have utilized the fact that $\langle \hat{a}_{\mathbf{k}\epsilon}(0) \rangle = 0$, and assumed that atomic motion is classical [229, 230]. Changing $\sum_{\mathbf{k}} = \frac{V}{(2\pi)^3} \int d\Omega dk k^2$, and applying rotating wave approximation, we have

$$\frac{d\hat{b}_j}{dt} = -i\omega_a \hat{b}_j + i \sum_{l \neq j} \hat{s}_j \hat{b}_l (g_{jl} - i f_{jl}) - \frac{\Gamma}{2} \hat{b}_j, \quad (\text{D.7})$$

with $f(0) = \Gamma$, and

$$g(r) = -\frac{3\Gamma}{4} \left[z_1(\theta) \frac{\cos k_0 r}{k_0 r} + z_2(\theta) \left(\frac{\cos k_0 r}{k_0^3 r^3} + \frac{\sin k_0 r}{k_0^2 r^2} \right) \right], \quad (\text{D.8})$$

$$f(r) = \frac{3\Gamma}{4} \left[z_1(\theta) \frac{\sin k_0 r}{k_0 r} + z_2(\theta) \left(\frac{\sin k_0 r}{k_0^3 r^3} - \frac{\cos k_0 r}{k_0^2 r^2} \right) \right], \quad (\text{D.9})$$

where $z_1(\theta) = \sin^2\theta$, and $z_2(\theta) = (3\cos^2\theta - 1)$. These expressions can also be obtained from Eq. (2.23)~ Eq. (2.22) by keeping only a single α component. We further assume that multi-atom correlations can be factorized, $\langle \hat{s}_j \hat{b}_l \rangle \approx \langle \hat{s}_j \rangle \langle \hat{b}_l \rangle$, so that the atomic coherence evolves as

$$\frac{db_j}{dt} = -i\omega_a b_j + i \sum_{l \neq j} s_j b_l (g_{jl} - if_{jl}) - \frac{\Gamma}{2} b_j, \quad (\text{D.10})$$

where $\mathcal{O} = \langle \hat{\mathcal{O}} \rangle$ for any atomic operator $\hat{\mathcal{O}}$. It is coupled to s_j , the equation of which can be derived in a similar way and is given by

$$\frac{ds_j}{dt} = -\Gamma s_j - 2i \sum_{l \neq j} (g_{jl} - if_{jl}) b_j^* b_l + 2i \sum_{l \neq j} (g_{jl} + if_{jl}) b_l^* b_j. \quad (\text{D.11})$$

If we consider very low external driving field and $s_j \approx -1$, Eq. (D.10) is decoupled from s_j and can be reduced to the form of Eq. (6.2). For the momentum,

$$\begin{aligned} \frac{d\hat{\mathbf{p}}_j}{dt} &= -\nabla \hat{H} \\ &= -\sum_{\mathbf{k}, \epsilon} g_{\mathbf{k}} (\mathbf{d}_j \cdot \boldsymbol{\epsilon}_{\mathbf{k}}) (i\mathbf{k} e^{i\mathbf{k} \cdot \mathbf{r}_j} \hat{a}_{\mathbf{k}\epsilon} \hat{b}_j^\dagger - i\mathbf{k} e^{-i\mathbf{k} \cdot \mathbf{r}_j} \hat{a}_{\mathbf{k}\epsilon}^\dagger \hat{b}_j \\ &\quad + i\mathbf{k} e^{i\mathbf{k} \cdot \mathbf{r}_j} \hat{a}_{\mathbf{k}\epsilon} \hat{b}_j - i\mathbf{k} e^{-i\mathbf{k} \cdot \mathbf{r}_j} \hat{a}_{\mathbf{k}\epsilon}^\dagger \hat{b}_j^\dagger). \end{aligned} \quad (\text{D.12})$$

After substituting Eq. (D.5), taking the quantum average and performing a similar integration procedure as above, we obtain

$$\frac{d\mathbf{p}_j}{dt} = \sum_{l \neq j} [\mathbf{g}_{jl} (b_j b_l^* + \text{H.c.}) - i\mathbf{f}_{jl} (b_j b_l^* - \text{H.c.})], \quad (\text{D.13})$$

with $\mathbf{g}_{jl} = -\nabla g_{jl}$ and $\mathbf{f}_{jl} = -\nabla f_{jl}$. As the dispersive force \mathbf{g}_{jl} is a steep function of r_{jl} , it dominates at short distance, and atoms are drastically accelerated/decelerated. Both the dispersive and dissipative forces are anisotropic and couple motion along different directions.

Due to the presence of spontaneous emission and radiative interactions, the atomic momentum also diffuses over time, which can be described by including classical noise $d\xi_i^\alpha$ in the equation of motion for p_i^α . The components of these noises are correlated, and characterized by the diffusion

matrix

$$E[d\xi_i^\alpha(t)d\xi_i^\beta(t')] = \delta_{\alpha,\beta} \frac{2 - \delta_{\alpha,z}}{10} \hbar^2 k_0^2 \Gamma(s_i + 1) \delta(t - t'), \quad (\text{D.14})$$

$$E[d\xi_i^\alpha(t)d\xi_j^\beta(t')] = -2\hbar^2 k_0^2 \nabla_\alpha \nabla_\beta f(r_{ij}) \Re[b_i^* b_j] \delta(t - t'), \quad (\text{D.15})$$

where $E[\cdot]$ denotes the expectation value.

The momentum diffusion matrix can be found from

$$\begin{aligned} \mathcal{D}_{jl} &= \frac{d\langle \hat{\mathbf{p}}_j \hat{\mathbf{p}}_l \rangle}{dt} - \langle \mathbf{p}_j \rangle \frac{d\langle \mathbf{p}_l \rangle}{dt} - \frac{d\langle \mathbf{p}_j \rangle}{dt} \langle \mathbf{p}_l \rangle \\ &= \sum_{\mathbf{k}_1, \epsilon_1} \sum_{\mathbf{k}_2, \epsilon_2} g_{k_1} g_{k_2} (\mathbf{d}_j \cdot \epsilon_1) (\mathbf{d}_l \cdot \epsilon_2) (i\mathbf{k}_1 e^{i\mathbf{k}_1 \cdot \mathbf{r}_j} \hat{a}_{\mathbf{k}_1 \epsilon_1} \hat{b}_j^\dagger \\ &\quad - i\mathbf{k}_1 e^{-i\mathbf{k}_1 \cdot \mathbf{r}_j} \hat{a}_{\mathbf{k}_1 \epsilon_1}^\dagger \hat{b}_j \\ &\quad + i\mathbf{k}_1 e^{i\mathbf{k}_1 \cdot \mathbf{r}_j} \hat{a}_{\mathbf{k}_1 \epsilon_1} \hat{b}_j - i\mathbf{k}_1 e^{-i\mathbf{k}_1 \cdot \mathbf{r}_j} \hat{a}_{\mathbf{k}_1 \epsilon_1}^\dagger \hat{b}_j^\dagger) \\ &\quad \times (i\mathbf{k}_2 e^{i\mathbf{k}_2 \cdot \mathbf{r}_l} \hat{a}_{\mathbf{k}_2 \epsilon_2} \hat{b}_l^\dagger - i\mathbf{k}_2 e^{-i\mathbf{k}_2 \cdot \mathbf{r}_l} \hat{a}_{\mathbf{k}_2 \epsilon_2}^\dagger \hat{b}_l \\ &\quad + i\mathbf{k}_2 e^{i\mathbf{k}_2 \cdot \mathbf{r}_l} \hat{a}_{\mathbf{k}_2 \epsilon_2} \hat{b}_l - i\mathbf{k}_2 e^{-i\mathbf{k}_2 \cdot \mathbf{r}_l} \hat{a}_{\mathbf{k}_2 \epsilon_2}^\dagger \hat{b}_l^\dagger) \\ &= -2\hbar^2 k_0^2 \nabla \nabla f_{ij} \Re[b_j^* b_l]. \end{aligned} \quad (\text{D.17})$$

In dense clouds momentum diffusion from radiative interactions can give rise at long times to significant heating. This heating was reported to be one of the main limiting mechanisms in laser cooling [42, 230]. At short times, $t\Gamma \sim 1$, with low densities and weak probes, $\Omega < \Gamma$, the momentum diffusion is not prominent, and since this is the regime we are interested in this work, we will ignore momentum diffusion in our calculations presented in the main text.

D.2 Effect of motion on single-atom fluorescence

Here we derive the fluorescence intensity emitted by a weakly driven atom, using a full quantum approach with motional effect included. We consider the states including at most one excitation, and label the relevant quantum states by $|\mathbf{p}\alpha, 0\rangle, |\mathbf{p}g, \mathbf{k}_\epsilon\rangle$, with $\alpha = \{e, g\}$, \mathbf{p} the

momentum of the atom, and $\mathbf{k}(\epsilon)$ being the momentum (polarization) of the photon in vacuum ($|\mathbf{p}\alpha, 0\rangle$ stands for no photon). For generality we assume here that two counter propagating lasers are used to drive the atoms, carrying momentum \mathbf{k}_0 and $-\mathbf{k}_0$ respectively. The Hamiltonian is ¹

$$\begin{aligned} \hat{H} = & \frac{\hat{\mathbf{p}}^2}{2m} + \hbar\omega_a \hat{b}^\dagger \hat{b} + \hbar\Omega [\cos(\mathbf{k}_0 \cdot \mathbf{r})(e^{-i\omega_L t} \hat{b}^\dagger + \text{H.c.})] \\ & + \sum_{\mathbf{k}, \epsilon} \hbar\omega_k \hat{a}_{\mathbf{k}\epsilon}^\dagger \hat{a}_{\mathbf{k}, \epsilon} - \hbar \sum_{\mathbf{k}, \epsilon} (\mathbf{d} \cdot \hat{\epsilon}_{\mathbf{k}}) g_k [e^{i\mathbf{k} \cdot \mathbf{r}} \hat{a}_{\mathbf{k}\epsilon} \hat{b}^\dagger + \text{H.c.}]. \end{aligned} \quad (\text{D.18})$$

The state vector of the system is

$$\begin{aligned} |\psi\rangle = & \sum_{\alpha} \int d\mathbf{p} |\mathbf{p}\alpha, 0\rangle A_{\alpha 0}(\mathbf{p}, t) e^{-i(E_{\alpha} + E_p)t/\hbar} \\ & + \sum_{\mathbf{k}, \epsilon} \int d\mathbf{p} |\mathbf{p}g, \mathbf{k}\epsilon\rangle B_{g\mathbf{k}\epsilon}(\mathbf{p}, t) e^{-i(E_g + E_p + \hbar\omega_k)t/\hbar}, \end{aligned} \quad (\text{D.19})$$

where $E_{\alpha} = \omega_a \delta_{\alpha, e}$, $E_p = \frac{p^2}{2m}$, $|A_{\alpha 0}(\mathbf{p}, t)|^2$ represents the population in the state α possessing momentum \mathbf{p} , and $B_{g\mathbf{k}\epsilon}(\mathbf{p}, t)$ is the amplitude of having a photon \mathbf{k} with polarization ϵ . The state

¹ Note: The counterrotating terms such as $\hat{a}_{\mathbf{k}\epsilon} \hat{b}$ have been dropped because the relevant states are restricted to including at most one excitation.

of the system evolves according to

$$\begin{aligned}
i\frac{dA_{g0}(\mathbf{p}, t)}{dt} &= \Omega A_{e0}(\mathbf{p} + \mathbf{k}, t)e^{i(\omega_L - \omega_a)t}e^{-iE_{\mathbf{p}+\mathbf{k}_0, \mathbf{p}}t/\hbar} \\
&\quad + \Omega A_{e0}(\mathbf{p} - \mathbf{k}, t)e^{i(\omega_L - \omega_a)t}e^{-iE_{\mathbf{p}-\mathbf{k}_0, \mathbf{p}}t/\hbar},
\end{aligned} \tag{D.20}$$

$$\begin{aligned}
i\frac{dA_{e0}(\mathbf{p}, t)}{dt} &= -\sum_{\mathbf{k}, \epsilon} (\mathbf{d} \cdot \hat{\epsilon}_{\mathbf{k}}) g_k B_{g\mathbf{k}\epsilon}(\mathbf{p} - \mathbf{k}, t) \\
&\quad \times e^{-i(\omega_k - \omega_a)t}e^{-iE_{\mathbf{p}-\mathbf{k}, \mathbf{p}}t/\hbar} \\
&\quad + \Omega A_{g0}(\mathbf{p} - \mathbf{k}, t)e^{-i(\omega_L - \omega_a)t}e^{-iE_{\mathbf{p}-\mathbf{k}_0, \mathbf{p}}t/\hbar} \\
&\quad + \Omega A_{g0}(\mathbf{p} + \mathbf{k}, t)e^{-i(\omega_L - \omega_a)t}e^{-iE_{\mathbf{p}+\mathbf{k}_0, \mathbf{p}}t/\hbar},
\end{aligned} \tag{D.21}$$

$$\begin{aligned}
i\frac{dB_{g\mathbf{k}\epsilon}(\mathbf{p}, t)}{dt} &= B_{g\mathbf{k}\epsilon}(\mathbf{p}, t) - (\mathbf{d} \cdot \hat{\epsilon}_{\mathbf{k}}) g_k A_{e0}(\mathbf{p} + \mathbf{k}, t) \\
&\quad \times e^{i(\omega_k - \omega_a)t}e^{-iE_{\mathbf{p}+\mathbf{k}, \mathbf{p}}t/\hbar},
\end{aligned} \tag{D.22}$$

where $E_{p_1, p_2} = \frac{p_1^2 - p_2^2}{2m}$. The first term in Eq. (D.21) describes the effect of vacuum photons, which according to Wigner-Weisskopf approach leads to the spontaneous decay with rate Γ , and can be rewritten as [137]

$$\begin{aligned}
i\frac{dA_{e0}(\mathbf{p}, t)}{dt} &= -i\frac{\Gamma}{2}A_{e0}(\mathbf{p}, t) + \Omega A_{g0}(\mathbf{p} - \mathbf{k}, t) \\
&\quad \times e^{-i(\omega_L - \omega_a)t}e^{-iE_{\mathbf{p}-\mathbf{k}_0, \mathbf{p}}t/\hbar} \\
&\quad + \Omega A_{g0}(\mathbf{p} + \mathbf{k}, t)e^{-i(\omega_L - \omega_a)t}e^{-iE_{\mathbf{p}+\mathbf{k}_0, \mathbf{p}}t/\hbar}.
\end{aligned} \tag{D.23}$$

Consider the initial condition $B_{g\mathbf{k}\epsilon}(\mathbf{p}, 0) = 0$, $A_{g0} = \delta(\mathbf{p} - \mathbf{p}_0)$, where \mathbf{p}_0 is the initial momentum of the atom. The steady state solution is

$$A_{e0}(\mathbf{p}, \infty) = \frac{\Omega[\delta(\mathbf{p}_0 - \mathbf{p} + \mathbf{k}_0) + \delta(\mathbf{p}_0 - \mathbf{p} - \mathbf{k}_0)]}{\Delta_L + E_{\mathbf{p}_0, \mathbf{p}} + i\frac{\Gamma}{2}}, \tag{D.24}$$

with $\Delta_L = \omega_L - \omega_a$. Thus the atomic excitation $\mathcal{A}_e = \int d\mathbf{p} |A_{e0}(\mathbf{p}, \infty)|^2$ indicates two Lorentzian with FWHM= Γ and centered at $\omega_r \pm \frac{\mathbf{k}_0 \cdot \mathbf{p}_0}{m}$. The photon emission rate along a given direction \mathbf{k}_s is

$$I_{\mathbf{k}_s} = \frac{V\hbar c}{(2\pi)^3} \int dk k^3 \sum_{\epsilon} \int d\mathbf{p} \lim_{t \rightarrow \infty} \frac{|B_{g\mathbf{k}\epsilon}(\mathbf{p}, t)|^2}{t}, \quad (\text{D.25})$$

with $\mathbf{k} = k\hat{\mathbf{k}}_s$. We consider the transverse intensity case where, $\mathbf{k} \cdot \mathbf{k}_0 = 0$, and for atomic transitions ω_r , $\mathbf{p}_0 \cdot \mathbf{k}_0/m \ll \omega_L$, then

$$I_{\mathbf{k}_s} \approx \frac{\omega_L^4}{c^3} \frac{d^2\Omega^2}{8\pi^2\epsilon_0} \left[\frac{1}{(\Delta - \omega_r + \frac{\mathbf{k}_0 \cdot \mathbf{p}_0}{m})^2 + \frac{\Gamma^2}{4}} + \frac{1}{(\Delta - \omega_r - \frac{\mathbf{k}_0 \cdot \mathbf{p}_0}{m})^2 + \frac{\Gamma^2}{4}} \right]. \quad (\text{D.26})$$

The emitted light intensity exhibits the same profile as the atomic excitation \mathcal{A}_e .

As indicated by the above expression, motion modifies the emitted light intensity by adding two natural corrections: a Doppler shift $\propto \frac{\mathbf{k}_0 \cdot \mathbf{p}_0}{m}$, modifying the effective laser detuning, and a velocity independent recoil shift, ω_r , which physically accounts for the fact that to compensate for the energy imparted to the atom via photon recoil, the incident laser needs to have a higher frequency to be resonant with the atomic transition.

Appendix E

Calculation of Weyl dispersion

E.1 Dispersion near Weyl nodes

We define the quasiparticle dispersion as the poles of the retarded Green's function averaged with respect to quenched disorder.

While long-wave quasiparticles ($\mathbf{k} \rightarrow 0$) are insensitive to the details of the lattice potential, their effective Hamiltonian preserves rotation and inversion symmetries, and in the absence of magnetic field–time-reversal symmetry, with the generic form of the Hamiltonian given by Eq. (7.1) and with the vector $\boldsymbol{\omega}$ parallel to the magnetic field.

We assume the existence of excitations with momentum $J = 1$ and focus on the respective manifold of states in what follows. The dispersion of such excitations has three branches for each momentum \mathbf{k} .

For momenta \mathbf{k} parallel to $\boldsymbol{\omega}$ the respective excitations have momentum projections $J_z = 0$ and $J_z = \pm 1$ on the direction $\boldsymbol{\omega}$. The branch with $J_z = 0$ intersects the branch with $J_z = \pm 1$ at momenta $\mathbf{K} \parallel \boldsymbol{\omega}$ such that

$$F(|\mathbf{K}|, K^2, 2) \pm \omega = F(|\mathbf{K}|, 0, 2), \quad (\text{E.1})$$

where we used that $\hat{J}^2 = J(J + 1) = 2$ for the states under consideration.

The quasiparticle dispersion near the nodes can be found by expanding the Hamiltonian in small momenta $\mathbf{p} = \mathbf{k} - \mathbf{K}$. Momentum deviation from a node along the z axis leads to the splitting $F[K + p_z, (K + p_z)^2, 2] \pm \omega - F[K + p_z, 0, 2]$ between the intersecting branches. Using

that $[(\mathbf{K} + \mathbf{p}) \cdot \hat{\mathbf{J}}]^2 \approx \frac{K^2}{2} + \frac{K^2}{2} \hat{\sigma}_z + K p_z + K p_z \hat{\sigma}_z \pm \frac{K}{\sqrt{2}} (p_x \hat{\sigma}_x + p_y \hat{\sigma}_y)$, with $\hat{\sigma}_i$ being the Pauli matrices in the space of momentum projections $J_z = +1$ ($J_z = -1$) and $J_z = 0$, we obtain the quasiparticle Hamiltonian (7.2) with

$$\begin{aligned} \zeta(\mathbf{p}) &= \frac{1}{2} F [K + p_z, (K + p_z)^2, 2] - \frac{1}{2} F [K, K^2, 2] \\ &\quad + \frac{1}{2} F(K + p_z, 0, 2) - \frac{1}{2} F(K, 0, 2), \end{aligned} \quad (\text{E.2})$$

$$v_{\perp} = \pm \frac{1}{\sqrt{2}} K F^{(2)}(K, K^2, 2) \quad (\text{E.3})$$

$$\begin{aligned} v_{\parallel} &= K F^{(2)}(K, K^2, 2) \\ &\quad + \frac{1}{2} [F^{(1)}(K, K^2, 2) - F^{(1)}(K, 0, 2)] \end{aligned} \quad (\text{E.4})$$

where the upper (lower) sign in Eq. (E.3) applies to the intersection of the $J_z = 0$ branch with $J_z = +1$ ($J_z = -1$), and $F^{(1)}$ and $F^{(2)}$ are the derivatives of the function F with respect to the first and the second argument.

E.2 Excitation dispersion in a deep lattice

As particles cannot move from site to site in a deep optical lattice, the quasiparticles are represented by the angular-momentum degrees of freedom that propagate through the system. Assuming there is one particle per site and introducing bosonic operators $\hat{d}_i^{\sigma\dagger}$ and \hat{d}_i^{σ} for creating and annihilating the particle state $|1\sigma\rangle_i$ on site i with angular momentum $J = 1$ and projection σ and the operators \hat{a}_i^{\dagger} and \hat{a}_i for creating and annihilating the momentum state $J = 0$ on site i , the

system Hamiltonian can be rewritten as

$$\begin{aligned}
\hat{H} = & \sum_{i,j,\sigma,\sigma'} \langle 1\sigma|_i \langle 00|_j \hat{H}_{\text{dip}} \left(\hat{\mathbf{d}}_i \hat{\mathbf{d}}_j, \mathbf{r}_{ij} \right) |00\rangle_i |1\sigma'\rangle_j \hat{d}_i^{\sigma\dagger} \hat{d}_j^{\sigma'} \hat{a}_j^\dagger \hat{a}_i \\
& + \sum_{i,j,\sigma,\sigma'} \left[\langle 1\sigma|_i \langle 1\sigma'|_j \hat{H}_{\text{dip}} \left(\hat{\mathbf{d}}_i \hat{\mathbf{d}}_j, \mathbf{r}_{ij} \right) |00\rangle_i |00\rangle_j \hat{d}_i^{\sigma\dagger} \hat{d}_j^{\sigma'\dagger} \hat{a}_j \hat{a}_i \right. \\
& \quad \left. + \langle 00|_i \langle 00|_j \hat{H}_{\text{dip}} \left(\hat{\mathbf{d}}_i \hat{\mathbf{d}}_j, \mathbf{r}_{ij} \right) |1\sigma\rangle_i |1\sigma'\rangle_j \hat{a}_j^\dagger \hat{a}_i^\dagger \hat{d}_i^\sigma \hat{d}_j^{\sigma'} \right] \\
& - B \sum_{i\sigma} \sigma \hat{d}_i^{\sigma\dagger} \hat{d}_i^\sigma \hat{a}_i \hat{a}_i^\dagger + B_J \sum_{i\sigma} \hat{d}_i \sigma^\dagger \hat{d}_i^\sigma \\
& + U \sum_{i\sigma} \left[\hat{d}_i^{\sigma\dagger} \hat{d}_i^\sigma \left(\hat{d}_i^{\sigma\dagger} \hat{d}_i^\sigma - 1 \right) + \hat{a}_i^\dagger \hat{a}_i \left(\hat{a}_i^\dagger \hat{a}_i - 1 \right) + \hat{d}_i^{\sigma\dagger} \hat{d}_i^\sigma \hat{a}_i^\dagger \hat{a}_i \right]. \tag{E.5}
\end{aligned}$$

The first term in the Hamiltonian (E.5) is responsible for moving angular-momentum excitations from site to site; the angular-momentum state $|1\sigma\rangle_i$ can be transferred by the dipole-dipole interactions from site i to another state $|1\sigma'\rangle_j$ on site j that initially was in the $J = 0$ state. The terms in the second sum in Eq. (E.5) change pairs of sites i and j from the $J = 0$ to $J = 1$ angular-momentum states or vice versa. The term $\propto B$ is the Zeeman energy. The term $\propto B_J$ accounts for the internal rotation (internal levels) of the particles. The terms $\propto U = \infty$ in Eq. (E.5) enforce the hard-core constraints for the bosons created by the operators $\hat{d}_i^{\sigma\dagger}$ and \hat{a}_i^\dagger , taking into account that there is one particle on each site.

In chapter 7 we consider excitations on top of the ground state with all sites (particles) in the $J = 0$ state. Exciting the internal degree of freedom of a particle on a site costs the rotation energy B_J that significantly exceeds all the other energy scales, except $U = \infty$, including the matrix elements $\sim |\hat{H}_{\text{dip}}|$ of hopping of such angular-momentum degrees of freedom between sites (for instance, for dipolar molecules and alkaline-earth atoms $|\hat{H}_{\text{dip}}|/B_J \lesssim 10^{-6}$). As a result, the number of sites excited to the $J = 1$ states is conserved to a good approximation, and the second sum in Eq. (E.5), that creates or annihilates pairs of $J = 1$ excitations, can be neglected when considering the angular-momentum dynamics.

Therefore, the quasiparticles in the system are hard-core bosons that carry angular-momentum ($J = 1$) degrees of freedom and hop from site to site as described by the effective Hamiltonian (7.6)-(7.7) with $\hat{b}_{i\sigma} = \hat{d}_i^{\sigma\dagger} \hat{a}_i^\dagger$.

E.3 Details of disorder averaging.

Realistic systems of particles pinned in deep optical lattices are inherently disordered due to the randomness of the spatial distribution of the particles. Each lattice site hosts either a particle with probability f or a vacancy with probability $1 - f$.

For a small concentration of vacancies, excitations in the system are delocalised and their dispersion is close to that in the disorder-free system but acquires a small finite imaginary part $\text{Im}E_{\mathbf{k}}$ due to the scattering on the vacancies.

In order to numerically obtain the quasiparticle spectra in such a disordered system we diagonalise the Hamiltonian $\hat{\mathcal{H}} = \hat{\mathcal{H}}_0 + \hat{V}$, where $\hat{\mathcal{H}}_0$ is the excitation Hamiltonian in the clean case and the operator \hat{V} models vacancies as sites with infinite potential $V(\mathbf{r}_i) = \infty$. We compute the retarded Green's function

$$G(\mathbf{r}_1\sigma_1, \mathbf{r}_2\sigma_2, E) = \sum_{\alpha} \frac{\psi_{\alpha\sigma_1}^*(\mathbf{r}_1)\psi_{\alpha\sigma_2}(\mathbf{r}_2)}{E - E_{\alpha} + i\eta} \quad (\text{E.6})$$

for multiple disorder realisations, where ψ_{α} and E_{α} are the eigenfunctions and eigenenergies for a particular disorder realisation, σ_1 and σ_2 label projections of the angular momentum $J = 1$, and η is a small positive number introduced to ensure that the disorder-averaged Green's function $\langle G(\mathbf{r}_1\sigma_1, \mathbf{r}_2\sigma_2, E) \rangle_{\text{dis}}$ is a smooth function of its arguments for a given number of disorder realisations. At the same time, η has to be chosen sufficiently small to not affect the results for the quasiparticle dispersion. The energy E has to be chosen close to the energies of the quasiparticles of interest.

Disorder averaging restores translational invariance, yielding an averaged Green's function that depends only on the coordinate difference $\mathbf{r}_2 - \mathbf{r}_1$. Computing the Fourier transform of the function $\langle G(\mathbf{r}_1\sigma_1, \mathbf{r}_2\sigma_2, E) \rangle_{\text{dis}}$ with respect to $\mathbf{r}_2 - \mathbf{r}_1$ and diagonalising it in the angular-momentum space gives $1/(E - E_{\mathbf{k}n})$, where $n = 1, 2, 3$ labels the dispersion branch for a given \mathbf{k} , $\text{Re}E_{\mathbf{k}n}$ is the quasiparticle dispersion and $-2\text{Im}E_{\mathbf{k}n}$ the scattering rate.

In chapter 7 we perform averaging over 100 disorder realisations on a $10 \times 10 \times 10$ cubic lattice with periodic boundary conditions for the filling fraction $f = 0.93$, close to that in the

recent experiments [126, 221, 92]. The results for the quasiparticle dispersion and scattering rates are shown in Fig. 7.3c.